THE RISE OF CALDERA FORMING ERUPTIONS:

REFINING TOOLS FOR UNDERSTANDING MAGMA ASCENT

by

Megan Ann Harris

A dissertation submitted in partial fulfillment
of the requirements for the degree

of

Doctor of Philosophy

in

Earth Sciences

MONTANA STATE UNIVERSITY
Bozeman, Montana

December 2022

DEDICATION

To my Mom

ACKNOWLEDGEMENTS

They say it takes a village. Luckily my village is pretty awesome. None of this would have been possible without all of you.

Thank you to my MOnSTER lab mates, and especially to (soon-to-be) Dr. Behnaz Hosseini, for always helping work through problems, being my writing accountability buddy and for the countless coffee walks. Thank you to my girl gang, Dr. Sheridan Moore and Ms. Jessica McGuire. You two keep me sane. Thank you for all the memes, gossip, advice, and guidance you've both given me over the years and for always being down to go on an adventure. I love you both so much!

To my advisor: Dr. Madison Myers, I am eternally grateful for your guidance on this wild journey. Thank you for always letting me be me and for always being my biggest champion. You have definitely made me a better scientist. Your relentless support of my goals allowed me to thrive, and I know I wouldn't be where I'm at without you. I'm so proud to be your first little MoNSTER and I couldn't dream of doing this with anyone else!

To my husband: Spencer, I really can't even start to describe how much you mean to me. Thank you for your encouragement and for always believing in me even when I didn't believe in myself. You inspire me every day. Finally, to my #1 fan since the beginning…Mom, thank you for all your love always. You've been there for me every step of the way and your support means everything to me. And yes, I finally finished "writing my paper." ☺

This work was made possible by funding from the National Science Foundation EAR award 1922513 to M. Myers

TABLE OF CONTENTS

TABLE OF CONTENTS CONTINUED

LIST OF TABLES

Table Page

LIST OF FIGURES

Figure Page

LIST OF FIGURES CONTINUED

Figure Page

DISSERTATION ABSTRACT

The rate at which magma moves from the magma chamber to the surface influences the amount of degassing and crystallization that occurs, which in turn controls the style and intensity of the ensuing eruption. Thus, our understanding of magma ascent rates is crucial to understanding and mitigating future volcanic hazards. The bulk of this dissertation revolves around using the diffusion of water through melt-filled pockets (embayments) in quartz crystals as an ascent speedometer, coupled with geochemical and textural analysis of co-erupted material. In Chapter Two, I apply and refine the water diffusion speedometer to establish timescales of ascent for the two eruptions that formed the modern-day Valles Caldera, with the aim of understanding whether these rates change during subsequent eruptions from the same caldera. In Chapter Three, I apply the diffusion speedometer to the opening behavior of the 1991 eruption of Mount. Pinatubo and compare the results to ascent rates obtained using independent petrologic methods (bubble number density and microlite number density). This chapter seeks to reconcile the several orders of magnitude offset in ascent rates produced by various geospeedometers. Finally, in Chapter Four, I explore the mechanisms by which embayments are formed in magmatic systems. I do this by conducting a survey of cathodoluminescence images of crystals taken from five volcanic systems to determine how the embayments interact with the internal zoning of the crystal. I then attempt to form embayments experimentally using a cold-seal pressure vessel under variable magmatic conditions. The culmination of this work emphasizes that embayments are robust and faithful recorders of a magma's journey from its source to the surface and may be a critical piece of evidence for unraveling the magmatic history leading to eruption. This dissertation includes both previously published and unpublished co-authored work.

CHAPTER ONE

PREAMBLE

The rate at which magma rises through the conduit during an eruption is one of the most important parameters controlling the style of the ensuing eruption. As this process is occurring below the surface, it is often difficult to quantify, and thus, we must rely on petrologic recorders to recover what can be highly dynamic and shifting conditions.

This dissertation seeks to answer the following questions:

1. How does the existence of a preexisting caldera system affect the ascent rate of a subsequent eruption?
2. Can we reconcile disagreement in ascent rates determined by various petrologic tools?
3. How reliably does an embayment in a mineral record decompression information, and are the models and assumptions we use to extract these rates robust?
4. What conditions within a magmatic system lead to the formation of embayments and what insights can this provide into silicic systems?

To answer these questions, I integrate geochemical analysis of embayments (major, trace, and volatile elements) with textural characterization of whole pumices (bubble and microlite textures) and chemical zoning patterns of quartz crystals (cathodoluminescence imaging).

Chapter Two was co-authored by Madison Myers (Montana State University), Rebecca deGraffenried (Arizona State University), Thomas Shea (University of Hawaii Manoa), and Clara Waelkens (Leibniz University Hannover). Chapter Two was published in the *Bulletin of Volcanology* in January 2022. This work sought to investigate how the magma ascent rate would be affected by a second eruption from an existing caldera system. While the ascent rate does not

vary significantly between the two eruptions, I find that the magma pathway is established more efficiently during the second eruption, hinting that preexisting structural weakness might influence subsequent eruptions. Additionally, in this chapter, I applied a 2D version of the diffusion model to assess the influence of embayment geometry on the recovered ascent rate. Agreeing with previous numerically driven studies, we found that while the most extremely shaped embayments show up to a 4x increase in ascent time between 2D vs. 1D approaches, embayments with more tubular shapes are unaffected. This study presents the first data on embayment ascent for two eruptions from the same caldera system, as well as the first time a 2D modeling approach has been carried out on natural samples.

Chapter Three was co-authored with Madison Myers (Montana State University), Behnaz Hosseini (Montana State University), and Logan Bouley (Montana State University) and is in preparation for submission to the *Journal of Volcanology and Geothermal Research*. I apply three different petrologic ascent rate speedometers to tephra produced during the first preclimactic eruption of Mount Pinatubo in 1991. These three petrologic tools have all been recently updated to include non-linear decompression paths in an attempt to better recreate the natural system and to narrow the gap between ascent rates from different tools. I find that by using a two-stage embayment diffusion model, the embayments return ascent rates that agree with the more traditional methods (bubble and microlite number densities), which previously varied by several orders of magnitude. This work emphasizes the fact that embayments are a reliable recorder of magma ascent through both the deep conduit and the shallow conduit, whereas both bubble and microlite number densities would be required to restore the same pathway.

Chapter Four, co-authored by Madison Myers (Montana State University) and Nathan Lenhard (Missouri State University) and in preparation for submission to *Geology*, tests the mechanisms of embayment formation in natural and experimental quartz. The results of cathodoluminescence imaging suggest that unstable rapid crystal growth is the major mechanism for embayment formation in natural samples; however, our experimental results show that crystal dissolution via superheating is an easier pathway to embayment genesis. The kinetic reaction timescale of these experiments has major implications for the lifespan of quartz crystals and highlights the importance of further experimentation to constrain the lifespan and reaction of quartz growth and dissolution in silicic systems.

CHAPTER TWO

ON THE RISE: USING EMBAYMENTS TO EXTRACT MAGMA ASCENT RATES IN THE BANDELIER TUFF CALDERA COMPLEX NEW MEXICO, USA

Contribution of Authors and Co-Authors

Manuscript in Chapter Two

Author: Megan A. Harris

Contributions: Sample preparation, data collection and modeling, manuscript preparation

Co-Author: Madison L. Myers

Contributions: Project conception, manuscript editing

Co-Author: Rebecca deGraffenried

Contributions: Development of 2D diffusion code

Co-Author: Thomas Shea

Contributions: Development of 2D diffusion code

Co-Author: Clara Waelkens

Contributions: Sample collection, melt inclusion analysis

Manuscript Information Page

Megan A. Harris, Madison L. Myers, Rebecca deGraffenried, Thomas Shea, Clara Waelkens
Bulletin of Volcanology
Status of Manuscript:
____ Prepared for submission to a peer-reviewed journal
____ Officially submitted to a peer-review journal
____ Accepted by a peer-reviewed journal
_X_ Published in a peer-reviewed journal

Published by International Association of Volcanology and Chemistry of the Earth`s Interior (IAVCEI)
June 17, 2021
December 8, 2021
Volume 84, January 2022

Abstract

The Bandelier Tuff is the result of two subsequent caldera-forming eruptions of similar volume and composition, which produced the Otowi (1.61 Ma) and Tshirege (1.26 Ma) members. Their remarkably similar characteristics and shared caldera boundaries provide a unique platform to investigate whether magma ascent is affected by the presence of a preexisting caldera boundary. Here, we present decompression rates for discrete layers within the initial Plinian phase of each member by modeling volatile gradients (H_2O, CO_2 absent) in quartz-hosted embayments (unsealed melt inclusions). Successful best-fit 1D diffusion models for the lower (n = 4/9) and upper (n = 11/13) units resulted in average decompression rates of 0.041 MPa/s and 0.026 MPa/s, respectively. Strong overlap between rates extracted from the two eruptions suggests there was no significant change in ascent dynamics. However, the older Otowi member contains a larger number of embayments that cannot be modeled adequately, suggesting a more complicated path than can be reconstructed with our constant decompression approach. In contrast, embayments from the Tshirege can be readily modeled from storage depths, an observation that suggests conduit formation was more efficient in the second eruption. To further evaluate the robustness of these extracted rates, we then applied a 2D diffusion model, which considers various embayment geometries; surprisingly, we find little alteration to 1D-derived rates. By contrast, incorporating the uncertainty in Bandelier temperature (~130°C) shifts rates by 340–440%. However, we argue that the largest source of variation from decompression rates extracted from embayments lies in the extreme range preserved within each fall deposit, each spanning three orders of magnitude, suggesting extreme conduit dynamic shifts and emphasizing that petrologic-based ascent rates may vary widely, even within a single-sampled layer. Finally,

the lack of detectable CO_2 concentrations in measured profiles is at odds with the amounts detected in sealed melt inclusions (< 200 ppm), an observation that has been made in other silicic systems (e.g., Bishop, USA; Oruanui, NZ; Santorini, GR). We propose two mechanisms to remove CO_2 from the system prior to eruption: 1) additional crystallization drove CO_2 into the fluid phase prior to ascent or 2) embayments reset to a CO_2-free environment due to a small, initial preeruptive pressure decrease. Both scenarios have important implications for the preeruptive state of the magma body.

Introduction

As magma decompresses during its ascent toward the surface, the solubility of volatiles (H_2O, CO_2, S) in the melt decreases, which results in the exsolution of volatiles into a separate fluid phase and the decrease of their concentration dissolved in the melt. The rate at which magma rises to the surface has a strong control over the behavior of these exsolved volatiles, which in turn directly affects the explosivity of an eruption and modulates explosive/effusive transitions (Eichelberger et al., 1986; Cashman, 2004; Castro and Gardner, 2008; Cassidy et al., 2018). Constraining variations in magma decompression rates through an eruptive sequence may help us to better interpret the evolution and timing of these degassing processes and determine how decompression conditions may relate to variations in eruption dynamics. A variety of techniques have been used to estimate decompression rates based on petrologic indicators of volatile loss, including the chemical breakdown of phenocrysts (i.e., amphibole rims; Rutherford and Hill 1993; Rutherford and Devine, 2003), microlite nucleation and growth (Hammer et al. 1999; Castro and Gardner, 2008), and bubble number density (Toramaru 2006; Hamada et al., 2010). However, in rhyolitic magma, these indicators are limited by kinetics and can only

resolve slower decompression histories (days to weeks) or are skewed by processes occurring in specific parts of the conduit (i.e., rapid bubble nucleation near the fragmentation front; Mangan et al., 1993; Giachetti et al., 2010; Hajimirza et al., 2021). Thus, many of these methods cannot be applied to study more explosive (often fast) eruptions, involving evolved (kinetically slow) magmas, or for determining decompression rates that represent ascent through the entire conduit system.

One promising technique is to use melt-filled embayments (unenclosed melt inclusions—herein referred to as embayments), which have been shown to respond to changing external conditions (degassing) on timescales of minutes to hours (Liu et al., 2007; Humphreys et al., 2008; Lloyd et al., 2014; Ferguson et al., 2016; Myers et al., 2016, 2018, 2021; Newcombe et al., 2020). Modeling of chemical profiles of volatile species in embayments is a method that can yield an integrated decompression history for rapid rhyolitic magma ascent. For this study, we focus on embayments in caldera-forming systems, where several open questions remain on the dynamics of magma ascent. For instance, embayments in many of these systems lack measurable CO_2, in contrast to the several hundred ppm measured from their co-erupted melt inclusions. Although this has been inferred in some systems to represent an initial slow ascent phase (Myers et al., 2018; Bishop Tuff, USA), there are examples of high H_2O, low CO_2 embayments that are thought to have quickly ascended from storage (Myers et al., 2021; Santorini, GR). While these studies have shed light on the ascent rates of single eruption episodes, no studies have been conducted to compare ascent rates between subsequent eruptive sequences. Lastly, thus far, all embayment modeling studies of natural systems have only employed a 1D modeling approach, even though the geometry of an embayment can significantly affect the calculated ascent rate

(deGraffenried and Shea, 2021). To shed light on some of these open questions, we utilized samples from two subsequent caldera-forming eruptions that together form the Bandelier Tuff, located in northern New Mexico, USA.

The modern-day Bandelier Tuff erupted as two separate eruptions, which were separated by 350,000 years (Izett and Obradovich, 1994; Phillips et al., 2007). A unique aspect of these two eruptions is that they were of similar volume, temperature, and composition and erupted from caldera systems that structurally overlap each other (e.g., Heiken et al., 1986; Self et al., 1986; Heiken et al., 1990). These characteristics allow us the unique opportunity to compare decompression rates between two consecutive eruptions in which all other variables are remarkably similar. Experimental work has shown that caldera-forming eruptions produced from the same magma chamber will reutilize the fracture systems formed during the previous eruption (Marti et al., 1994). The fact that the Bandelier Tuff created two calderas that are perfectly coincident would suggest that the system reactivated an existing ring-fracture system. The reactivation of a previous fracture system has been hypothesized to allow magma pathways between the reservoir and the surface to be established more quickly, resulting in efficient magma ascent directly from the storage conditions (Myers et al., 2021). One overarching question we seek to investigate is whether magma ascent toward the surface at the onset of a subsequent eruption is affected by the reactivation of a previously healed fracture system.

Geologic Background

The Bandelier Tuff and its associated calderas are a part of the Jemez Mountains Volcanic Field (JMVF) (Figure 2.1). The JMVF lies at the intersection of the Jemez Volcanic Lineament and the Rio Grande Rift, where the current spreading rate is <1mm/year (Woodward,

1977; Savage et al., 1980). The JMVF has been volcanically active for 13 Myr, with the first 11 Myr being dominated mostly by mafic and intermediate volcanism (Aldrich, 1986; Wolff and Gardner, 1995). The Bandelier Tuff deposit was formed from two caldera-forming eruptions, each producing ~400 km^3 of material. The Otowi member is the first caldera-forming eruption of the JMVF and is dated at 1.61 Ma (Izett and Obradovich, 1994). This eruption created the Toledo Caldera, the rim of which is partly exposed northeast of the modern-day Valles Caldera that formed during the second eruption (Figure 2.1). The basal unit of the Otowi member is referred to as the Guaje pumice airfall unit, reaching up to 8 meters thick. Due primarily to the decrease in coarse pumice fragments, the Guaje pumice developed bedding in the uppermost 2 meters of the airfall unit (Crowe et al., 1978; Figure 2.2). The upper member of the Bandelier Tuff, formed by the eruption and collapse of the Valles Caldera, is the Tshirege member, dated at 1.26 Ma (Phillips et al., 2007). The Tsankawi pumice, a 3.5-meter thick, massive bed of Plinian airfall deposits, occurs at the base of the Tshirege member (Figure 2.2). In this work, the member names (Otowi/Tshirege) are used when talking about widescale processes occurring within the magma or when referring to the entirety of the deposit including the ignimbrite. When specifically referring to the airfall deposit, the unit names (Guaje/Tsankawi) are used.

Stratigraphically constrained geochemical analysis of erupted pumice clasts and bulk ash suggests that a normal compositionally zoned magma chamber fed the eruption of the Tshirege member. This is indicated by a systematic up-section decrease in whole rock SiO_2 content, from ~78 to 70 wt.% (Sussman et al., 2011; Goff et al., 2014). Within this overall normal compositional zonation, the Tshirege member has a distinct region of reverse zoning (more silicic up section) in the late-stage ignimbrite deposits (Goff et al., 2014). The Otowi member is

less variable in its glass chemistry, with erupted material ranging from ~76-78 wt.% SiO_2 and no relationship between composition and stratigraphic position (Kuentz, 1988). However, the Otowi member displays sharp reverse zoning patterns (increase in Sr and Ba concentrations rimward) in quartz and sanidine crystals from the later erupted portions of the ignimbrite, inferred to be records of an increase in magmatic temperature, suggesting that the recharge of less evolved material could have triggered the eruption (Wark and Wolff, 2006). Similarly, the presence of hornblende dacite pumice fragments in the Tshirege member point to the intrusion of an intermediate or mafic magma body as the eruption trigger (Stimac, 1996, Boro et al., 2020).

Both eruptions contain 10–20% phenocrysts with an assemblage of alkali feldspar and quartz, with minor amounts of plagioclase, iron–titanium oxides, apatite, zircon, and chevkinite (Smith and Bailey, 1966; Goff et al., 2014). The pre-eruption temperature of both airfall deposits was determined to be ~700ºC based on pyroxene-fayalite thermometry (Warshaw and Smith, 1988). This estimate is supported by Ti-in-quartz thermometry (TitaniQ; Wark and Watson, 2006) which gives temperatures of ~660–700 ºC for the Otowi ignimbrite and 685–725 ºC for the Tshirege ignimbrite (Campbell et al., 2009). Other estimates for the Tsankawi airfall are based on amphibole liquid (avg. 725ºC) and feldspar-liquid (avg. 736ºC) thermometry (Boro, 2019). Additional temperatures for the Otowi ignimbrite are based on zircon saturation thermometry and are higher than estimates from Ti-in-quartz thermometry (819–883ºC; Audétat, 2013). The temperature of the Tshirege ignimbrite was also found using Fe-Ti oxides, which yield temperatures of 651–903ºC (avg. 720ºC), and amphibole-melt thermometry, which provides a narrower range ~770–810ºC (avg. 797ºC; Boro et al., 2020). From this review, it is

clear that the pre-eruptive temperatures for the Bandelier Tuff are widely variable (perhaps stratified) and depend on the thermometer applied.

Quartz-hosted, bubble-free, melt inclusions from the airfall contain variable amounts of H_2O (analyzed by Fourier-Transform Infrared—FTIR), ranging from 2.14 to 5.20 wt.%, (avg. 4.05 wt.%) in the Guaje and 1.96 to 5.48 wt.%, (avg. 3.60 wt.%) in the Tsankawi (Waelkens et al., in review). These values are slightly lower than those measured via ion microprobe by Dunbar and Hervig (1992), where Guaje and Tsankawi melt inclusions range from 3.1–6.0 wt.% and 3.5–5.9 wt.% H_2O respectively. Carbon dioxide concentrations in melt inclusions are generally lower in the Tsankawi (<150 ppm), reaching 225 ppm in the top of the Guaje airfall deposit (Waelkens et al., in review). Based on volatile solubility (Newman and Lowenstern, 2002) and the assumption of lithostatic conditions, these combined concentrations correlate to magmatic storage depths of 5–6 km. This is consistent with magma chamber depths of 5–7 km based on fayalite-orthopyroxene barometry and structural modeling (Nielson and Hulen, 1984; Warshaw and Smith, 1988; Stix and Layne, 1996; Goff et al., 2014).

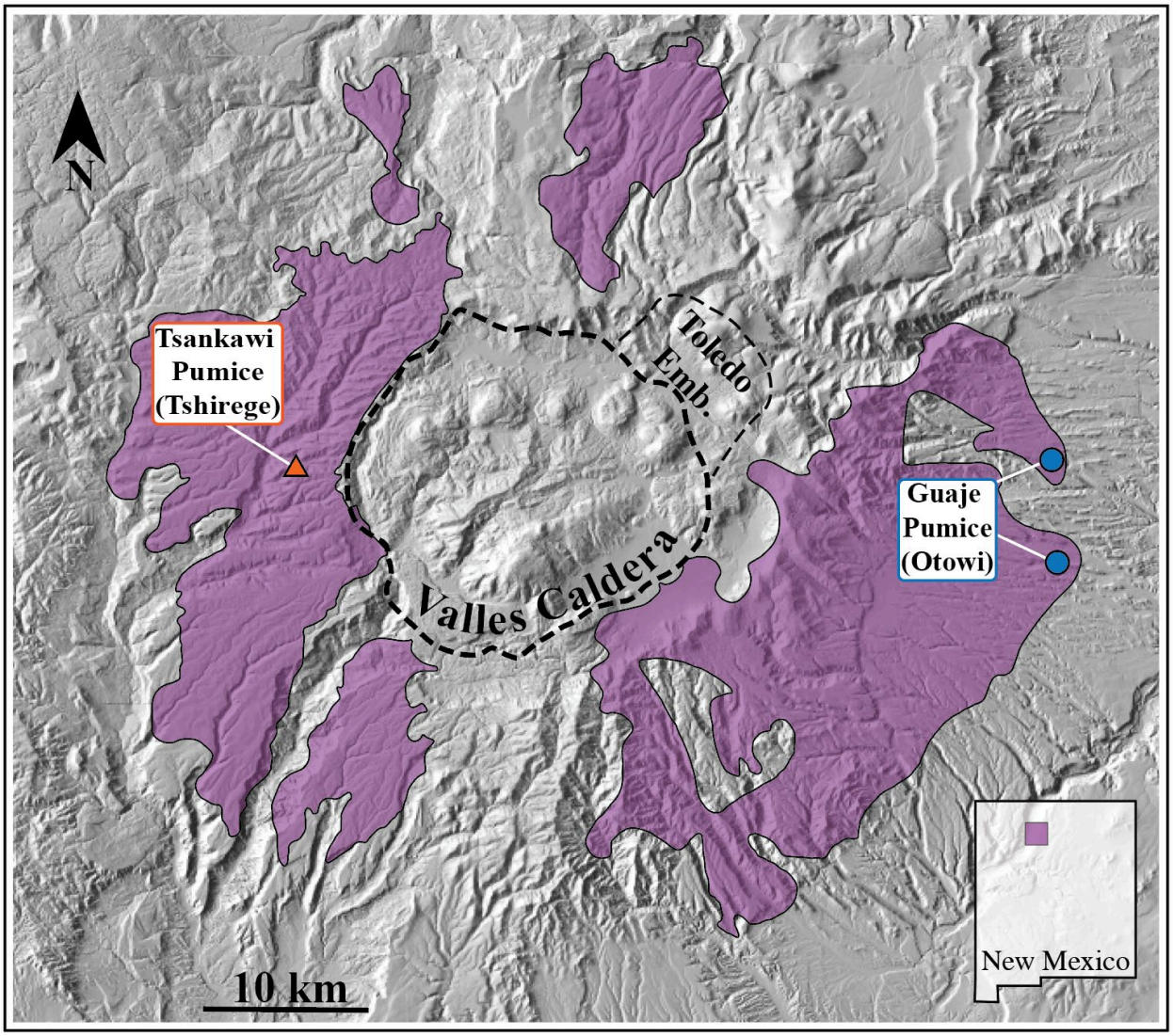

Figure 2.1. Map of the modern-day Valles Caldera (thick dashed line) highlighting the extent of the Bandelier Tuff deposits (purple unit), including Otowi and Tshirege members (modified from Boro et al., 2020). The Valles Caldera is defined by a topographic rim and was formed during the eruption of the Tshirege member (1.26 Ma). It is coincident with the older Toledo Caldera (Otowi member; 1.61 Ma). The Toledo Embayment (possibly associated with eruptions prior to the Otowi member and currently filled with Cerro Toledo Rhyolite domes) is exposed to the northeast of the Valles Caldera and is outlined by the thin dashed line. Orange and blue symbols highlight sample locations.

Methods

Sampling and Polishing

Seven layers of pumice were sampled from the Tsankawi (3 layers) and Guaje (4 layers) airfall units (Figures 2.1 and 2.2). Quartz crystals containing long, tube-like embayments with large external openings were found in all sampled layers. Qualifying embayments (glassy, >100 μm long, bubble at mouth) were picked, mounted to glass slides using crystal bond, and doubly polished along the length of the embayment. All embayments had a visible bubble at the mouth that spanned the width of the embayment, a requirement for diffusive loss of H_2O in an exsolved fluid phase (see Lloyd et al., 2014). We aimed to prepare 3–5 embayments from each unit, although due to challenges with preparation, some units only yielded 1–2 embayments. For one of the Guaje layers (sample G0), every crystal shattered during hand-sample preparation; thus, no embayments were analyzed. Intersected embayments (9 for the Guaje and 13 for the Tsankawi) ranged from 80 to 250 μm in length, ~20–80 μm wide at their narrowest point, and most were either tubular or slightly wider toward the interior (Supplementary Figure 1). Three of the 21 total embayments measured showed significant narrowing toward the rim.

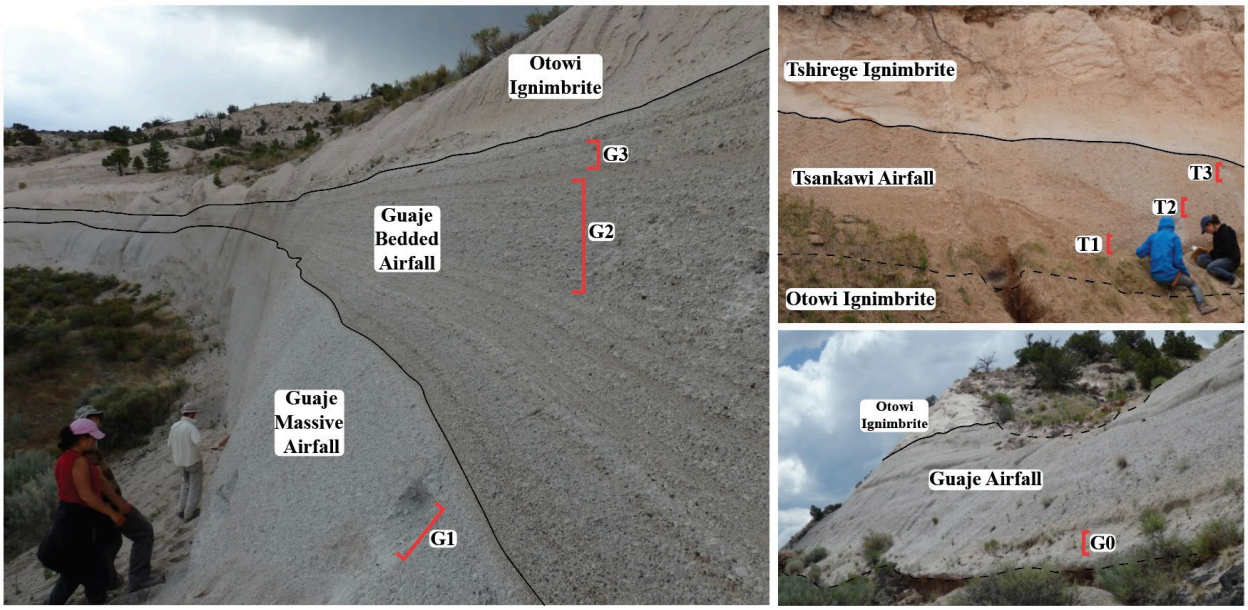

Figure 2.2. Field photos showing the stratigraphic boundaries (sub-horizontal black lines) between the Tsankawi (Tshirege Member) and Guaje (Otowi Member) airfall units and their overlying ignimbrites. Locations of whole pumice and bulk samples are bracketed in red.

FTIR H_2O and CO_2 Analysis

Freed crystal wafers were analyzed using an FTIR spectrometer at the University of Oregon. Concentrations of H_2O and CO_2 were measured with 20–25 μm square spots along the length of the embayment. Embayment lengths allowed for up to 25 FTIR analyses per transect (at 10 μm spacing). Analysis was conducted using a white light source, 256 scans per spot, and a wavelength resolution of 4 (cm^{-1}). FTIR absorbances were measured using a linear regression baseline and were converted to concentration by applying the Beer-Lambert law to the relevant baseline-subtracted peak heights (equation 1):

$$C = \frac{A \cdot M}{\rho \cdot \varepsilon \cdot t} \qquad \text{equation 1}$$

where C is the concentration (wt.%), ρ is the density of rhyolite glass (g/L), M is the molecular mass of the volatile (g/mol), ε is the molar absorbance coefficient (L/mol-cm^2), A is the height of

the absorbance peak, and t is the thickness of the sample (μm), determined using both a micrometer and the reflectance method of Wysoczanski and Tani (2006). Because ρ and ε are both strongly dependent on water concentration, we assume initial values of 2350 kg/m^3 and 80 L·mol^{-1}·cm^{-1}, respectively and then iterate through the calculation until all three values converge (Skirius, 1990; Leschik et al., 2004). If the 3550 cm^{-1} (total water) peak was saturated, water concentrations were measured using the absorbance peak heights of the 4520 cm^{-1} bound hydroxyl and 5230 cm^{-1} molecular water peaks, following the equation of Zhang et al. (1997). Errors for H_2O are calculated using Gaussian error propagation and range from ±0.05–0.55 wt. % (average = ±0.25 wt.%). For CO_2, measured at the 2350 cm^{-1} (molecular CO_2) peak, all values were found to be below the detection limit of ~20 ppm. Full transect data can be found in Supplementary Table 1.

EPMA Major and LA-ICP-MS Trace Element Analysis

Following FTIR analysis, the doubly polished quartz wafers were mounted in 1-inch diameter epoxy mounts for major and trace element analysis at Boise State University. Embayments were first analyzed on a Cameca SXFive electron microprobe with operating conditions of 15 kV and an unfocused 10-μm beam for all analyses. To evaluate for compositional variability along the length of the embayment, measurements were taken at 15 μm intervals for embayments < 150 μm in length. For longer embayments, measurements were taken every 5 μm for the 30 μm nearest the rim, and one additional point was taken at the interior of the embayment. For each analysis, Si, Na, K, Al, and Fe were measured first using a beam current of 10 nA and then conditions were changed to 50 nA for Mg, Ca, Cl, Ti, and F. Error for each element was calculated using repeat analyses of the standard VG-2 (basaltic glass) and was

generally found to be <1.5% except for FeO (2.5%), Na_2O (4.0 %), K_2O (9.7%), F (15.0%), and Cl (24.7%). Trace elements were then analyzed using laser ablation inductively coupled plasma mass spectrometry (LA-ICP-MS) in the Boise State University Isotope Geology Laboratory. Line analyses, 30 μm long by 12 μm wide and perpendicular to the length of the embayment, were measured at 20 μm spacing and a repetition rate of 10 Hz in order to evaluate trace element variations. For trace element analysis, we used three external glass standards (GSE-1G, ATHO-1G, and T1-G) to evaluate error, with ^{29}Si used as an internal standard. Errors for trace elements were calculated by taking the standard deviation of measured standards from their known values and were generally found to be less than 12%, except for Zn, Cu, Co, F, and P, which have errors around 22%. The average major and trace element concentrations collected from each transect are listed in Table 2.3 with the full dataset available in Supplementary Table 2.

Diffusion Model Setup

Best fit decompression rates were obtained by simulating measured H_2O profiles using a one-dimensional diffusion MATLAB script (Table 2.1; Myers et al. 2018). The input parameters required for this model include the starting H_2O and CO_2 concentrations (converted to pressure using the solubility laws of Liu et al., 2005) and temperature. The model assumes constant decompression, isothermal magma ascent, and equilibrium at the rim/melt boundary. At each time step, a new exterior boundary solubility condition is calculated based on the pressure at that time step. Although the model allows for the input of an exsolved gas content, for all model runs, we assume open system degassing (gas is removed from the system upon formation). The lack of CO_2 in the melt results in a degassing path that is less sensitive to the exsolved gas content; therefore, open-system degassing is a reasonable assumption. Each model run cycled through a

range of decompression rates (dP/dt) and fragmentation pressures (P_f; where diffusion effectively ceases in the model) to solve for the set of dP/dt and P_f conditions which best approximate the measured data using the diffusivity model of Zhang et al., 2007. Error (also referred to here as misfit) is calculated using the chi-squared goodness of fit test (χ^2) of the calculated volatile gradient compared to the measured gradient (see supplementary material for error calculation). We consider any model with a χ^2 equal to or less than 1 a 'good fit,' and the model with the lowest χ^2 value is referred to as the 'best fit.'

Results

Embayment Major and Trace Element Chemistry

Although no variation in major or trace elements was observed along embayment transects in either eruption, we do find that transect analyses for nearly all samples show increasing concentrations of Li toward the rim of the embayment (Figure 2.4). Lithium concentrations overlap between the two eruptions, with interiors from both the Guaje and Tsankawi airfall deposits ranging from 70–100 ppm and rim concentrations preserving higher values of 90–125 ppm. These concentrations are higher than the mean melt inclusion value (~85 ppm) determined by Dunbar and Hervig (1992), although there is significant variability in their melt inclusion data (17–203 ppm Li).

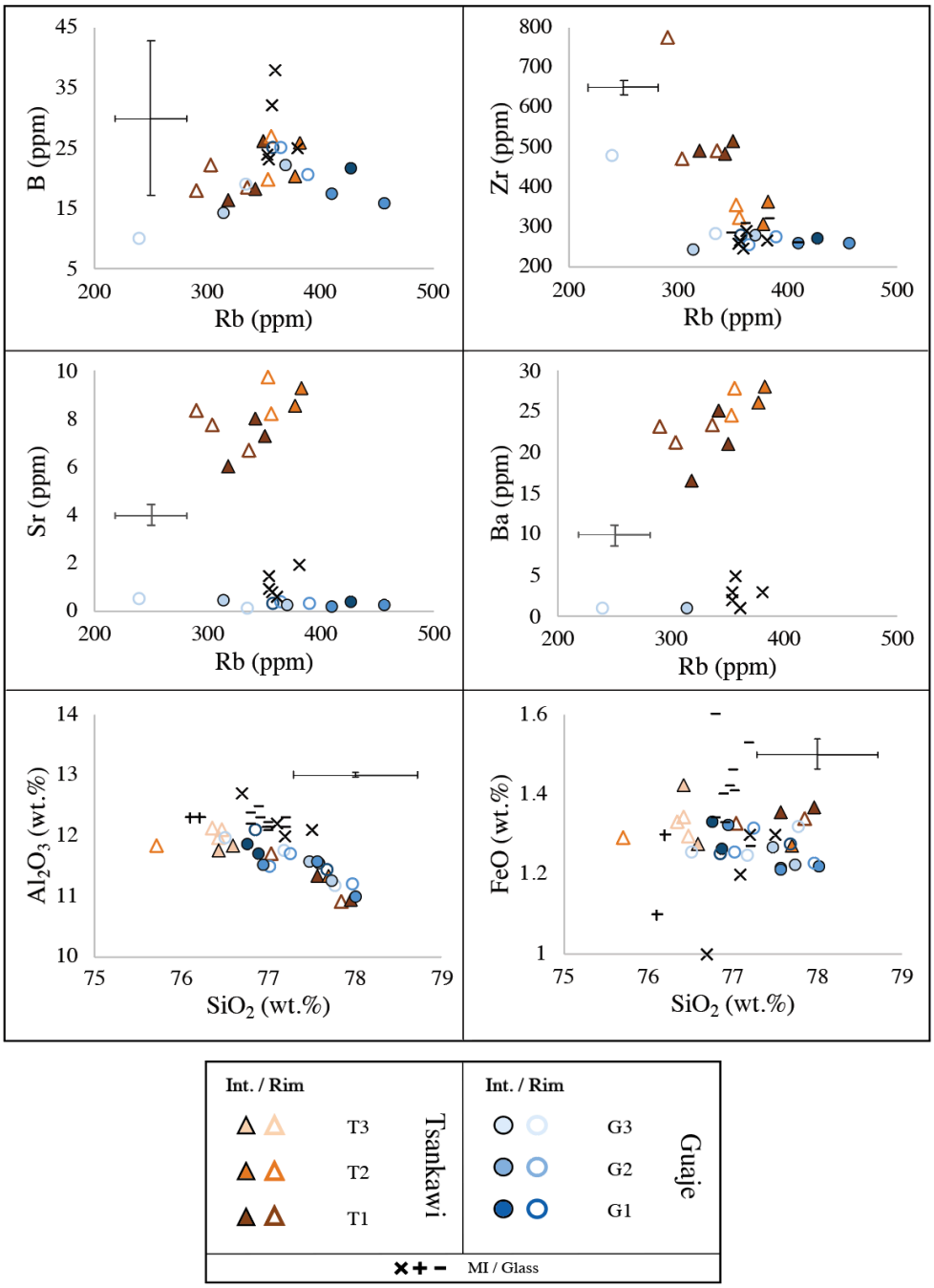

Figure 2.3. (previous page) Compositional plots of select major and trace element concentrations. Circles and triangles represent embayment analysis, either near the opening of the embayment (open symbol) or in the interior (closed symbol). Errors represent 1σ standard deviation on repeat standard glass analyses. Melt inclusion data from Plinian airfall deposits by Dunbar and Hervig (1992) is shown as plus signs (Tsankawi) and crosses (Guaje). Tsankawi glass shard data from Westgate et al. (2019) is indicated by dashes. Blue symbols represent embayments from the Guaje fall unit, and burnt orange symbols represent samples from the Tsankawi fall unit.

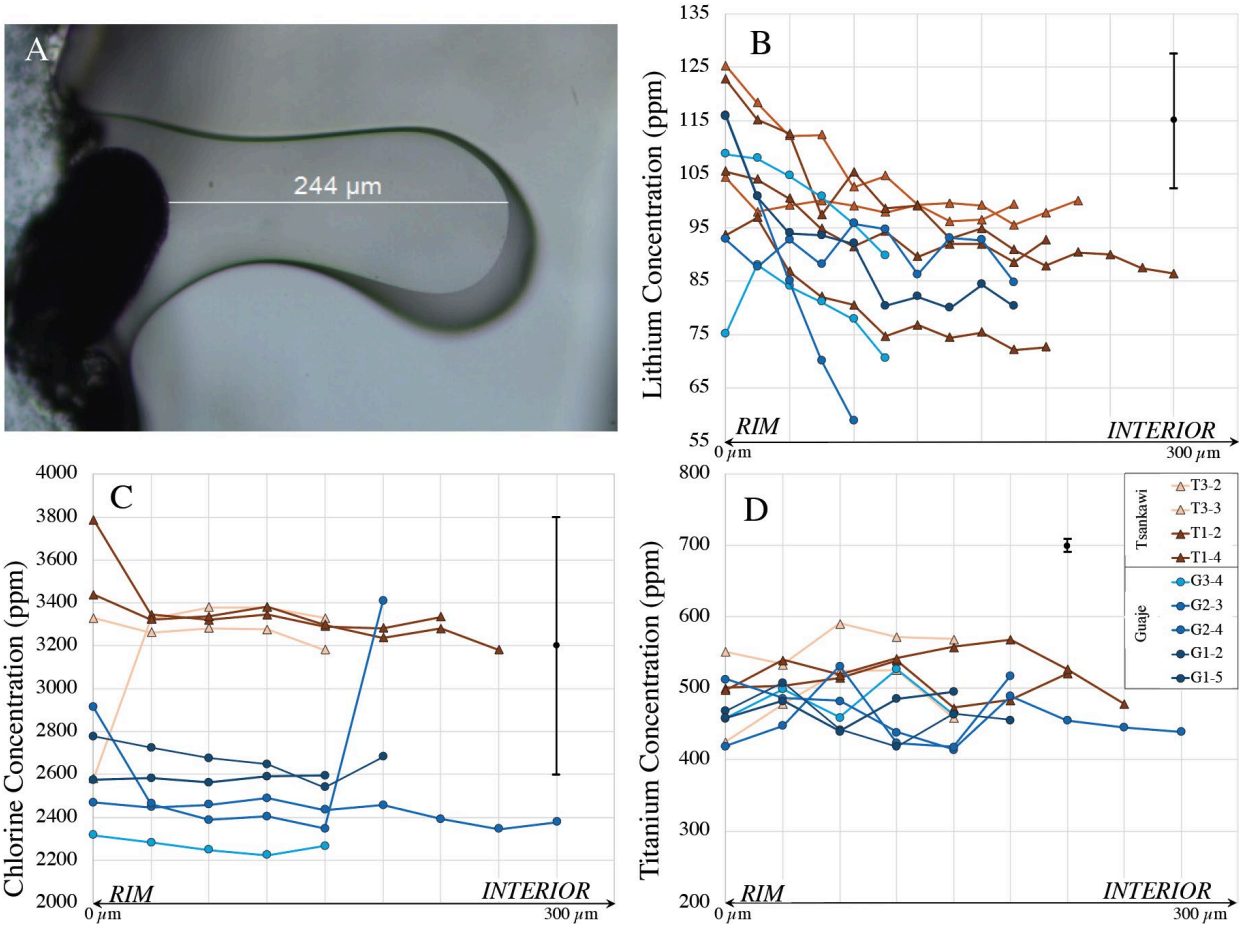

Figure 2.4. (A) Photomicrograph of embayment 03A-3 (Guaje). (B-D) Transect trace element analyses of Li, Cl, and Ti where each symbol represents a single point analysis, with profiles going from embayment rims (left) toward embayment interiors (right). Blue symbols represent embayments from the Guaje fall unit,and burnt orange symbols represent samples from the Tsankawi fall unit.

H_2O and CO_2 Gradients in REs and 1D Modeling

All Bandelier embayments contain H_2O concentrations ranging from 1.21–5.37 wt.% in the interior, with normal gradients going to lower concentrations at the rims (0.65–4.14 wt.%). Although interior H_2O concentrations represent a large variation, values mimic the range measured from co-erupted melt inclusions (2.0–5.2 wt.%; Figure 2.5; Waelkens et al. in review). Embayment H_2O contents are generally higher in the Guaje samples (n = 9), with average interior concentrations of 3.63 wt.% compared to 2.80 wt.% in the Tsankawi samples (n = 13).

All measured embayment profiles lack detectable CO_2 (detection limit ~20 ppm) (Figure 2.5; Waelkens et al. in review).

As volatile diffusivity is strongly temperature dependent, we applied the Boehnke et al. (2013) zircon saturation thermometer to our samples. This thermometer returned temperatures of 823 ± 23°C (2 σ) for the Guaje airfall and 835 ± 81°C for the Tsankawi airfall. Although these temperatures align very well with the results from Audétat (2013) using the same method on ignimbrite samples (819–883ºC), they are significantly higher than the ~700 – 800°C estimate for both airfall deposits provided by other thermometers (e.g., Warshaw and Smith, 1988; Campbell et al., 2009; Boro et al., 2021). As temperature is crucial for diffusion modeling, we consider the implications of a large temperature uncertainty in determining decompression rates but choose to represent the results based on the lowest temperature to provide conservative decompression estimates.

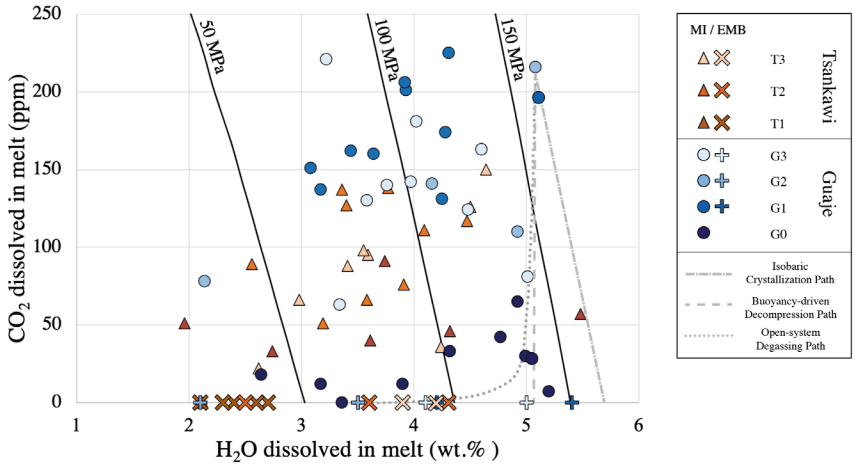

Figure 2.5. Water and CO_2 concentrations of melt inclusions (MI; Waelkens et al., in review) and innermost embayment data (RE), where each symbol represents a single MI or RE. Isobars (solid lines) and open-system degassing (dotted grey line) pathway calculated using Volatile Calc (Newman & Lowenstern, 2002). Dashed gray lines highlight two separate scenarios for exsolving CO_2 from the melt (isobaric crystallization and buoyancy-driven decompression), producing the high H_2O, low CO_2 starting pressures. This was found to produce better model fits to measured RE profiles.

Starting H_2O and CO_2 concentrations for model runs have traditionally been chosen based on measured melt inclusion data (*high* H_2O/*high* CO_2 ascent from storage) or by using the volatile concentrations found in the innermost part of the embayment (*moderate* H_2O/*no* CO_2; reset by an initial stalling or slow ascent phase; e.g., Myers et al., 2018; Figure 2.6); we explore both options here and present a third alternative (*high* H_2O/*no* CO_2). We note that many caldera-forming silicic systems exhibit a reduction or absence of measurable CO_2 concentrations in embayments in comparison to melt inclusions from the same deposits (Liu et al., 2007; Myers et al., 2018, 2021). However, most embayments still contain relatively high H_2O concentrations. Although this has now been noted in multiple systems, including the Bandelier, the implications of this observation are still unclear. We envision two potential explanations: 1) late-stage, isobaric crystallization drove CO_2 into a fluid phase, removing all traces from the embayment through diffusive reequilibration or 2) a small decompression event occurred, driving the remaining CO_2, into the fluid phase, followed by reequilibration of the embayment to a H_2O saturated pressure. This reequilibration to low CO_2 conditions would require 10s of hours to days to occur (based on solubility and diffusivity of CO_2; Liu et al., 2005; Zhang et al., 2007). Although we later discuss the probability of each scenario for the Bandelier system, for now, we accept that both ideas result in a *high* H_2O, *no* CO_2 starting melt for modeling embayment profiles. The third series of diffusion models therefore explored the scenario where only the melt inclusion-derived H_2O was present in the embayments initially and CO_2 had already degassed (referred to hereafter as the 'high H_2O/no CO_2' starting condition). This third scenario eliminates the need for a slow initial ascent/stalling event required by the embayment interior starting condition.

We find that most diffusion profiles from the Guaje can *only be* fit using the *moderate* H_2O/*no* CO_2 embayment interior measurements (*n* = 4 of 9) or the *high* H_2O/*no* CO_2 as starting conditions (*n* = 5 of 9), with only two successfully fit using the *high* H_2O/*high* CO_2 melt inclusions as starting conditions (Table 2.2). Four of nine could not be fit with any of these starting conditions. For the Tsankawi samples, the majority of profiles (*n* = 11 of 13) are fit using either the embayment interior or *high* H_2O/*no* CO_2 start, with 8 of 13 able to be fit using the melt inclusion start; one profile could not be fit with any starting condition (Table 2.2). There is no correlation between the calculated ascent rate and stratigraphic position for either eruption (Supplementary Figure 2). However, we do find that the model generally fits the data better in the Tsankawi than in the Guaje embayments, in which the measured interior water concentrations are rarely fit, with model results providing significantly lower H_2O concentrations (Supplementary Figure 2). The better model fits found for the Tsankawi embayments could suggest that the assumptions laid out in our model (constant ascent from some starting condition) better recreate the natural dataset in the Tsankawi member, where magma ascent occurs more directly from storage to the surface without stalling and reequilibrating in the conduit. By contrast, some aspect of the Guaje ascent is being missed by our current framework.

Table 2.1. Results of 1D decompression modeling.

Embayment Name		Embayment Starting Conditions			Ascent based on embayment starting conditions					
Tsankawi		Starting Pressure (MPa)	Starting CO_2 (ppm)	Starting H_2O (wt. %)	Rim Pressure (MPa)	Ascent rate (MPa/s)	dP/dt error (MPa/s)	Ascent time (min)	Ascent rate (m/s), *F=1000m	$\chi 2$
TOP	T3-1	83.2	20	3.9	10	0.0105	0.0016	116	0.325	0.62
	T3-3	95.5	20	4.2	30	0.9850		1	41.262	4.81
MIDDLE	T2-1	71.7	20	3.6	30	0.1000	0.0300	8	3.915	1.00
	T2-3	83.2	20	3.9	30	0.0162	0.0250	55	0.690	0.19
	T2-4	37.3	20	2.5	15	0.0014	0.0011	265	0.029	0.14
	T2-5	100	20	4.3	30	0.0106	0.0030	110	0.443	0.96
BOTTOM	T1-1	27.5	20	2.1	10	0.0049	0.0020	60	0.022	0.24
	T1-2	34.7	20	2.4	20	0.0007	0.0010	350	0.017	0.33
	T1-3	39.9	20	2.6	10	0.0192	0.0060	26	0.363	0.20
	T1-4	42.7	20	2.7	15	0.0940	0.0750	5	2.293	0.45
	T1-5	32.2	20	2.3	20	0.0004	0.0006	508	0.009	0.29
Guaje										
BEDDED AIRFALL	G3-4	132.9	20	5	25	0.0210	0.0100	86	0.821	2.45
	G3-5	91.4	20	4.1	30	0.0700	0.0300	15	2.950	1.65
	G3-2	95.6	20	4.2	30	0.1060	0.0700	10	4.447	0.65
	G2-3	27.5	20	2.1	20	0.0004	0.0015	313	0.004	0.23
	G2-4	68.1	20	3.5	20	0.0080	0.0030	100	0.278	2.85
	G2-4	95.6	20	4.2	15	0.0410		33	1.400	0.97
MASSIVE AIRFALL	G1-2	153	20	5.4	30	0.1000	0.0300	21	4.069	7.06
	G1-5	95.6	20	4.2	25	0.0170	0.0100	69	0.663	0.40

Table 2.1. (continued) Results of 1D decompression modeling.

Embayment Name		Melt Incl. Starting Conditions			Ascent based on melt inclusion starting conditions					
Tsankawi		Starting Pressure (MPa)	Starting CO_2 (ppm)	Starting H_2O (wt. %)	Rim Pressure (MPa)	Ascent rate (MPa/s)	dP/dt error (MPa/s)	Ascent time (min)	Ascent rate (m/s), *F=1000m	$\chi 2$
TOP	T3-1	132.9	150	4.64	25	0.0040	0.0015	450	0.153	4.51
	T3-2	132.9	150	4.64	10	0.0010		2048	0.034	0.15
	T3-3	132.9	150	4.64	30	0.0650	0.0300	26	2.610	17.86
MIDDLE	T2-1	120.6	117	4.47	30	0.0050	0.0020	302	0.202	7.29
	T2-2	120.6	117	4.47	5	0.0010		1927	0.032	0.63
	T2-3	120.6	117	4.47	30	0.0070	0.0030	215	0.283	4.22
	T2-4	120.6	117	4.47	15	0.0009	0.0003	1956	0.031	0.18
	T2-5	120.6	117	4.47	30	0.0080	0.0040	189	0.323	4.75
BOTTOM	T1-1	162.1	57	5.48	10	0.0014	0.0005	1811	0.048	0.09
	T1-2	162.1	57	5.48	20	0.0005	0.0004	4737	0.019	0.30
	T1-3	162.1	57	5.48	15	0.0049	0.0005	500	0.175	0.33
	T1-4	162.1	57	5.48	25	0.0048	0.0010	476	0.184	0.64
	T1-5	162.1	57	5.48	20	0.0003	0.0002	7894	0.011	0.26
Guaje										
BEDDED AIRFALL	G3-3	162.9	216	5.08	10	0.0012	0.0006	2124	0.042	0.36
	G3-4	162.9	216	5.08	30	0.0120	0.0050	185	0.478	9.62
	G3-5	162.9	216	5.08	30	0.0090	0.0050	246	0.358	17.81
	G3-2	162.9	216	5.08	25	0.0090	0.0050	246	0.358	25.09
	G2-3	162.9	216	5.08	20	0.0003	0.0002	7939	0.011	1.00
	G2-4	162.9	216	5.08	30	0.0030	0.0010	738	0.119	3.85
	G2-4	162.9	216	5.08	30	0.0140	0.0040	158	0.557	4.76
MASSIVE AIRFALL	G1-2	161.8	196	5.11	30	0.0480	0.0300	46	1.911	36.36
	G1-5	161.8	196	5.11	30	0.0070	0.0020	314	0.279	3.63

Table 2.1. (continued) Results of 1D decompression modeling.

Embayment Name		High H_2O/No CO_2 Starting Conditions			Ascent based on melt inclusion starting conditions					
Tsankawi		Starting Pressure (MPa)	Starting CO_2 (ppm)	Starting H_2O (wt. %)	Rim Pressure (MPa)	Ascent rate (MPa/s)	dP/dt error (MPa/s)	Ascent time (min)	Ascent rate (m/s), *F=1000m	$\chi 2$
TOP	T3-1	114.4	0	4.64	10	0.0079	0.0750	220	0.259	0.58
	T3-2	114.4	0	4.64	10	0.0010	0.0010	1740	0.033	0.15
	T3-3	114.4	0	4.64	50	0.0649	--	17	3.444	1.70
MIDDLE	T2-1	106.8	0	4.47	50	0.0028	0.0550	338	0.154	0.53
	T2-3	106.8	0	4.47	35	0.0079	0.1175	151	0.344	0.17
	T2-4	106.8	0	4.47	15	0.0010	0.0100	1530	0.034	0.12
	T2-5	106.8	0	4.47	35	0.0082	0.0525	146	0.357	0.91
BOTTOM	T1-1	156.4	0	5.48	10	0.0014	0.0350	1743	0.048	0.09
	T1-2	156.4	0	5.48	15	0.0010	0.0025	2357	0.036	0.85
	T1-3	156.4	0	5.48	15	0.0049	0.0825	481	0.175	0.32
	T1-4	156.4	0	5.48	25	0.0048	0.0650	456	0.184	0.64
	T1-5	156.4	0	5.48	20	0.0050	0.0050	4547	0.019	0.47
Guaje										
BEDDED AIRFALL	G3-3	135.5	0	5.08	10	0.0012	0.0350	1743	0.041	0.36
	G3-4	135.5	0	5.08	25	0.0210	--	88	0.804	2.39
	G3-5	135.5	0	5.08	30	0.0890	--	20	3.570	1.65
	G3-2	135.5	0	5.08	40	0.0789	0.2425	20	3.496	0.71
	G2-3	135.5	0	5.08	15	0.0006	0.0125	3347	0.021	0.37
	G2-4	135.5	0	5.08	20	0.0048	--	401	0.176	2.62
	G2-4	135.5	0	5.08	30	0.0242	0.2050	73	0.971	0.72
MASSIVE AIRFALL	G1-2	137.0	0	5.11	50	0.1000	--	15	4.931	3.37
	G1-5	137.0	0	5.11	30	0.0097	0.0650	184	0.389	0.37

Table 2.2. Summary of good profile fits (χ^2 misfits <1) from the decompression model, based on starting conditions from embayment (EMB) and melt inclusion (MI). Based on these results, we determined the average ascent rate for all model conditions.

	All conditions	No CO_2	EMB	MI	No fit	No CO_2 Start (m/s)	EMB Start (m/s)	MI Start (m/s)
Tsankawi (n=13)	6	11	10	8	1	0.149	1.15	0.03
Guaje (n=9)	1	5	4	2	4	0.984	1.70	0.04

Table 2.3. Average major and trace element concentrations, including 1σ error (average deviation of all analyses), for the five embayments from the Tsankawi member, and eight embayments from the Otowi member.

	Tsankawi Major Elements						Error (1σ)
(wt.%)	*T1-2*	*T1-4*	*T2-2*	*T3-1*	*T3-2*	*T3-3*	*(wt.%)*
SiO_2	77.59	77.62	76.70	76.41	77.46	76.54	0.71
TiO_2	0.05	0.05	0.05	0.06	0.05	0.06	0.00
Al_2O_3	11.45	11.10	11.59	12.11	11.25	11.90	0.04
FeO	1.35	1.36	1.28	1.31	1.36	1.30	0.03
MgO	0.02	0.03	0.03	0.03	0.01	0.03	0.00
CaO	0.25	0.26	0.25	0.28	0.24	0.28	0.00
Na_2O	4.56	4.38	4.90	4.61	3.98	4.52	0.18
K_2O	4.11	4.59	4.37	4.53	5.04	4.71	0.44
Cl	0.34	0.33	0.56	0.32	0.32	0.33	0.09
F	0.29	0.28	0.29	0.34	0.29	0.34	0.05

	Tsankawi Trace Elements						Error (1σ)
(ppm)	*T1-2*	*T1-4*	*T2-2*	*T3-1*	*T3-2*	*T3-3*	*(ppm)*
Li	77.5	95.0	131.7	130.4	71.7	131.3	14.5
Be	17.8	23.6	18.7	5.8	9.7	11.7	6.2
B	19.7	21.8	24.2	21.8	29.5	24.2	10.0
P	59.3	46.3	51.0	43.3	40.9	38.8	11.2
Sc	3.3	4.0	0.3	0.1	b.d.l.	1.2	0.3
V	0.5	1.0	b.d.l.	0.2	b.d.l.	0.2	0.1
Cr	15.0	17.9	0.7	b.d.l.	b.d.l.	7.7	5.3
Mn	714.8	705.5	696.7	577.9	681.4	583.1	72.6
Co	0.4	0.8	0.2	0.2	0.2	0.1	0.1
Ni	0.9	0.8	1.4	2.8	2.7	2.7	0.3
Cu	6.7	1.2	1.6	b.d.l.	1.9	b.d.l.	0.7
Zn	143.3	145.1	144.4	174.3	226.7	172.8	36.8
Ga	26.9	27.1	30.6	30.3	31.8	30.8	3.1
Rb	323.9	326.6	376.2	349.0	428.8	357.8	45.9
Sr	6.3	7.6	5.4	9.1	0.6	7.8	0.7
Y	176.5	167.2	123.1	61.9	63.5	65.7	12.8
Zr	507.2	476.4	355.8	196.7	217.9	210.4	37.9
Nb	237.9	236.8	212.3	181.7	210.9	183.1	26.5
Cs	11.7	11.8	13.4	12.3	15.3	12.9	1.6
Ba	19.1	22.4	20.0	28.8	2.0	28.0	2.6
La	60.4	59.3	40.9	29.9	28.2	30.7	4.8
Ce	107.3	108.9	94.6	94.1	92.5	95.6	11.3
Pr	12.4	12.0	9.3	7.3	6.6	7.2	1.0
Nd	47.0	44.3	33.7	24.1	22.0	25.4	4.2
Sm	13.4	13.1	9.3	6.1	6.0	6.0	1.0
Eu	0.0	0.0	0.0	0.0	b.d.l.	0.0	0.0

Table 2.3 Continued

Gd	17.1	16.4	10.5	7.2	6.8	6.9	1.3
Tb	3.4	3.3	2.3	1.4	1.3	1.3	0.2
Dy	25.8	24.3	17.6	9.7	10.0	10.5	1.7
Ho	5.6	5.3	4.1	2.1	2.1	2.1	0.4
Er	17.2	15.7	11.3	6.4	6.3	6.4	1.1
Tm	2.8	2.5	2.0	0.9	1.0	1.1	0.2
Yb	17.3	16.1	11.8	6.3	6.6	6.7	1.1
Lu	2.8	2.7	1.9	1.1	1.0	0.9	0.2
Hf	25.2	22.3	16.6	8.9	10.2	9.8	1.8
Ta	17.2	15.7	13.6	10.3	10.3	10.2	1.4
Pb	56.8	55.8	66.0	63.2	76.3	64.2	6.1
Th	51.4	48.2	34.8	22.7	23.1	22.8	3.7
U	14.3	14.1	15.9	15.9	18.5	15.9	1.9

	Guaje Major Elements								Error (1σ)
(wt.%)	*G2-3*	*G2-4*	*G2-4*	*G3-4*	*G3-5*	*G3-2*	*G1-2*	*G1-5*	*(wt.%)*
SiO_2	77.46	77.66	77.53	77.67	77.26	77.19	76.78	77.03	0.71
TiO_2	0.05	0.05	0.05	0.05	0.05	0.05	0.05	0.05	0.00
Al_2O_3	11.33	11.48	11.54	11.24	11.66	11.78	12.00	11.70	0.04
FeO	1.25	1.22	1.28	1.27	1.25	1.23	1.28	1.27	0.03
MgO	0.02	0.01	0.02	0.01	0.02	0.02	0.01	0.01	0.00
CaO	0.26	0.24	0.26	0.26	0.26	0.26	0.26	0.25	0.00
Na_2O	4.16	4.47	4.31	4.08	4.31	4.27	4.65	4.40	0.17
K_2O	4.98	4.44	4.54	4.96	4.72	4.75	4.43	4.80	0.46
Cl	0.24	0.23	0.27	0.23	0.22	0.28	0.27	0.26	0.06
F	0.27	0.21	0.22	0.23	0.25	0.18	0.27	0.24	0.04

	Guaje Trace Elements								Error (1σ)
(ppm)	*G2-3*	*G2-4*	*G2-4*	*G3-4*	*G3-5*	*G3-2*	*G1-2*	*G1-5*	*(ppm)*
Li	90.9	122.7	86.2	67.2	103.3	79.5	96.1	90.3	12.6
Be	26.4	14.4	b.d.l.	16.4	13.3	b.d.l.	14.7	33.6	8.4
B	21.9	18.3	20.7	20.9	19.0	12.6	22.3	21.8	8.4
P	83.9	44.6	82.2	50.9	33.2	65.8	47.9	78.9	14.7
Sc	3.5	b.d.l.	2.8	b.d.l.	b.d.l.	10.9	b.d.l.	1.6	0.7
V	b.d.l.	0.1	b.d.l.	b.d.l.	0.1	0.5	b.d.l.	0.3	0.0
Cr	13.2	7.5	7.1	b.d.l.	2.0	27.2	5.4	13.9	5.6
Mn	687.1	636.8	710.8	608.2	603.3	610.5	695.8	683.6	72.0
Co	0.7	b.d.l.	0.3	b.d.l.	b.d.l.	b.d.l.	0.3	0.6	0.1
Ni	1.8	1.6	2.1	1.5	1.8	2.0	1.6	1.7	0.2
Cu	b.d.l.	0.3	b.d.l.	0.3	b.d.l.	b.d.l.	18.9	0.1	1.1
Zn	139.0	128.2	135.1	146.0	135.8	98.7	129.3	136.7	28.7
Ga	29.4	28.3	29.9	26.2	27.3	24.5	27.6	29.2	2.9
Rb	412.0	424.2	420.1	383.1	392.3	285.6	401.1	392.1	49.5
Sr	0.3	0.1	0.4	0.1	0.1	0.4	0.2	0.3	0.0
Y	93.6	102.6	93.3	79.9	78.9	99.1	107.4	95.6	10.9
Zr	265.6	286.2	261.8	219.6	221.0	282.1	307.3	279.7	30.7
Nb	258.1	250.0	259.3	209.5	207.0	188.1	248.5	265.0	29.7
Cs	13.2	14.2	14.1	10.9	11.7	8.8	13.0	13.4	1.5
Ba	b.d.l.	0.0	b.d.l.	0.2	0.3	0.8	1.5	b.d.l.	0.1
La	32.4	30.8	30.1	30.6	29.8	41.4	33.6	30.2	3.7
Ce	91.7	83.6	86.7	88.9	88.0	99.2	84.3	85.5	10.1
Pr	8.8	8.3	8.4	8.7	8.6	10.6	8.8	8.3	1.0
Nd	33.8	32.3	31.8	32.1	29.9	40.9	33.5	30.3	4.2
Sm	9.4	9.9	9.0	9.5	9.3	11.3	10.8	9.1	1.1
Eu	0.0	0.0	0.0	0.0	0.0	b.d.l.	0.0	0.0	0.0
Gd	10.7	10.3	10.3	10.1	9.7	12.4	11.6	10.5	1.3

Table 2.3 Continued

Tb	2.1	2.3	2.0	2.0	2.0	2.4	2.4	2.0	0.2
Dy	15.0	15.6	13.9	13.7	13.4	16.8	17.5	14.5	1.5
Ho	3.1	3.4	2.9	2.8	2.9	3.5	3.6	3.1	0.3
Er	9.2	9.9	8.8	8.2	7.9	9.1	10.8	9.1	1.0
Tm	1.5	1.6	1.5	1.3	1.2	1.5	1.8	1.4	0.1
Yb	9.3	10.1	9.2	8.2	7.9	9.5	11.1	9.3	1.0
Lu	1.4	1.6	1.4	1.2	1.2	1.6	1.7	1.5	0.1
Hf	12.4	13.5	11.4	11.1	9.7	12.9	14.5	13.0	1.4
Ta	17.4	17.1	17.7	13.8	13.4	13.3	17.7	17.7	1.7
Pb	53.3	50.8	55.0	47.2	46.9	38.7	53.0	54.8	4.8
Th	40.7	41.6	39.5	31.7	32.0	37.8	44.3	40.1	4.2
U	22.2	20.3	22.6	18.3	19.2	14.5	21.0	22.4	2.4

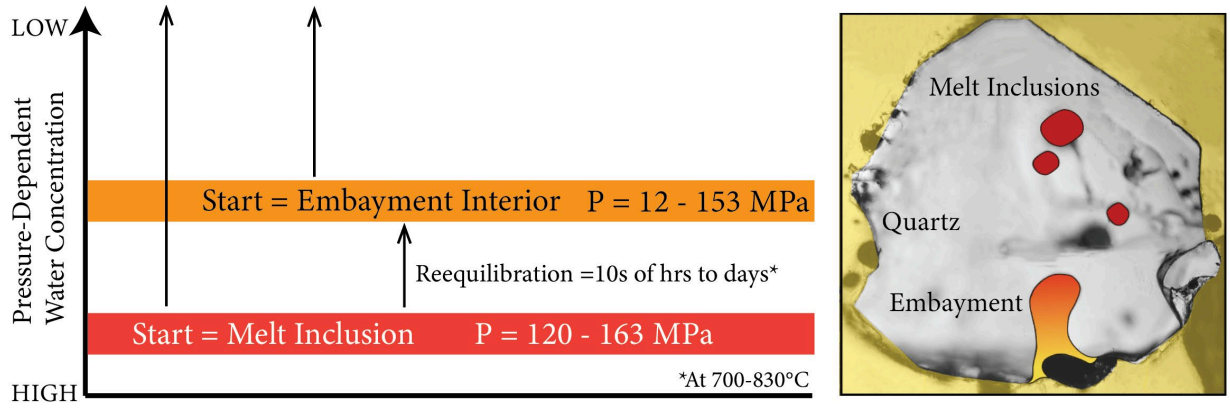

Figure 2.6. Schematic diagram illustrating the melt inclusion vs. the embayment starting conditions. Using the melt inclusion concentrations to derive starting pressures indicates magma ascent directly from storage conditions without any major stalling (left long arrow). Starting pressures derived from the embayment interior volatile concentrations require an initial slow ascent and reequilibration to lower saturation pressures (middle short arrow) prior to the final ascent (right arrow). Reequilibration times are calculated based on solubility and diffusivity of H_2O and CO_2 (Liu et al., 2005; Zhang et al., 2007).

Based on embayment starting conditions (*moderate* H_2O/*no* CO_2), successful best-fit decompression rates for the Guaje range from 0.0012–0.1060 MPa/s, overlapping with the Tsankawi 0.0003–0.1000 MPa/s. Decompression rates using melt inclusion-starting conditions are slower (~ 1 to 1.5 orders of magnitude) than those recovered using the embayment start, whereas the best-fit decompression rates for the high H_2O/no CO_2 models fall in between. The results of decompression modeling using each of the three starting conditions are shown in

Figure 2.8. In most cases, the Guaje samples record decompression rates that are similar to the Tsankawi; however, they are generally associated with poorer model fits when applying the melt inclusion-derived starting conditions (*high* H_2O/*high* CO_2). Presented decompression rates were determined using a temperature of 700°C, however, we evaluate the error of this assumption by presenting rates for the fastest and slowest embayments at the higher temperature estimate of 830°C. This increased temperature increases the decompression rates by 340–440% (Figure 2.8).

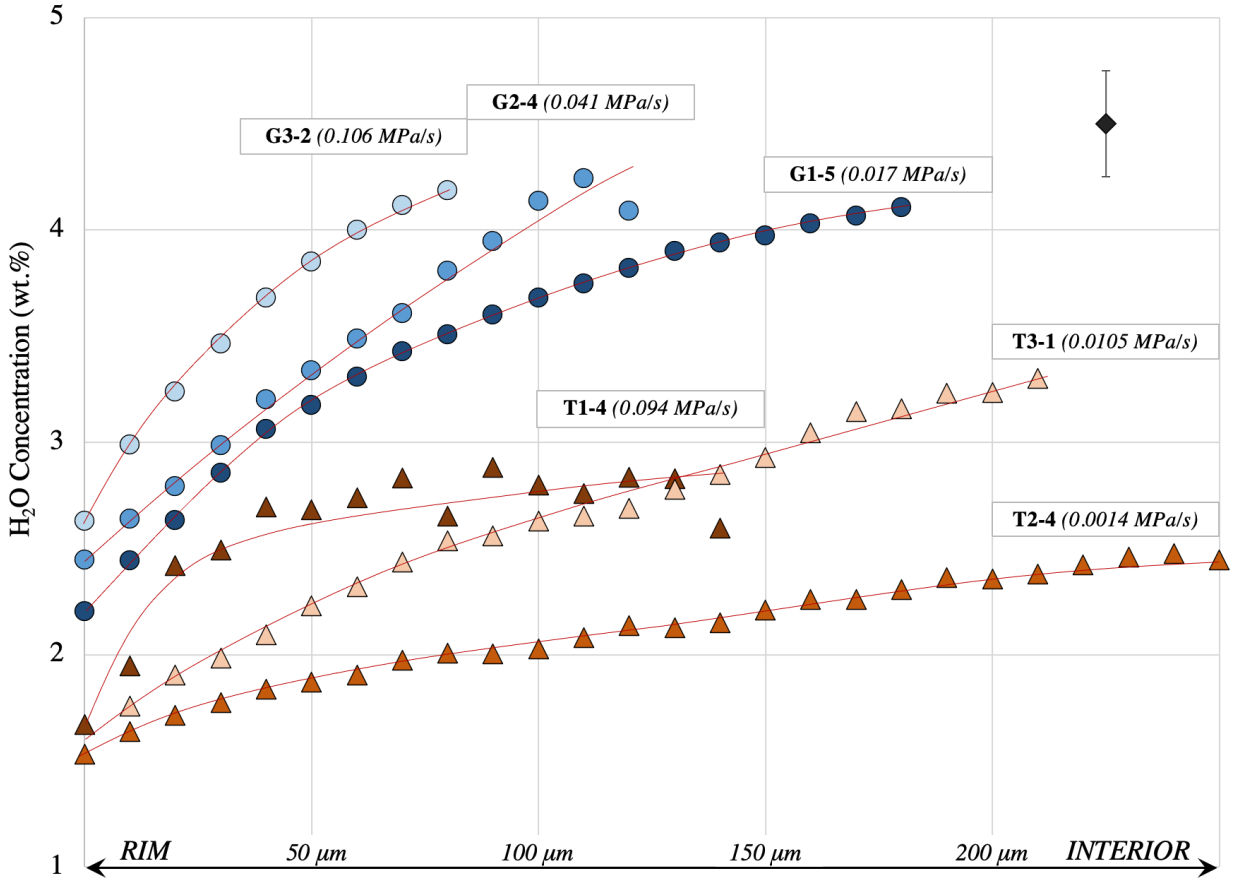

Figure 2.7. Examples of water transect data collected by FTIR, with each symbol representing a single point analysis and each line representing the best fit decompression rate for one embayment from an individual layer. Error bar represents average analytical error of ± 0.25 wt.% H_2O. Blue symbols represent embayments from the Guaje fall unit and burnt orange symbols represent samples from the Tsankawi fall unit. The labels contain the best fit decompression rate obtained via 1-D diffusion modeling using the embayment interior starting conditions. Full transect data is available in Supplementary Table 1.

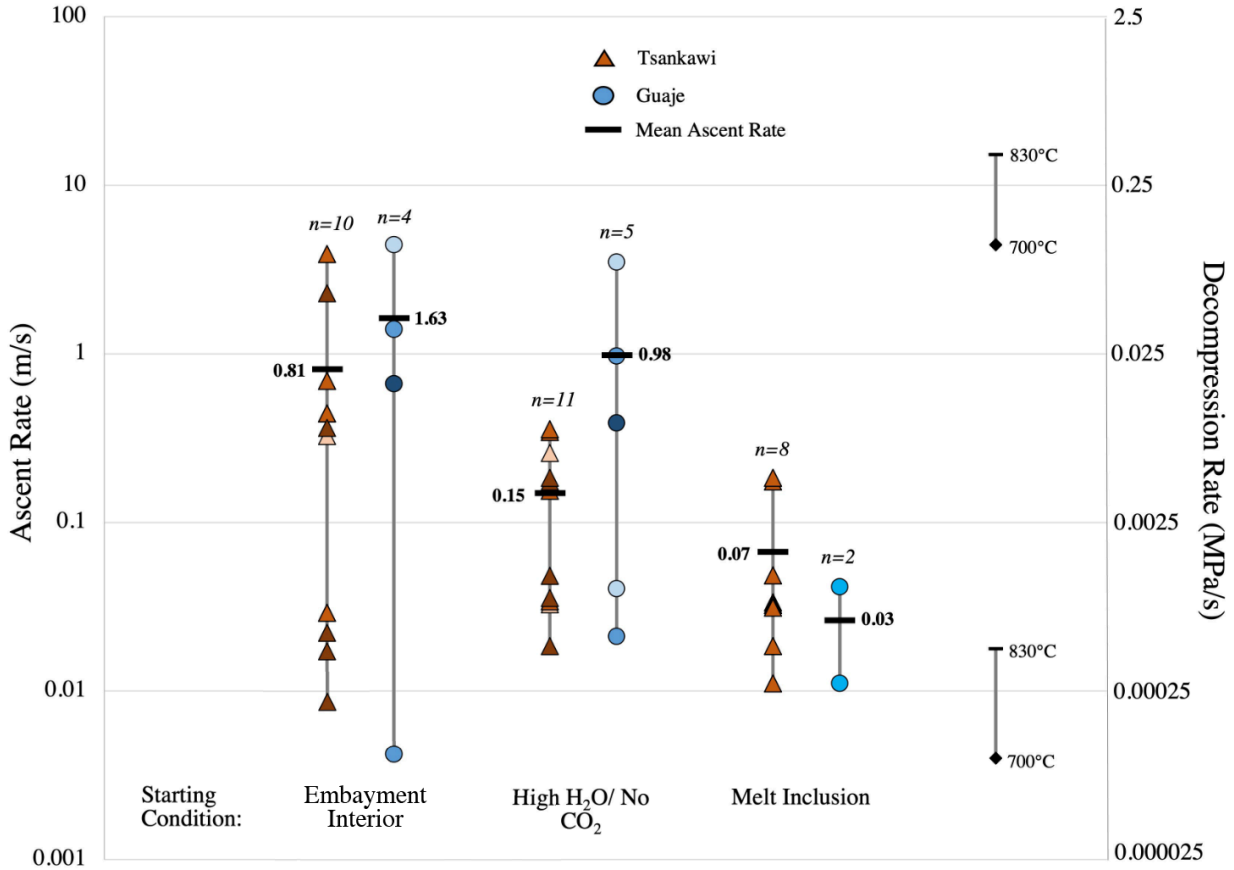

Figure 2.8. Results of decompression modeling using three different starting conditions, where best fit decompression rates (MPa/s) were translated into ascent rate (m/s) (see section 5.3 for discussion). Each symbol represents a single embayment. Best fits for the largest number of embayments were achieved using the embayment interior and high H_2O/no CO_2 starting conditions. The error bar presented represents the shift in the determined ascent rate based on a 130°C temperature increase (see section 4.2 for discussion). This approach as applied to both the slowest and fastest ascent rate, which results in a 340–440% shift.

2-Dimensional Diffusion Modeling

A major assumption of the embayment models presented here is that diffusion occurs only along 1 dimension, parallel to the length of the embayment, from the interior to the mouth. However, natural embayments have complicated 3D geometries that impact diffusive flux pathways, and thus the assumption of 1D diffusion may introduce significant errors on determined decompression rates (deGraffenried and Shea, 2021). A common embayment

geometry that challenges the 1D assumption is when the embayment constricts toward the mouth (e.g., Figure 2.4a). This constriction creates a 'bottlenecking effect,' where diffusion is slowed and results in higher water concentrations being recorded further into the embayment than would be expected when compared to a perfect cylindrical geometry (deGraffenried and Shea, 2021). To evaluate the effects of complex natural embayment geometries on our modeled decompression rates, we implemented a 2D model based on deGraffenried and Shea (2021). The 2D model was modified to use the same water diffusivity as the 1D code (Zhang et al., 2007). All 2D modeling was conducted using the conservative Bandelier temperature of 700°C, the same initial and fragmentation pressures as the 1D model, and the embayment interior starting conditions. Due to computational limitations and the fact that the chosen parameters resulted in very good model fits, we chose not to iterate through different fragmentation pressures or starting conditions. We selected only four embayments to evaluate, again because of the computational intensity associated with a 2D model, representing the full range of observed embayment shapes: necked 0% (tubular), 24%, 38%, and 44% (strongly necked). The degree of necking was calculated by dividing the narrowest part of the embayment by the widest. In theory, the tubular embayment should record nearly identical ascent rates using the 1D and 2D methods, and as the degree of necking increases, the difference between the two methods should also increase.

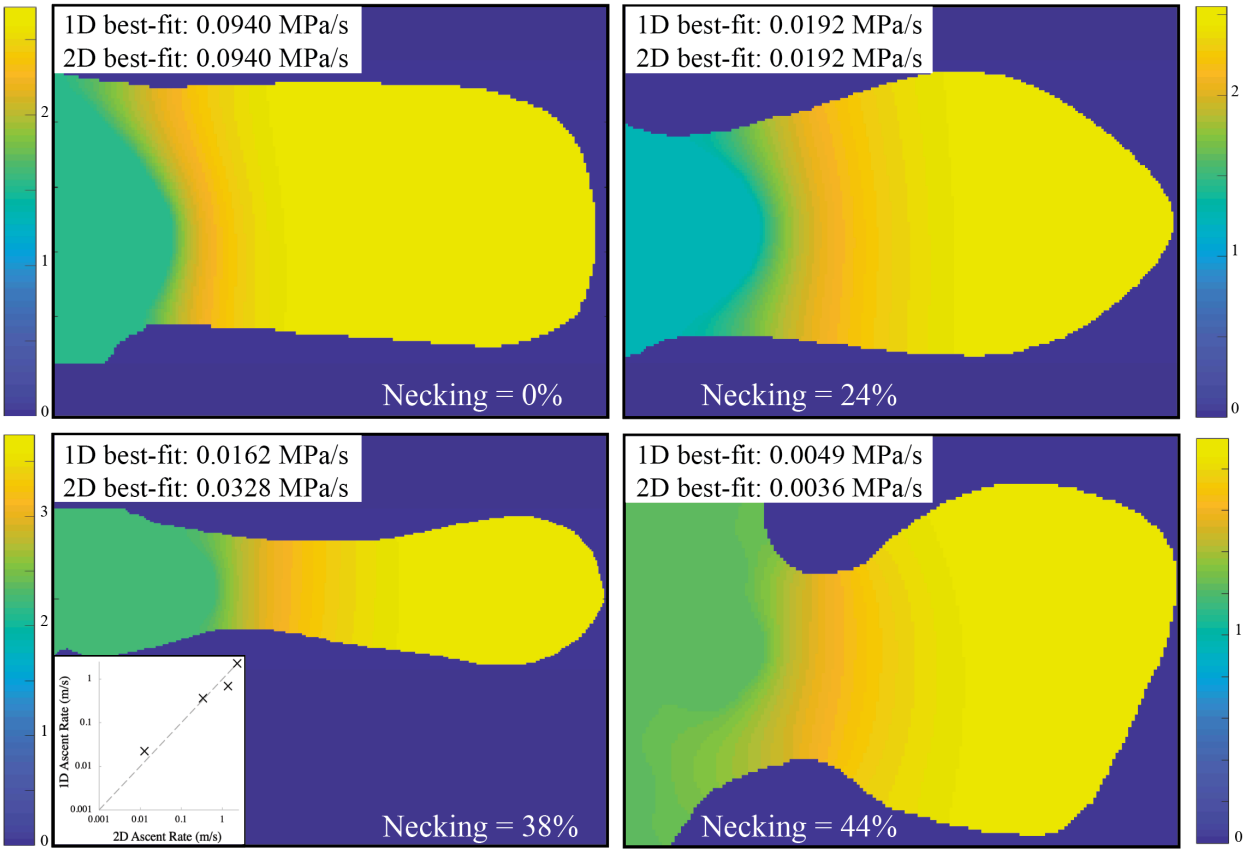

Figure 2.9. Results of diffusion modeling in two dimensions (2D) for four Tsankawi embayments with different necking ratios. Color gradients and correlated scale bar represent water concentration in weight percent. Necking ratio is determined by dividing the width of the narrowest part of the embayment by the widest part. Inset chart shows comparison of ascent rates in 1D vs. 2D, dashed gray line is 1:1 line.

As predicted, we found that the non-necked embayment retrieved a best-fit 2D decompression rate that was identical to 1D (Figure 2.9). The 24% necked embayment returned a slightly slower decompression rate (0.0185 MPa/s in 2D vs. 0.0192 MPa/s in 1D), whereas the most strongly necked embayment (44% necked) fit a decompression rate 27% slower than the 1D results (0.0036 MPa/s vs. 0.0049 MPa/s). Lastly, the 38% necked embayment was the only sample that produced a decompression rate that was *faster* when using the 2D model, by 50% (0.0328 MPa/s vs 0.0162 MPa/s). This may be due to the diffusion front interacting with a more

complex 3D morphology. While the 2D model returns slightly different best-fit values than the 1D model, it is important to note that all 2D model results are within the misfit uncertainty of the 1D model. The full results are shown in Figure 2.9, Supplementary Figure 3, and can be found in Supplementary Table 3.

Discussion

Lithium Gradients

Although most major and trace elements show little to no significant difference between units or within a given embayment, lithium concentrations near the mouths of each embayment increase by up to 55 ppm above interior compositions, an increase of ~25%. Charlier et al. (2012) also found reverse gradients in Li preserved in feldspar and quartz phenocrysts for the Oruanui supereruption (NZ). To explain this observation, they postulate that during the very last stages of decompression (less than ~22 MPa, 125 to 720 s before quenching) interactions between LiCl and high-temperature steam caused a hydrolysis reaction, affecting the partitioning of Li and resulting in a 50% increase of Li concentration in crystal rims. Thus, there is potential that a similar mechanism was occurring in the Bandelier tuffs with the breakdown of a fluid phase in the shallow conduit system. This reaction should also result in large amounts of Cl partitioning into the fluid phase; however, gradients of Cl in all Bandelier embayments are lacking. Although a diffusion coefficient for Li in hydrous rhyolite melt has been determined (Holycross et al., 2018), this does not take into account how Li would react during degassing and ascent. Thus, modeling Li profiles would require too many assumptions about its behavior to provide meaningful results. While the cause of lithium gradients preserved in embayment glasses

of the Bandelier are currently unknown and beyond the scope of this paper, the application of Li diffusion as an eruption chronometer remains an exciting avenue for future work.

Decompression Rates for the Tsankawi and Guaje Eruptions

When H_2O diffusion in more than one direction is taken into account, we find that the best fit decompression rates of embayments with a necked geometry differ from their 1D best-fit decompression rates by up to 50% (Figure 2.9). While the embayment geometry clearly affects the decompression rate, the best-fit rates in 2D and 1D are still within the uncertainty range of each other for all geometries tested. This indicates that the embayment geometry is not a significant factor affecting rates extracted from Bandelier embayments and concludes that diffusion modeling in 1D is sufficient for reasonable geometries (necking < 50%). In contrast, the error introduced by modeling at a higher temperature results in a more dramatic change (~300–500% difference). But importantly, both error sources pale in comparison to the three orders of magnitude variation represented by each airfall deposit (Figure 2.8). This highlights the extreme variations in ascent dynamics experienced over the course of a single eruption and that accurate quantification of ascent rate cannot be accomplished through limited petrological sample sizes.

Evaluating the 1D results, decompression rates recorded by embayments from the Guaje and Tsankawi initial airfall deposits are largely indistinguishable for all starting conditions (Figure 2.7). However, a major difference is that the majority of the Tsankawi samples can be modeled using all three starting conditions, whereas the Guaje samples can only be fit using the *moderate* H_2O/*no* CO_2 embayment interior or the *high* H_2O/*no* CO_2 starting conditions. Additionally, a higher number of Guaje embayments (n = 4) cannot be fit by any modeling

scenario. We interpret these observations to suggest that the Guaje likely experienced an initial period of slower ascent (hours to days) deeper in the conduit and re-equilibrated at a lower pressure before its final ascent (e.g., Figures 2.2 and 2.4). Although this idea explains part of our dataset, half of the Guaje embayments cannot be fit from any starting condition. Our only interpretation to explain this result is that there is an assumption built into our model (e.g., constant-rate decompression) that is not recreating the ascent history of this system. In contrast, Tsankawi embayments are likely recording a decompression event with little or no stalling in the conduit. This suggests that the Tsankawi magma, the second of the two caldera-forming eruptions, was able to develop a conduit system more effectively, potentially exploiting some preexisting weakness (e.g., the interpretation of Myers et al., 2021). Regardless of the initial opening behavior, the remarkable overlap in the integrated decompression rate of these two systems, especially compared to the range observed in rhyolitic systems (see 5.3), suggests that regional stress, crustal structure, and intrinsic magma properties may ultimately control the ascent rates of rhyolite magma.

Comparison with Other Caldera-Forming Systems

Although both the embayment interior and the high H_2O/no CO_2 models provide good fits to a similar number of embayments in the two fall deposits, here we present ascent rates based on the embayment interior volatile concentration in order to draw comparisons with other caldera-forming systems. Decompression rates can be converted to ascent rates by converting the starting pressure into depth using the assumption of lithostatic conditions, assuming a fragmentation depth of 1000 meters (Myers et al., 2018) and applying an assumed crustal density of 2600 kg/m^3. Ascent rates obtained for the Guaje embayments range from 0.28 – 4.45 m/s, and again,

largely overlap with the Tsankawi (0.32–3.92 m/s). These ascent rates obtained for the Bandelier members are comparable to those of other rhyolitic caldera-forming eruptions, most notably the results from the Oruanui (0.06–3.47 m/s) and Huckleberry Ridge (0.25–3.88 m/s) eruptions, which both show large scatter of H_2O compositions in enclosed melt inclusions, similar to that of the Bandelier melt inclusions (Myers et al., 2018; Figure 2.10). However, these rates are much slower than those determined for the Bishop Tuff (0.4–12.99 m/s; Figure 2.10) and the Bronze-Age eruption of Santorini (0.4–11 m/s; Myers et al., 2021). Notably, the opening behavior of both the Oruanui and Huckleberry Ridge eruptions is thought to be modulated by tectonic forces (Myers et al., 2016, 2018).

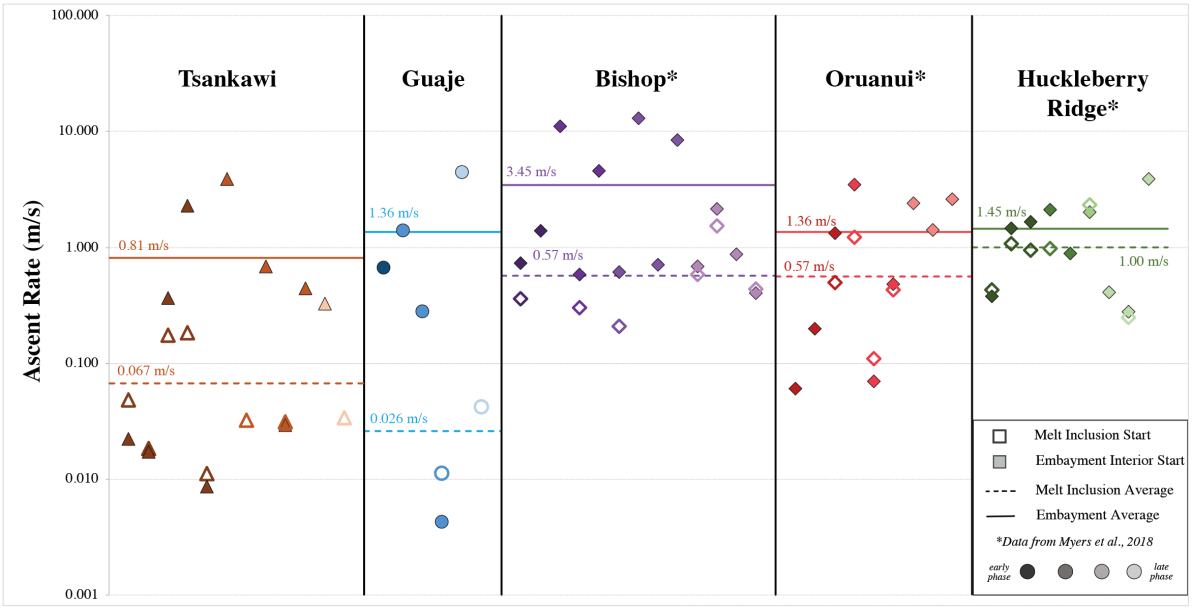

Figure 2.10. Comparison of ascent rates obtained from 1D embayment volatile diffusion from the Tsankawi and Guaje airfalls to studies of other caldera forming eruptions (Myers et al., 2018). Model starting conditions are determined by the saturation pressure from either the volatile content of the interior of the embayment (solid shapes) or the volatile content of melt inclusions (open shapes). Labeled horizontal bars indicate the average ascent rate for each eruption based on embayment (solid line) and melt inclusion (dashed line) starting conditions, with melt inclusion starts generally resulting in slower ascent rates. Darker colors represent samples from earlier eruption phases and lighten toward later eruption phases.

Removal of CO_2: Implications for Silicic Caldera-Forming Eruptions

It has been observed that embayments measured from several silicic, caldera-forming eruptions (e.g., Oruanui, Bishop Tuff, Santorini) commonly contain little or no CO_2, while coexisting melt inclusions have concentrations up to several hundred ppm (Myers et al., 2018, 2021). Similarly, the Guaje and Tsankawi embayments lack detectable CO_2 compositions compared to their melt inclusion counterparts. In fact, most embayments here require CO_2 to be absent from their starting conditions in order to retrieve good model fits (Figure 2.8). This observation suggests that embayments in most silicic systems are recording the removal of CO_2 from the melt into a fluid phase prior to the final ascent, where water begins to exsolve and degas. One way to remove CO_2 from the system is represented by the *moderate* H_2O/*no* CO_2 embayment interior starting condition, where an initial stage of decompression occurs prior to stalling and reequilibration. This initial stage of ascent would require a significant decompression event (upwards of 100 MPa) to remove CO_2 and lower H_2O, however, is unsatisfactory in that it requires different starting pressures for each embayment (starting pressures range from 12 to 153 MPa). An alternative model for which we found successfully modeled the majority of embayments is one that maintains the high H_2O content but removes the CO_2 fully from the system. As previously mentioned in Section 4.2, we have proposed two mechanisms: late-stage crystallization and a minor decompression event (less than ~30 MPa), which we model below to explore their validity. One final explanation for the lack of CO_2 observed in embayments compared to their corresponding melt inclusions is that of a multi-stage ascent model, however, that is beyond the scope of this paper.

The first idea we explore is that additional isobaric crystallization occurred for both the Otowi and Tshirege magmas after melt inclusion entrapment, driving H_2O enrichment and CO_2

exsolution into a fluid phase. To determine if this process could occur due to a feasible amount of crystallization (e.g., less than the crystallinity of the erupted magma), we modeled crystallization along a cooling path using rhyolite-MELTs (Gualda et al., 2012; Ghiorso and Gualda, 2015). Conditions used for MELTs modeling are provided in the Supplementary Material. Starting with H_2O/CO_2 conditions based on melt inclusion concentrations from the highest pressure (~160 MPa) for each layer, we allowed the temperature to drop, triggering crystallization and driving H_2O enrichment, until all CO_2 was removed from the system. The results of this modeling suggest that this process would require only 7–13% of additional crystallization, well within the range of the erupted products (5–20%; Kuentz, 1988).

The second method explored was a small buoyancy-driven decompression event in which magma density decreases due to small amounts of fractional crystallization or volatile exsolution, causing the magma to rise buoyantly within the storage region. The amount of decompression required to drive CO_2 from the system was determined assuming open-system degassing and based on solubility/pressure relationships taken from VolatileCalc (Newman and Lowenstern, 2002; Figure 2.5). Starting H_2O/CO_2 conditions were based on the melt inclusion with the highest CO_2 for each layer. For both the Otowi and Tshirege magmas, a small drop in pressure (7–28 MPa, equivalent to 0.3–1.1 kilometers) is required to evolve from melt inclusion starting conditions to a CO_2-free system, while still maintaining a high-water concentration. The necessary decrease in pressure is highest in the upper layers of each member, requiring 28 MPa in the Guaje and 20 MPa in the Tsankawi. The lowest layer of the Guaje requires the smallest pressure decrease (7.1 MPa), while the middle and lower layers of the Tsankawi require intermediate pressure decreases (16 and 12 MPa, respectively).

This process of consistent CO_2 removal in late-stage silicic chambers could be significant because it would support the existence of a pre-eruptive exsolved fluid phase. Although overpressurization of the magma chamber (i.e., via injection of new magma) is often called upon as the triggering mechanism for smaller volcanic eruptions, including for both Bandelier units, large-scale magma chambers (> 1000 km^3) may require a different triggering mechanism to initiate movement toward the surface (Jellinek and DePaolo, 2003; Gregg et al. 2012). One mechanism that has been suggested is buoyancy-driven overpressurization, by which a volatile-rich buoyant magma layer forms near the top of the chamber and creates enough overpressure to initiate diking and potentially lead to eruption (McLeod and Tait, 1999; Caricchi et al., 2014; Malfait et al., 2014). Our results suggest that only a small drop in pressure is necessary to remove CO_2 from the system. This small pressure change could be a record of early diking and decompression events in the upper portion of the magmatic system prior to eruption onset (Papale et al., 2017).

Another classic internal triggering mechanism is due to isobaric crystallization in a closed system, where additional crystallization promotes the exsolution of a volatile phase, leading to internal instability and eruption of the magma chamber (Fowler and Spera, 2008; Tramontano et al., 2017). Tramontano et al. (2017) demonstrate that only ~10% crystallization under fluid-saturated conditions is required to reach the suggested ~25 MPa overpressure threshold to trigger an eruption. The amount of crystallization necessary to remove CO_2 from the Bandelier embayments (determined via MELTS modeling to be 7–13%) thus would more than likely create enough overpressure to drive the start of an eruption, assuming a saturated system.

These two scenarios are both plausible for removing CO_2 from the Guaje and Tsankawi magmas and likely exert feedback on each other, making it difficult to identify a dominant process. The observed lack of CO_2 in embayments may therefore be recording the internal triggering mechanisms responsible for initiating eruption of the Tsankawi magma. However, several of the Guaje samples are still unable to be modeled using the high H_2O/No CO_2 starting condition; thus, if the Guaje samples are recording these processes of CO_2 removal, they are then being overprinted by a more complex ascent path.

Conclusions

This study sought to examine the effect of a previous caldera-forming eruption on the ascent rate of subsequent eruptions and to thoroughly evaluate the assumptions in the embayment volatile diffusion modeling technique used to extract magma ascent dynamics through the application to the Guaje and Tsankawi airfall units of the Bandelier Tuff. Notably, this work is the first to compare ascent rates of two eruptions from an overlapping caldera complex, as well as the first to compare 1D and 2D diffusion models in natural samples. The major results are as follows:

1) Ascent rates obtained for the Guaje and Tsankawi members do not show significant differences; however, we found that many of the later erupted Tsankawi embayments could be successfully modeled using the melt inclusion starting conditions, whereas the Guaje embayments yielded better fits using shallower, embayment starting conditions. This indicates a slow initial decompression of the Guaje magma, while the Tsankawi magma was able to rise more directly from depth. We interpret this to suggest that the latter eruption was able to establish a connected conduit system earlier in the eruption,

but that this process does not correlate to a change in ascent rate. Rather, the remarkable similarity between ascent rates from these two eruptions could point to the importance of regional stress, crustal structure, and intrinsic magma properties to modulating magma ascent.

2) Comparisons of diffusion models in 1D and 2D reveal that embayment geometry affects decompression rates by as much as 50%. However, the 1D and 2D results are within the model uncertainty of each other. We find that temperature uncertainty has a large effect on modeled decompression rates, resulting in a 340–440% increase in ascent rate when applying the large temperature uncertainty ranging from 700ºC to 830ºC. This is the largest source of uncertainty within the model and highlights the importance of constraining the preeruptive temperature.
3) Each airfall deposit shows three orders of magnitude of variation in the ascent rate, suggesting that a few embayments from one layer are not enough to constrain the variation of magma ascent within a given eruption.
4) The absence of CO_2 in embayments compared to their coexisting melt inclusions is a common occurrence in silicic eruptions. The removal of CO_2 indicates a pre-eruptive exsolution event and is potentially a record of eruption triggering. We investigate two CO_2 removal mechanisms—isobaric crystallization and initial decompression, potentially due to buoyancy—and find that both mechanisms are reasonable for removing CO_2 from these systems and possibly supporting eruption onset.

Acknowledgements

This work is supported by the EAR award 1922513 to M. Myers. Computational efforts were performed on the Hyalite High Performance Computing System, operated, and supported by the University Information Technology Research Cyberinfrastructure at Montana State University. The authors thank T. Fischer, R.J. Bodnar, and one anonymous reviewer for their thorough and constructive feedback, which has greatly improved this manuscript.

References Cited

Aldrich Jr, M., 1986, Tectonics of the Jemez lineament in the Jemez Mountains and Rio Grande rift: Journal of Geophysical Research: Solid Earth, v. 91, p. 1753-1762.

Audétat, A., 2013, Origin of Ti-rich rims in quartz phenocrysts from the Upper Bandelier Tuff and the Tunnel Spring Tuff, southwestern USA: Chemical Geology, v. 360, p. 99-104.

Boehnke, P., Watson, E.B., Trail, D., Harrison, T.M., and Schmitt, A.K., 2013, Zircon saturation re-revisited: Chemical Geology, v. 351, p. 324-334.

Boro, J.R., 2019, Recharge and Mobilization of Crystal Mush to Produce and Erupt a Zoned Magma Chamber–the Tshirege Member of the Bandelier Tuff, Valles Caldera, New Mexico, USA: .

Boro, J.R., Wolff, J.A., and Neill, O.K., 2020, Anatomy of a Recharge Magma: Hornblende Dacite Pumice from the rhyolitic Tshirege Member of the Bandelier Tuff, Valles Caldera, New Mexico, USA: Contributions to Mineralogy and Petrology, v. 175, p. 1-26.

Boro, J.R., Wolff, J.A., Neill, O.K., Steiner, A.R., and Ramos, F.C., 2021, Titanium diffusion profiles and melt inclusion chemistry and morphology in quartz from the Tshirege Member of the Bandelier Tuff: American Mineralogist: Journal of Earth and Planetary Materials, v. 106, p. 620-632.

Campbell, M.E., Hanson, J.B., Minarik, W.G., and Stix, J., 2009, Thermal history of the Bandelier magmatic system: Evidence for magmatic injection and recharge at 1.61 Ma as revealed by cathodoluminescence and titanium geothermometry: The Journal of Geology, v. 117, p. 469-485.

Caricchi, L., Annen, C., Blundy, J., Simpson, G., and Pinel, V., 2014, Frequency and magnitude of volcanic eruptions controlled by magma injection and buoyancy: Nature Geoscience, v. 7, p. 126-130.

Cashman, K.V., 2004, Volatile controls on magma ascent and eruption: Washington DC American Geophysical Union Geophysical Monograph Series, v. 150, p. 109-124.

Cassidy, M., Manga, M., Cashman, K., and Bachmann, O., 2018, Controls on explosive-effusive volcanic eruption styles: Nature Communications, v. 9, p. 1-16.

Castro, J.M., and Gardner, J.E., 2008, Did magma ascent rate control the explosive-effusive transition at the Inyo volcanic chain, California? Geology, v. 36, p. 279-282.

Charlier, B., Morgan, D., Wilson, C., Wooden, J., Allan, A., and Baker, J., 2012, Lithium concentration gradients in feldspar and quartz record the final minutes of magma ascent in an explosive supereruption: Earth and Planetary Science Letters, v. 319, p. 218-227.

Crowe, B.M., Linn, G.W., Heiken, G., and Bevier, M.L., 1978, Stratigraphy of the Bandelier tuff in the Pajarito plateau: Applications to Waste Management. Los Alamos National Laboratory Informal Report LA-7225-MS.

deGraffenried, R., and Shea, T., 2021, Using Volatile Element Concentration Profiles in Crystal-Hosted Melt Embayments to Estimate Magma Decompression Rate: Assumptions and Inherited Errors: Geochemistry, Geophysics, Geosystems, v. 22, p. e2021GC009672.

Dunbar, N.W., and Hervig, R.L., 1992, Volatile and trace element composition of melt inclusions from the Lower Bandelier Tuff: implications for magma chamber processes and eruptive style: Journal of Geophysical Research: Solid Earth, v. 97, p. 15151-15170.

Eichelberger, J., Carrigan, C., Westrich, H., and Price, R., 1986, Non-explosive silicic volcanism: Nature, v. 323, p. 598-602.

Ferguson, D.J., Gonnermann, H.M., Ruprecht, P., Plank, T., Hauri, E.H., Houghton, B.F., and Swanson, D.A., 2016, Magma decompression rates during explosive eruptions of Kīlauea volcano, Hawaii, recorded by melt embayments: Bulletin of Volcanology, v. 78, p. 71.

Fowler, S.J., and Spera, F.J., 2008, Phase equilibria trigger for explosive volcanic eruptions: Geophysical Research Letters, v. 35.

Ghiorso, M.S., and Gualda, G.A., 2015, An H 2 O–CO 2 mixed fluid saturation model compatible with rhyolite-MELTS: Contributions to Mineralogy and Petrology, v. 169, p. 1-30.

Giachetti, T., Druitt, T.H., Burgisser, A., Arbaret, L., and Galven, C., 2010, Bubble nucleation, growth and coalescence during the 1997 Vulcanian explosions of Soufrière Hills Volcano, Montserrat: Journal of Volcanology and Geothermal Research, v. 193, p. 215-231.

Goff, F., Warren, R., Goff, C.J., and Dunbar, N., 2014, Eruption of reverse-zoned upper Tshirege Member, Bandelier Tuff from centralized vents within Valles caldera, New Mexico: Journal of Volcanology and Geothermal Research, v. 276, p. 82-104.

Gregg, P., De Silva, S., Grosfils, E., and Parmigiani, J., 2012, Catastrophic caldera-forming eruptions: Thermomechanics and implications for eruption triggering and maximum caldera dimensions on Earth: Journal of Volcanology and Geothermal Research, v. 241, p. 1-12.

Gualda, G.A., Ghiorso, M.S., Lemons, R.V., and Carley, T.L., 2012, Rhyolite-MELTS: a modified calibration of MELTS optimized for silica-rich, fluid-bearing magmatic systems: Journal of Petrology, v. 53, p. 875-890.

Hajimirza, S., Gonnermann, H.M., and Gardner, J.E., 2021, Reconciling bubble nucleation in explosive eruptions with geospeedometers: Nature Communications, v. 12, p. 1-8.

Hamada, M., Laporte, D., Cluzel, N., Koga, K.T., and Kawamoto, T., 2010, Simulating bubble number density of rhyolitic pumices from Plinian eruptions: constraints from fast decompression experiments: Bulletin of Volcanology, v. 72, p. 735-746.

Hammer, J.E., Cashman, K.V., Hoblitt, R., and Newman, S., 1999, Degassing and microlite crystallization during pre-climactic events of the 1991 eruption of Mt. Pinatubo, Philippines: Bulletin of Volcanology, v. 60, p. 355-380.

Heiken, G., Goff, F., Gardner, J.N., Baldridge, W., Hulen, J., Nielson, D.L., and Vaniman, D., 1990, The Valles/Toledo Caldera Complex, Jemez Volcanic Field, New Mexico: Annual Review of Earth and Planetary Sciences, v. 18, p. 27-53.

Heiken, G., Goff, F., Stix, J., Tamanyu, S., Shafiqullah, M., Garcia, S., and Hagan, R., 1986, Intracaldera volcanic activity, Toledo caldera and embayment, Jemez Mountains, New Mexico: Journal of Geophysical Research: Solid Earth, v. 91, p. 1799-1815.

Holycross, M., Watson, E., Richter, F., and Villeneuve, J., 2018, Diffusive fractionation of Li isotopes in wet, highly silicic melts: Geochemical Perspectives Letters, v. 6, p. 39-42.

Humphreys, M.C., Menand, T., Blundy, J.D., and Klimm, K., 2008, Magma ascent rates in explosive eruptions: Constraints from H2O diffusion in melt inclusions: Earth and Planetary Science Letters, v. 270, p. 25-40.

Izett, G.A., and Obradovich, J.D., 1994, 40Ar/39Ar age constraints for the Jaramillo Normal Subchron and the Matuyama-Brunhes geomagnetic boundary: Journal of Geophysical Research: Solid Earth, v. 99, p. 2925-2934.

Jellinek, A.M., and DePaolo, D.J., 2003, A model for the origin of large silicic magma chambers: precursors of caldera-forming eruptions: Bulletin of Volcanology, v. 65, p. 363-381.

Kuentz, D.C., 1988, The Otowi member of the Bandelier Tuff: A study of the petrology, petrography, and geochemistry of an explosive silicic eruption, Jemez Mountains, New Mexico. Master's Thesis, University of Texas at Arlington.

Leschik, M., Heide, G., Frischat, G., Behrens, H., Wiedenbeck, M., Wagner, N., Heide, K., Geißler, H., and Reinholz, U., 2004, Determination of H2O and D2O contents in rhyolitic glasses: Physics and Chemistry of Glasses, v. 45, p. 238-251.

Liu, Y., Zhang, Y., and Behrens, H., 2005, Solubility of H2O in rhyolitic melts at low pressures and a new empirical model for mixed H2O–CO2 solubility in rhyolitic melts: Journal of Volcanology and Geothermal Research, v. 143, p. 219-235.

Liu, Y., Anderson, A.T., and Wilson, C.J., 2007, Melt pockets in phenocrysts and decompression rates of silicic magmas before fragmentation: Journal of Geophysical Research: Solid Earth, v. 112.

Lloyd, A.S., Ruprecht, P., Hauri, E.H., Rose, W., Gonnermann, H.M., and Plank, T., 2014, NanoSIMS results from olivine-hosted melt embayments: magma ascent rate during explosive basaltic eruptions: Journal of Volcanology and Geothermal Research, v. 283, p. 1-18.

Malfait, W.J., Seifert, R., Petitgirard, S., Perrillat, J., Mezouar, M., Ota, T., Nakamura, E., Lerch, P., and Sanchez-Valle, C., 2014, Supervolcano eruptions driven by melt buoyancy in large silicic magma chambers: Nature Geoscience, v. 7, p. 122-125.

Mangan, M.T., Cashman, K.V., and Newman, S., 1993, Vesiculation of basaltic magma during eruption: Geology, v. 21, p. 157-160.

Marti, J., Ablay, G., Redshaw, L.T., and Sparks, R., 1994, Experimental studies of collapse calderas: Journal of the Geological Society, v. 151, p. 919-929.

McLeod, P., and Tait, S., 1999, The growth of dykes from magma chambers: Journal of Volcanology and Geothermal Research, v. 92, p. 231-245.

Myers, M.L., Wallace, P.J., Wilson, C.J., Morter, B.K., and Swallow, E.J., 2016, Prolonged ascent and episodic venting of discrete magma batches at the onset of the Huckleberry Ridge supereruption, Yellowstone: Earth and Planetary Science Letters, v. 451, p. 285-297.

Myers, M.L., Wallace, P.J., Wilson, C.J., Watkins, J.M., and Liu, Y., 2018, Ascent rates of rhyolitic magma at the onset of three caldera-forming eruptions: American Mineralogist, v. 103, p. 952-965.

Myers, M.L., Druitt, T.H., Schiavi, F., Gurioli, L., and Flaherty, T., 2021, Evolution of magma decompression and discharge during a Plinian event (Late Bronze-Age eruption, Santorini) from multiple eruption-intensity proxies: Bulletin of Volcanology, v. 83, p. 1-17.

Newcombe, M.E., Plank, T., Barth, A., Asimow, P., and Hauri, E., 2020, Water-in-olivine magma ascent chronometry: Every crystal is a clock: Journal of Volcanology and Geothermal Research, p. 106872.

Newman, S., and Lowenstern, J.B., 2002, VolatileCalc: a silicate melt–H2O–CO2 solution model written in Visual Basic for excel: Computers & Geosciences, v. 28, p. 597-604.

Nielson, D.L., and Hulen, J.B., 1984, Internal geology and evolution of the Redondo dome, Valles caldera, New Mexico: Journal of Geophysical Research: Solid Earth, v. 89, p. 8695-8711.

Papale, P., Montagna, C.P., and Longo, A., 2017, Pressure evolution in shallow magma chambers upon buoyancy-driven replenishment: Geochemistry, Geophysics, Geosystems, v. 18, p. 1214-1224.

Phillips, E.H., Goff, F., Kyle, P.R., McIntosh, W.C., Dunbar, N.W., and Gardner, J.N., 2007, The 40Ar/39Ar age constraints on the duration of resurgence at the Valles caldera, New Mexico: Journal of Geophysical Research: Solid Earth, v. 112.

Rutherford, M.J., and Devine, J.D., 2003, Magmatic conditions and magma ascent as indicated by hornblende phase equilibria and reactions in the 1995–2002 Soufriere Hills magma: Journal of Petrology, v. 44, p. 1433-1453.

Rutherford, M.J., and Hill, P.M., 1993, Magma ascent rates from amphibole breakdown: an experimental study applied to the 1980–1986 Mount St. Helens eruptions: Journal of Geophysical Research: Solid Earth, v. 98, p. 19667-19685.

Savage, J., Lisowski, M., Prescott, W., and Sanford, A., 1980, Geodetic measurement of horizontal deformation across the Rio Grande Rift near Socorro, New Mexico: Journal of Geophysical Research: Solid Earth, v. 85, p. 7215-7220.

Self, S., Goff, F., Gardner, J.N., Wright, J.V., and Kite, W.M., 1986, Explosive rhyolitic volcanism in the Jemez Mountains: Vent locations, caldera development and relation to regional structure: Journal of Geophysical Research: Solid Earth, v. 91, p. 1779-1798.

Skirius, C.M., Peterson, J.W., and Anderson, A.T., 1990, Homogenizing rhyolitic glass inclusions from the Bishop Tuff: American Mineralogist, v. 75, p. 1381-1398.

Smith, R.L., and Bailey, R.A., 1966, The Bandelier Tuff: A study of ash-flow eruption cycles from zoned magma chambers: Bulletin of Volcanology, v. 29, p. 83-103.

Stimac, J.A., 1996, Hornblende-dacite pumice in the Tshirege member of the Bandelier Tuff: Implications for magma chamber and eruptive processes, *in* New Mexico Geological Society Fall Field Conference Guidebook 47, Jemez Mountains Region. Socorro: New Mexico Geological Society, p. 269-274.

Stix, J., and Layne, G.D., 1996, Gas saturation and evolution of volatile and light lithophile elements in the Bandelier magma chamber between two caldera-forming eruptions: Journal of Geophysical Research: Solid Earth, v. 101, p. 25181-25196.

Sussman, A.J., Lewis, C.J., Mason, S.N., Geissman, J.W., Schultz-Fellenz, E., Oliva-Urcia, B., and Gardner, J., 2011, Paleomagnetism of the Quaternary Bandelier Tuff: Implications for the tectonic evolution of the Española Basin, Rio Grande rift: Lithosphere, v. 3, p. 328-345.

Toramaru, A., 2006, BND (bubble number density) decompression rate meter for explosive volcanic eruptions: Journal of Volcanology and Geothermal Research, v. 154, p. 303-316.

Tramontano, S., Gualda, G.A., and Ghiorso, M.S., 2017, Internal triggering of volcanic eruptions: tracking overpressure regimes for giant magma bodies: Earth and Planetary Science Letters, v. 472, p. 142-151.

Waelkens, C.M. et al., in review, H_2O and CO_2 evolution in the Bandelier Tuff sequence reveals multiple and discrete magma replenishments: Contributions to Mineralogy and Petrology.

Wark, D., and Wolff, J., 2006, Mafic-recharge eruption trigger for the Bandelier and Bishop Tuffs, *in* AGU Fall Meeting Abstracts.

Wark, D.A., and Watson, E.B., 2006, TitaniQ: a titanium-in-quartz geothermometer: Contributions to Mineralogy and Petrology, v. 152, p. 743-754.

Warshaw, C.M., and Smith, R.L., 1988, Pyroxenes and fayalites in the Bandelier Tuff, New Mexico; temperatures and comparison with other rhyolites: American Mineralogist, v. 73, p. 1025-1037.

Westgate, J.A., Woldegabriel, G., Halls, H.C., Bray, C.J., Barendregt, R.W., Pearce, N.J., Sarna-Wojcicki, A.M., Gorton, M.P., Kelley, R.E., and Schultz-Fellenz, E., 2019, Quaternary tephra from the Valles caldera in the volcanic field of the Jemez Mountains of New Mexico identified in western Canada: Quaternary Research, v. 91, p. 813-828.

Wolff, J., and Gardner, J., 1995, Is the Valles caldera entering a new cycle of activity? Geology, v. 23, p. 411-414.

Woodward, L.A., 1977, Rate of crustal extension across the Rio Grande rift near Albuquerque, New Mexico: Geology, v. 5, p. 269-272.

Wysoczanski, R., and Tani, K., 2006, Spectroscopic FTIR imaging of water species in silicic volcanic glasses and melt inclusions: an example from the Izu-Bonin arc: Journal of Volcanology and Geothermal Research, v. 156, p. 302-314.

Zhang, Y., Jenkins, J., and Xu, Z., 1997, Kinetics of the reaction H2O O→ 2 2OH in rhyolitic glasses upon cooling: Geospeedometry and comparison with glass transition: Geochimica Et Cosmochimica Acta, v. 61, p. 2167-2173.

Zhang, Y., Xu, Z., Zhu, M., and Wang, H., 2007, Silicate melt properties and volcanic eruptions: Reviews of Geophysics, v. 45.

CHAPTER THREE

ON THE RECONCILIATION OF MAGMA ASCENT SPEEDOMETERS FOR THE JUNE 12TH 1991 ERUPTION OF MT. PINATUBO

Contribution of Authors and Co-Authors

Manuscript in Chapter Three

Author: Megan A. Harris

Contributions: Sample preparation, data collection, modeling, analysis, and manuscript preparation

Co-Author: Madison L. Myers

Contributions: Project conception and funding, sample acquisition, manuscript editing

Co-Author: Logan Bouley

Contributions: Thin section preparation, SEM data collection and analysis

Co-Author: Behnaz Hosseini

Contributions: Development of 2-stage diffusion model

Manuscript Information Page

Megan A. Harris, Madison L. Myers, Logan Bouley, Behnaz Hosseini Volcanica
Status of Manuscript:
__X__ Prepared for submission to a peer-reviewed journal
____ Officially submitted to a peer-review journal
____ Accepted by a peer-reviewed journal
____ Published in a peer-reviewed journal

To be self-published

Abstract

Decompression rates determined using different magma ascent speedometers commonly vary by several orders of magnitude between technique and are thought to provide insight into magma storage and ascent through different regions of the conduit system. This study seeks to determine whether magma decompression rates derived from three petrologic techniques can be reconciled or integrated to create a more complete model of magma ascent that is representative of the full decompression history from the source to the surface. We focus our study on the earliest Plinian eruptions (June 12, 1991) of Mount Pinatubo, comprising some of the most well-studied and well-documented Plinian events of the 20th century. Updated models for extracting decompression rates from microlite crystallization, bubble nucleation and growth, and volatile diffusion through embayments (unenclosed melt inclusions) are used to reconstruct magma ascent conditions. Using a newly developed two-stage decompression model, embayments reveal an initial phase of decompression nearly two orders of magnitude slower than the final ascent rates, with the acceleration occurring between 20–60 MPa (1–3 km depth). Application of the SNGPlag model (Andrews and Befus, 2020) to number densities of plagioclase microlites suggests that microlite crystallization for the June 12th eruptions can be produced by decompression rates equivalent to those of the initial stage of slower decompression rates retrieved from the embayment diffusion model. Further, applying the speedometer of Hajimirza et al. (2021) to measured bubble number densities, we retrieve decompression rates in close agreement with the second, faster stage of decompression from the embayment diffusion model. The consistency of the extracted decompression rates from the two-stage embayment diffusion model with the decompression rates from microlite and bubble number densities supports the

fidelity of embayments as recorders of decompression through the entire conduit. The ascent timescales derived by the embayment models range from hours to several days, coinciding with the onset of extrusion of the andesitic lava dome. This overlap in timescales is consistent with existing models of the preclimactic activity, where eruptive activity was modulated by the confining pressure of a degassed plug in the shallow conduit.

Introduction

The path of magma decompression and degassing during ascent exerts a strong control over the nature of an eruption, where fluctuations in internal properties (e.g., viscosity) are thought to control shifts in eruption intensity (e.g., Papale and Polacci, 1999; Gonnerman and Manga, 2007; Cassidy et al., 2018). This relationship is largely driven by the behavior of volatiles responding to a decrease in pressure. Although decompression can occur independently of ascent, it is generally assumed that the two processes are correlated. As magma ascends, the solubility of dissolved volatile species (primarily H_2O and CO_2) decreases, which leads to the exsolution of the volatile species into a fluid phase. This history of decompression and volatile exsolution is recorded in all three phases of the magma and has commonly been examined for explosive eruptions by measuring 1) the size and abundance of vesicles (e.g., Toramaru, 2006; Hamada et al., 2010; Shea et al., 2010), 2) the size and abundance of microlites (e.g., Hammer et al., 1999; Toramaru et al., 2008; Brugger and Hammer, 2010; Befus and Andrews, 2018), and 3) the volatile gradients dissolved in groundmass glass trapped in crystal embayments (unsealed melt inclusions) (e.g., Liu et al., 2007, Myers et al., 2018, 2021; Saalfeld et al., 2022). Processes of vesiculation, crystallization, and gas exsolution are enhanced by a feedback loop of gas exsolution and magma decompression; however, the kinetics of their respective formations

operate on very different timescales (Brandeis and Jaupart, 1987; Mangan et al., 1993; Shea, 2017; Cassidy et al., 2018). For instance, although bubble textures inherited from the storage region number densities (BND) are susceptible to processes of gas migration and coalescence, the latest bubble nucleation events occur rapidly in response to decompression and can therefore record the final, syn-eruptive decompression. Thus, compared to other techniques, bubbles may provide information about the latest stage of ascent, and the BND speedometer has classically provided extremely fast decompression rates (1–100 MPa/s using the calibration by Toramaru (2006). On the other end of the resolvable decompression rate spectrum are rates determined from modeling plagioclase crystal size distribution (CSD). CSD is based on compositionally dependent crystal nucleation and growth rates, triggered by undercooling that includes H_2O loss from the melt, forming relatively slow processes (10^{-6}–10^{-9} mm/s for plagioclase in silicic melt; Brugger and Hammer, 2010). This technique provides a record of decompression in the order of hours to days (0.0001–0.0006 MPa/s; Brugger and Hammer, 2010). Therefore, evaluating the CSD of microlites is often better suited to measuring timescales of pre-eruptive magma ascent and/or stalling in the conduit (Hammer et al., 1999). Compared to the bubble and microlite techniques, recent studies measuring and modeling the volatile gradients preserved in melt embayments have found rates that bridge the gap between the BND and CSD methods, providing decompression rates of 0.0001–0.1 MPa/s (Liu et al., 2007; Myers et al., 2018), corresponding to timescales of minutes to days. We seek to understand whether rates from all three methods, for a given erupted clast, are fundamentally recording information specific to independent regions of the conduit system or if the rates retrieved are limited by the modeling parameters used to extract decompression information.

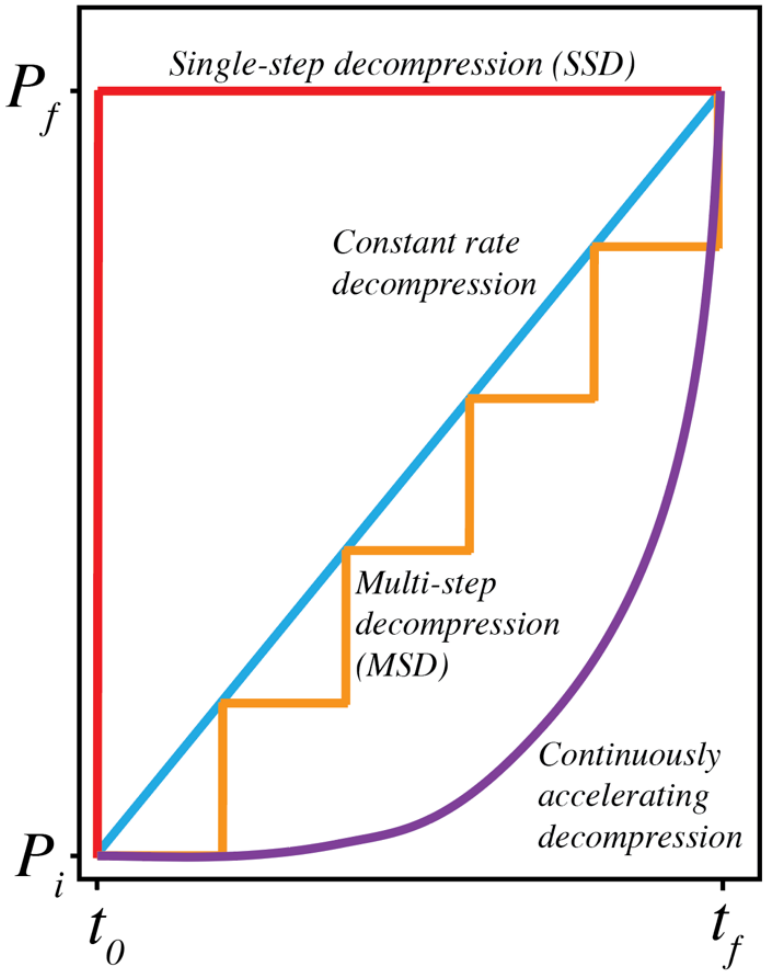

Figure 3.1. Examples of various magma decompression paths used in ascent rate modeling. The red line represents single-step decompression (SSD), the orange line represents multi-step decompression (MSD), the blue line represents constant-rate, continuous decompression, and the purple line represents continuously accelerating decompression.

These three petrologic methods for estimating magma ascent rates have traditionally assumed a simplified single-step, multi-step, or continuous constant-rate decompression path (Figure 3.1). While simplifications are always necessary when modeling natural systems, magma ascent is a non-linear process (Wilson et al., 1980; Mastin, 2002), and thus bubble and microlite nucleation and growth, as well as volatile diffusion models, must also follow a non-linear path. Recent advances in petrologic ascent rate modeling have produced models that more accurately

reflect natural systems. For instance, where the original BND modeling approach is skewed toward peak nucleation rates, a new modeling approach by Hajimirza et al. (2021) retrieves a time-averaged decompression rate, accounting for both the decompression pathway associated with the nucleation of bubbles deep in the conduit and the accelerating decompression during bubble growth. Using these time-averaged decompression rates negates the bias toward faster ascent rates associated with shallow bubble nucleation. A similar effort exists within the CSD community. Previous work by Hammer and Rutherford (2002) used single-step decompression (SSD) and multi-step decompression (MSD) paths to calculate average nucleation and growth rates. While the SSD and MSD models provide a good first-order approximation of microlite growth, they do not represent a decompression path but instead simulate instantaneous intrusion and stalling. Assuming an SSD or MSD path creates a higher supersaturation, and thus the system is initially more nucleation-dominated in comparison to a constant or accelerating decompression pathway, resulting in an overestimation of decompression rate. A new model for simulating microlite nucleation and growth, SNGPlag (Andrews and Befus, 2020), has sought to improve microlite geospeedometry by applying time-integrated nucleation and growth rates based on updated experiments and allows for constant and continuously accelerating decompression pathways. This model allows the user to simulate crystallization along a constant decompression path, rather than a step-function (punctuated drops in pressure), which is a more likely approximation of the natural system. Additionally, unlike previous models, SNGPlag considers the presence of preexisting phenocrysts and antecrysts, which can facilitate crystal growth during decompression. This results in lower supersaturation in the system and thus fewer microlites due to the reduced nucleation rates. Finally, while modeling volatile gradients in

embayments is a powerful new tool, the current model also assumes a continuous, constant decompression rate that can only provide an average ascent rate output, which again blurs the effect of acceleration in the shallow conduit. Although a continually accelerating decompression path model would be computationally prohibitive, work by Hosseini et al. (in prep) has improved upon this by creating a two-stage decompression-diffusion model (two constant rates), which attempts to capture both the initial slow stage of decompression deeper in the conduit as well as the final faster stage of ascent just prior to fragmentation. By applying the two-stage model to diffusion-limited gradients in natural embayments, Hosseini et al. (in prep) find that two-stage models generally provide better fits to the measured data, and total ascent time is increased by a minimum of 4–5x over existing models.

Here, we apply both the original and updated models for extracting decompression rates to a sample suite from the 1991 eruption of Mount Pinatubo, characterized by robust independent observations (e.g., plume height, precursory activity, eruption frequency). The 1991 eruption of Pinatubo is one of the most well-observed and well-studied large-volume silicic eruptions in recorded history (see *Fire and Mud,* 1996). This allows us to answer two important questions: 1) whether magma decompression rates derived from these three different petrologic techniques can be reconciled or integrated to create a more complete model of magma ascent from the source to the surface, and 2) through comparison with other observational datasets, whether the petrologic record preserves evidence for what ended up being an escalation in eruptive energy, and how this information pairs with external monitoring datasets.

The 1991 Eruption of Mount Pinatubo

Mount Pinatubo is located on the island of Luzon in the Philippines, along the Bataan arc and <200 km west of the Manila trench (Figure 3.2). Over its 30,000-year eruptive history, Pinatubo has consistently produced large volumes of dacitic magma that preserve evidence of intrusion and mixing with hotter basalt (Newhall et al., 1996). In the months leading up to the climactic eruption on June 15, 1991, there was significant volcanic unrest, including strong increases in seismicity, small ash emissions and, beginning on June 7, the extrusion of a hybrid andesitic lava dome. The andesitic lava extruded during this early dome formation has been shown to be the product of the injection and mixing of basalt into the dacitic magma reservoir (Pallister et al., 1996). Between June 12–14, four larger eruptions produced vertical columns (19–24 km high), which increased in frequency with time and transitioned from dominantly hybrid andesite (59 wt. % SiO_2) to dacite (64 wt. % SiO_2) in whole-rock composition (Pallister et al., 1996). The andesitic scoria erupted during the June 12 vertical eruptions is identical to the dome andesite in terms of phenocryst assemblage and bulk composition but differs in vesicularity and groundmass crystallization (Pallister et al., 1996). Following these early vertical eruptions, a series of 13 surge deposits were produced during June 14–15. These surge-forming eruptions generally grew less intense with shorter repose intervals, as described by Hoblitt et al. (1996). Hammer et al. (1999) analyzed CSD of plagioclase microlites in the degassed plug material that was erupted during the 13 surge-producing blasts. Based on the microlite crystallinities and repose intervals, Hammer et al. (1999) argued that the pressure of the rising magma continuously increased over time, overcoming the confining pressure of a degassed plug at successively shorter time intervals. During this time, seismicity began to rapidly increase

(Harlow et al., 1996) and culminating in the climactic eruption of June 15, beginning at 1:42 pm, which produced a Plinian column 34 km high and an umbrella cloud over 400 km in diameter that deposited ash predominantly to the southwest (Figure 3.2). The first major explosive eruption, occurring on June 12 at 8:51 am, is the focus of this study.

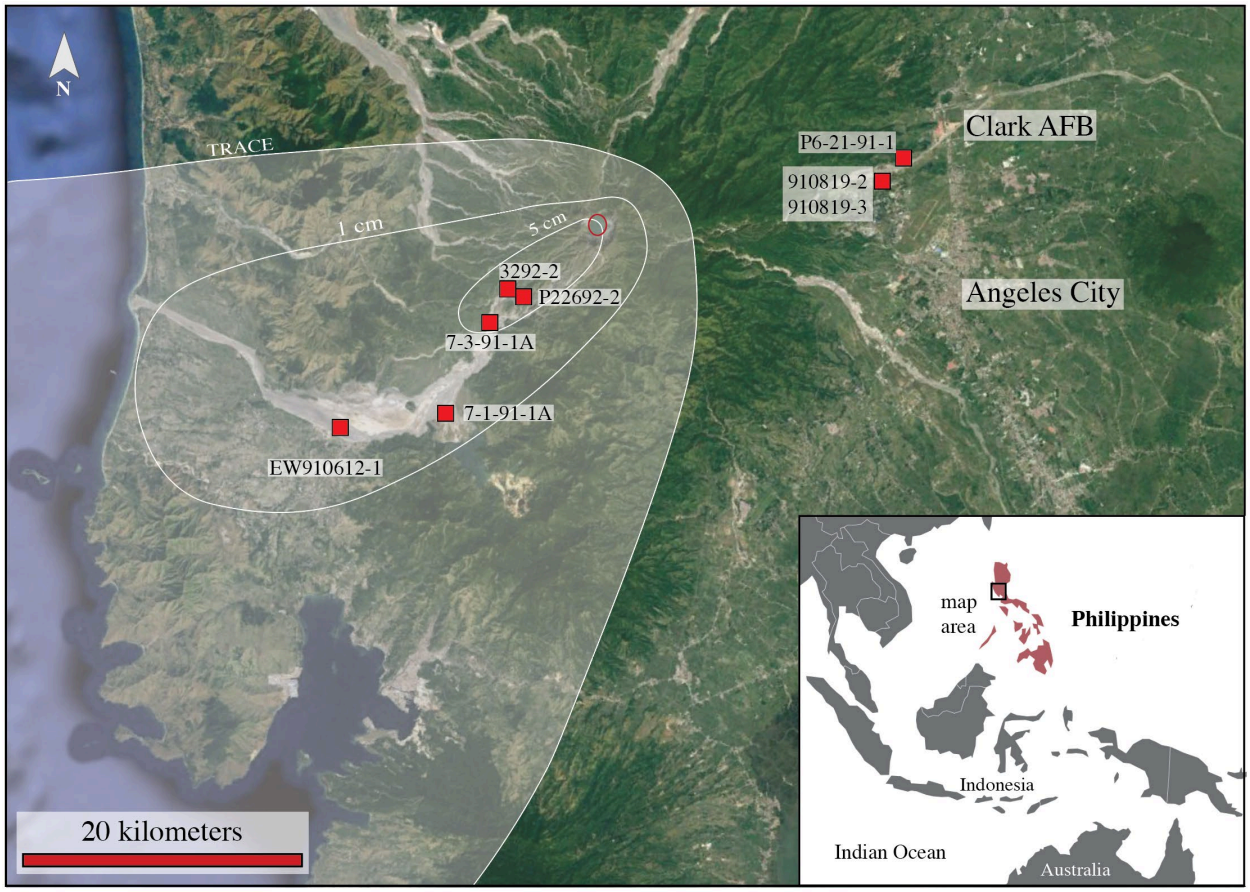

Figure 3.2. Map of Pinatubo and surrounding area, showing the site locations where samples were collected. Isopach lines show thickness of tephra deposits from the 8:51 am June 12th eruption (Paladio-Melasantos et al., 1996). Samples within the isopach lines are from the 8:51 am June 12th eruption. Samples from the 10:51 pm June 12th eruption (910819-2 and 910819-3) and the climactic June 15th eruption (P6-21-91-1) were collected near Clark Air Force Base. The red circle denotes the summit caldera that formed during the climactic eruption. Inset shows the location of the map area.

Extensive work has been done to understand the pre-eruptive conditions of the Pinatubo magma, which we use in this study as input parameters for decompression models. The dominant dacitic magma feeding the later explosive eruptions has a phenocryst assemblage of plagioclase and hornblende (with lesser amounts of cummingtonite overgrowths), Fe-Ti oxides, quartz, apatite, and anhydrite (Pallister et al., 1996). The dacitic magma was stored at 7–11 km (220 ± 50 MPa) beneath Pinatubo based on Al-in-hornblende (rim) geobarometry, with magmatic temperatures around 780 ºC based on Fe-Ti oxide geothermometry (Rutherford and Devine, 1996). Furthermore, the presence of cummingtonite rims on hornblende indicates a temperature of <800°C and a pressure range of 200–320 MPa (Pallister et al., 1996), which agree well with the Al-in-hornblende geobarometry (220 ± 50 MPa). In addition to the mineral assemblage noted for the dacite, the hybrid andesite contains olivine, clinopyroxene, and biotite and yields an elevated Fe-Ti oxide temperature of 950 ºC (Pallister et al., 1996).

Quartz- and plagioclase-hosted melt inclusions from the dacitic magma record pre-eruptive dissolved volatile contents of 5.5–6.4 wt. % H_2O, 55 – 78 ppm S, and less than 20 ppm CO_2 (Rutherford and Devine, 1996). The low sulfur concentrations recorded in the melt inclusions conflict with that required to produce the 17 megatons of SO_2 released during the climactic eruption (Gerlach et al., 1996). The origin of the excess sulfur has been interpreted as resulting from long-term fluxing of volatiles from basaltic magma underlying the main dacitic reservoirs and the formation of a separate fluid phase, with other sources of sulfur (degassing of dacite magma, decomposition of anhydrite, and flash vaporization of hydrothermal fluids) contributing only minor amounts (Gerlach et al., 1996).

Although several geospeedometry methods have been employed in previous studies to evaluate the magma ascent for the 1991 eruptions of Pinatubo, none have yet looked at the earliest Plinian eruptions. In addition, the two methods that have been applied (BND and CSD) were used on different parts of the eruption sequence, meaning we are unable to determine if and how they relate to each other. The BND-based decompression rate for the climactic June 15 eruption was previously determined by Toramaru (2006) to be 100 MPa/s, when assuming homogeneous nucleation. By implementing models of heterogeneous nucleation, the calculated decompression rates are reduced to values of ~4.5 MPa/s (Shea, 2017); however, these rates are still several orders of magnitude faster than other geospeedometry results (i.e., microlites, embayments; <0.1 MPa/s; Brugger and Hammer, 2010; Liu et al., 2007).

Methods

Sample Preparation

Eight pumice clasts and bulk ash material from the 8:51 am and 10:52 pm June 12 explosive eruptions, as well as three samples from the climactic 1:42 pm June 15 eruption, were obtained from the sample archives of the U.S. Geological Survey Cascades Volcano Observatory (Figure 3.2). Seven of the eight samples from the 8:51 am eruption contained pumice clasts large enough to create thin sections for bubble number density (BND) and crystal size distribution (CSD) analysis. These, and one pumice clast from June 15, were cut into billets, impregnated with epoxy using a vacuum system, and sent to the National Petrographic for preparation of thick sections. Two of the climactic June 15 samples lacked pumice clasts large enough to create thin sections. The remainders of each sample, along with 4 samples of fine-grained material, were lightly crushed and sieved to obtain the 500–1000 μm size fraction. Quartz crystals containing

embayments were then picked from this size fraction, where eleven glassy embayments were obtained from seven samples, five of which have accompanying thick sections. Glassy embayments are quite rare in the Pinatubo products, where most embayments (~80% of the examined crystal population) are either highly vesiculated or completely hollow. Glassy embayments analyzed in this work are derived from the June 12 eruptions, as only 1 glassy embayment was found in the June 15 samples. The embayments that were found in the June 15 samples. Were often vesiculated or crystallized and thus unsuitable for diffusion modeling.

Table 3.1. List of samples studied, indicating location, eruption, and which analyses were performed for each sample. X's denote samples that had pumice clasts suitable for CSD and/or BND analysis.

Sample #	*Location*	*Description*	*Eruption*	*Microlites*	*Bubbles*	*Embayments*
7-1-91-1a	Mt. Bagang	6/12/91 tephra (scoria)	12th	X	X	3
EW910612-1	Castillejos	6/12/91 tephra	12th			1
P22692-2a	SW flank	6/12 scoria	12th		X	
P22692-2c	SW flank	6/12/91 tephra	12th	X	X	
P22692-2e	SW flank	Upper 1 cm tephra bed	12th	X	X	3
3292-2a	SW flank	6/12 tephra, Scoria and dacite pumice	12th	X	X	1
3292-2c	SW flank	Blast above 6/12 tephra	12th		X	1
7-3-91-1A	DMA Mt.	Lowermost unit Pinatubo tephra	12th	X	X	1
910819-2	Clark AFB	6/15/91 tephra, top-plinian fall	15th			
910819-3	Clark AFB	6/15/91 tephra, mid-plinian fall	15th			1
P-6-21-91-1	Clark AFB	Pinatubo tephra	15th		X	

Bubble Number Density & Microlite Crystal Size Distribution

All seven thick sections from the June 12 pre-climactic eruption, as well as one thick section from the climactic June 15 eruption, were studied for BND and CSD. Thick sections were imaged at the Montana Technological University Center for Advanced Material Processing using a Tescan TIMA SEM. Operating conditions included a beam intensity of 20, an accelerating voltage of 15 kV, a working distance of 15 mm, and an absorbance current of 20 nA. Images were taken using a nested imaging scheme outlined in Shea et al. (2010) at magnifications of 250x (3 images), 500x (6 images), 1000x (12 images), and 2000x (12 images), for a total of 33 images per thick section (Figure 3.3). When possible, areas with sheared or elongated bubbles were avoided as these areas make 3D (volumetric) projections difficult.

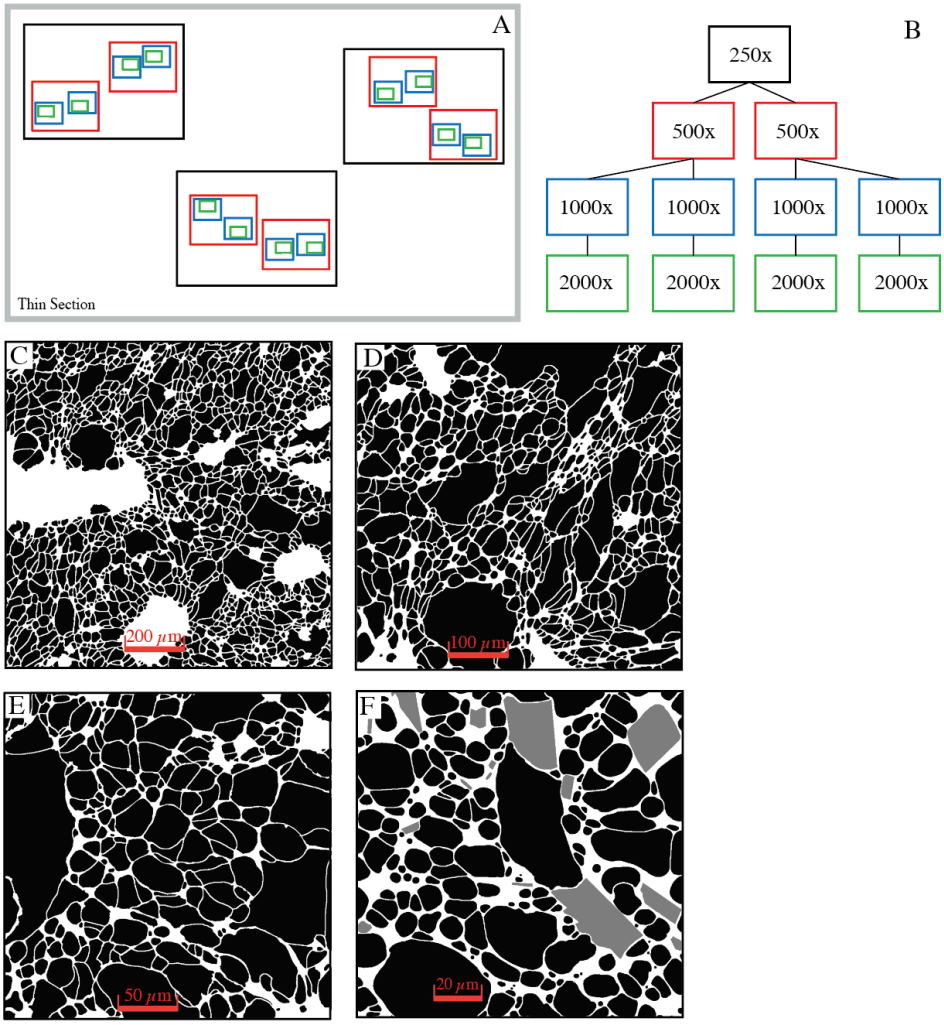

Figure 3.3. SEM photomicrographs were collected using a nested imaging scheme, described by Shea (2010). A) plan view schematic of how images were taken. Three spots were chosen within each thin section and imaged at a magnification of 250x. B) Within each 250x image, a nest of higher magnification images was taken, for a total of 11 images per spot. C – F) Images taken at 250x, 500x, 1000x, and 2000x magnifications were processed in Photoshop to reconstruct bubble walls and to create trinary colored images, where black = bubble, white = glass, and gray = microlite (2000x images only).

Images were processed using Photoshop to produce trinary-colored images (bubbles = black, glass = white, and crystals = gray) and to reconstruct thin or broken bubble walls. The processed images were then loaded into the FOAMS interface (Shea et al., 2010). A minimum bubble size of 5 pixels was chosen (below this value, uncertainty exceeds 5%), and samples were

normalized to a known vesicularity of 0.53 associated with the June 12 scoria (Pallister et al., 1996). The work by Toramaru (2006) is one of the most widely used tools for relating BND to the decompression rate. The output vesicularity-corrected BND (N_{Vcorr}) is used to estimate the decompression rate using the calibration meter of Toramaru (2006), with two surface tension values (the energy required to nucleate and maintain a bubble; σ) explored: 0.06 N m^{-1} for heterogeneous nucleation and 0.025 N m^{-1} for homogeneous nucleation (Shea, 2017).

We then compared these results with those obtained using the updated BND geospeedometer of Hajimirza et al. (2021). Input parameters for this model include mass discharge rate (MDR), initial pressure, temperature, crystallinity, wetting angle (θ), and conduit radius. We calculate an average mass discharge rate of 4.8–7.8 x10^6 kg/s using an ejected volume of 4–6.5 million m^3 DRE for the 8:51 am June 12 eruption (Paladio-Melosantos et al., 1996) and assuming a magma density of 2600 kg/m^3, resulting in a mass of 1.04–1.69 x10^{10} kg of material erupted over a span of 38 minutes (based on seismic observation; Wolfe and Hoblitt, 1996). We iterate through different wetting angles between bubble and crystal surface (values of θ) and conduit radii until modeled BND values match the values determined from our SEM images. The wetting angle is dependent on the mineral phase and dictates whether heterogeneous or homogeneous nucleation occurs (Hurwitz and Navon, 1994). Homogeneous nucleation occurs if the contact angle θ is less than 60° (associated with plagioclase and pyroxene; correlated with higher surface tension values, σ = 0.045 – 0.083 N m^{-1}), and heterogeneous nucleation will occur when θ is greater than 90° (associated with hematite and magnetite; correlated with lower surface tension value, σ = 0.017 – 0.03 N m^{-1}) (Hurwitz and Navon, 1994; Shea, 2017).

Processed images of the 2000x magnifications were then used for textural analysis. Images were analyzed using ImageJ to determine plagioclase microlite number density (N_A = # of crystals/mm^2]), crystallinity (ϕ_m = microlite area/groundmass area), characteristic crystal size ($S_N = (\phi/N_A)^{1/2}$), and the volumetric number density ($MN_V = N_A/S_N$) for each pumice clast (Hammer and Rutherford, 2002; Table 3.2). Plagioclase microlite crystallinity and microlite number density are determined on a bubble- and phenocryst-free (crystals > 50 μm) basis, where bubble volume was determined based on earlier FOAMS results. Twelve images were analyzed per clast for five clasts from the 8:51 am June 12 eruption; the other three thin-sectioned samples, including one from the June 15th eruption, which was completely glassy. We characterize only plagioclase microlites, the most abundant groundmass mineral phase, and only consider crystals <50 μm in length as microlites (Benage et al., 2021). Other crystal phases (i.e., oxides) and plagioclases larger than 50 μm are not included in the microlite calculations.

To determine the decompression conditions that lead to observed MN_V and ϕ values for the June 12 eruption, we applied the decompression model SNGPlag developed by Andrews and Befus (2020). SNGPlag utilizes a range of plagioclase microlite growth and nucleation rates along with decompression pathways, allowing for the simulation of single-step decompression (SSD), multi-step decompression (MSD), and continuous decompression paths. In the SNGPlag model, the nucleation and growth rates at every time step are updated based on the calculated degree of supersaturation. This improvement results in a model of microlite crystallization that better approximates the natural system. We apply this model to recreate our microlite textures for the 8:51 a.m. June 12 eruption and to estimate decompression conditions that could produce the observed crystallinities. We included the presence of plagioclase phenocrysts (volume fraction

calculated by MELTS; Gualda et al., 2012; Ghiorso and Gualda, 2015) in all model simulations. In our modeling, we used microlite growth and nucleation rates based on the experimental calibration of Befus and Andrews (2018), which provides instantaneous nucleation and growth rates, as well as the time-integrated rates from Hammer and Rutherford (2002). We ran models using constant decompression rates ranging from 0.1–100 MPa/hour (0.001–1 m/s). Additionally, we modeled our microlite data using 10x accelerating and single-step decompression paths. For each time step, SNGPlag calculates the degree of supersaturation based on the difference between the model-calculated crystallinity and the equilibrium crystallinity (calculated using MELTS; Gualda et al., 2012). The supersaturation was then used to calculate the instantaneous plagioclase nucleation and growth rates for the given pressure and temperature conditions. Complete model input parameters can be found in Supplementary Table 1.

FTIR Analysis of Volatile Concentrations

Glassy embayments were doubly polished to create crystal wafers that intersect the length of the embayment on both sides. Embayments measured 50–180 μm in length and every embayment had a bubble present at the mouth, important for ensuring equilibrium between the melt and gas phase (Lloyd et al., 2014). Transect measurements of volatile concentrations were conducted using a Nicolet iN10 Fourier-transform infrared (FTIR) spectrometer at Montana State University. Transects were measured along the length of the embayment using an aperture of 20x20 μm, a step size of 10 μm, a resolution of 8 cm^{-1}, and 256 scans per spot. The CO_2 peak, measured at a wavelength of 2350 cm^{-1}, was absent; the H_2O absorbance was measured using the

total water peak (3570 cm^{-1}) and was converted to concentration using the Beer-Lambert law (equation 1):

$$C = \frac{A \cdot M}{\rho \cdot \varepsilon \cdot t} \qquad \text{equation 1}$$

where C is the concentration (wt.%), ρ is the density of the glass (g/L), M is the molecular mass of the volatile (g/mol), ε is the molar absorption coefficient (L/mol-cm^2), A is the height of the absorbance peak, and t is the thickness of the sample (cm), determined using both a digital micrometer and the reflectance fringe method of Wysoczanski and Tani (2006). The micrometer and reflectance methods were generally in agreement; however, if they differed by >4 μm, only the reflectance method thickness was used. To convert from measured absorbance values to water concentration, we assume initial values of 2600 kg/m^3 for ρ and 80 L mol^{-1} cm^{-1} for ε (based on a rhyolitic glass composition) and then iterate through the Beer-Lambert calculation until values for density, molar absorption, and water concentration converge (Skirius, 1990; Leschik et al., 2004). The error on H_2O measurements ranges from ± 0.05 to 0.44 wt. %, with an average of ± 0.22 wt. %. Full transect data can be found in Supplementary Table 2.

Electron Probe Micro Analysis (EPMA)

Due to the changing whole rock composition of erupted materials over the course of the pre-climactic eruptions, compositional analyses of the embayment glasses are necessary to confirm the validity of multiple model parameters, including the appropriate temperature, density, and diffusion coefficients, which all depend on the major elemental composition. Due to the significance that sulfur fluxing may have had on magma degassing in the Pinatubo eruption (Van Hoose et al., 2013), we also analyzed the concentration of sulfur in the embayment glass.

Wafers were placed in 1-inch epoxy mounts and analyses of major elements (Si, Al, Ti, Na, K, Mg, Ca, Fe, Mn, Cl) and S were conducted using a Cameca SX-100 electron microprobe at Oregon State University. Transects were analyzed along the length of the embayment using a spot size of 10 µm, a step size ranging from 15 to 22 µm, and analytical errors were calculated based on analyses of the silicate glass standard RHYO (Smithsonian Microbeam Standard VG 568). Operating conditions included an accelerating voltage of 15 keV, a beam current of 10 nA, and a 10 µm defocused beam. Major elements had counting times that ranged from 10–30 seconds. Sulfur had a longer counting time of 90 seconds, resulting in a detection limit of ~100 ppm. Totals were calculated by adding in the known melt water concentration (determined from FTIR analysis of the interior part of the embayment), and all other elements were normalized using a mean atomic number correction. Analyses with totals below 98.5% or above 101.5% were discarded.

Diffusion Modeling

Diffusion modeling was conducted using a constant-rate decompression model developed by Myers et al. (2018), adapted from Liu et al. (2007). A range of decompression rates and fragmentation pressures (where diffusion ceases due to rapid glass quenching) were iterated to determine the rate that best fit the measured volatile gradients. The H_2O and CO_2 conditions at the melt–bubble boundary were determined by solubility relationships at a given pressure and were updated at every decompression step (Liu et al., 2005). With these boundary conditions, we assume equilibrium between the gas bubble present at the mouth of the embayment and the surrounding magma. The best-fit model was determined by identifying the decompression rate and fragmentation pressure that produced the lowest misfit value, determined by a chi-squared

test of the difference between the measured and modeled gradients. Best-fit models with misfit values ≤ 1 were deemed successful. Due to the lack of CO_2 measured in the melt, all models were run assuming open-system degassing.

Results

Electron Probe Microanalysis

The calibrations and assumptions inherent in the following ascent models first require an understanding of the embayment glass composition. Although the June 12 eruptions produced a hybrid andesite (whole rock), the embayment glass in all quartz hosts is rhyolitic in composition, with an average of 75.2 wt% SiO_2. This allows us to use the rhyolitic diffusion coefficients and solubility relationships (Zhang et al., 2007; Liu et al., 2005), densities (2350 kg/m^3; White and Harris, 1997), and the temperature (780°C; Rutherford and Devine, 1996) associated with the dacite magma in all models. Measured major element concentrations are consistent within error along the length of the embayment, and both Mn and S fall below the detection limits (800 and 100 ppm, respectively). Full major element transect data can be found in Supplementary Table 3.

Bubble Number Density

The corrected volumetric number density (N_{Vcorr}) for the seven clasts representing the first June 12 event ranged from 2.3 x 10^5 – 4.2 x 10^6 mm^{-3} (average = 1.6 x 10^6 mm^{-3}). The N_{Vcorr} of the single clast from the climactic June 15 eruption falls within the range of the pre-climactic samples, with an N_{Vcorr} of 2.01 x 10^6 mm^{-3}. Polacci et al. (2001) found similar values for the climactic dacite pumice, with N_V = 3.0–9.0 x 10^6 mm^{-3}. These values were then used to extract a decompression rate, first using the approach of Toramaru (2006) and then applying the recent calibration from Hajimirza et al. (2021). Initial magma is assumed to be stored at 220 MPa, 780

°C, and to contain a phenocryst crystallinity of 38% (Pallister et al., 1996). If we assume heterogeneous nucleation ($\sigma = 0.06$) and the Toramaru (2006) calibration, observed bubble number densities for all samples correlate to decompression rates ranging from 2.5–17 MPa/s (Figure 3.4). If instead we assume homogeneous nucleation ($\sigma = 0.025$), the corresponding decompression rates are nearly an order of magnitude higher, ranging from 14.5–100 MPa/s. Through applying the Hajimirza et al. (2021) BND ascent rate meter to our samples, where temperature, crystallinity, and nucleation contact angle (θ) are kept constant, the observed BND measurements are best fit by decompression rates ranging from 0.085–0.867 MPa/s (average = 0.386 MPa/s), with $\theta = 155°$ (heterogeneous nucleation), and conduit radius = 14–23 m (Figure 3.4). This fits well with the observed conduit diameter (10's of meters; Gerlach et al., 1991). There is no discernable difference in ascent rates between the June 12 and June 15 samples; however, the June 15 BND measurements require a larger conduit radius (80–130 m; Hajimirza et al., 2021).

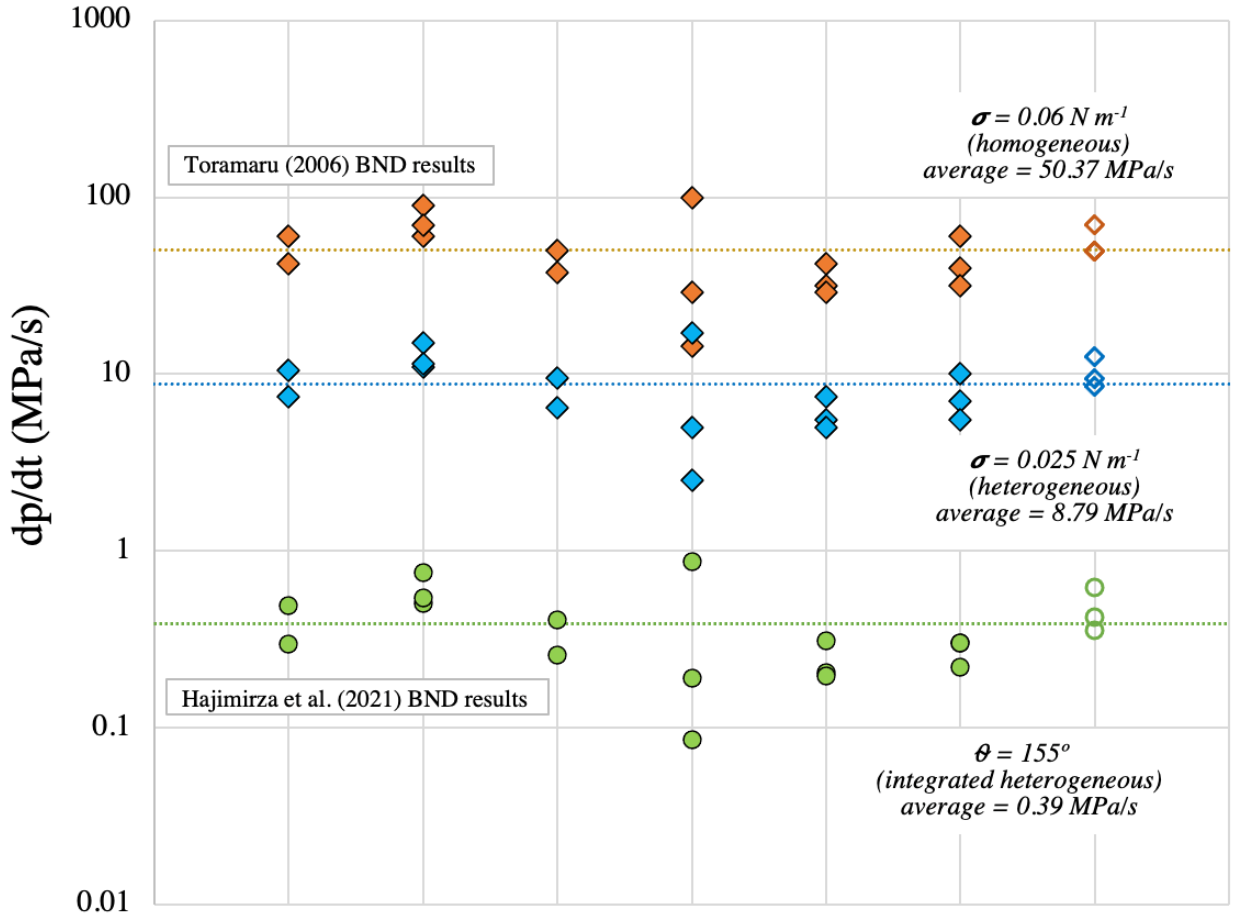

Figure 3.4. Decompression modeling results based on bubble number density, using the model by Toramaru (2006) and the updated model by Hajimirza et al. (2021). Surface tension values of 0.06 and 0.025 N m^{-1} were chosen for the Toramaru (2006) models to represent homogeneous (orange diamonds) and heterogeneous (blue diamonds) nucleation, respectively. Non-integrated, homogeneous models (orange diamonds) result in the highest calculated decompression rates, while integrated, heterogeneous models (green circles) result in slower calculated decompression rates. Open symbols represent the June 15th sample.

Plagioclase Microlite Textural Data

For the five thin sections from the June 12 tephra, microlite number density (MN_V) ranges from 4.2–8.4 x 10^4 mm^{-3} and microlite crystallinity (ϕ) is between 0.06–0.09 (Table 3.2). In comparison, many of the June 14–15 pre-climactic surge deposits made up mostly of dense degassed plug material have higher values, with maximum MN_V values between 7.1 x 10^7–3.1 x 10^9 mm^{-3} and ϕ of 0.01–0.22 (Hammer et al., 1999). However, microlites from the June 12

deposits have a larger characteristic crystal size (S_N), ranging from 10–12 μm, than that found for the surge-forming deposits, which range from 0.49–1.80 μm (Hammer et al., 1999). Some highly vesicular samples from the surge-producing deposits studied by Hammer et al. (1999), as well as the climactic sample and two of the June 12 samples analyzed here, were found to lack microlites altogether.

Table 3.2. Microlite crystallinity, characteristic size, and number density calculation results.

Sample	# of microlites	ϕ	S_N (μm)	MN_V
7-3-91-1A	43	0.067	11.0	5.1E+04
7-1-91-1A	53	0.092	11.3	6.3E+04
3292-2A	74	0.093	10.3	8.4E+04
P22692-2E	63	0.060	11.1	4.4E+04
P22692-2C	60	0.080	12.4	4.2E+04

Calculated volumetric microlite volume densities (MN_V) are recreated in SNGPlag using the Befus and Andrews (2018) nucleation and growth rates and a constant rate decompression path with average rates of 11–43 MPa/hour (0.0031 – 0.0119 MPa/s) (Figure 3.5). These rates agree well with those determined for the June 14–15 surge-forming eruptions, where Befus and Andrews (2018) remodel microlite data from Hammer et al. (1999) under constant decompression and find best fit rates ranging from 5–50 MPa/hour (0.0014–0.014 MPa/s). However, Befus and Andrews (2018) also find that some surge deposit samples are unable to be fit by the continuous decompression models and may instead be recording unsteady decompression, as suggested by Hammer et al. (1999). Intriguingly, models that included even a short stalling event at 70 MPa produced crystallinities that were up to an order of magnitude greater than what was observed in the natural samples (Figure 3.5). The three samples that were

found to be microlite-free are produced by ascent timescales totaling less than 40 minutes (Hammer et al., 1999) or decompression rates ≥ 0.08 MPa/s.

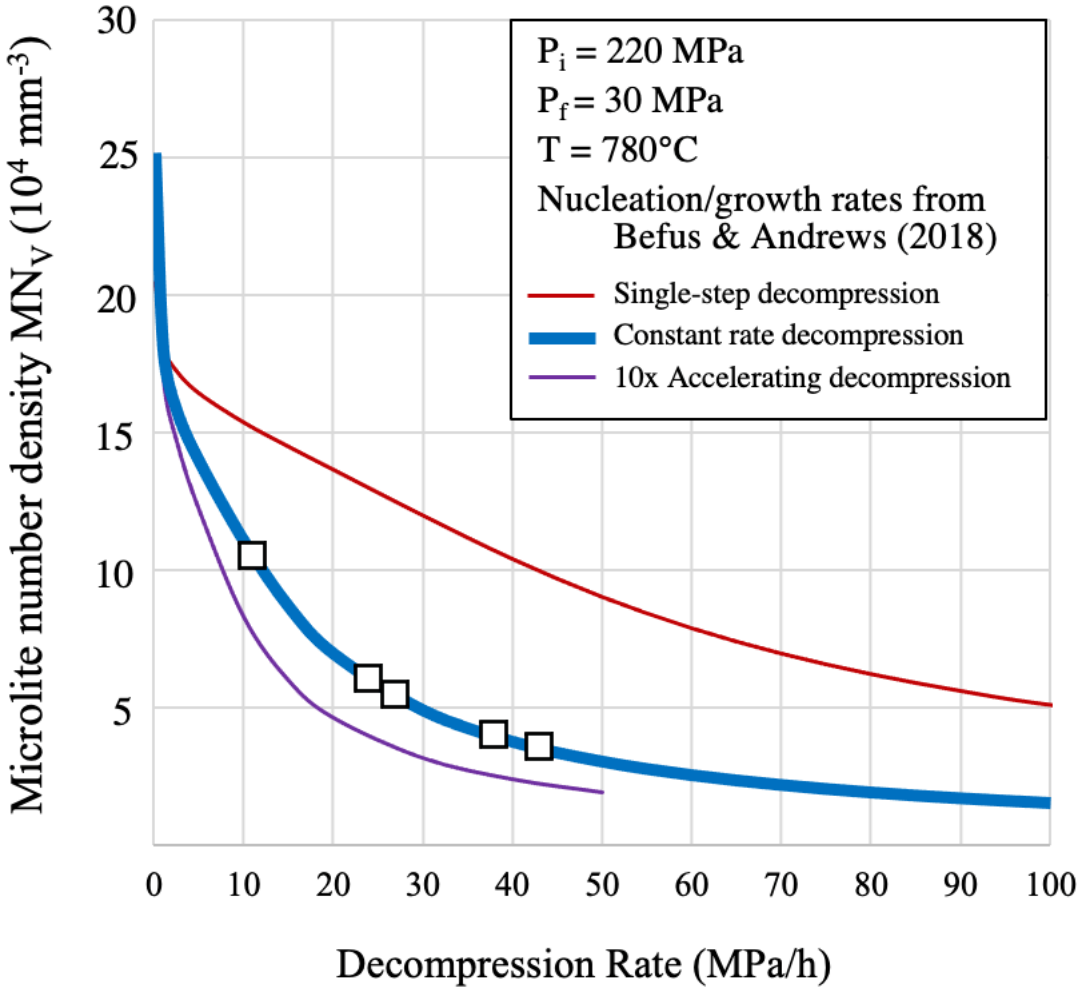

Figure 3.5. Microlite number density values resulting from SNGPlag decompression modeling for models using single-step decompression paths (thin red line), constant-rate decompression paths (thick blue line), and 10x accelerating decompression paths (thin purple line). Observed microlite number densities for the June 12th pumices are shown by the white squares. Inset box shows model input parameters used for all model runs.

Volatile Diffusion in Embayments

We find that the interiors of the June 12 embayments contain 1.82–4.32 wt.% H_2O and lack detectable CO_2 (<20 ppm) and S (<100 ppm). Embayment rims have lower water

concentrations ranging from 1.05–2.46 wt.%, and again lack measurable CO_2 and S. Interior embayment volatile contents represent saturation pressures of 26–113 MPa (1–5 km depth), with an average of 60 MPa (3 km; Newman and Lowenstern, 2002). In comparison, melt inclusions from the June 14–15 phase of the eruption preserve volatile contents of 5.5–6.4 wt % H_2O, less than 20 ppm CO_2 and 55–77 ppm S (Rutherford and Devine, 1996), placing them at saturation pressures of 170–220 MPa, corresponding to depths of 7–11 kilometers below the surface (Rutherford and Devine, 1996). This provides us with two possible starting conditions for our diffusion modeling: the inferred magma storage pressure of 220 MPa and the embayment interiors saturation pressures of 26–113 MPa, which would be akin to stalling within the conduit. Based upon the results from microlites, we prefer the melt inclusion start, as it represents ascent through the entire conduit, but we explore both options below.

Using the magma storage pressure of 220 MPa and a water concentration of 6.35 wt.% as the initial model conditions, we find that six of 11 embayments are able to be modeled successfully using the single-stage (constant-rate decompression with no stalling or acceleration) diffusion code. Extracted decompression rates range from 0.015 to 0.083 MPa/s (average = 0.034 MPa/s) (Figure 3.4), equivalent to ascent rates of 0.58–2.89 m/s (average = 1.25 m/s), with fragmentation pressures ranging from 5–30 MPa when assuming a lithospheric density of 2600 kg/m^3. If instead we use the water content of the embayment interior and the corresponding pressures as the decompression model starting conditions, eight of 11 embayments are able to be fit with the single-stage diffusion model. Best-fit decompression rates range from 0.074–0.500 MPa/s (average = 0.216 MPa/s) (Figure 3.4), and the fragmentation pressures range from 10–30

MPa. These decompression rates are equivalent to ascent rates of 0.81 – 13.55 m/s (average = 7.98 m/s).

As previously discussed, a single-stage continuous decompression path is likely not representative of natural magma, as ascent velocity should increase toward the surface (due to an increase in magma buoyancy via the growth of bubbles; Burgisser and Degruyter, 2015). Thus, the decompression rates derived from the constant-rate, continuous decompression model above are averages of the entire decompression path. To better approximate the effect of accelerating decompression on volatile gradients, we employed a two-stage decompression code developed by Hosseini et al. (in prep). While a continuously accelerating diffusion model would be computationally prohibitive, this model allows for an accelerating profile to be constrained by two separate constant decompression rates. The two-stage decompression code first calculates volatile diffusion during constant-rate decompression from the initial saturation pressure to some intermediate pressure (a free parameter). Once the model reaches the intermediate pressure, the final calculated H_2O concentration gradient is used as the initial condition for the second stage of decompression. The second stage consists of another constant decompression rate, and diffusion is modeled until the system reaches the fragmentation depth.

Applying the two-stage model, we again use the melt inclusion starting conditions (initial pressure = 220 MPa, initial H_2O = 6.35 wt. %) and leave the first- and second-stage decompression rates and the intermediate pressure (the pressure at which the ascent rate changes) as free variables. The fragmentation pressure was chosen based on the best fit single-stage model results, which ranged from 10–30 MPa. We find that the two-stage model provides good fits for the greatest number of embayments (n = 9 of 11), where the remaining two embayments were

unable to be fit by any model. These two embayments had abnormally shaped profiles, with lower water content in the interior and at the rim and higher concentrations in the middle, potentially due to interference with the host crystal (i.e., embayment not fully intersected). All best-fit two-stage decompression models require the presence of an initially slow ascent phase (average dP/dt = 0.004 MPa/s = 0.16 m/s), followed by a much faster period of ascent near the surface (average dP/dt = 0.26 MPa/s = 10.26 m/s) (Figure 3.4). The best fit intermediate pressure varies from 20–60 MPa and is generally within ~10 MPa of the pressure associated with the volatile concentrations in the interior of the embayment.

Table 3.3. Summary of good model fits retrieved from each starting condition. EMB = embayment interior starting condition; MI = melt inclusion starting condition.

	EMB only	MI only	Both EMB/MI	2-stage	None
n = 11	3	1	5	9	2

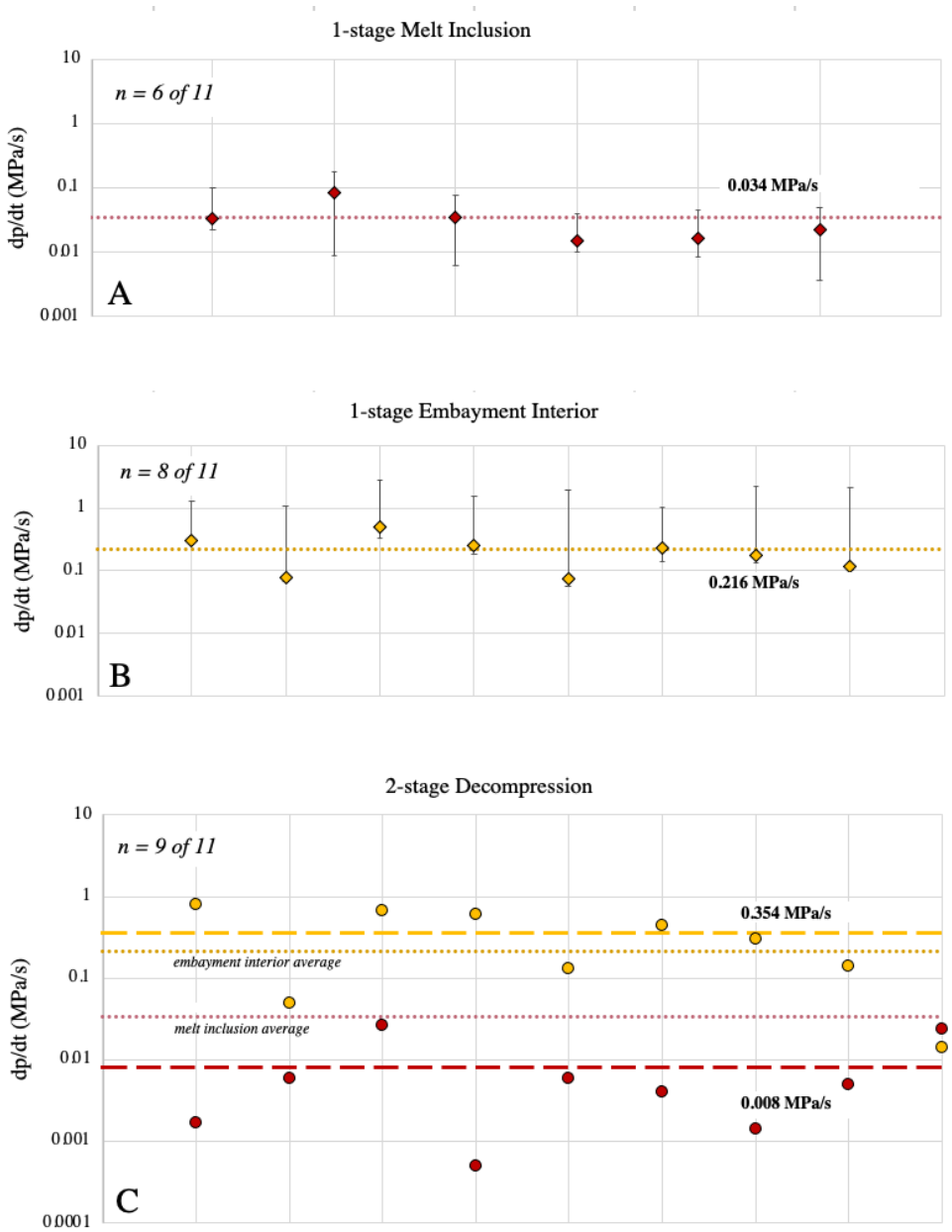

Figure 3.6. (previous page) Results for embayment diffusion modeling. A) continuous, constant decompression-diffusion modeling using the melt inclusion saturation pressure as the starting pressure results in good fits for six of 11 embayments, with an average decompression rate of 0.034 MPa/s (red dotted line). B) 1-stage decompression modeling using the embayment interior saturation pressure as the starting pressure results in good fits for nine of 11 embayments, with an average decompression rate of 0.216 MPa/s (yellow dotted line). C) Implementing a 2-stage model also results in good fits for nine of 11 embayments, with the first stage of decompression being slower than the melt inclusion average (red dashed line; 0.008 MPa/s) and the second stage being slightly faster than the embayment interior average (yellow dashed line; 0.354 MPa/s). Two embayments were unable to be successfully modeled using any of the three modeling approaches.

Discussion

Accounting for Non-linear Decompression

When using the traditional models for extracting the ascent rate, we find that estimates for the Pinatubo June 12 eruption vary by up to 3 orders of magnitude between microlite number density, embayment volatile diffusion, and bubble number density (0.005 to >10 MPa/s). This offset has been previously observed between geospeedometers (compiled by Shea, 2017); however, this study presents the first dataset demonstrating that for a given sample assumed to have experienced a specific decompression pathway, the disagreement still holds. It could be that this difference is due to the kinetic limitations of each technique and will always be weighted toward different regions of the conduit system (Benage et al., 2021; Myers et al., 2021).

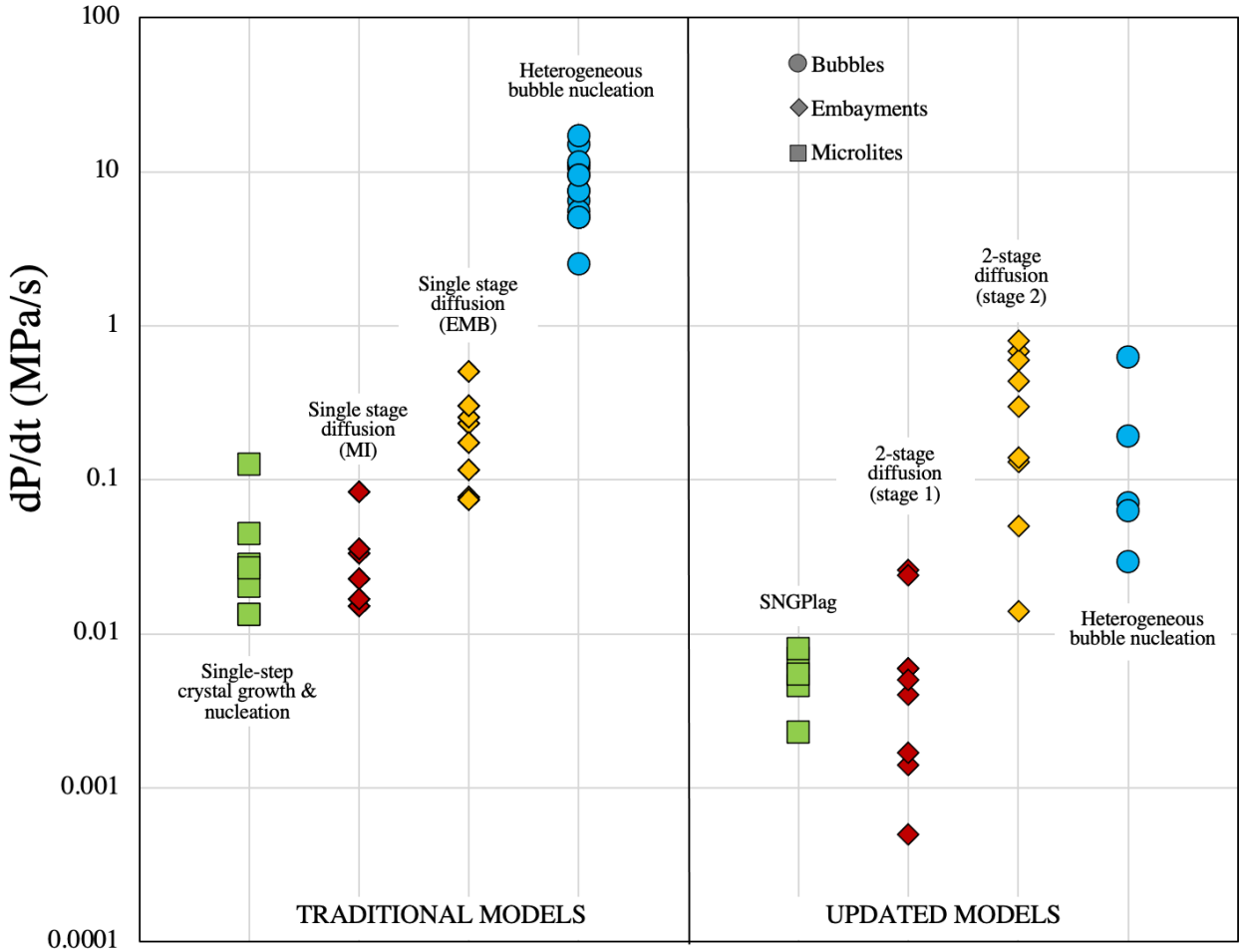

Figure 3.7. Comparison of decompression rate results using traditional models (left) and updated models (right). When using the traditional models, we find there are 3 – 4 orders of magnitude spread across the different models. By implementing the updated models, we find better agreement between the speedometers, where the initial stage of decompression from the embayment model (red diamonds) overlaps well with the SNGPlag model (green squares), and the second stage of decompression from the embayment model (yellow diamonds) correlates well with the updated model of Hajimirza et al. (2021) simulating heterogeneous bubble nucleation (blue circles).

By integrating three newly updated decompression models, which consider the nonlinearity of magma ascent to differing degrees, we show that geospeedometry results are in much better agreement with each other and together better resolve a complete picture of magma ascent from storage to the surface. Most intriguingly, we find that the decompression rates

retrieved from the first stage of the embayment diffusion model (average = 0.008 MPa/s) align closely with the average decompression rate obtained via CSD modeling (0.005 MPa/s), while decompression rates from the second stage of the embayment diffusion model (0.354 MPa/s) align well with those obtained from BND models (0.06–0.62 MPa/s). This implies that the 2-stage embayment diffusion model is capable of resolving information retrieved from both the BND and CSD methods. However, there is still some degree of offset between rates recovered from BND and CSD, although both techniques now implement time-integrated ascent pathways. This offset is likely due to the inherently different kinetic processes controlling the nucleation and growth of bubbles and microlites. For example, when measuring the Pinatubo surge forming deposits, Hammer et al. (1999) show that there is a ~40-minute nucleation lag where ascent rates exceeding this will not produce any microlites, which skews crystallinity-based ascent models to slower timescales. Likewise, heterogeneous nucleation of bubbles may require up to 50 MPa of decompression to reach the necessary supersaturation levels (Shea, 2017), skewing results toward the shallower conduit characterized by faster decompression. Ultimately, this dataset suggests that the two-stage embayment method may be the most comprehensive method for determining ascent-driven magma decompression rates at depth and near the surface. However, embayments may not be found in every eruption or, when present, may be marred by textures that preclude their use in diffusion-based studies (e.g., Reufer et al., 2021). In this case, we suggest that using bubble number density and microlite crystallinity in tandem may provide similar decompression pathway resolution through the conduit system.

Comparison with Other Decompression Rate Estimates

Previous studies have focused on the topic of magma ascent rates for different portions of the Pinatubo eruption sequence. For instance, the BND speedometer developed by Toramaru (2006) has been used to calculate decompression rates of up to 100 MPa/s for the climactic June 15 eruption. This speedometer, however, assumes homogenous nucleation. Shea (2017) argues that heterogeneous nucleation of bubbles occurs on magnetite, resulting in a decompression rate of 4.6 MPa/s for the climactic June 15 event. These values, however, are still several orders of magnitude greater than our BND modeling results for the June 15 event (0.06–0.62 MPa/s). Hammer et al. (1999) examined dense tephras produced during the June 14–15 pre-climactic eruptions. Based on CSD and volatile content, they concluded that magma that produced the dense tephras rapidly ascended from depth to shallow pressures of 6–16 MPa, where it stalled for 28–262 minutes (~4.4 hours). This step-function decompression path results in an initial stage of high nucleation (from ~40–170 minutes), followed by a period of crystal growth (after ~170 minutes). Using time-integrated nucleation and growth of plagioclase microlites, Befus and Andrews (2018) model the CSD measurements from Hammer et al. (1999) and determine ascent rates of 0.001–0.005 MPa/s, three orders of magnitude slower than the rates derived by the BND decompression rate meters. These rates, determined by Befus and Andrews (2018), are comparable to those derived for the June 12 samples using the SNGPlag model. Despite the observed increases in plume height and seismic energy release leading up to the climactic eruption (Harlow et al., 1996), the decompression rates obtained from the three petrologic speedometers do not show evidence of systematic change over time. This suggests that the observed increases in eruptive intensity were not primarily controlled by the magma ascent rate. Cassidy et al. (2018) suggest four scenarios for explosive eruption controls based on degassing

style and viscosity: ascent-controlled, exsolved gas/plug controlled, viscosity-controlled, or decompression-wave controlled. We argue that rather than a "bottom-up" ascent control, the intensity of the preclimactic Pinatubo eruptions was instead controlled by the confining pressure of a shallow plug or by an "unzipping" enlargement of the caldera vent. To further test this, future work on embayment diffusion profiles for the entire suite of preclimactic eruptions is necessary.

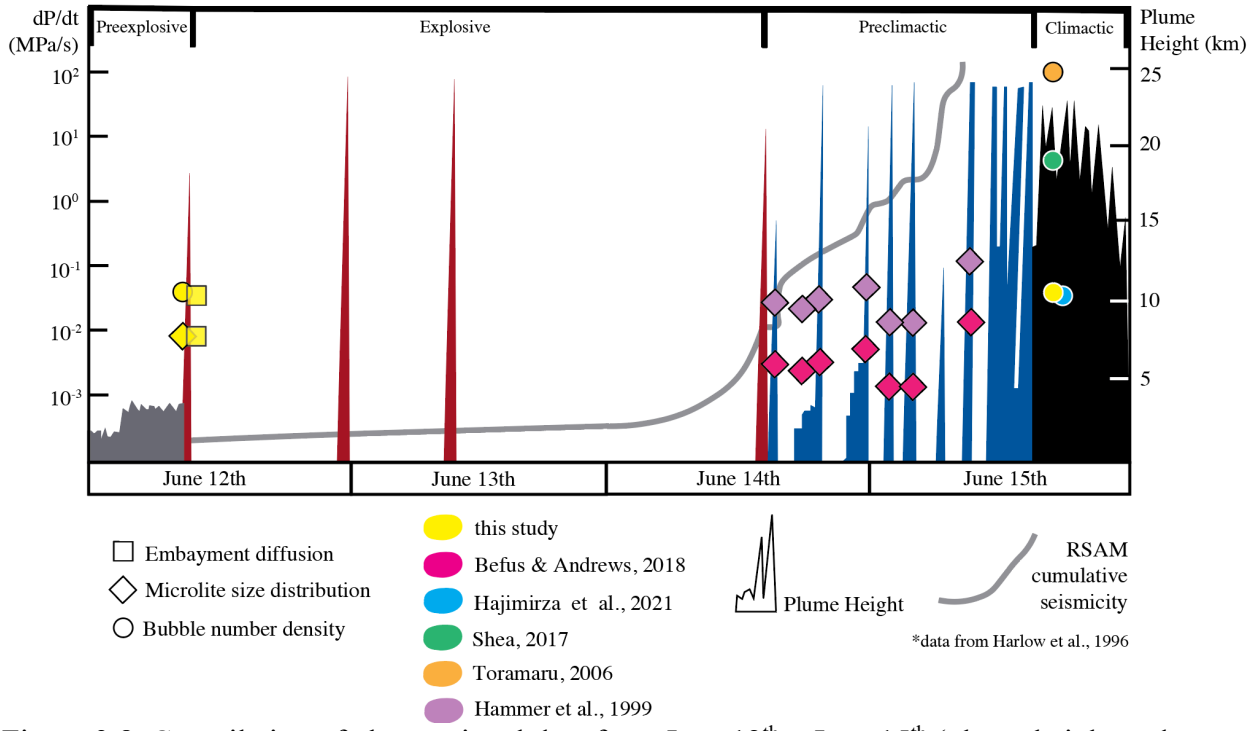

Figure 3.8. Compilation of observational data from June 12th – June 15th (plume height and cumulative RSAM; Harlow et al., 1996) with decompression rates determined by crystal size distribution (Befus and Andrews, 2018; this study), bubble number density (Hajimirza et al., 2021; this study) and embayment diffusion modeling (this study).

Top-down Control of Magma Ascent

One interesting result from the two-stage model is that it reveals, for the June 12 eruption, that there was an initial slower stage of decompression followed by a shorter, faster

final ascent, where the total time of ascent from the embayment model ranges from two hours up to four days. This ascent time is dominated by the first, slower stage. The recognition of a dominant slower initial stage of decompression was also a primary result of the development and application of the two-stage model to previously studied silicic caldera-forming eruptions (Hosseini et al. in prep). When applied to embayments from the 1980 eruption of Mount St. Helens, it was found that the ascent time associated with the slower initial phase (0.008–0.01 MPa/s) aligned closely with previous estimates based on the observed timing between the initial lateral blast and subsequent Plinian explosion 3.5 hours later (Hosseini et al. in prep). For Pinatubo, the timing of this initial slow stage of magma ascent (hours–4 days) coincides with the emplacement of an andesitic lava dome as observed at the surface, where growth was intermittent between June 7 and June 12. The overlap in timescale between these two observations suggests a link in the process, whereby the magma feeding the dome eruption could have been the same magma drawing up the slowest ascending embayments from their storage region, with the explosive phase resulting in a transition to a faster magma ascent. A similar 'top-down' control on magma ascent has been previously speculated for the June 12–14 erupted materials (Hoblitt et al., 1996), meaning that the ascent and eruption of material was driven by a pressure balance from the above plug and feeding magma from below. As more magma was input into the system, the decompressing magma eventually exceeded the confining pressure from the above plug, and the eruption initiated. The eruption ends once the conduit becomes clogged with pyroclasts, resulting in a confining pressure that exceeds the pressure of the magma supply. This process repetitively occurred at faster intervals leading up to the climactic eruption on June 15 (Hammer et al. 1999). We thus interpret the ascent of volatile-rich magma in the days

leading up to the first explosive eruption on June 12 as exceeding the confining pressure of the overlying andesitic lava dome and clearing the path for subsequent eruptions.

The Excess Sulfur Problem

The 1991 eruption of Pinatubo produced an enormous volume of SO_2 gas during the course of its 2-month period of unrest leading up to the climactic eruption, totaling over 17 megatons (Gerlach et al., 1996). Beginning May 13, remotely sensed gas measurements indicated SO_2 emissions of ~500 tons/day, increasing up to 5000 tons/day on May 28. Sulfur output then briefly dropped to a minimum of ~260 tons/day, but quickly ramped up again with the extrusion of the lava dome beginning June 7. In the lead-up to the climactic eruption (June 13–15), sulfur emissions increased exponentially, reaching up to 20 million tons on June 15–16 (Daag et al., 1996). Previous work has found that sulfur concentrations in the matrix glass are similar to that of quartz-hosted melt inclusions (~80 ppm), indicating that the dacite magma was not the primary source of the sulfur. Instead, the excess sulfur is thought to have been derived by fluxing of SO_2-rich fluid degassed from the body of basalt underplating the dacitic reservoir (Gerlach et al., 1996). The presence of apatite with S-rich cores and quartz-hosted H_2O-CO_2-S fluid inclusions indicate that sulfur fluxing from a basalt source caused compositional changes in the dacitic magma over an extended period prior to the onset of unrest at Pinatubo (Van Hoose et al., 2013; Borisova et al., 2014).

Fluxing of excess gas through the system could trigger further crystallization of microlites, which would skew the crystallinity data and negate the comparisons made in this work. The lack of sulfur recorded in all embayment glass from this study (at least below 100 ppm) may provide further insights into the mechanism of gas fluxing in the Pinatubo magmatic

system. The first explanation could be that the embayments are not recording the changes in the surrounding melt. However, we see evidence that the embayments record changes in the external concentrations of other volatile species, so there is no reason to believe that they would not record changes in sulfur concentration. Another possibility is that sulfur fluxing is happening too quickly to re-equilibrate with the melt. Sulfur has a diffusivity that is one to two orders of magnitude slower than other volatiles in silicate melts (Baker and Rutherford, 1995). If the fluxing of sulfur was a short-lived event, the low solubility and diffusivity of sulfur in the melt may have prevented it from re-equilibrating with the embayment melt. However, surface sulfur emissions occurred for months leading up to and throughout the eruption, meaning that it was consistently being supplied to the system and would have likely had time to re-equilibrate. It has also been postulated that sulfur migrates as a bubble-rich foam, which rises through the dacitic reservoir as a low-density plume (Kayzar et al., 2009). The lack of sulfur in the embayments may support the theory that the excess sulfur did not flux homogeneously throughout the entire melt, but rather was transported through the system via discrete preferential pathways (i.e., cracks/plumes).

Conclusion

This study sought to reconcile three common petrologic methods for estimating magma decompression rate, to create an integrated model of magma ascent from source to surface for the precursory June 12, 1991, eruption of Mount Pinatubo (Philippines). By implementing three updated models that more closely approximate inferred natural magma decompression pathways to an individual sample, this work highlights that melt embayments are a robust tool for restoring magma ascent from storage to surface. In the event that embayments cannot be found or

otherwise leveraged, microlite and bubble number densities may be used together to provide similar information, assuming that the system has not experienced cooling- or flux-driven crystallization. The two-stage decompression model applied to embayment volatile gradients resolves an accelerating ascent pathway, where the initial stage of ascent is now in agreement with microlite decompression rates and the final stage is in agreement with bubble number density decompression rates. We find that the two-stage embayment model timescales align well with the extrusion of a lava dome, supporting the model of top-down control on eruptive behavior.

References Cited

Andrews, B. J., & Befus, K. S. (2020). Supersaturation Nucleation and Growth of Plagioclase: a numerical model of decompression-induced crystallization. *Contributions to Mineralogy and Petrology*, *175*(3), 1-20.

Befus, K. S., & Andrews, B. J. (2018). Crystal nucleation and growth produced by continuous decompression of Pinatubo magma. *Contributions to Mineralogy and Petrology*, *173*(11), 1-20.

Benage, M. C., Wright, H., & Coombs, M. L. (2021). Eruption of compositionally heterogeneous andesites from a complex storage region during the 2006 eruption of Augustine Volcano. *Bulletin of Volcanology*, *83*(3), 1-23.

Borisova, A. Y., Toutain, J. P., Dubessy, J., Pallister, J., Zwick, A., & Salvi, S. (2014). H2O–CO2–S fluid triggering the 1991 Mount Pinatubo climactic eruption (Philippines). *Bulletin of Volcanology*, *76*(2), 1-9.

Brandeis, G., & Jaupart, C. (1987). The kinetics of nucleation and crystal growth and scaling laws for magmatic crystallization. *Contributions to Mineralogy and Petrology*, *96*(1), 24-34.

Brugger, C. R., & Hammer, J. E. (2010). Crystallization kinetics in continuous decompression experiments: implications for interpreting natural magma ascent processes. *Journal of Petrology*, *51*(9), 1941-1965.

Cassidy, M., Manga, M., Cashman, K., & Bachmann, O. (2018). Controls on explosive-effusive volcanic eruption styles. *Nature communications*, *9*(1), 1-16.

Daag, A. S., Tubianosa, B. S., Newhall, C. G., Tungol, N. M., Javier, D., Dolan, M. T., ... & Regalado, T. M. (1996). Monitoring sulfur dioxide emission at Mount Pinatubo. Fire and mud: eruptions and lahars of Mount Pinatubo, Philippines, Newhall CG, Punongbayan RS.

Ferguson, D. J., Gonnermann, H. M., Ruprecht, P., Plank, T., Hauri, E. H., Houghton, B. F., & Swanson, D. A. (2016). Magma decompression rates during explosive eruptions of Kīlauea volcano, Hawaii, recorded by melt embayments. *Bulletin of Volcanology*, *78*(10), 1-12.

Ghiorso, M. S., & Gualda, G. A. (2015). An H_2O–CO_2 mixed fluid saturation model compatible with rhyolite-MELTS. *Contributions to Mineralogy and Petrology*, *169*(6), 1-30.

Gerlach, T. M., Westrich, H. R., & Symonds, R. B. (1996). Preeruption vapor in magma of the climactic Mount Pinatubo eruption: Source of the giant stratospheric sulfur dioxide cloud. Fire and mud: eruptions and lahars of Mount Pinatubo, Philippines, Newhall CG, Punongbayan RS.

Gonnermann, H. M., & Manga, M. (2007). The fluid mechanics inside a volcano. *Annual Review of Fluid Mechanics*, *39*(1), 321-356.

Gualda, G. A., Ghiorso, M. S., Lemons, R. V., & Carley, T. L. (2012). Rhyolite-MELTS: a modified calibration of MELTS optimized for silica-rich, fluid-bearing magmatic systems. *Journal of Petrology*, *53*(5), 875-890.

Hajimirza, S., Gonnermann, H. M., & Gardner, J. E. (2021). Reconciling bubble nucleation in explosive eruptions with geospeedometers. *Nature communications*, *12*(1), 1-8.

Hamada, M., Laporte, D., Cluzel, N., Koga, K. T., & Kawamoto, T. (2010). Simulating bubble number density of rhyolitic pumices from Plinian eruptions: constraints from fast decompression experiments. *Bulletin of Volcanology*, *72*(6), 735-746.

Hammer, J. E., Cashman, K. V., Hoblitt, R. P., & Newman, S. (1999). Degassing and microlite crystallization during pre-climactic events of the 1991 eruption of Mt. Pinatubo, Philippines. *Bulletin of Volcanology*, *60*(5), 355-380.

Hammer, J. E., & Rutherford, M. J. (2002). An experimental study of the kinetics of decompression-induced crystallization in silicic melt. *Journal of Geophysical Research: Solid Earth*, *107*(B1), ECV-8.

Harlow, D. H., Power, J. A., Laguerta, E. P., Ambubuyog, G., White, R. A., & Hoblitt, R. P. (1996). Precursory seismicity and forecasting of the June 15, 1991, eruption of Mount Pinatubo. Fire and Mud: eruptions and lahars of Mount Pinatubo, Philippines, Newhall CG, Punongbayan RS.

Hoblitt, R. P. (1996). The preclimactic eruptions of Mount Pinatubo, June 1991. Fire and Mud: eruptions and lahars of Mount Pinatubo, Philippines, Newhall CG, Punongbayan RS.

Hosseini et al. (in prep). Are we recording? ……

Hurwitz, S., & Navon, O. (1994). Bubble nucleation in rhyolitic melts: Experiments at high pressure, temperature, and water content. *Earth and Planetary Science Letters*, *122*(3-4), 267-280.

Kayzar, T. M., Cooper, K. M., Reagan, M. K., & Kent, A. J. (2009). Gas transport model for the magmatic system at Mount Pinatubo, Philippines: Insights from (210Pb)/(226Ra). *Journal of Volcanology and Geothermal Research*, *181*(1-2), 124-140.

Leschik, M., Heide, G., Frischat, G. H., Behrens, H., Wiedenbeck, M., Wagner, N., Reinholz, U. (2004). Determination of H_2O and D2O contents in rhyolitic glasses. *Physics and Chemistry of Glasses*, *45*(4), 238-251.

Liu, Y., Zhang, Y., & Behrens, H. (2005). Solubility of H_2O in rhyolitic melts at low pressures and a new empirical model for mixed H2O–CO2 solubility in rhyolitic melts. *Journal of Volcanology and Geothermal Research*, *143*(1-3), 219-235.

Liu, Y., Anderson, A. T., & Wilson, C. J. (2007). Melt pockets in phenocrysts and decompression rates of silicic magmas before fragmentation. *Journal of Geophysical Research: Solid Earth*, *112*(B6).

Lloyd, A. S., Ruprecht, P., Hauri, E. H., Rose, W., Gonnermann, H. M., & Plank, T. (2014). NanoSIMS results from olivine-hosted melt embayments: Magma ascent rate during explosive basaltic eruptions. *Journal of Volcanology and Geothermal Research*, *283*, 1-18.

Mangan, M. T., Cashman, K. V., & Newman, S. (1993). Vesiculation of basaltic magma during eruption. *Geology*, *21*(2), 157-160.

Mastin, L. G. (2002). Insights into volcanic conduit flow from an open-source numerical model. *Geochemistry, Geophysics, Geosystems*, *3*(7), 1-18.

Mercado, R. A. (1996). Socioeconomic impacts of the Mount Pinatubo eruption. Fire and Mud: eruptions and lahars of Mount Pinatubo, Philippines, Newhall CG, Punongbayan RS.

Myers, M. L., Wallace, P. J., Wilson, C. J., Watkins, J. M., & Liu, Y. (2018). Ascent rates of rhyolitic magma at the onset of three caldera-forming eruptions. *American Mineralogist*, *103*(6), 952-965.

Myers, M. L., Druitt, T. H., Schiavi, F., Gurioli, L., & Flaherty, T. (2021). Evolution of magma decompression and discharge during a Plinian event (Late Bronze-Age eruption, Santorini) from multiple eruption-intensity proxies. *Bulletin of Volcanology*, *83*(3), 1-17.

Newhall, C. G., & Punongbayan, R. (Eds.). (1996). *Fire and mud: eruptions and lahars of Mount Pinatubo, Philippines* (p. 1126). Quezon City: Philippine Institute of Volcanology and Seismology.

Paladio-Melosantos, M. L. O., Solidum, R. U., Scott, W. E., Quiambao, R. B., Umbal, J. V., Rodolfo, K. S., & Punongbayan, R. S. (1996). Tephra falls of the 1991 eruptions of Mount Pinatubo, Fire and mud: eruptions and lahars of Mount Pinatubo, Philippines, Newhall CG, Punongbayan RS.

Pallister, J. S., Hoblitt, R. P., Meeker, G. P., Knight, R. J., & Siems, D. F. (1996). Magma mixing at Mount Pinatubo: petrographic and chemical evidence from the 1991 deposits. Fire and mud: eruptions and lahars of Mount Pinatubo, Philippines, Newhall CG, Punongbayan RS.

Papale, P., & Polacci, M. (1999). Role of carbon dioxide in the dynamics of magma ascent in explosive eruptions. *Bulletin of volcanology*, *60*(8), 583-594.

Rutherford, M. J., & Devine, J. D. (1996). Preeruption pressure-temperature conditions and volatiles in the 1991 dacitic magma of Mount Pinatubo, Fire and mud: eruptions and lahars of Mount Pinatubo, Philippines, Newhall CG, Punongbayan RS.

Saalfeld, M. A., Myers, M. L., deGraffenried, R., Shea, T., & Waelkens, C. M. (2022). On the rise: using reentrants to extract magma ascent rates in the Bandelier Tuff caldera complex, New Mexico, USA. *Bulletin of Volcanology*, *84*(1), 1-21.

Shea, T., Houghton, B. F., Gurioli, L., Cashman, K. V., Hammer, J. E., & Hobden, B. J. (2010). Textural studies of vesicles in volcanic rocks: an integrated methodology. *Journal of Volcanology and Geothermal Research*, *190*(3-4), 271-289.

Shea, T. (2017). Bubble nucleation in magmas: a dominantly heterogeneous process?. *Journal of Volcanology and Geothermal Research*, *343*, 155-170.

Skirius, C. M., Peterson, J. W., & Anderson, A. T. (1990). Homogenizing rhyolitic glass inclusions from the Bishop Tuff. *American Mineralogist*, *75*(11-12), 1381-1398.

Spence, R. J., Pomonis, A., Baxter, P. J., Coburn, A. W., White, M., & Dayrit, M. (1996). Building damage caused by the Mount Pinatubo eruption of June 15, 1991. Fire and Mud: Eruptions and Lahars of Mount Pinatubo, Philippines. Newhall CG, Punongbayan RS.

Toramaru, A. (2006). BND (bubble number density) decompression rate meter for explosive volcanic eruptions. *Journal of Volcanology and Geothermal Research*, *154*(3-4), 303-316.

Toramaru, A., Noguchi, S., Oyoshihara, S., & Tsune, A. (2008). MND (microlite number density) water exsolution rate meter. *Journal of Volcanology and Geothermal Research*, *175*(1-2), 156-167.

Van Hoose, A. E., Streck, M. J., Pallister, J. S., & Wälle, M. (2013). Sulfur evolution of the 1991 Pinatubo magmas based on apatite. *Journal of Volcanology and Geothermal Research*, *257*, 72-89.

Wilson, L., Sparks, R. S. J., & Walker, G. P. (1980). Explosive volcanic eruptions—IV. The control of magma properties and conduit geometry on eruption column behavior. *Geophysical Journal International*, *63*(1), 117-148.

White, J. P., & Harris, M. N. (1997). Changing sources: Early Lapita period obsidian in the Bismarck Archipelago. *Archaeology in Oceania*, *32*(1), 97-107.

Wolfe, E. W., & Hoblitt, R. P. (1996). Overview of the eruptions, Fire and mud: Eruptions and lahars of Mount Pinatubo, Philippines. Newhall CG, Punongbayan RS.

Wysoczanski, R., & Tani, K. (2006). Spectroscopic FTIR imaging of water species in silicic volcanic glasses and melt inclusions: An example from the Izu-Bonin arc. *Journal of Volcanology and Geothermal Research*, *156*(3-4), 302-314.

Zhang, Y., Xu, Z., Zhu, M., & Wang, H. (2007). Silicate melt properties and volcanic eruptions. *Reviews of Geophysics*, *45*(4).

CHAPTER FOUR

ON THE ORIGIN OF EMBAYMENTS

Contribution of Authors and Co-Authors

Manuscript in Chapter Four

Author: Megan A. Harris

Contributions: Project conception, sample preparation, data collection and analysis, manuscript preparation

Co-Author: Madison L. Myers

Contributions: Project conception and funding, manuscript editing

Co-Author: Nathaniel Lenhard

Contributions: Sample preparation, CL imaging

Manuscript Information Page

Megan A. Harris, Madison L. Myers, Madison L. Myers, Nathaniel Lenhard
Geology
Status of Manuscript:
__X__ Prepared for submission to a peer-reviewed journal
____ Officially submitted to a peer-review journal
____ Accepted by a peer-reviewed journal
____ Published in a peer-reviewed journal

Published by Geological Society of America

Abstract

Although embayments are increasingly being used to understand processes occurring within magmatic systems (e.g., magma decompression and degassing), it is still highly debated as to how they form. Exploring the origin of embayments may allow for increased understanding of the pre-erupted conditions (e.g., pressure and temperature) prior to the onset of eruptions that contain them in abundance. Currently, two mechanisms have been proposed to explain the formation of embayments: 1) rapid growth due to undercooling driven by magma decompression or volatile fluxing or 2) dissolution due to superheating, potentially aided by bubble drilling, occurring during recharge of warmer magma into the system. To discriminate between these two mechanisms, we first analyzed the relationship between the embayment boundary and zoning bands using cathodoluminescence (CL) images of quartz crystals from five silicic centers. Of the 295 crystals imaged, we find that the majority (79%) preserve zoning relationships indicative of growth (zoning wraps around embayment or oscillatory/sector zoning). Only 5% of images show clear dissolution relationships (embayment cross cuts zoning), however, dissolution surfaces are common in the interiors of crystals with growth zoning relationships (22% of total images). This highlights that while growth dynamics (aka undercooling) are likely dominating for much of the embayment's formation, dissolution is still an important factor for embayment development. We next sought to form embayments experimentally using a cold-seal pressure vessel, where crystals are subjected to undercooled and superheated conditions. Experiments were conducted at temperatures 55 – 80°C above/below quartz stability to promote dissolution/growth, respectively, and ranged in duration from 24-672 hours. We employed 3D microtomography before and after the experiments to identify morphological changes. In contrast to CL results, we

find that indentations in the crystal surface from adhering bubbles and bulbous hollow embayments 50 – 80 μm deep are more readily formed in superheated conditions, indicating quartz dissolution rates of 10^{-10} – 10^{-9} m/s. Meanwhile undercooled conditions resulted in some moderate crystal faceting but no embayments, indicating that our growth experiments are not fully reproducing embayment formation conditions. This work highlights that embayments are easily formed under disequilibrium conditions, but that their common growth origin in natural systems requires a more complex combination of both dissolution and growth processes.

Introduction

Understanding the conditions and timescales of magma accumulation, ascent, and eventual eruption is imperative to forecasting and mitigating the dangers posed by volcanic eruptions (Sparks and Cashman, 2017). Melt embayments (unenclosed melt inclusions, also known as melt pockets, reentrants, or hourglass inclusions) have become an important tool in attempting to unravel the history of magmatic evolution and eruption (Myers et al., 2018; 2021; Befus et al., 2019; Barbee et al., 2020; Reufer et al., 2021; Saalfeld et al., 2022; Zuccarello et al., 2022). However, there is uncertainty as to how these features form (Loewen et al., 2016; Barbee et al., 2020). This question has implications surrounding the magmatic storage conditions prior to eruption and, if answered, could serve to better inform our understanding of the pre-eruptive conditions. For instance, most models of magmatic processes (crystallization, ascent, degassing) assume initial equilibrium conditions (e.g., Andrews and Befus, 2020; Liu et al., 2007; Gardner et al., 2000), however, the existence of melt embayments in many erupted products implies the system was in disequilibrium for some period of time preceding eruption (Barbee et al., 2020). The disequilibrium mechanisms responsible for forming embayments likely follow similar

principals to melt inclusions, either by rapid crystal growth in an undercooled magma (liquidus temperature is higher than magma temperature), or by dissolution of the crystal during superheating causing imperfect crystal boundaries to form (Faure and Schiano, 2005; Brugger and Hammer, 2015; Barbee et al., 2020). Alternatively, systems that lack melt inclusions and embayments likely formed during phases of polyhedral growth under near-equilibrium conditions (Barbee et al., 2020). Identifying crystal growth and dissolution patterns and textures is an important record of magmatic evolution and has been used to interpret multiple recharge, mixing and triggering processes from basaltic to silicic systems (Peppard et al., 2001; Costa et al., 2008; Shea et al., 2015; Boro et al., 2021). By understanding the conditions that lead to embayment development, the very presence or absence of this feature can inform on the pre-eruptive history.

Rapid crystal growth of quartz in response to undercooling of the magma has been shown experimentally to form crystal growth textures such as skeletal, hopper, and dendritic crystals at magmatic pressures (1 – 5 kbar) and undercooling amounts of 50 – 186 °C (Swanson and Fenn, 1986; MacLellan and Trembath, 1991; Table 4.1). Formation of quartz via unstable rapid growth results in arborescent and oscillatory zoning, where continued periods of slower growth produce zoning adaptations that eventually may seal off any embayment-like feature to form melt inclusions (Barbee et al., 2020). Thus, smooth embayments found in natural samples are thought to form when the hopper cavities between the arborescent frameworks begin to infill during continued periods of slower growth (Blackerby 1968; Müller et al. 2000; Barbee et al., 2020; Figure 4.1).

Crystal dissolution via heating of magma is another method that has been called upon to explain the formation of embayments (Roedder 1979; Harris and Anderson 1984; Manley 1996; Bachmann et al. 2002; Girard and Stix 2009; Wilcock et al. 2013; Seitz et al. 2018; Befus and Manga 2019). However, preferentially removing atoms from a crystal face is kinetically difficult and experimental studies of heating have shown that dissolution results in rounded crystals with smooth, embayment-free surfaces (Kuo and Kirkpatrick, 1985; Donaldson, 1985; MacLellan and Trembath, 1991). As an alternative to this kinetic barrier, Donaldson and Henderson (1988) propose that embayments are the result of superheating in an H_2O-saturated magma due to a gas bubble interacting with the crystal face and causing locally enhanced dissolution. This has been further supported by Befus and Manga (2019), who found that bubble-driven drilling could account for the occurrence of concave depressions in the surface of experimental quartz crystals. However, bubble drilling has not yet been explored in a mixed-volatile system. This mechanism would result in embayments that crosscut existing growth zoning patterns in crystals.

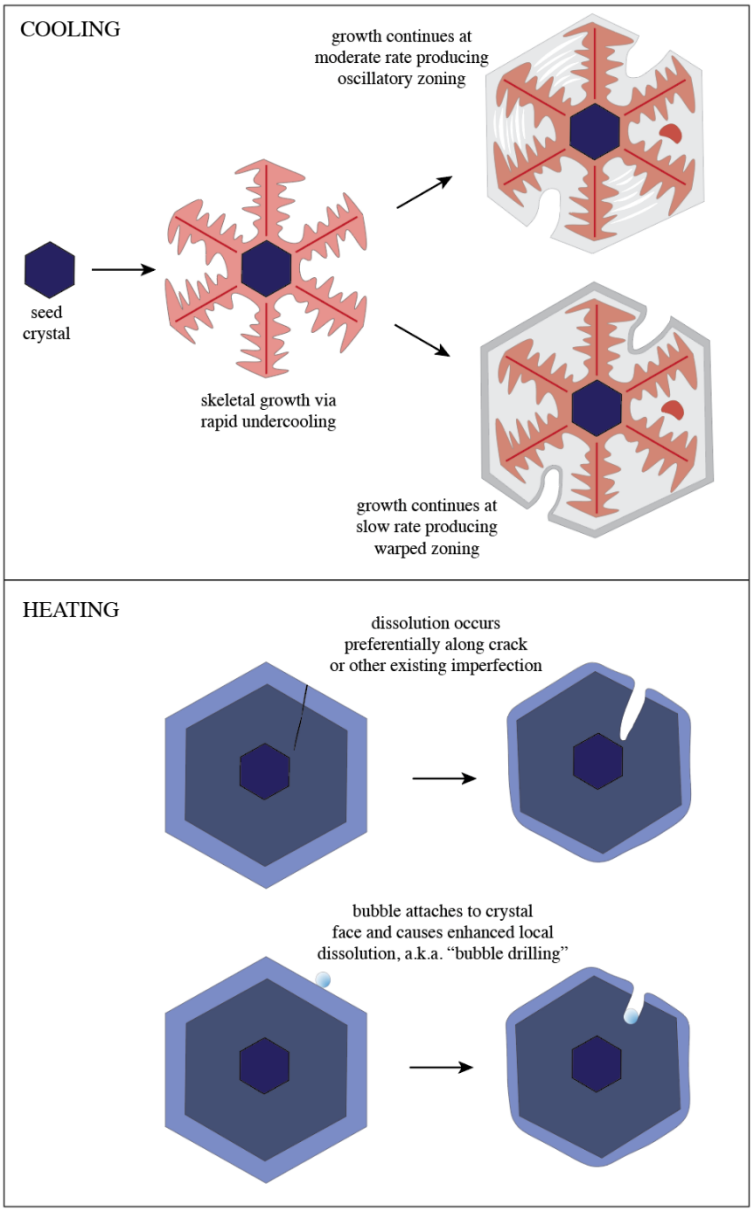

Figure 4.1. (next page) Schematic diagrams showing the proposed embayment formation mechanisms. (top) Rapid growth due to undercooling of the magma will produce skeletal protrusions. As growth begins to slow down, the void spaces between the skeletal protrusions will begin to fill in and form smooth, tubular embayments, surrounded by either an oscillatory lens or warped zoning patterns. (bottom) Superheating of the magma will begin to dissolve and round the crystal surface. Existing imperfections, such as a crack may allow for preferential dissolution, resulting in an embayment. Alternatively, it has been proposed that bubbles attached to the crystal surface in a volatile-saturated magma may create a "flux-line attack" by which enhanced dissolution along the intersection of the bubble and the crystal surface results in bubbles drilling inward (Busby and Barker, 1966).

Quartz is one of the most abundant mineral phases in silicic eruptions and is commonly found to contain embayments that are then used for diffusion modeling to provide timescales of magma ascent. By examining the texture and morphology of embayment-bearing quartz crystals, we can begin to unravel the magmatic storage conditions prior to eruption. Similar to how tree rings record the growth history of trees, zoning in magmatic crystals records the history of growth and dissolution in an evolving magma chamber (e.g., Anderson, 1984; Peppard et al., 2001; Shea et al., 2015; Barbee et al., 2020). In quartz, this zoning can be seen in cathodoluminescence imaging as bright or dark regions and depends on differences in trace element concentrations, largely driven by Ti concentration (e.g., Wark and Watson 2006; Wark et al., 2007; Thomas et al. 2010; Acosta et al. 2020; Boro et al., 2021). For instance, bright zones indicate higher concentrations of Ti, and dark zones represent lower concentrations. The Ti concentration in quartz is dependent on numerous factors, including the temperature, pressure and composition of the melt in which it is crystallizing, where the patterns of Ti zoning can reveal significant changes occurring in the magma chamber, such as magma recharge, magma mixing and decompression (e.g., Wark and Watson 2006; Wark et al., 2007; Thomas et al. 2010; Acosta et al. 2020; Jollands et al., 2020; Barbee et al., 2020; Audétat et al., 2021; Boro et al., 2021). This work aims to identify the prevalence of embayment formation in quartz samples from multiple volcanic systems and then compare these results to high P-T experiments where we attempt to explore both growth and dissolution dynamics. The results of this study have implications for the conditions of silicic magmas prior to eruption and the timescales of crystal residence at those conditions.

Methods

Cathodoluminescence Imaging

Embayment-bearing quartz crystals were selected from six caldera-forming eruptions: Upper and Lower Bandelier tuffs (Valles Caldera; *USA*), June 12th, 1991 Mt. Pinatubo (Philippines), Huckleberry Ridge tuff pre-C pumice fall (Yellowstone Caldera; *USA*), Oruanui phase 1-3 (Taupō Volcanic Zone; *NZ*), and Bishop tuff fall units 2, 4, 8, and 9 (Long Valley Caldera; *USA*). Crystals were picked from crushed and sieved individual pumices, with the exception of the Huckleberry Ridge tuff, where loose crystals were picked from single eruptive layers. Embayments were singly intersected, polished, then mounted in epoxy, with at least 38 embayments representing each individual volcanic system. Cathodoluminescence (CL) imaging was conducted using a MiraTescan SEM at Montana Technical University. Operating conditions included a beam current of 20, an accelerating voltage of 20 kV, a working distance of 15mm, and absorbance current of 50 nA.

Growth/Dissolution Experiments and MicroCT Imaging

We attempt to recreate the conditions under which embayment formation occurs by conducting high temperature, high pressure experiments using a cold-seal pressure vessel at University of Oregon. Twenty-seven quartz crystals in the 250 – 500 μm size fraction were picked from crushed pumice material of the Bishop Tuff F9 fall deposit of Long Valley caldera (CA). Only crystals that were completely whole and showed minimal cracks and inclusions were used. Before conducting the experiments, we preformed X-ray micro computed tomographic (micro-CT) imaging of the 27 experimental quartz crystals at Lawrence Berkeley National Lab's Advanced Light Source facility. Micro CT imaging was conducted in two phases. The first round

of imaging took place before the cold-seal pressure vessel experiments to establish the original morphology of each crystal. These images were used as a baseline to compare with the MicroCT images taken after the experiments, which allowed us to identify any preexisting crystal features (i.e., embayments, melt inclusions) and to identify morphological changes that occurred during the experiment (Figure 4.2). A total of 1,996 images were taken for each quartz crystal at a resolution of 0.6 µm/pixel. The images were resolved using Jupyter notebooks and then processed using ImageJ. Dragonfly software was used to project the images in 3D, and we were then able to visually determine the changes that occurred during the experiments.

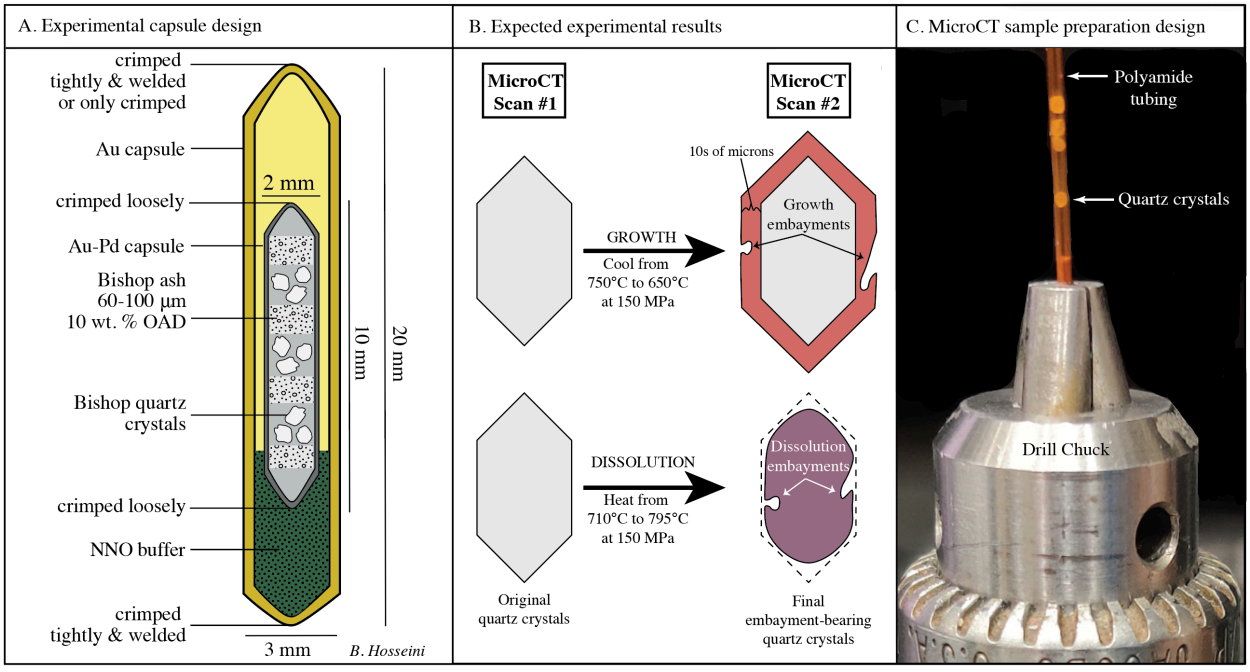

Figure 4.2. A) Experimental double capsule design (schematic adapted from Hosseini et al. (in prep)). B) Theoretical before/after imaging results for growth and dissolution experiments. C) MicroCT imaging sample mounting technique.

For the dissolution and growth experiments, three scenarios were explored, each containing nine crystals. The crystals were packed into 1-cm-long gold-palladium capsules with

a mixture of Bishop tuff ash powder + 10% oxalic acid dihydrate (OAD; $(COOH)_2 \cdot 2H_2O$), which acts as the fluid source to vapor saturate the experimental melt. The gold-palladium capsules were crimped tightly on both ends and packed into a 2-cm-long gold capsule which contained a nickel-nickel oxide (NNO) buffer. The gold capsule was tightly crimped shut and then welded (Figure 4.2). For the single heating experiment, both ends of the gold capsule were crimped and welded, however, for both of the two cooling experiments, one end of the gold capsule was crimped and welded, and the other end was only crimped. The unwelded capsules allows for full equilibration with the surrounding H_2O pressurizing medium, resulting in an H_2O only system ($P_{H2O} = P_{TOT}$) but overall results in better recovery of crystals from the capsules post-experiment. The welded capsule produces a mixed-volatile $H_2O + CO_2$ system ($P_{H2O} + P_{CO2} = P_{TOT}$). Despite being riskier in terms of crystal recovery, the closed capsule design was chosen for the heating experiment to better approximate the natural environment, in which a heating event may be associated with CO_2 fluxing (Bachmann and Bergantz, 2006). This mixed volatile saturation condition has not been explored in any previous dissolution experiments, although postulated to be important for embayment formation (e.g., Anderson 1991). The capsules were loaded into the cold-seal pressure vessel and brought up to a pressure of 140 MPa. The cold-seal pressure vessel allows us to control both temperature and pressure at shallow crustal magma storage conditions. The capsules were first held at this pressure for 1 hour to ensure that the pressure was holding, and then the vessel was placed into the furnace. Pressure was held constant within ±5 MPa for the duration of all experiments.

Growth and dissolution experimental conditions were chosen based on a review of previous experimental research (Table 4.1). For crystal growth, previous work indicates that

formation of embayments by skeletal growth in quartz occurs at relatively minor degrees undercooling (~50 – 80°C below the liquidus: Swanson and Fenn, 1986; MacLellan and Trembath, 1991; Faure and Schiano, 2005). Additionally, many growth experimental runs include a short period, from 20 minutes up to 2 hours, of reequilibration at temperatures slightly above the liquidus temperature prior to subjecting the material to undercooling. This reequilibration period ensures that all the starting ash material is fully melted into a homogeneous glass prior to commencing the cooling stage. Our cooling experiments expand upon previous work by attempting to form late-stage embayments on preexisting seed crystals using a more moderate cooling rate (as opposed to a step-function decrease in temperature). For dissolution experiments, previous work explored super heating conditions ranging from 12 - 100°C in excess of the liquidus temperature. These experiments have variable results, with some producing rounded crystals and others producing scalloped or pitted crystal faces (Table 4.1). Our heating experiment expands on previous work by testing a mixed-volatile saturation condition, which is thought to be important to the bubble drilling concept and more accurately mimics a reheating scenario.

At a pressure of 140 MPa and under water-saturated conditions, quartz stability for the Bishop tuff ash starting material is expected at ~715°C (Gardner et al., 2014). Following the design of previous experiments, both cooling experiments (C1 and C2) began at a slightly elevated temperature of 750°C whereas the heating experiment began at a near-liquidus temperature of 710°C. The first cooling experiment (C1) was cooled from 750°C to a final temperature of 658°C at a rate of 4°C/hr. It was held at this final temperature for 1 hour before

being removed from the furnace and quenching slowly at the ambient air temperature. The second cooling experiment (C2)

Table 4.1. Selection of previous dissolution and growth studies including the parameters used and the resulting crystal morphologies. T = experimental temperature (°C).

Dissolution

Citation	Crystal phase	Experimental instrument	Volatile conditions	T	△T	Pressure	time	result
Donaldson and Henderson, 1988	quartz	1 atm furnace	water saturated	850	100	0.83 kbar	197 hrs	pitting on crystal surface 20 - 100 μm diameter
Befus and Manga, 2019	quartz	CSPV	water saturated	800	50 - 75	150 MPa	24 hrs	curved indentations of quartz surface along interface with
Busby and Barker 1966	ice and NaCl	glycerol tank	NA	-5	0	1 atm	20 min	bubbles drill cavities in medium up to 24 mm deep
Wark and Stimac, 2005	plagioclase	piston cylinder	5% H_2O	850 - 975	100	800 MPa	2 - 48 hrs	scalloped dissolution surface
Donaldson, 1985	quartz	1 atm furnace	anhydrous	1122 - 1300	12 - 100	1 atm	0.5 - 163 hrs	rounding of crystals

Growth

Citation	Crystal phase	Experimental instrument	Volatile conditions	T	△T	Pressure	time	result
Donaldson, 1976	olivine	1 atm furnace	anhydrous	1200	20 - 80	1 atm	21 hrs	hopper / skeletal crystals
Faure and Schiano, 2005	olivine	1 atm furnace	water saturated	1300	44	1 atm	44 hrs	dendritic/skeletal growth, melt inclusion formation
Swanson and Fenn, 1986	quartz	IHPV	water saturated	750 - 900	55 - 186	2 - 5 kbar	6 - 500 hrs	skeletal and dendritic crystals
Maclellan and Trembath 1991	quartz	CSPV	saturated	650 - 725	50 - 125	1 kbar	24 - 4320 hrs	skeletal, hexagonal bipyramidal, micropoikiolitic, anhedral,
Zieg and Lofgren, 2006	olivine	1 atm furnace	CO_2 saturated	1545 - 1176	67 - 374	1 atm	40 - 240 min	skeletal overgrowths on seed crystals

began at 750°C and was cooled at a rate of 10°C/hr to a final temperature of 650°C. The experiment was held at the final temperature for 662 hours (28 days) before being quenched.

The sole heating experiment (H1) has heated at a rate of 4°C/hr from its initial temperature of 710°C to a final temperature of 794°C. The capsule was held at the final temperature for a period of 15 hours before quenching. The slow air quench, used in all three experiments, takes about 3 – 5 minutes for the capsule to cool below the glass transition temperature, (glass transition temperature = 477°C; = 2/3 of liquidus temperature (Hammer and Rutherford, 2002)) and significantly improves crystal recovery, whereas a rapid quench in chilled water has been found to lead to crystal rupturing. Time-series temperature data for all three experiments can be found in Figure 4.3.

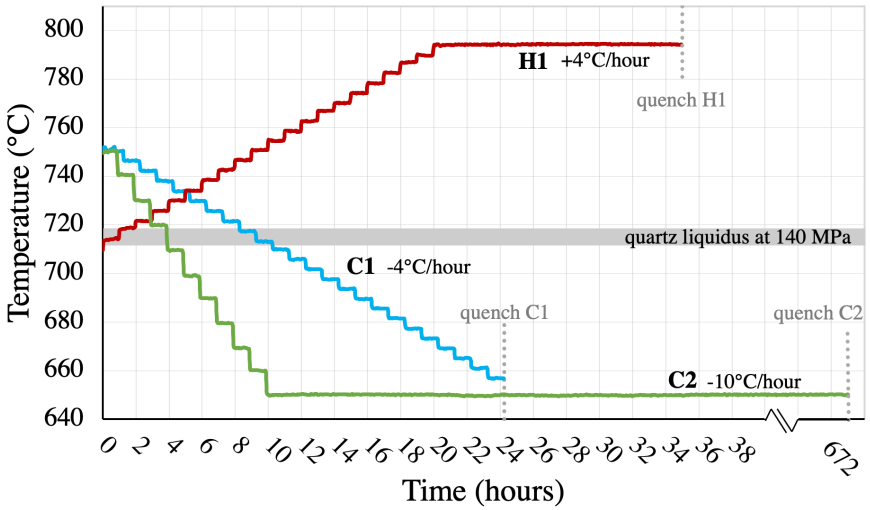

Figure 4.3. (previous page) Output of temperature time series from LabView software of cooling (C1, C2) and heating (H1) experiments. Cooling experiments initially dwelled at 750°C and were cooled at a rate of 4°C/hr. and 10°C/hr., respectively. Experiment C1 (blue line) was quenched immediately upon reaching its final temperature, while experiment C2 (green line) was left to dwell at its final temperature for 28 days prior to being quenched. Experiment H1 (red line) initially dwelled just below the liquidus at 715°C before being heated at a rate of 4°C /hr. Once it reached its final temperature, it dwelled for 15 hours prior to being quenched. The grey bar represents the quartz liquidus temperature at a pressure of 140 MPa of 716°C (Gardner et al., 2014).

Results

Cathodoluminescence Imaging

A total of 295 CL images were taken of embayment-bearing quartz crystals from five volcanic systems spanning a wide range of tectonic settings (Table 2): Bandelier tuffs (continental rift; *n = 38*), Mt. Pinatubo (subduction zone; *n = 48*), Huckleberry Ridge tuff (mantle plume; *n = 63*), Oruanui (rifted arc; *n = 66*), and Bishop tuff (continental rift; *n = 80*). These five volcanic systems produced six eruptions (the two Bandelier eruptions, Lower Bandelier and Upper Bandelier, have been grouped here) containing crystals with distinct zoning patterns, indicative of the unique history of each magmatic system (Figure 4.4). Bandelier tuff crystals are the most homogeneously zoned, showing either faint oscillatory zoning or homogeneously bright cores with moderately darker, thick rims (Figure 4.4). Pinatubo crystals have distinctive thin (~20 μm) bright bands that are sharp toward the interior with skeletal protrusions toward the rim. Pinatubo crystals typically have darker cores with very diffuse zoning and often have internal rounded dissolution boundaries (Figure 4.4). Huckleberry Ridge crystals also often display internal dissolution surfaces overgrown by thick, brighter rims. The cores of many Huckleberry Ridge crystals exhibit complex oscillatory or sector zoning. Oruanui crystals have similar zoning patters to the Huckleberry Ridge crystals, with the exception that some crystals have prominent, internal bright bands (~40-50 μm) with skeletal protrusions (similar to Pinatubo crystals). Crystals from the Bishop tuff generally have very distinct oscillatory zoning, with select crystals containing very bright rims (Figure 4.4).

Table 4.2. Summary of key characteristics for each of the five eruptions studied. Ascent rates determined by Saalfeld et al. (2022) – Lower and Upper Bandelier; Myers et al. (2018) – Bishop tuff, Oruanui, and Huckleberry Ridge tuff; and Saalfeld et al. (Chapter 3, this volume) – Pinatubo.

Eruption	Location	Tectonic setting	Age	VEI	Erupted volume (km^3)	Ascent rate (m/s)
Bandelier tuffs (Valles Caldera)	New Mexico, USA	Continental rift	1.25 - 1.61 Ma	8	800	0.02 - 3.5
Bishop tuff (Long Valley Caldera)	California, USA	Continental rift	0.76 Ma	7	650	0.2 - 7.8
Oruanui (Taupo Volcanic Zone)	North Island, New Zealand	Rifted arc	25 ka	8	530	0.1 - 1.2
Huckleberry Ridge tuff (Yellowstone Caldera)	Wyoming, USA	Mantle plume	2.08 Ma	8	2500	0.3 - 2.3
1991 Mount Pinatubo	Luzon, Philippines	Subduction zone	1991 AD	6	10	0.6 - 13.5

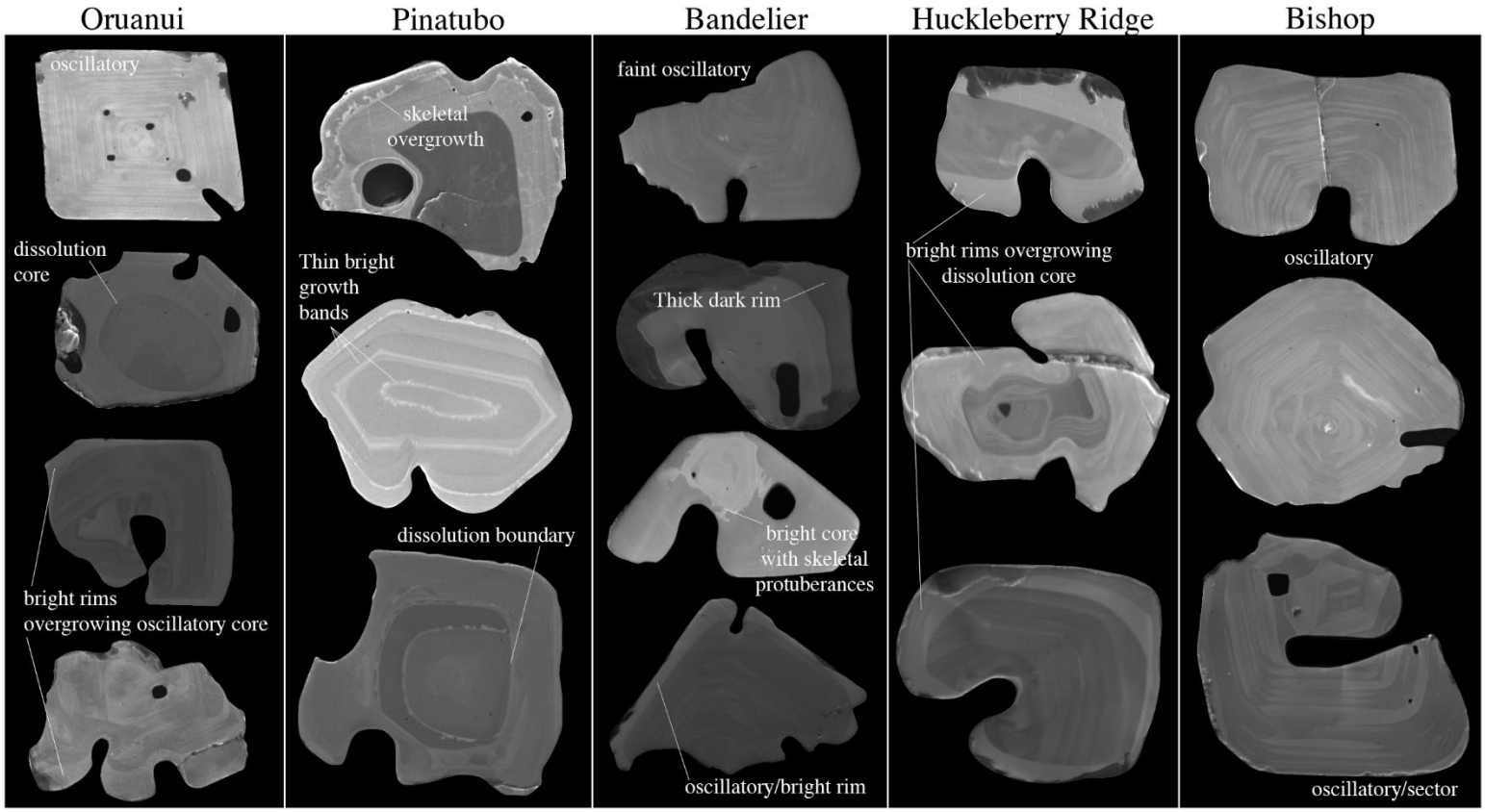

Figure 4.4. (previous page) Examples of growth zoning patterns observed in CL for each of the five systems studied.

Although many crystals display more than one type of zoning, we find that the images can be sorted into four major categories based on the relationships between the zoning and the embayment margins (Figure 4.5): 1) **Warped**- crystal zones that bend or wrap around embayments, indicating that the embayment was formed by differential or rapid crystal growth; 2) **Crosscut**- zoning that is truncated by embayment boundaries indicate that embayments were formed via dissolution after the initial growth of crystals; 3) **Oscillatory/Sector**- defined by feathery or lens zoning, with non-zoned regions surrounding the embayment; 4) **Undefined**- crystals that lack defined zoning. The relationship between embayments and zoning was visually analyzed to determine whether the embayment was formed by growth or dissolution and then quantified for each eruption studied (Table 4.3; Figure 4.6).

Warped Growth Zones

This group is characterized by quartz growth zoning that either fully wraps around the embayment or is deflected as it nears the embayment (Figure 4.5). This category makes up 49% of the total images (*n = 144/295*). The warped growth zone relationship is most strongly seen in the Oruanui (*n = 36/66*; 55%), Pinatubo (*n = 31/48*; 65%), and Huckleberry Ridge (*n = 45/63*; 71%) eruptions. The warped zoning makes up a minor proportion of images form the Bandelier tuff (*n = 7/38*; 18%), and the Bishop tuff (*n = 25/80*; 31%).

Oscillatory/Sector Zoning

Oscillatory and sector zoning are common features. Oscillatory zoned crystals are defined by growth zoning that forms thin lenses that alternate between light (higher Ti) and dark (lower Ti) zones, whereas sector zoned crystals contain arborescent (tree-like) patterns of bright zones, filled in by darker zones (see examples in Figure 4.4). These two patterns often occur in tandem

in the same crystal and are thus grouped together here. Notably, oscillatory and sector zoned crystals all display a homogeneous halo of darker zoning around the margins of the embayment so that the brighter zones do not interact with the embayment boundary (Figure 4.5). Oscillatory zoning is very common in the Bandelier (*n = 21/38*; 55%) and Bishop (*n = 39/80*; 49%) tuffs. It is much less common in the Huckleberry Ridge tuff (*n = 8/63*; 13%) and Oruanui (*n = 10/66*; 15%) eruptions and is not observed in the Pinatubo crystals. In all eruptions, sector zoning is less common than oscillatory, ranging from 3% in the Oruanui, up to 13% in the Bishop tuff (*n = 10/80*). Sector zoning is not observed in either the Pinatubo, Bandelier tuff, or Huckleberry Ridge tuff eruptions.

Undefined

The undefined group represents images where the crystal had no distinguishable zoning bands, or the zoning bands did not interact with the embayment in any distinguishable way (Figure 4.5). This group makes up a significant portion of the observed images (*n = 48/295*; 16%). The Bishop has the lowest portion of undefined embayments (*n = 4/80*; 5%), while Pinatubo had the highest (*n =13/48*; 27%).

Crosscut

This group is defined by embayments that crosscut the existing quartz growth zones with the growth zones not being deflected or altered in any way (Figure 5). This relationship is the least common, making up only 5% of the total observed images (*n = 16/295*). Crosscutting embayments are observed in all five eruptions studied here, with the Huckleberry Ridge having the fewest (*n = 1/63*; 2%), and Pinatubo having the most (*n = 4/48*; 8%).

In addition to the four major groups defined above, we note a subpopulation within the warped growth zoning group where these warped zones occur as overgrowths on earlier dissolution surfaces (Figure 4.7). Nearly half of the above "warped" population contains internal dissolution surfaces (*n = 64/144; 45%*) and makes up 22% of the total images analyzed ((*n =64/295*; Table 4.3). This subpopulation is most prevalent in the Pinatubo samples ((*n = 13/31; 27%* of the warped growth zone population), and the least common in the Bandelier tuff samples ((*n = 2/7; 5%* of the warped growth zone population). Similarly, the Bishop tuff, Oruanui, and Huckleberry Ridge tuff samples preserve this internal dissolution surface on ~24% of their warped populations.

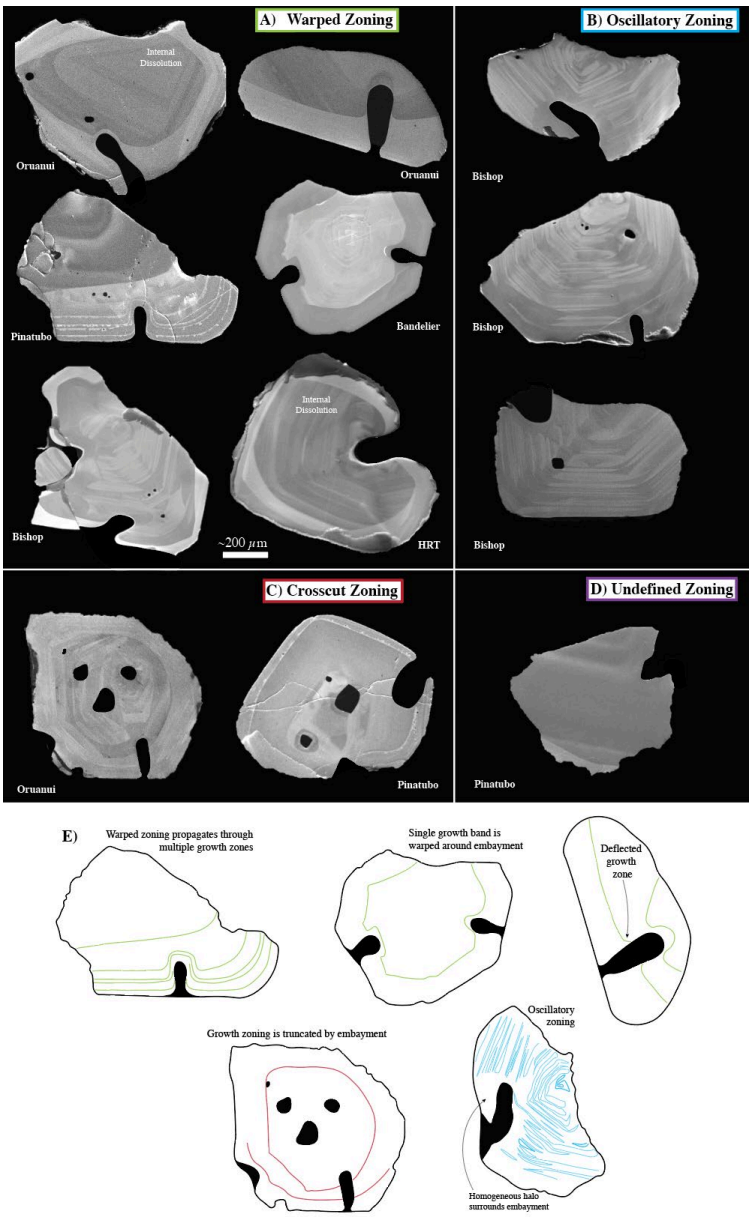

Figure 4.5. (next page) Examples of the different zoning types observed in CL images. A) Warped zoning (quartz growth zones wrap around or are deflected by the embayment) is the most common relationship observed and is present in samples from all five volcanic centers. B) Oscillatory zoning, seen most prominently in the samples of the Bishop tuff, is defined by thin alternating lenses of bright and dark growth zones. Notably, every embayment in the oscillatory zoning group is surrounded by a "homogeneous halo" of Ti-poor (darker CL) quartz C) Crosscut zoning is not common but is present in samples from all five volcanic centers. This group is distinguished by zoning bands that are truncated by the embayment. The final zoning type is D) Undefined. This group has no distinguishable zoning or zoning that does not interact with the embayment. E) Selected annotations of the different zoning types, showing variations in the types of warped zoning observed (green lines), as well as an example of crosscut zoning (red lines) and oscillatory zoning (blue lines).

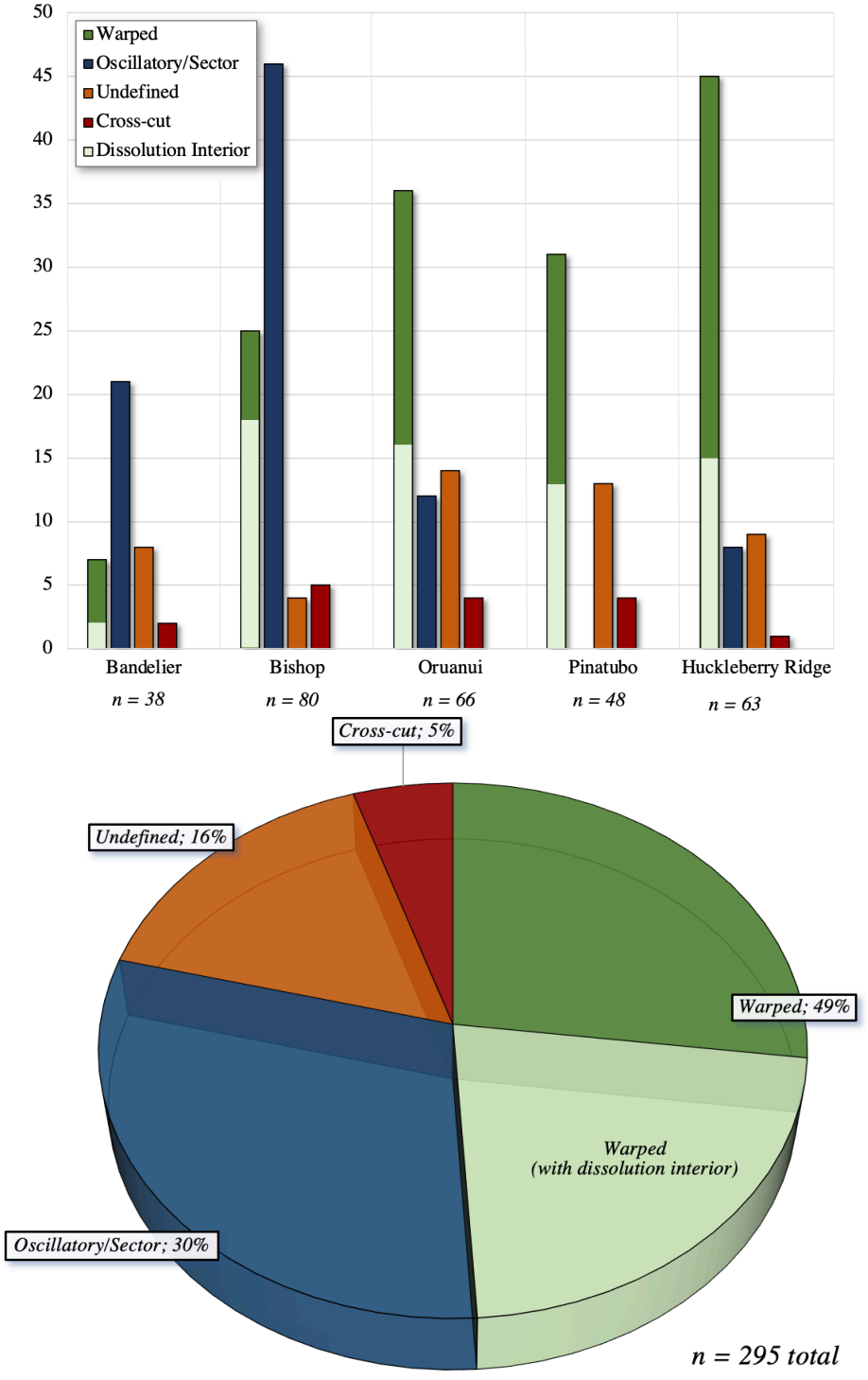

Figure 4.6. (top) Summary of CL image embayment-zoning relationship count results for each volcanic center studied; Bandelier (1.61 and 1.25 Ma); Bishop (760 ka); Oruanui (26.5 ka); Pinatubo (1991 AD); and Huckleberry Ridge (2.1 Ma). (bottom) Combined results for all eruptions showing percentage of total images (*n = 295*) of each observed zoning type.

Table 4.3. Summary table of CL counts for each eruption and zoning pattern type.

	Bandelier *	%	Bishop	%	Oruanui	%	Pinatubo	%	Huckleberry Ridge	%	TOTAL	%
n =	*38*		*80*		*66*		*48*		*63*		*295*	
Warped	7	*18.4*	25	*31.3*	36	*54.5*	31	*64.6*	45	*71.4*	144	*48.2*
Oscillatory	21	*55.3*	39	*48.8*	10	*15.2*	0	*0.0*	8	*12.7*	76	*27.1*
Sector	0	*0.0*	10	*12.5*	2	*3.0*	0	*0.0*	0	*0.0*	11	*4.3*
Uncertain	8	*21.1*	4	*5.0*	14	*21.2*	13	*27.1*	9	*14.3*	48	*15.8*
Dissolution	2	*5.3*	2	*2.5*	4	*6.1*	4	*8.3*	1	*1.6*	16	*4.6*
Dissolution interior**	2	*5.3*	18	*22.5*	16	*24.2*	13	*27.1*	15	*23.8*	64	*21.7*

*Bandelier samples include samples from both the Lower Bandelier Tuff Guaje pumice, and the Upper Bandelier Tuff Tsankawi pumice.

**Dissolution interior refers to warped growth zoning relationships in crystals which exhibit dissolution surfaces in the interior of the crystal.

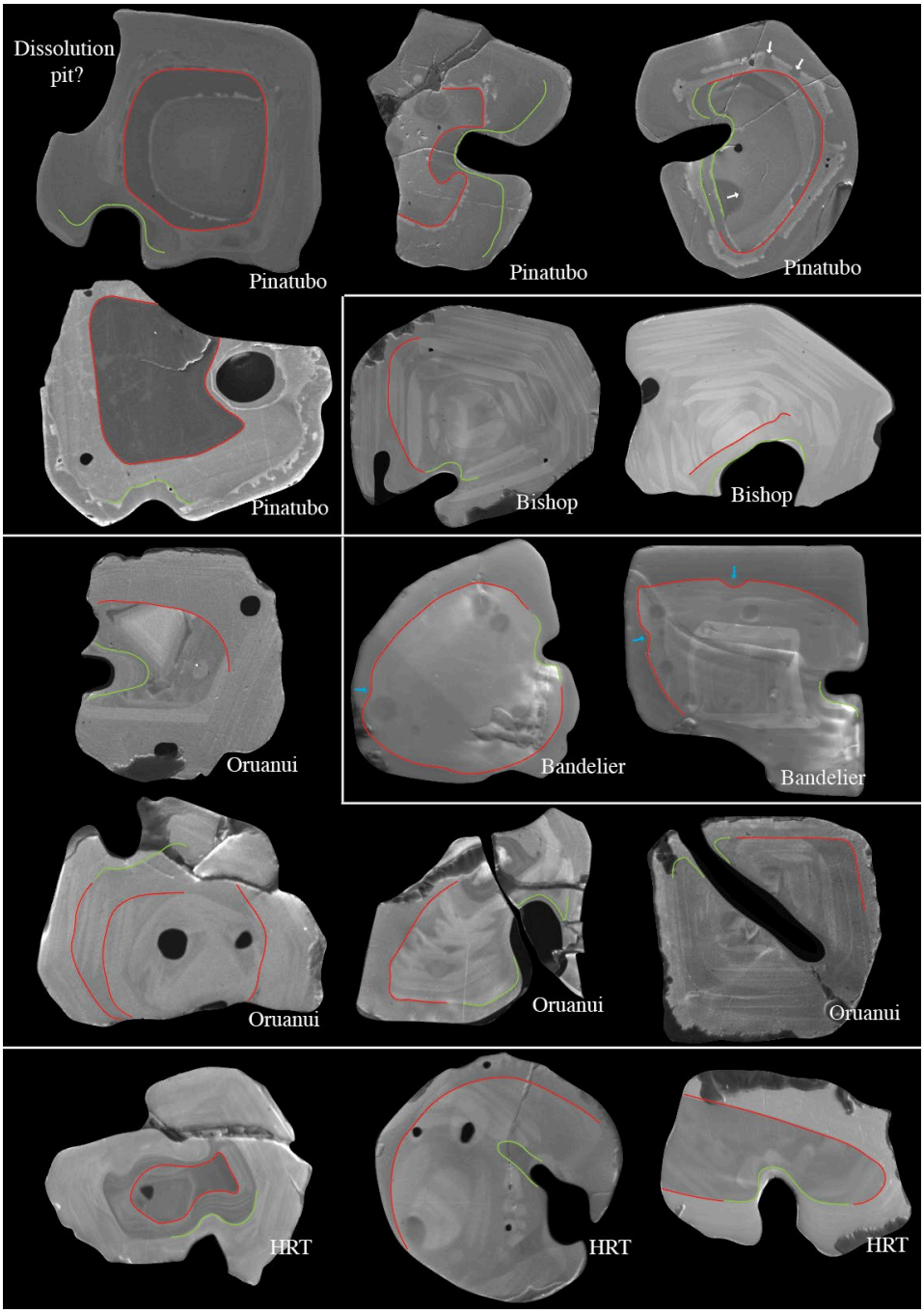

Figure 4.7 (previous page) Examples of the dissolution interior, warped growth zone overgrowth subpopulation for each eruption. The red lines represent dissolution surfaces, the green lines represent the warped zoning, blue arrows indicate infilled indentations in dissolution surfaces from bubble drilling, and white arrows indicate infilled embayments. Note that often times, the dissolution surface is the same boundary that is warped around the embayment (red line turns to green line). One Pinatubo crystal (top left) preserves a wide, shallow indentation which looks to be a dissolution pit.

Cold Seal Pressure Vessel Experiments

Of the nine crystals originally loaded into each experimental capsule, all nine crystals were recovered for experiments H1 (mixed volatile, *t = 35* hours) and C1 (H_2O-only, *t= 24* hours). However, for experiment C2 (H_2O-only*, t = 672* hours) only one crystal was recovered from the capsule. The other eight crystals that were not found are speculated to have either shattered during quenching or were fully resorbed during the initial 1-hour heating stage of the experiment. However, broken quartz pieces were not found in the capsule, and the crystals from C1 were not resorbed under the same conditions, thus the explanation for the missing eight crystals is unclear.

Micro tomography results from the first cooling experiment (C1, t = 24 hours) show that none of the experimental crystals produced skeletal growth patterns as expected. Rather, we note that the experimental crystals became slightly more faceted compared to before the experiments, with no observed formation of embayments. Additionally, we find that several of the C1 experimental quartz crystals are coated in a highly crystalline groundmass consisting of feldspar crystals ranging from 1 – 40 μm in length (Figure 4.7). However, this groundmass crystallization was not seen in the longer duration C2 experiment. The single crystal retrieved from cooling experiment C2 (t = 672 hours) produced a notch-like embayment that penetrated ~300 μm into the crystal, ~30 μm wide, and ~200 μm deep, running semi-parallel to the crystal face (Figure 4.8). The notch-like embayment was found to be completely hollow, devoid of glassy or vesiculated material.

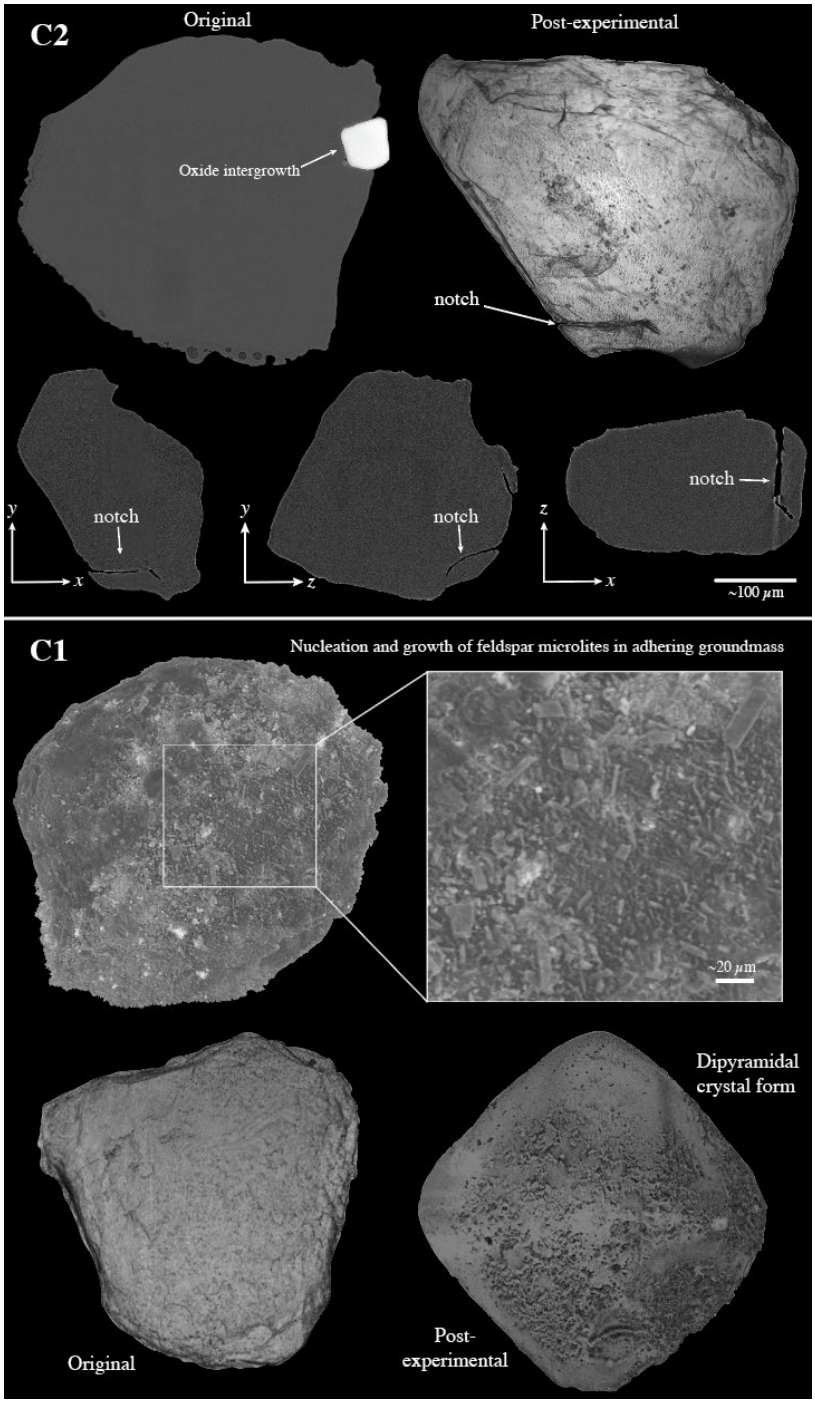

Figure 4.8. (top) Showing the notch-like embayment from experiment C2 in 3-dimension along with the original crystal prior to cooling. Note the original crystal initially contained an intergrown oxide crystal which was resorbed during the experiment. (bottom) Results from cooling experiment C1 show evidence of extensive nucleation and growth of feldspar microlites in the adhering groundmass, as well as faceting of the crystals to form subhedral dipyramids.

Images of the crystals recovered from the mixed-volatile heating experiment (H1; t = 35 hours) show evidence of extensive dissolution. The crystals are not significantly smaller in diameter, rather, the most prominent features formed in the experimental crystals are large bulbous to botryoidal shaped embayments in the crystal faces (Figure 4.9). These features are present in all nine crystals, with each crystal containing 1 – 8 embayments. These embayments vary from a simple single bulb (bulbous) to a complex amalgamation of multiple bulbs (botryoidal). The bulbous embayments range from 80 μm wide (single bulb) to upwards of 200 μm wide (multi-bulb), but typically only extend ~50 – 100 μm into the crystal. Without exception, all bulbous/botryoidal embayments are hollow, containing no evidence of melt. Occasionally, we find small glassy "embayments" where the dissolution surface has intersected and breached near surface melt inclusions (Figure 4.9). The next features we note in H1 are numerous (~10 – 25 per crystal) small bubbles that have attached to the face of the quartz crystal and have produced small, concave indentations where the bubble is in contact with the crystal surface (Figure 4.9). The attached bubbles are typically < ~10 – 30 μm in diameter and produce indentations that extend no more than 5 – 10 μm into the crystal face. Finally, we find that large glassy embayments that existed in the crystals prior to the experiments often became vesiculated during the heating process. The discrete bubbles in these embayments range from 5 – 20 μm and generally occur near the embayment margins where the melt is in contact with the quartz (Figure 4.9).

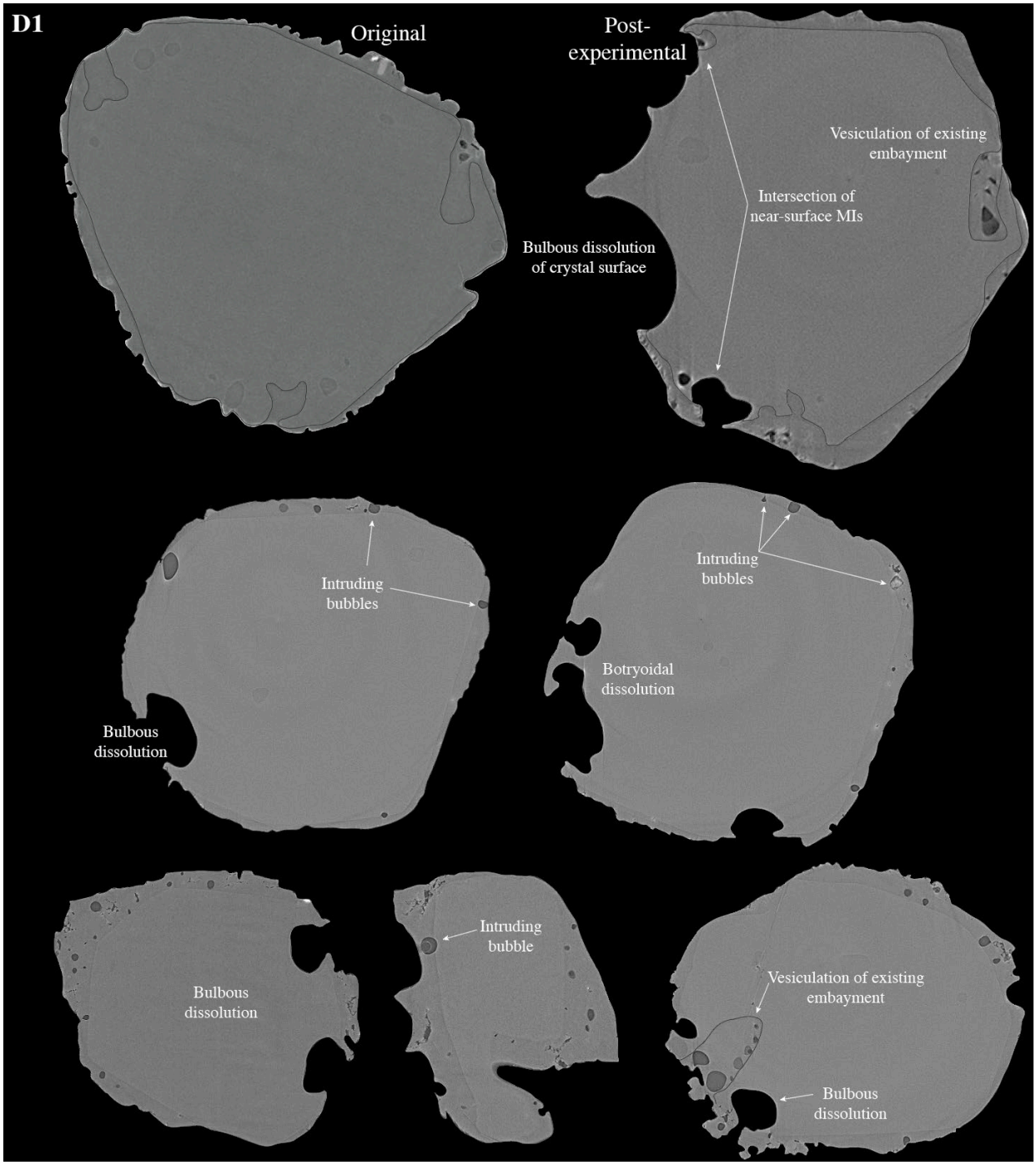

Figure 4.9. Results of the textures produced from experiment H1. (top left) Original pre-experimental crystal. (top right) Post-experimental crystal showing changes that have occurred during heating, including the vesiculation of the previously glassy embayment, intersection of near-surface melt inclusions, and bulbous dissolution pits on the crystal face. (middle and bottom) examples of attached bubbles forming indentations into crystal surface, and extensive evidence of bulbous and botryoidal dissolution.

Discussion

Interaction between Embayment Margins and Zoning Patterns Seen in CL Imaging

Oscillatory and sector zoning make up 30% of all observed crystals. Lens-shaped oscillatory zoning in magmatic crystals has previously been interpreted to be the result of growth kinetics, whereby rapid crystal growth creates a battle between depletion of the melt boundary and diffusion of new material toward the crystal, which is then incorporated into the crystal as growth continues (Allègre et al., 1981; Milman-Barris et al., 2008; Seitz et al., 2015). We thus assume that embayments hosted in oscillatory and sector zoned crystals are products of rapid crystal growth. In addition, 49% of crystals exhibit warped zoning, also inferred to be a growth feature (Barbee et al., 2020), indicating that growth is the major driver of embayment formation for the natural samples studied here. Crystal growth occurs during periods of effective undercooling, where the magma temperature is below the liquidus temperature of the phase of interest. Undercooling may be initiated by an increase in the liquidus temperature (driven by devolatilization due to decompression, mixing with undersaturated magma, or assimilation of dry country rock), producing the observed oscillatory zoning, skeletal growth, and bright overgrowth rims, or by decreasing the temperature of the magma through mixing with colder magma or loss of heat to the surrounding country rock, producing the darker rims observed (Hibbard, 1981; Mollo and Hammer, 2017). However, of the warped growth zoning population, nearly half of the crystals display interior dissolution surfaces. These dissolution surfaces may be providing the initial imperfections that that lay the foundation for future crystal growth to form embayments, indicating that a combination of processes may be important for embayment development.

While growth-formed embayments make up the vast majority of observed natural embayments (79%), dissolution-formed embayments (crosscut zoning) are also present, albeit at low numbers, in natural samples from all studied eruptions. While dissolution is clearly present, it is a minor observation of the embayment host's history, perhaps indicating that dissolution either: 1) is happening but is not well preserved in the record (i.e. crystal is fully dissolved) or 2) requires specific circumstances (volatile saturated magma, high enough ΔT, crystals with preexisting cracks or near surface melt inclusions, or large original crystals that won't fully dissolve) that are not be experienced by these dacitic-rhyolitic systems.

Experimental Conditions of Embayment Formation

The conditions of embayment formation in natural systems, which have been found to be largely growth-dominated are not fully reproduced by the heating and cooling experiments presented here, which were found to be more dissolution dominated. However, the results of these experiments give insight into the dynamics of quartz growth and dissolution on a broader scale and indicate that the development of embayments likely occurs via a more complex series of events. Here we discuss the implications of our dissolution and growth results and explore explanations for their divergence.

Large amounts of dissolution occurred during the mixed-volatile heating experiment to produce hollow, bulbous shaped embayments. However, these dissolution embayments do not resemble the tubular, glass-filled embayments that we find in natural samples, indicating that a different process is responsible for forming them. Experiments by Busby and Barker (1966) originally showed that the contact between a bubble and solid in a liquid medium will result in increased dissolution of the solid, producing pits around the bubble as it drills into the solid.

Donaldson and Henderson (1988) also proposed the idea of bubble drilling as an explanation for the results of their quartz dissolution experiments, where they were able to produce 20 – 100μm pits in the surfaces of their crystals. In our study, development of hollow, bulbous shaped embayments in H1 indicate that their formation via enhanced dissolution of the crystal (aka bubble drilling) is quite plausible. This is further supported by the existence of smaller bubbles attached to the crystal faces which represent the initial stages of the larger dissolution embayments. However, the lack of melt in these embayments requires some secondary mechanism of filling. Although natural empty embayments have been found in quartz crystals of the Lava Creek tuff, Yellowstone (Befus and Manga 2019), the majority of natural samples contain glass filled embayments. Befus and Manga (2019) argue that the existence of hollow and crosscutting embayments is evidence for an exsolved volatile phase at some late stage in the magma's history, where initially hollow embayments are formed by bubble drilling and may subsequently be filled by melt.

The lack of embayments formed in our growth experiments could be explained by 1) a lack of CO_2 to help facilitate bubble drilling, 2) a difference in rates of quartz growth vs. dissolution where quartz growth is slow enough to not result in perceptible changes during the experiment duration, or 3) a kinetic barrier between nucleation- or growth-dominated regimes. While the fluxing of CO_2 through silicic systems has been called upon as a mechanism for promoting crystallization (e.g., Cashman and Blundy, 2013), we chose to run the growth experiments water-saturated, with no CO_2, in an attempt to make crystal recovery easier. We postulate that CO_2 may have aided in promoting rapid crystal growth, however, other CO_2-free experimental designs (see Table 4.1) have been successful in growing skeletal quartz. Therefore,

we do not believe that this is the main factor in the lack of observed embayment growth in C1 and C2. The next explanation is that the rate of quartz growth is too slow for measurable progress to have been made under the experimental conditions in C1 (t=24 hrs). If the rate of growth is significantly slower than dissolution, the amount of change we would expect to see might be too small to accurately quantify. Previous work has estimated rates of skeletal quartz growth that range from 10^{-12} – 10^{-9} m/s (ΔT = 55 - 200°C; Swanson and Fenn, 1986; Baker and Freda, 2001). Assuming a rapid skeletal quartz growth rate of 10^{-10} m/s would have resulted in ~9µm of new growth in the 24-hour experiment, and upwards of 240µm of growth in the 28-day experiment, both of which would have been prominently noticeable. A growth rate of 10^{-11} m/s would have produced a <1µm growth in the 24-hour experiment, and ~20µm in the 28-day experiment. Thus, we find that quartz growth would have to be ~10^{-12} – 10^{-11} m/s or slower in order to not produce observable changes during the growth experiments. Finally, we propose that the chosen starting material (namely, using seed crystals rather than a homogeneous glass) may not have been kinetically conducive to promoting rapid growth, thus limiting the formation of embayments in these experiments. During periods of high degrees of undercooling (ΔT_{eff} > 125°C), the system will initially be in a nucleation-dominated regime. As the system reequilibrates the degree of undercooling will transition to a growth-dominated regime (Hammer and Rutherford, 2002). These lower degrees of undercooling in turn are associated with slower crystal growth rates (Swanson, 1977). Growth on the preexisting seed crystals likely requires longer periods of time in the growth dominant phase (at growth rates that may be too slow for skeletal growth) or much higher rates/degrees of undercooling. For example, Zieg and Lofgren (2006) were able to produce skeletal overgrowths on olivine crystals during experiments at

cooling rates of 92°C/hr, which is much higher than our imposed rates of 4 – 10°C/hr. Additionally, Baker and Freda (2001) formed vermicular (wormy) overgrowths on quartz at an undercooling of 100°C, which is still higher than our undercooling of 60 – 65°C.

Reconciling Natural and Experimental Results

Upon first inspection, it seems that the results from natural crystals are at odds with the results from the heating and cooling experiments. While the natural samples show an abundance of growth relationships between embayments and crystal zoning patterns, the experiments show that preferential dissolution during superheating, rather than rapid growth during undercooling, was very effective for forming embayments. We propose that this juxtaposition can be resolved if we assume a compound formation mechanism, such as the "dissolve then refill" scenario discussed by Barbee et al. (2020). In this scenario, the existing crystal is partially dissolved during a period of heating or volatile fluxing. The partial dissolution creates the foundation for future embayment growth by either intersecting preexisting melt inclusions, or by forming new indentations in the crystal surface via bubble drilling. A subsequent phase of growth will then begin to infill the dissolution-formed pits, resulting in CL zoning that wraps around the newly formed embayment. We see strong evidence for this in the "dissolution interior" subpopulation of the natural samples (Figure 4.7), and it would explain the results of the experimental crystals. The experiments show that undercooling alone is not conducive to forming embayments on existing crystals, while heating alone readily dissolved the crystal but does not form glassy embayments. This indicates that a combination of dissolution followed by growth may be necessary to produce the textures seen in natural samples. The dissolution interior subpopulation is especially prominent in the Pinatubo samples, which also tend to have vesiculated or hollow

embayments, adding further support for dissolution via volatile fluxing and drilling. This mechanism of embayment formation, dissolution overprinted by subsequent growth, can be further tested in future work by completing a series of experiments that combine an initial stage of heating (24 – 36 hours) to promote bubble drilling, followed by a long dwell (weeks to months) at subliquidus temperatures to promote overgrowth on the dissolution surface.

Implications for the Longevity of Quartz

The results of our heating experiment allow us to calculate the rate of quartz dissolution in a volatile-saturated magma. The observed dissolution pits extend anywhere from a few microns, up to several 10s of micron into the crystal. This results in a dissolution rate of <1 – 3 μm/hr over the course of the 35-hour experiment, about an order of magnitude slower than the dissolution rate of 36 μm/hr measured by Donaldson (1985) for quartz in basaltic melt (1250°C, 1-atm, anhydrous). This discrepancy is expected considering dissolution is diffusion-limited, where the lower temperatures and more silicic compositions used in this study would result in a higher viscosity melt, hindering diffusion away from the crystal. The dissolution rate of 1 – 3 μm/hr is equivalent to 10^{-10} – 10^{-9} m/s, which is comparable to albeit slightly faster than the estimated rates of skeletal quartz growth (10^{-12} – 10^{-9} m/s; Swanson and Fenn, 1986; Baker and Freda, 2001). Using these rates obtained by previous researchers, a 500 μm crystal would take 1.6 – 15.8 years to grow (assuming growth rates of 10^{-12} – 10^{-11} m/s). On the other hand, the same crystal would only take 5 – 60 days to dissolve (assuming dissolution rates of 10^{-10} – 10^{-9} m/s). The extensive dissolution of the experimental crystals in such a short timespan indicates that embayments formed during dissolution (5% from our natural samples) form in short periods

of superheating in a volatile-saturated magma, likely in the final few days prior to eruption; otherwise, it is likely that they could be completely dissolved away from the crystal record.

The growth rates calculated from our experiments, and the lack of embayment formation observed, suggests that growth-driven embayments likely form during periods of strong undercooling in the system, promoting skeletal growth early in a crystal's history or that an initial period of dissolution is a prerequisite for creating imperfections in the crystal surface. These features are then likely propagated through a series of prolonged, slower growth periods, producing the warped textures that dominant our natural embayments. Based on diffusion timescales calculated across titanium zoning boundaries (Boro et al., 2021; Gualda et al., 2012) and crystal size distributions (Pamukcu et al., 2012), the growth of quartz phenocrysts are thought to occur on timescales of years to thousands of years. Considering the interaction between these zones and the placement of the embayment, this implies that the growth embayments, which warp and thus must predate or coincide with the formation of the Ti zoning, began forming long before the eruption began and are not late-stage relics of eruption triggering. This interpretation is supported by work from Barbee et al. (2020) who conclude that tapering of CL zones around embayments is evidence that embayments form from the interior outward. We can assume that the embayments that deflect the growth zoning boundaries form over similar timescales, perhaps recording an early priming of the system rather than a final trigger.

Conclusion

Understanding the origin of embayments, a feature prominent in silicic, intermediate, and basaltic systems, allows us to develop a better picture of the disequilibrium history of magmatic

crystals. We find that the overwhelming majority of quartz-hosted embayments from 5 volcanic systems display zoning relationships indicative of a crystal growth origin. Crosscutting dissolution relationships account for only 5% of total embayments, however, we find that 45% of the warped growth zoning relationships occur as overgrowth rims on interior dissolution surfaces, indicating dissolution may have a larger role in the origin of embayments. This suggests that after an initial period of either rapid skeletal growth or dissolution, the crystals are then stored at sub-liquidus temperatures for extended periods of time, promoting embayment formation via continued crystal growth. However, we contrarily show experimentally that dissolution via bubble-drilling in a volatile-saturated melt is a viable and rapid mechanism for producing embayments. From these experiments we calculate quartz dissolution rates of 10^{-10} – 10^{-9} m/s, rates that are slightly slower than existing dissolution rates and comparable to or faster than those previously published on quartz growth rates. Based on the results of this work, we propose that growth-formed embayments are long-lasting features, forming early in the crystals history and often persisting through multiple phases of growth. In contrast, dissolution-formed embayments are more ephemeral features, with quartz likely to be fully dissolved over a few days if conditions persist, and possibly recording a final heating/fluxing just prior to eruption.

References Cited

Allègre, C. J., Provost, A., & Jaupart, C. (1981). Oscillatory zoning: a pathological case of crystal growth. *Nature*, *294*(5838), 223-228.

Anderson, A. T. (1991). Hourglass inclusions: theory and application to the Bishop Rhyolitic Tuff. *American Mineralogist*, *76*(3-4), 530-547.

Andrews, B. J., & Befus, K. S. (2020). Supersaturation Nucleation and Growth of Plagioclase: a numerical model of decompression-induced crystallization. *Contributions to Mineralogy and Petrology*, *175*(3), 1-20.

Audétat, A., Miyajima, N., Wiesner, D., & Audinot, J. N. (2021). Confirmation of slow Ti diffusion in quartz by diffusion couple experiments and evidence from natural samples. *Geology*, *49*(8), 963-967.

Bachmann, O., Dungan, M. A., & Lipman, P. W. (2002). The Fish Canyon magma body, San Juan volcanic field, Colorado: rejuvenation and eruption of an upper-crustal batholith. *Journal of Petrology*, *43*(8), 1469-1503.

Bachmann, O., & Bergantz, G. W. (2006). Gas percolation in upper-crustal silicic crystal mushes as a mechanism for upward heat advection and rejuvenation of near-solidus magma bodies. *Journal of Volcanology and Geothermal research*, *149*(1-2), 85-102.

Baker, D. R., & Freda, C. (2001). Eutectic crystallization in the undercooled Orthoclase-Quartz-H2O system experiments and simulations. *European Journal of Mineralogy*, *13*(3), 453-466.

Barbee, O., Chesner, C., & Deering, C. (2020). Quartz crystals in Toba rhyolites show textures symptomatic of rapid crystallization. *American Mineralogist*, *105*(2), 194-226.

Befus, K. S., & Manga, M. (2019). Supereruption quartz crystals and the hollow reentrants. *Geology*, *47*(8), 710-714.

Blackerby, B. A. (1968). Convolute zoning of plagioclase phenocrysts in miocene volcanics from the Western Santa Monica Mountains. California. *American Mineralogist: Journal of Earth and Planetary Materials*, *53*(5-6), 954-962.

Boro, J. R., Wolff, J. A., Neill, O. K., Steiner, A. R., & Ramos, F. C. (2021). Titanium diffusion profiles and melt inclusion chemistry and morphology in quartz from the Tshirege Member of the Bandelier Tuff. *American Mineralogist: Journal of Earth and Planetary Materials*, *106*(4), 620-632.

Brugger, C. R., & Hammer, J. E. (2015). Prevalence of growth twins among anhedral plagioclase microlites. *American Mineralogist*, *100*(2-3), 385-395.

Busby, T. S., & Barker, J. (1966). Simulative studies of upward drilling. *Journal of the American Ceramic Society*, *49*(8), 441-446.

Cashman, K., & Blundy, J. (2013). Petrological cannibalism: the chemical and textural consequences of incremental magma body growth. *Contributions to Mineralogy and Petrology*, *166*(3), 703-729.

Costa, F., Dohmen, R., & Chakraborty, S. (2008). Time scales of magmatic processes from modeling the zoning patterns of crystals. *Reviews in Mineralogy and Geochemistry*, *69*(1), 545-594.

Donaldson, C. H. (1976). An experimental investigation of olivine morphology. *Contributions to Mineralogy and Petrology*, *57*(2), 187-213.

Donaldson, C. H. (1985). The rates of dissolution of olivine, plagioclase, and quartz in a basalt melt. *Mineralogical Magazine*, *49*(354), 683-693.

Donaldson, C. H., & Henderson, C. M. B. (1988). A new interpretation of round embayments in quartz crystals. *Mineralogical Magazine*, *52*(364), 27-33.

Faure, F., & Schiano, P. (2005). Experimental investigation of equilibration conditions during forsterite growth and melt inclusion formation. *Earth and Planetary Science Letters*, *236*(3-4), 882-898.

Gardner, J. E., Befus, K. S., Gualda, G. A., & Ghiorso, M. S. (2014). Experimental constraints on rhyolite-MELTS and the Late Bishop Tuff magma body. *Contributions to Mineralogy and Petrology*, *168*(2), 1-14.

Gardner, J. E., Hilton, M., & Carroll, M. R. (2000). Bubble growth in highly viscous silicate melts during continuous decompression from high pressure. *Geochimica et Cosmochimica Acta*, *64*(8), 1473-1483.

Girard, G., & Stix, J. (2009). Magma recharge and crystal mush rejuvenation associated with early post-collapse Upper Basin Member rhyolites, Yellowstone caldera, Wyoming. *Journal of Petrology*, *50*(11), 2095-2125.

Götze, J., Pan, Y., & Müller, A. (2021). Mineralogy and mineral chemistry of quartz: A review. *Mineralogical Magazine*, *85*(5), 639-664.

Gualda, G. A., Pamukcu, A. S., Ghiorso, M. S., Anderson Jr, A. T., Sutton, S. R., & Rivers, M. L. (2012). Timescales of quartz crystallization and the longevity of the Bishop giant magma body. *PloS one*, *7*(5), e37492.

Hammer, J. E., & Rutherford, M. J. (2002). An experimental study of the kinetics of decompression-induced crystallization in silicic melt. *Journal of Geophysical Research: Solid Earth*, *107*(B1), ECV-8.

Harris, D. M., & Anderson, A. T. (1984). Volatiles H2O, CO2, and Cl in a subduction related basalt. *Contributions to Mineralogy and Petrology*, *87*(2), 120-128.

Hibbard, M. J. (1981). The magma mixing origin of mantled feldspars. *Contributions to Mineralogy and Petrology*, *76*(2), 158-170.

Jollands, M. C., Bloch, E., & Müntener, O. (2020). New Ti-in-quartz diffusivities reconcile natural Ti zoning with time scales and temperatures of upper crustal magma reservoirs. *Geology*, *48*(7), 654-657.

Kuo, L. C., & Kirkpatrick, R. J. (1985). Kinetics of crystal dissolution in the system diopside-forsterite-silica. *American Journal of Science*, *285*(1), 51-90.

Liu, Y., Anderson, A. T., & Wilson, C. J. (2007). Melt pockets in phenocrysts and decompression rates of silicic magmas before fragmentation. *Journal of Geophysical Research: Solid Earth*, *112*(B6).

Lofgren, G., & Hargraves, R. B. (1980). Experimental studies on the dynamic crystallization of silicate melts. *Physics of magmatic processes*, *487*, 551.

MacLellan, H. E., & Trembath, L. T. (1991). The role of quartz crystallization in the development and preservation of igneous texture in granitic rocks; experimental evidence at 1 kbar. *American Mineralogist*, *76*(7-8), 1291-1305.

Manley, C. R. (1996). Morphology and maturation of melt inclusions in quartz phenocrysts from the Badlands rhyolite lava flow, southwestern Idaho. *American Mineralogist*, *81*(1-2), 158-168.

Milman-Barris, M. S., Beckett, J. R., Baker, M. B., Hofmann, A. E., Morgan, Z., Crowley, M. R., ... & Stolper, E. (2008). Zoning of phosphorus in igneous olivine. *Contributions to Mineralogy and Petrology*, *155*(6), 739-765.

Müller, A., Seltmann, R., & Behr, H. J. (2000). Application of cathodoluminescence to magmatic quartz in a tin granite–case study from the Schellerhau Granite Complex, Eastern Erzgebirge, Germany. *Mineralium Deposita*, *35*(2), 169-189.

Myers, M. L., Wallace, P. J., Wilson, C. J., Watkins, J. M., & Liu, Y. (2018). Ascent rates of rhyolitic magma at the onset of three caldera-forming eruptions. *American Mineralogist*, *103*(6), 952-965.

Myers, M. L., Druitt, T. H., Schiavi, F., Gurioli, L., & Flaherty, T. (2021). Evolution of magma decompression and discharge during a Plinian event (Late Bronze-Age eruption, Santorini) from multiple eruption-intensity proxies. *Bulletin of Volcanology*, *83*(3), 1-17.

Peppard, B. T., Steele, I. M., Davis, A. M., Wallace, P. J., & Anderson, A. T. (2001). Zoned quartz phenocrysts from the rhyolitic Bishop Tuff. *American Mineralogist*, *86*(9), 1034-1052.

Roedder, E. (1979). Origin and significance of magmatic inclusions. *Bulletin de Mineralogie*, *102*(5), 487-510.

Ruefer, A. C., Befus, K. S., Thompson, J. O., & Andrews, B. J. (2021). Implications of Multiple Disequilibrium Textures in Quartz-Hosted Embayments. Front. *Earth Sci*, *9*, 742895.

Saalfeld, M. A., Myers, M. L., deGraffenried, R., Shea, T., & Waelkens, C. M. (2022). On the rise: using reentrants to extract magma ascent rates in the Bandelier Tuff caldera complex, New Mexico, USA. *Bulletin of Volcanology*, *84*(1), 1-21.

Seitz, S., Putlitz, B., Baumgartner, L. P., Escrig, S., Meibom, A., & Bouvier, A. S. (2016). Short magmatic residence times of quartz phenocrysts in Patagonian rhyolites associated with Gondwana breakup. *Geology*, *44*(1), 67-70.

Seitz, S., Putlitz, B., Baumgartner, L., Meibom, A., Escrig, S., & Bouvier, A. S. (2018). A NanoSIMS investigation on timescales recorded in volcanic quartz from the silicic Chon Aike Province (Patagonia). *Frontiers in Earth Science*, *6*, 95.

Shea, T., Lynn, K. J., & Garcia, M. O. (2015). Cracking the olivine zoning code: Distinguishing between crystal growth and diffusion. *Geology*, *43*(10), 935-938.

Sparks, R. S. J., & Cashman, K. V. (2017). Dynamic magma systems: Implications for forecasting volcanic activity. *Elements*, *13*(1), 35-40.

Swanson, S. E. (1977). Relation of nucleation and crystal-growth rate to the development of granitic textures. *American Mineralogist*, *62*(9-10), 966-978.

Swanson, S. E., & Fenn, P. M. (1986). Quartz crystallization in igneous rocks. *American Mineralogist*, *71*(3-4), 331-342.

Wark, D. A., Hildreth, W., Spear, F. S., Cherniak, D. J., & Watson, E. B. (2007). Pre-eruption recharge of the Bishop magma system. *Geology*, *35*(3), 235-238.

Wark, D. A., & Stimac, J. A. (1992). Origin of mantle (rapakivi) feldspars: Experimental evidence of a dissolution-and diffusion-controlled mechanism. *Contributions to Mineralogy and Petrology*, *111*(3), 345-361.

Wark, D. A., & Watson, E. B. (2006). TitaniQ: a titanium-in-quartz geothermometer. *Contributions to Mineralogy and Petrology*, *152*(6), 743-754.

Wilcock, J., Goff, F., Minarik, W. G., & Stix, J. (2013). Magmatic recharge during the formation and resurgence of the Valles Caldera, New Mexico, USA: evidence from quartz compositional zoning and geothermometry. *Journal of Petrology*, *54*(4), 635-664.

Zieg, M. J., & Lofgren, G. E. (2006). An experimental investigation of texture evolution during continuous cooling. *Journal of Volcanology and Geothermal Research*, *154*(1-2), 74-88.

Zuccarello, F., Schiavi, F., & Viccaro, M. (2022). The eruption run-up at Mt. Etna volcano: Constraining magma decompression rates and their relationships with the final eruptive energy. *Earth and Planetary Science Letters*, *597*, 117821.

CHAPTER FIVE

DISSERTATION SUMMARY

My dissertation research investigated magma ascent rates for both members of the Bandelier Tuff and the preclimactic 1991 eruption of Mount Pinatubo using volatile diffusion through melt-filled embayments as well as other more traditional petrologic geospeedometers. The results of this work have been used to validate and improve the assumptions made during modeling. In addition to ascent speedometry, I additionally sought to use embayments as a record of pre-eruptive disequilibrium in the magma chamber. The results of this work show that undercooling was the dominant condition experienced during the crystals' history.

Modeling of any natural system requires that several assumptions and simplifications be made. In modeling magmatic ascent rates, we assume isothermal conditions, 1-dimension diffusion (from the interior toward the rim), starting pressures associated with melt inclusion or embayment saturation, and continuous decompression rates. In Chapter Two, I find that while 1-dimensional diffusion is generally a sufficient assumption, increasing temperature leads to the greatest amount of uncertainty in modeled ascent rates. Additionally, I propose a new intermediate starting pressure condition associated with high water and no CO_2. This condition requires minor amounts of initial decompression and/or crystallization but provides the best fit for the greatest number of embayments. Chapter Three seeks to reconcile the several orders of magnitude disagreement between ascent rates derived by various geospeedometry methods. This disagreement is rectified by using new modeling techniques that impose rate-accelerating decompression paths. We find that a 2-stage embayment diffusion model bridges the gap

between slower microlites and faster bubbles and is a useful tool for modeling ascent in both the deep and shallow conduit.

Beyond estimating ascent rates, embayments can be useful tools for recording disequilibrium crystal growth and dissolution in the magma chamber. Zoning relationships indicate that embayments mostly form due to crystal growth, indicating that the magma experiences significant amounts of undercooling. Dissolution makes up a small portion of the embayments, indicating that superheating is less common or not as well preserved in the crystal record. Finally, through laboratory experiments of heating and cooling, I find that crystal dissolution via bubble drilling is capable of rapidly dissolving quartz crystals, while crystal growth occurs at either higher cooling rates or slower growth rates than expected.

REFERENCES CITED

Aldrich Jr, M. (1986). Tectonics of the Jemez lineament in the Jemez Mountains and Rio Grande rift. *Journal of Geophysical Research: Solid Earth*, *91*, 1753-1762.

Allègre, C. J., Provost, A., & Jaupart, C. (1981). Oscillatory zoning: a pathological case of crystal growth. *Nature*, *294*(5838), 223-228.

Anderson, A. T. (1991). Hourglass inclusions: theory and application to the Bishop Rhyolitic Tuff. *American Mineralogist*, *76*(3-4), 530-547.

Andrews, B. J., & Befus, K. S. (2020). Supersaturation Nucleation and Growth of Plagioclase: a numerical model of decompression-induced crystallization. *Contributions to Mineralogy and Petrology*, *175*(3), 1-20.

Audétat, A. (2013). Origin of Ti-rich rims in quartz phenocrysts from the Upper Bandelier Tuff and the Tunnel Spring Tuff, southwestern USA: *Chemical Geology*, *360*, 99-104.

Audétat, A., Miyajima, N., Wiesner, D., & Audinot, J. N. (2021). Confirmation of slow Ti diffusion in quartz by diffusion couple experiments and evidence from natural samples. *Geology*, *49*(8), 963-967.

Bachmann, O., Dungan, M. A., & Lipman, P. W. (2002). The Fish Canyon magma body, San Juan volcanic field, Colorado: rejuvenation and eruption of an upper-crustal batholith. *Journal of Petrology*, *43*(8), 1469-1503.

Bachmann, O., & Bergantz, G. W. (2006). Gas percolation in upper-crustal silicic crystal mushes as a mechanism for upward heat advection and rejuvenation of near-solidus magma bodies. *Journal of Volcanology and Geothermal research*, *149*(1-2), 85-102.

Baker, D. R., & Freda, C. (2001). Eutectic crystallization in the undercooled Orthoclase-Quartz-H2O system experiments and simulations. *European Journal of Mineralogy*, *13*(3), 453-466.

Barbee, O., Chesner, C., & Deering, C. (2020). Quartz crystals in Toba rhyolites show textures symptomatic of rapid crystallization. *American Mineralogist*, *105*(2), 194-226.

Befus, K. S., & Andrews, B. J. (2018). Crystal nucleation and growth produced by continuous decompression of Pinatubo magma. *Contributions to Mineralogy and Petrology*, *173*(11), 1-20.

Befus, K. S., & Manga, M. (2019). Supereruption quartz crystals and the hollow reentrants. *Geology*, *47*(8), 710-714.

Benage, M. C., Wright, H., & Coombs, M. L. (2021). Eruption of compositionally heterogeneous andesites from a complex storage region during the 2006 eruption of Augustine Volcano. *Bulletin of Volcanology*, *83*(3), 1-23.

Blackerby, B. A. (1968). Convolute zoning of plagioclase phenocrysts in miocene volcanics from the Western Santa Monica Mountains. California. *American Mineralogist: Journal of Earth and Planetary Materials*, *53*(5-6), 954-962.

Boehnke, P., Watson, E.B., Trail, D., Harrison, T.M., & Schmitt, A.K. (2013). Zircon saturation re-revisited. *Chemical Geology*, *351*, 324-334.

Borisova, A. Y., Toutain, J. P., Dubessy, J., Pallister, J., Zwick, A., & Salvi, S. (2014). H2O–CO2–S fluid triggering the 1991 Mount Pinatubo climactic eruption (Philippines). *Bulletin of Volcanology*, *76*(2), 1-9.

Boro, J.R. (2019) Recharge and Mobilization of Crystal Mush to Produce and Erupt a Zoned Magma Chamber–the Tshirege Member of the Bandelier Tuff, Valles Caldera, New Mexico, USA.

Boro, J.R., Wolff, J.A., & Neill, O.K. (2020) Anatomy of a Recharge Magma: Hornblende Dacite Pumice from the rhyolitic Tshirege Member of the Bandelier Tuff, Valles Caldera, New Mexico, USA. *Contributions to Mineralogy and Petrology*, *175*, 1-26.

Boro, J. R., Wolff, J. A., Neill, O. K., Steiner, A. R., & Ramos, F. C. (2021). Titanium diffusion profiles and melt inclusion chemistry and morphology in quartz from the Tshirege Member of the Bandelier Tuff. *American Mineralogist: Journal of Earth and Planetary Materials*, *106*(4), 620-632.

Brandeis, G., & Jaupart, C. (1987). The kinetics of nucleation and crystal growth and scaling laws for magmatic crystallization. *Contributions to Mineralogy and Petrology*, *96*(1), 24-34.

Brugger, C. R., & Hammer, J. E. (2010). Crystallization kinetics in continuous decompression experiments: implications for interpreting natural magma ascent processes. *Journal of Petrology*, *51*(9), 1941-1965.

Brugger, C. R., & Hammer, J. E. (2015). Prevalence of growth twins among anhedral plagioclase microlites. *American Mineralogist*, *100*(2-3), 385-395.

Busby, T. S., & Barker, J. (1966). Simulative studies of upward drilling. *Journal of the American Ceramic Society*, *49*(8), 441-446.

Campbell, M.E., Hanson, J.B., Minarik, W.G., & Stix, J. (2009). Thermal history of the Bandelier magmatic system: Evidence for magmatic injection and recharge at 1.61 Ma as revealed by cathodoluminescence and titanium geothermometry. *The Journal of Geology*, *117*, 469-485.

Caricchi, L., Annen, C., Blundy, J., Simpson, G., & Pinel, V. (2014). Frequency and magnitude of volcanic eruptions controlled by magma injection and buoyancy. *Nature Geoscience*, *7*, 126-130.

Cashman, K.V. (2004). Volatile controls on magma ascent and eruption. *Washington DC American Geophysical Union Geophysical Monograph Series*, *150*, 109-124.

Cashman, K., & Blundy, J. (2013). Petrological cannibalism: the chemical and textural consequences of incremental magma body growth. *Contributions to Mineralogy and Petrology*, *166*(3), 703-729.

Cassidy, M., Manga, M., Cashman, K., & Bachmann, O. (2018). Controls on explosive-effusive volcanic eruption styles. *Nature communications*, *9*(1), 1-1

Castro, J.M., & Gardner, J.E. (2008). Did magma ascent rate control the explosive-effusive transition at the Inyo volcanic chain, California? *Geology*, *36*, 279-282.

Charlier, B., Morgan, D., Wilson, C., Wooden, J., Allan, A., & Baker, J. (2012). Lithium concentration gradients in feldspar and quartz record the final minutes of magma ascent in an explosive supereruption. *Earth and Planetary Science Letters*, *319*, 218-227.

Costa, F., Dohmen, R., & Chakraborty, S. (2008). Time scales of magmatic processes from modeling the zoning patterns of crystals. *Reviews in Mineralogy and Geochemistry*, *69*(1), 545-594.

Crowe, B.M., Linn, G.W., Heiken, G., & Bevier, M.L. (1978). Stratigraphy of the Bandelier tuff in the Pajarito plateau. *Applications to Waste Management*. Los Alamos National Laboratory Informal Report LA-7225-MS.

Daag, A. S., Tubianosa, B. S., Newhall, C. G., Tungol, N. M., Javier, D., Dolan, M. T., ... & Regalado, T. M. (1996). Monitoring sulfur dioxide emission at Mount Pinatubo. Fire and mud: eruptions and lahars of Mount Pinatubo, Philippines, Newhall CG, Punongbayan RS.

deGraffenried, R., & Shea, T. (2021). Using Volatile Element Concentration Profiles in Crystal-Hosted Melt Embayments to Estimate Magma Decompression Rate: Assumptions and Inherited Errors. *Geochemistry, Geophysics, Geosystems*, *22*, e2021GC009672.

Donaldson, C. H. (1976). An experimental investigation of olivine morphology. *Contributions to Mineralogy and Petrology*, *57*(2), 187-213.

Donaldson, C. H. (1985). The rates of dissolution of olivine, plagioclase, and quartz in a basalt melt. *Mineralogical Magazine*, *49*(354), 683-693.

Donaldson, C. H., & Henderson, C. M. B. (1988). A new interpretation of round embayments in quartz crystals. *Mineralogical Magazine*, *52*(364), 27-33.

Dunbar, N.W., & Hervig, R.L. (1992). Volatile and trace element composition of melt inclusions from the Lower Bandelier Tuff: implications for magma chamber processes and eruptive style. *Journal of Geophysical Research: Solid Earth*, *97*, 15151-15170.

Eichelberger, J., Carrigan, C., Westrich, H., & Price, R. (1986). Non-explosive silicic volcanism. *Nature*, *323*, 598-602.

Faure, F., & Schiano, P. (2005). Experimental investigation of equilibration conditions during forsterite growth and melt inclusion formation. *Earth and Planetary Science Letters*, *236*(3-4), 882-898.

Ferguson, D. J., Gonnermann, H. M., Ruprecht, P., Plank, T., Hauri, E. H., Houghton, B. F., & Swanson, D. A. (2016). Magma decompression rates during explosive eruptions of Kīlauea volcano, Hawaii, recorded by melt embayments. *Bulletin of Volcanology*, *78*(10), 1-12, 71.

Fowler, S.J., & Spera, F.J. (2008)3. Phase equilibria trigger for explosive volcanic eruptions. *Geophysical Research Letters*, *35*.

Gardner, J. E., Befus, K. S., Gualda, G. A., & Ghiorso, M. S. (2014). Experimental constraints on rhyolite-MELTS and the Late Bishop Tuff magma body. *Contributions to Mineralogy and Petrology*, *168*(2), 1-14.

Gardner, J. E., Hilton, M., & Carroll, M. R. (2000). Bubble growth in highly viscous silicate melts during continuous decompression from high pressure. *Geochimica et Cosmochimica Acta*, *64*(8), 1473-1483.

Gerlach, T. M., Westrich, H. R., & Symonds, R. B. (1996). Preeruption vapor in magma of the climactic Mount Pinatubo eruption: Source of the giant stratospheric sulfur dioxide cloud. Fire and mud: eruptions and lahars of Mount Pinatubo, Philippines, Newhall CG, Punongbayan RS.

Ghiorso, M. S., & Gualda, G. A. (2015). An H_2O–CO_2 mixed fluid saturation model compatible with rhyolite-MELTS. *Contributions to Mineralogy and Petrology*, *169*(6), 1-30.

Giachetti, T., Druitt, T.H., Burgisser, A., Arbaret, L., & Galven, C. (2010). Bubble nucleation, growth and coalescence during the 1997 Vulcanian explosions of Soufrière Hills Volcano, Montserrat. *Journal of Volcanology and Geothermal Research*, *193*, 215-231.

Girard, G., & Stix, J. (2009). Magma recharge and crystal mush rejuvenation associated with early post-collapse Upper Basin Member rhyolites, Yellowstone caldera, Wyoming. *Journal of Petrology*, *50*(11), 2095-2125.

Goff, F., Warren, R., Goff, C.J., & Dunbar, N. (2014). Eruption of reverse-zoned upper Tshirege Member, Bandelier Tuff from centralized vents within Valles caldera, New Mexico. *Journal of Volcanology and Geothermal Research*, *276*, 82-104.

Gonnermann, H. M., & Manga, M. (2007). The fluid mechanics inside a volcano. *Annual Review of Fluid Mechanics*, *39*(1), 321-356.

Götze, J., Pan, Y., & Müller, A. (2021). Mineralogy and mineral chemistry of quartz: A review. *Mineralogical Magazine*, *85*(5), 639-664.

Gregg, P., De Silva, S., Grosfils, E., & Parmigiani, J. (2012). Catastrophic caldera-forming eruptions: Thermomechanics and implications for eruption triggering and maximum caldera dimensions on Earth. *Journal of Volcanology and Geothermal Research*, *241*, 1-12.

Gualda, G. A., Ghiorso, M. S., Lemons, R. V., & Carley, T. L. (2012). Rhyolite-MELTS: a modified calibration of MELTS optimized for silica-rich, fluid-bearing magmatic systems. *Journal of Petrology*, *53*(5), 875-890.

Gualda, G. A., Pamukcu, A. S., Ghiorso, M. S., Anderson Jr, A. T., Sutton, S. R., & Rivers, M. L. (2012). Timescales of quartz crystallization and the longevity of the Bishop giant magma body. *PloS one*, *7*(5), e37492.

Hajimirza, S., Gonnermann, H. M., & Gardner, J. E. (2021). Reconciling bubble nucleation in explosive eruptions with geospeedometers. *Nature communications*, *12*(1), 1-8.

Hamada, M., Laporte, D., Cluzel, N., Koga, K. T., & Kawamoto, T. (2010). Simulating bubble number density of rhyolitic pumices from Plinian eruptions: constraints from fast decompression experiments. *Bulletin of Volcanology*, *72*(6), 735-746.

Hammer, J. E., Cashman, K. V., Hoblitt, R. P., & Newman, S. (1999). Degassing and microlite crystallization during pre-climactic events of the 1991 eruption of Mt. Pinatubo, Philippines. *Bulletin of Volcanology*, *60*(5), 355-380.

Hammer, J. E., & Rutherford, M. J. (2002). An experimental study of the kinetics of decompression-induced crystallization in silicic melt. *Journal of Geophysical Research: Solid Earth*, *107*(B1), ECV-8.

Harlow, D. H., Power, J. A., Laguerta, E. P., Ambubuyog, G., White, R. A., & Hoblitt, R. P. (1996). Precursory seismicity and forecasting of the June 15, 1991, eruption of Mount Pinatubo. Fire and Mud: eruptions and lahars of Mount Pinatubo, Philippines, Newhall CG, Punongbayan RS.

Harris, D. M., & Anderson, A. T. (1984). Volatiles H2O, CO2, and Cl in a subduction related basalt. *Contributions to Mineralogy and Petrology*, *87*(2), 120-128.

Heiken, G., Goff, F., Gardner, J.N., Baldridge, W., Hulen, J., Nielson, D.L., & Vaniman, D. (1990). The Valles/Toledo Caldera Complex, Jemez Volcanic Field, New Mexico. *Annual Review of Earth and Planetary Sciences*, *18*, 27-53.

Heiken, G., Goff, F., Stix, J., Tamanyu, S., Shafiqullah, M., Garcia, S., & Hagan, R. (1986). Intracaldera volcanic activity, Toledo caldera and embayment, Jemez Mountains, New Mexico. *Journal of Geophysical Research: Solid Earth*, *91*, 1799-1815.

Hibbard, M. J. (1981). The magma mixing origin of mantled feldspars. *Contributions to Mineralogy and Petrology*, *76*(2), 158-170.

Hoblitt, R. P. (1996). The preclimactic eruptions of Mount Pinatubo, June 1991. Fire and Mud: eruptions and lahars of Mount Pinatubo, Philippines, Newhall CG, Punongbayan RS.

Holycross, M., Watson, E., Richter, F., & Villeneuve, J. (2018). Diffusive fractionation of Li isotopes in wet, highly silicic melts. *Geochemical Perspectives Letters*, *6*, 39-42.

Hosseini et al. (in prep). Are we recording? ……

Humphreys, M.C., Menand, T., Blundy, J.D., & Klimm, K. (2008). Magma ascent rates in explosive eruptions: Constraints from H2O diffusion in melt inclusions. *Earth and Planetary Science Letters*, *270*, 25-40.

Hurwitz, S., & Navon, O. (1994). Bubble nucleation in rhyolitic melts: Experiments at high pressure, temperature, and water content. *Earth and Planetary Science Letters*, *122*(3-4), 267-280.

Izett, G.A., & Obradovich, J.D. (1994). 40Ar/39Ar age constraints for the Jaramillo Normal Subchron and the Matuyama-Brunhes geomagnetic boundary. *Journal of Geophysical Research: Solid Earth*, *99*, 2925-2934.

Jellinek, A.M., & DePaolo, D.J. (2003). A model for the origin of large silicic magma chambers: precursors of caldera-forming eruptions. *Bulletin of Volcanology*, *65*, 363-381.

Jollands, M. C., Bloch, E., & Müntener, O. (2020). New Ti-in-quartz diffusivities reconcile natural Ti zoning with time scales and temperatures of upper crustal magma reservoirs. *Geology*, *48*(7), 654-657.

Kayzar, T. M., Cooper, K. M., Reagan, M. K., & Kent, A. J. (2009). Gas transport model for the magmatic system at Mount Pinatubo, Philippines: Insights from (210Pb)/(226Ra). *Journal of Volcanology and Geothermal Research*, *181*(1-2), 124-140.

Kientz, D.C. (1988). The Otowi member of the Bandelier Tuff: A study of the petrology, petrography, and geochemistry of an explosive silicic eruption, Jemez Mountains, New Mexico. Master's Thesis, University of Texas at Arlington.

Kuo, L. C., & Kirkpatrick, R. J. (1985). Kinetics of crystal dissolution in the system diopside-forsterite-silica. *American Journal of Science*, *285*(1), 51-90.

Leschik, M., Heide, G., Frischat, G. H., Behrens, H., Wiedenbeck, M., Wagner, N., Reinholz, U. (2004). Determination of H_2O and D2O contents in rhyolitic glasses. *Physics and Chemistry of Glasses*, *45*(4), 238-251.

Liu, Y., Zhang, Y., & Behrens, H. (2005). Solubility of H_2O in rhyolitic melts at low pressures and a new empirical model for mixed H2O–CO2 solubility in rhyolitic melts. *Journal of Volcanology and Geothermal Research*, *143*(1-3), 219-235.

Liu, Y., Anderson, A. T., & Wilson, C. J. (2007). Melt pockets in phenocrysts and decompression rates of silicic magmas before fragmentation. *Journal of Geophysical Research: Solid Earth*, *112*(B6).

Lloyd, A. S., Ruprecht, P., Hauri, E. H., Rose, W., Gonnermann, H. M., & Plank, T. (2014). NanoSIMS results from olivine-hosted melt embayments: Magma ascent rate during explosive basaltic eruptions. *Journal of Volcanology and Geothermal Research*, *283*, 1-18.

Lofgren, G., & Hargraves, R. B. (1980). Experimental studies on the dynamic crystallization of silicate melts. *Physics of magmatic processes*, *487*, 551.

MacLellan, H. E., & Trembath, L. T. (1991). The role of quartz crystallization in the development and preservation of igneous texture in granitic rocks; experimental evidence at 1 kbar. *American Mineralogist*, *76*(7-8), 1291-1305.

Malfait, W.J., Seifert, R., Petitgirard, S., Perrillat, J., Mezouar, M., Ota, T., Nakamura, E., Lerch, P., & Sanchez-Valle, C. (2014). Supervolcano eruptions driven by melt buoyancy in large silicic magma chambers. *Nature Geoscience*, *7*, 122-125.

Mangan, M. T., Cashman, K. V., & Newman, S. (1993). Vesiculation of basaltic magma during eruption. *Geology*, *21*(2), 157-160.

Manley, C. R. (1996). Morphology and maturation of melt inclusions in quartz phenocrysts from the Badlands rhyolite lava flow, southwestern Idaho. *American Mineralogist*, *81*(1-2), 158-168.

Marti, J., Ablay, G., Redshaw, L.T., & Sparks, R. (1994). Experimental studies of collapse calderas. *Journal of the Geological Society*, *151*, 919-929.

Mastin, L. G. (2002). Insights into volcanic conduit flow from an open-source numerical model. *Geochemistry, Geophysics, Geosystems*, *3*(7), 1-18.

Mercado, R. A. (1996). Socioeconomic impacts of the Mount Pinatubo eruption. Fire and Mud: eruptions and lahars of Mount Pinatubo, Philippines, Newhall CG, Punongbayan RS.

McLeod, P., and Tait, S. (1999). The growth of dykes from magma chambers. *Journal of Volcanology and Geothermal Research*, *92*, 231-245.

Milman-Barris, M. S., Beckett, J. R., Baker, M. B., Hofmann, A. E., Morgan, Z., Crowley, M. R., ... & Stolper, E. (2008). Zoning of phosphorus in igneous olivine. *Contributions to Mineralogy and Petrology*, *155*(6), 739-765.

Myers, M.L., Wallace, P.J., Wilson, C.J., Morter, B.K., &Swallow, E.J. (2016). Prolonged ascent and episodic venting of discrete magma batches at the onset of the Huckleberry Ridge supereruption, Yellowstone. *Earth and Planetary Science Letters*, *451*, 285-297.

Myers, M. L., Wallace, P. J., Wilson, C. J., Watkins, J. M., & Liu, Y. (2018). Ascent rates of rhyolitic magma at the onset of three caldera-forming eruptions. *American Mineralogist*, *103*(6), 952-965.

Myers, M. L., Druitt, T. H., Schiavi, F., Gurioli, L., & Flaherty, T. (2021). Evolution of magma decompression and discharge during a Plinian event (Late Bronze-Age eruption, Santorini) from multiple eruption-intensity proxies. *Bulletin of Volcanology*, *83*(3), 1-17.

Newcombe, M.E., Plank, T., Barth, A., Asimow, P., & Hauri, E. (2020). Water-in-olivine magma ascent chronometry: Every crystal is a clock. *Journal of Volcanology and Geothermal Researc*h, 106872.

Newhall, C. G., & Punongbayan, R. (Eds.). (1996). *Fire and mud: eruptions and lahars of Mount Pinatubo, Philippines* (p. 1126). Quezon City: Philippine Institute of Volcanology and Seismology.

Newman, S., & Lowenstern, J.B. (2002). VolatileCalc: a silicate melt–H2O–CO2 solution model written in Visual Basic for excel. *Computers & Geosciences*, *28*, 597-604.

Nielson, D.L., & Hulen, J.B. (1984). Internal geology and evolution of the Redondo dome, Valles caldera, New Mexico. *Journal of Geophysical Research: Solid Earth*, *89*, 8695-8711.

Paladio-Melosantos, M. L. O., Solidum, R. U., Scott, W. E., Quiambao, R. B., Umbal, J. V., Rodolfo, K. S., & Punongbayan, R. S. (1996). Tephra falls of the 1991 eruptions of Mount Pinatubo, Fire and mud: eruptions and lahars of Mount Pinatubo, Philippines, Newhall CG, Punongbayan RS.

Pallister, J. S., Hoblitt, R. P., Meeker, G. P., Knight, R. J., & Siems, D. F. (1996). Magma mixing at Mount Pinatubo: petrographic and chemical evidence from the 1991 deposits. Fire and mud: eruptions and lahars of Mount Pinatubo, Philippines, Newhall CG, Punongbayan RS.

Papale, P., Montagna, C.P., & Longo, A. (2017). Pressure evolution in shallow magma chambers upon buoyancy-driven replenishment. *Geochemistry, Geophysics, Geosystems*, *18*, 1214-1224.

Papale, P., & Polacci, M. (1999). Role of carbon dioxide in the dynamics of magma ascent in explosive eruptions. *Bulletin of volcanology*, *60*(8), 583-594.

Peppard, B. T., Steele, I. M., Davis, A. M., Wallace, P. J., & Anderson, A. T. (2001). Zoned quartz phenocrysts from the rhyolitic Bishop Tuff. *American Mineralogist*, *86*(9), 1034-1052.

Phillips, E.H., Goff, F., Kyle, P.R., McIntosh, W.C., Dunbar, N.W., & Gardner, J.N. (2007). The 40Ar/39Ar age constraints on the duration of resurgence at the Valles caldera, New Mexico. *Journal of Geophysical Research: Solid Earth*, *112*.

Roedder, E. (1979). Origin and significance of magmatic inclusions. *Bulletin de Mineralogie*, *102*(5), 487-510.

Ruefer, A. C., Befus, K. S., Thompson, J. O., & Andrews, B. J. (2021). Implications of Multiple Disequilibrium Textures in Quartz-Hosted Embayments. Front. *Earth Sci*, *9*, 742895.

Rutherford, M. J., & Devine, J. D. (1996). Preeruption pressure-temperature conditions and volatiles in the 1991 dacitic magma of Mount Pinatubo, Fire and mud: eruptions and lahars of Mount Pinatubo, Philippines, Newhall CG, Punongbayan RS.

Rutherford, M.J., & Devine, J.D. (2003). Magmatic conditions and magma ascent as indicated by hornblende phase equilibria and reactions in the 1995–2002 Soufriere Hills magma. *Journal of Petrology*, *44*, 1433-1453.

Rutherford, M.J., & Hill, P.M. (1993). Magma ascent rates from amphibole breakdown: an experimental study applied to the 1980–1986 Mount St. Helens eruptions. *Journal of Geophysical Research: Solid Earth*, *98*, 19667-19685.

Saalfeld, M. A., Myers, M. L., deGraffenried, R., Shea, T., & Waelkens, C. M. (2022). On the rise: using reentrants to extract magma ascent rates in the Bandelier Tuff caldera complex, New Mexico, USA. *Bulletin of Volcanology*, *84*(1), 1-21.

Savage, J., Lisowski, M., Prescott, W., & Sanford, A. (1980). Geodetic measurement of horizontal deformation across the Rio Grande Rift near Socorro, New Mexico. *Journal of Geophysical Research: Solid Earth*, *85*, 7215-7220.

Seitz, S., Putlitz, B., Baumgartner, L. P., Escrig, S., Meibom, A., & Bouvier, A. S. (2016). Short magmatic residence times of quartz phenocrysts in Patagonian rhyolites associated with Gondwana breakup. *Geology*, *44*(1), 67-70.

Seitz, S., Putlitz, B., Baumgartner, L., Meibom, A., Escrig, S., & Bouvier, A. S. (2018). A NanoSIMS investigation on timescales recorded in volcanic quartz from the silicic Chon Aike Province (Patagonia). *Frontiers in Earth Science*, *6*, 95.

Self, S., Goff, F., Gardner, J.N., Wright, J.V., & Kite, W.M. (1986). Explosive rhyolitic volcanism in the Jemez Mountains: Vent locations, caldera development and relation to regional structure. *Journal of Geophysical Research: Solid Earth*, *91*, 1779-1798.

Shea, T., Houghton, B. F., Gurioli, L., Cashman, K. V., Hammer, J. E., & Hobden, B. J. (2010). Textural studies of vesicles in volcanic rocks: an integrated methodology. *Journal of Volcanology and Geothermal Research*, *190*(3-4), 271-289.

Shea, T., Lynn, K. J., & Garcia, M. O. (2015). Cracking the olivine zoning code: Distinguishing between crystal growth and diffusion. *Geology*, *43*(10), 935-938.

Skirius, C. M., Peterson, J. W., & Anderson, A. T. (1990). Homogenizing rhyolitic glass inclusions from the Bishop Tuff. *American Mineralogist*, *75*(11-12), 1381-1398.

Smith, R.L., & Bailey, R.A. (1966). The Bandelier Tuff: A study of ash-flow eruption cycles from zoned magma chambers. *Bulletin of Volcanology*, *29*, 83-103.

Sparks, R. S. J., & Cashman, K. V. (2017). Dynamic magma systems: Implications for forecasting volcanic activity. *Elements*, *13*(1), 35-40.

Spence, R. J., Pomonis, A., Baxter, P. J., Coburn, A. W., White, M., & Dayrit, M. (1996). Building damage caused by the Mount Pinatubo eruption of June 15, 1991. Fire and Mud: Eruptions and Lahars of Mount Pinatubo, Philippines. Newhall CG, Punongbayan RS.

Stimac, J.A. (1996). Hornblende-dacite pumice in the Tshirege member of the Bandelier Tuff: Implications for magma chamber and eruptive processes, *in* New Mexico Geological Society Fall Field Conference Guidebook 47, Jemez Mountains Region. Socorro. *New Mexico Geological Society*, 269-274.

Stix, J., and Layne, G.D. (1996). Gas saturation and evolution of volatile and light lithophile elements in the Bandelier magma chamber between two caldera-forming eruptions. *Journal of Geophysical Research: Solid Earth*, *101*, 25181-25196.

Sussman, A.J., Lewis, C.J., Mason, S.N., Geissman, J.W., Schultz-Fellenz, E., Oliva-Urcia, B., & Gardner, J. (2011). Paleomagnetism of the Quaternary Bandelier Tuff: Implications for the tectonic evolution of the Española Basin, Rio Grande rift. *Lithosphere*, *3*, 328-345.

Swanson, S. E. (1977). Relation of nucleation and crystal-growth rate to the development of granitic textures. *American Mineralogist*, *62*(9-10), 966-978.

Swanson, S. E., & Fenn, P. M. (1986). Quartz crystallization in igneous rocks. *American Mineralogist*, *71*(3-4), 331-342.

Toramaru, A. (2006). BND (bubble number density) decompression rate meter for explosive volcanic eruptions. *Journal of Volcanology and Geothermal Research*, *154*(3-4), 303-316.

Toramaru, A., Noguchi, S., Oyoshihara, S., & Tsune, A. (2008). MND (microlite number density) water exsolution rate meter. *Journal of Volcanology and Geothermal Research*, *175*(1-2), 156-167.

Tramontano, S., Gualda, G.A., & Ghiorso, M.S. (2017). Internal triggering of volcanic eruptions: tracking overpressure regimes for giant magma bodies. *Earth and Planetary Science Letters*, *472*, 142-151.

Van Hoose, A. E., Streck, M. J., Pallister, J. S., & Wälle, M. (2013). Sulfur evolution of the 1991 Pinatubo magmas based on apatite. *Journal of Volcanology and Geothermal Research*, *257*, 72-89.

Waelkens, C.M. et al., in review, H_2O and CO_2 evolution in the Bandelier Tuff sequence reveals multiple and discrete magma replenishments. *Contributions to Mineralogy and Petrology*.

Wark, D. A., Hildreth, W., Spear, F. S., Cherniak, D. J., & Watson, E. B. (2007). Pre-eruption recharge of the Bishop magma system. *Geology*, *35*(3), 235-238.

Wark, D. A., & Stimac, J. A. (1992). Origin of mantle (rapakivi) feldspars: Experimental evidence of a dissolution-and diffusion-controlled mechanism. *Contributions to Mineralogy and Petrology*, *111*(3), 345-361.

Wark, D. A., & Watson, E. B. (2006). TitaniQ: a titanium-in-quartz geothermometer. *Contributions to Mineralogy and Petrology*, *152*(6), 743-754.

Wark, D., & Wolff, J. (2006). Mafic-recharge eruption trigger for the Bandelier and Bishop Tuffs, *in* AGU Fall Meeting Abstracts.

Warshaw, C.M., & Smith, R.L. (1988). Pyroxenes and fayalites in the Bandelier Tuff, New Mexico; temperatures and comparison with other rhyolites. *American Mineralogist*, *73*, 1025-1037.

Westgate, J.A., Woldegabriel, G., Halls, H.C., Bray, C.J., Barendregt, R.W., Pearce, N.J., Sarna-Wojcicki, A.M., Gorton, M.P., Kelley, R.E., & Schultz-Fellenz, E. (2019) Quaternary tephra from the Valles caldera in the volcanic field of the Jemez Mountains of New Mexico identified in western Canada. *Quaternary Research*, *91*, 813-828.

Wilcock, J., Goff, F., Minarik, W. G., & Stix, J. (2013). Magmatic recharge during the formation and resurgence of the Valles Caldera, New Mexico, USA: evidence from quartz compositional zoning and geothermometry. *Journal of Petrology*, *54*(4), 635-664.

Wilson, L., Sparks, R. S. J., & Walker, G. P. (1980). Explosive volcanic eruptions—IV. The control of magma properties and conduit geometry on eruption column behavior. *Geophysical Journal International*, *63*(1), 117-148.

White, J. P., & Harris, M. N. (1997). Changing sources: Early Lapita period obsidian in the Bismarck Archipelago. *Archaeology in Oceania*, *32*(1), 97-107.

Wolfe, E. W., & Hoblitt, R. P. (1996). Overview of the eruptions, Fire and mud: Eruptions and lahars of Mount Pinatubo, Philippines. Newhall CG, Punongbayan RS.

Wolff, J., & Gardner, J. (1995). Is the Valles caldera entering a new cycle of activity? *Geology*, *23*, 411-414.

Woodward, L.A., 1977, Rate of crustal extension across the Rio Grande rift near Albuquerque, New Mexico. *Geology*, *5*, 269-272.

Wysoczanski, R., & Tani, K. (2006). Spectroscopic FTIR imaging of water species in silicic volcanic glasses and melt inclusions: An example from the Izu-Bonin arc. *Journal of Volcanology and Geothermal Research*, *156*(3-4), 302-314.

Zhang, Y., Jenkins, J., & Xu, Z. (1997). Kinetics of the reaction H2O O→ 2 2OH in rhyolitic glasses upon cooling: Geospeedometry and comparison with glass transition. *Geochimica Et Cosmochimica Acta*, *61*, 2167-2173.

Zhang, Y., Xu, Z., Zhu, M., & Wang, H. (2007). Silicate melt properties and volcanic eruptions. *Reviews of Geophysics*, *45*(4).

Zieg, M. J., & Lofgren, G. E. (2006). An experimental investigation of texture evolution during continuous cooling. *Journal of Volcanology and Geothermal Research*, *154*(1-2), 74-88.

Zuccarello, F., Schiavi, F., & Viccaro, M. (2022). The eruption run-up at Mt. Etna volcano: Constraining magma decompression rates and their relationships with the final eruptive energy. *Earth and Planetary Science Letters*, *597*, 117821.

APPENDICES

APPENDIX A

CHAPTER TWO SUPPLEMENTARY INFORMATION

SUPPLEMENT- **On the rise: pushing reentrant boundaries to extract magma ascent in the nested caldera system of the Bandelier Tuff.**

Saalfeld, M. A.[1*], Myers, M.L.[1], deGraffenried, R.[2], Shea, T.[2], Waelkens, C.[3]

[1]*Department of Earth Sciences, Montana State University, Bozeman, MT 59715*
[2]*Department of Earth Sciences, University of Hawai'i at Manoa, Honolulu, HI 96822*
[3]*Department of Earth & Planetary Sciences, McGill University, Montreal, Canada*

Sample Location Data

GPS points using NAD27 CONUS projection:

Samples G1, G2, G3: 13S 0389698, 3975485

Samples T1, T2, T3: 13S 0347149, 3984706

Sample G0: 13S 0391814, 3969803

Misfit Calculation

Misfit is calculated using the following equation:

$Misfit = ((H_2Omodel-H_2Omeasured)/errorH_2O)^2 + ((CO_2model-CO_2measured)/errorCO_2)^2)/length(reentrant)$

Where H_2O is in wt.%, CO_2 is in ppm, errorH_2O = 0.25 wt.%, and errorCO_2 = 20 ppm

MELTs Modeling Parameters

Composition: See melt inclusion compositions from Dunbar and Hervig (1992) samples BB-005 (Guaje) and BB-092 (Tsankawi).

Starting Temperature: 750ºC
Stop Temperature: 700 ºC

Pressure: 1600 bar

fO_2: QFM

Supplementary Figure 1. Photomicrographs of glassy reentrants singly exposed in quartz crystals, showing the geometry of all modeled reentrants.

Tsankawi Reentrants

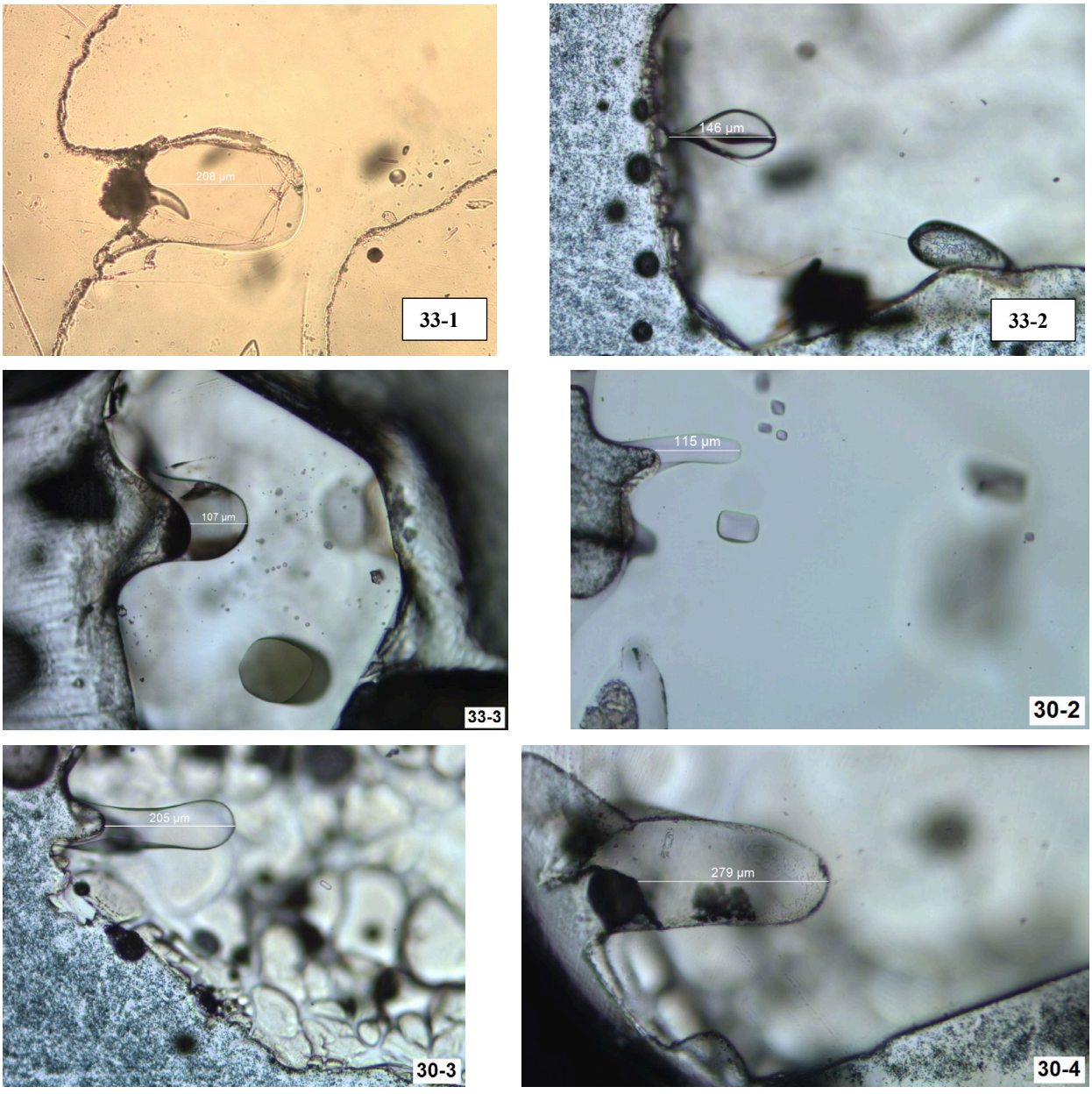

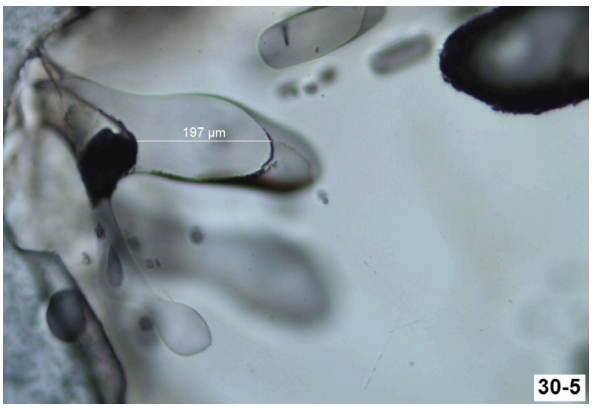
197 µm
30-5

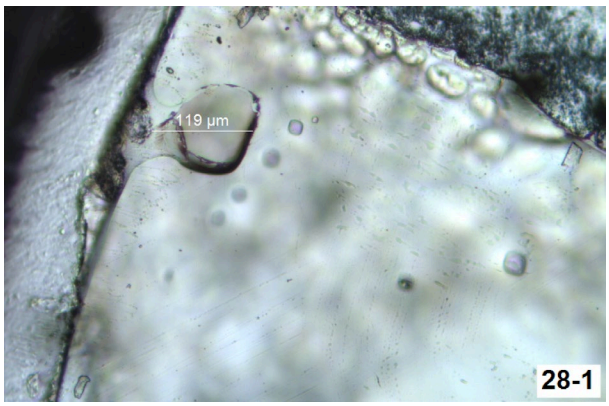
119 µm
28-1

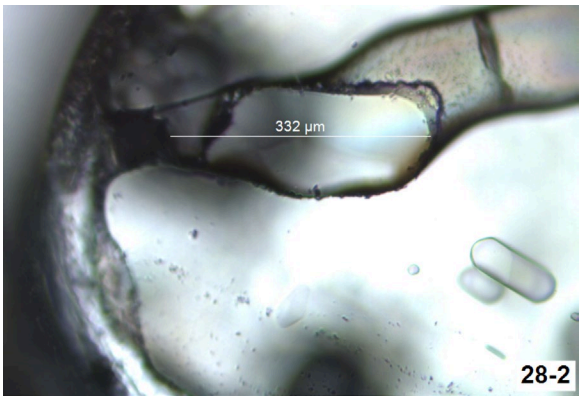
332 µm
28-2

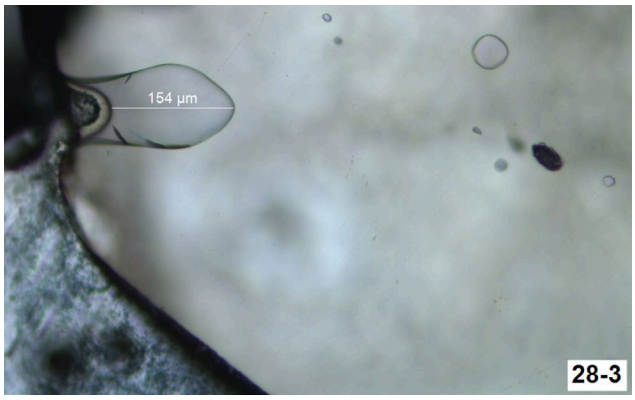
154 µm
28-3

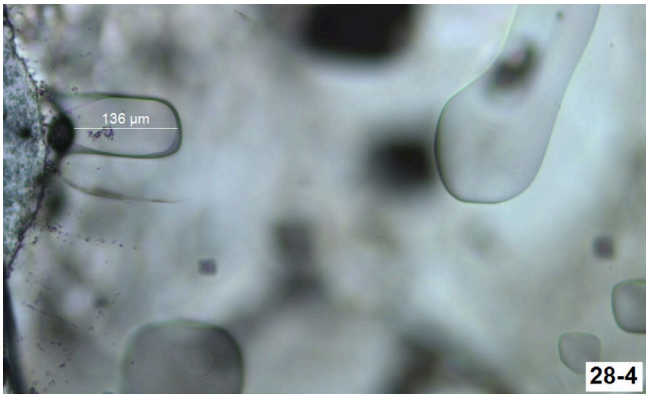
136 µm
28-4

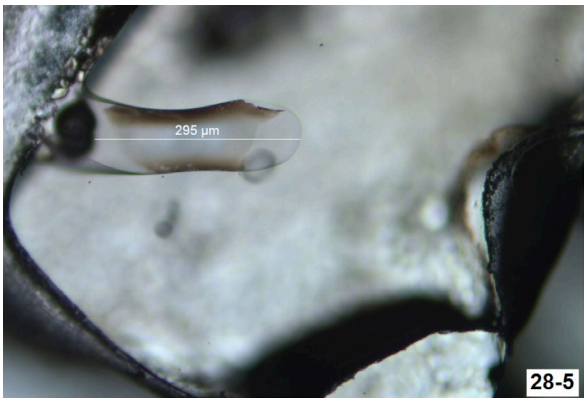
295 µm
28-5

Guaje Reentrants

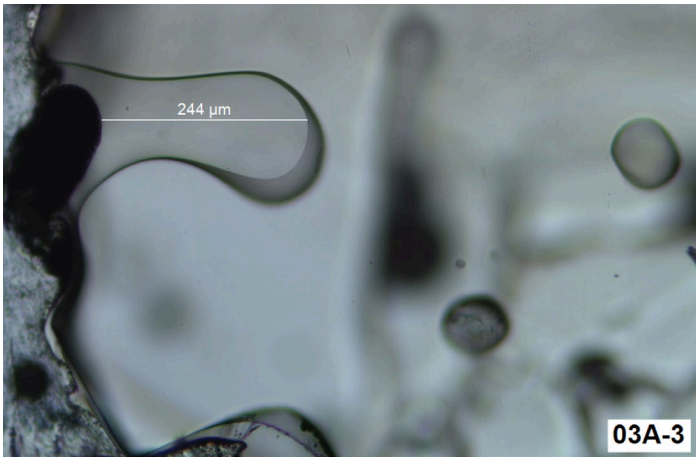

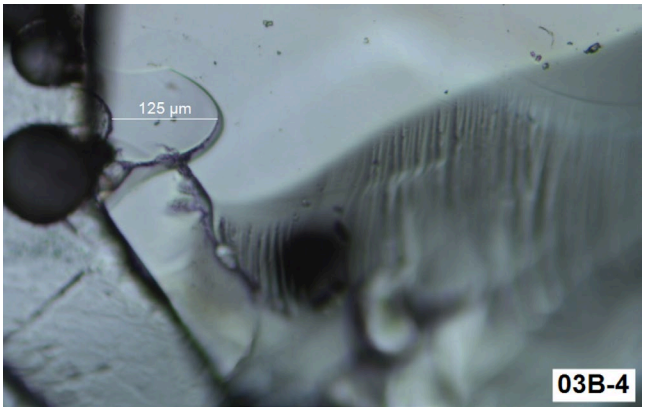

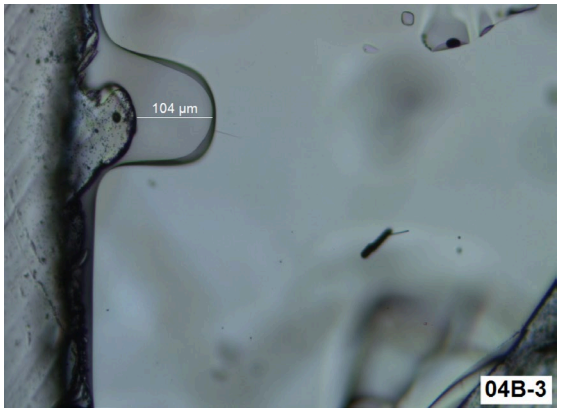

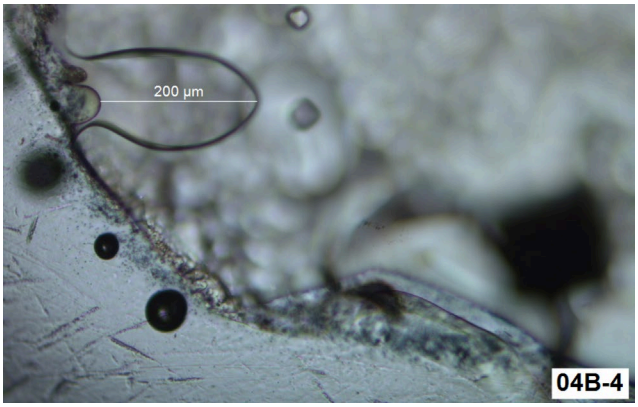

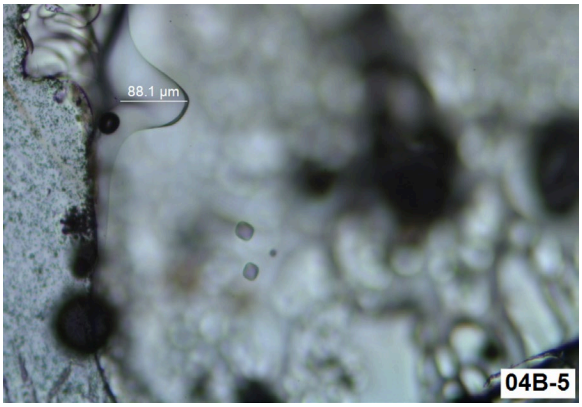

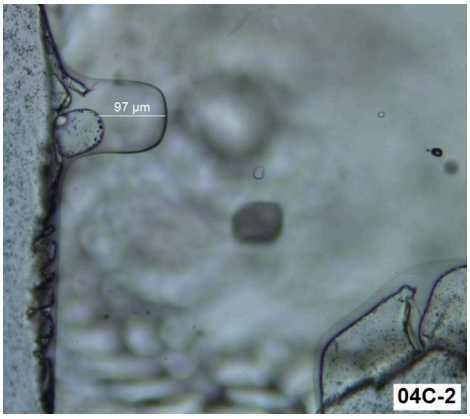
97 µm
04C-2

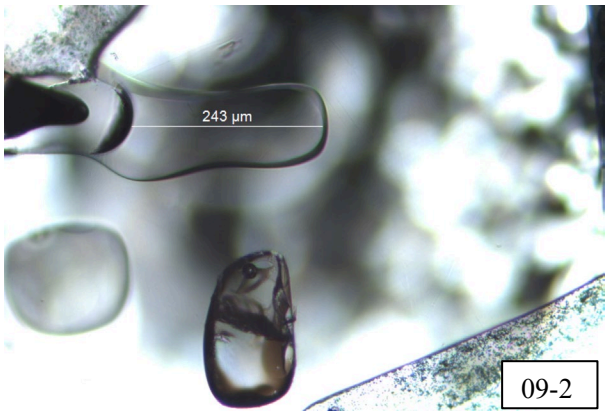
243 µm
09-2

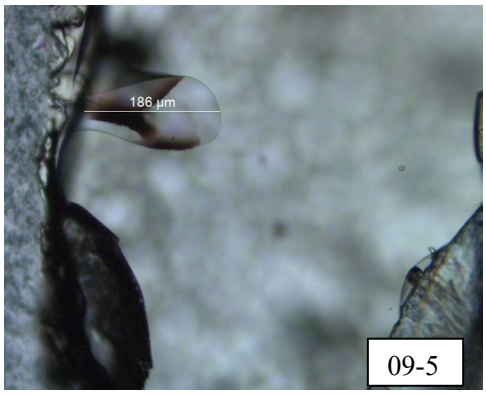
186 µm
09-5

Stratigraphy vs. Ascent

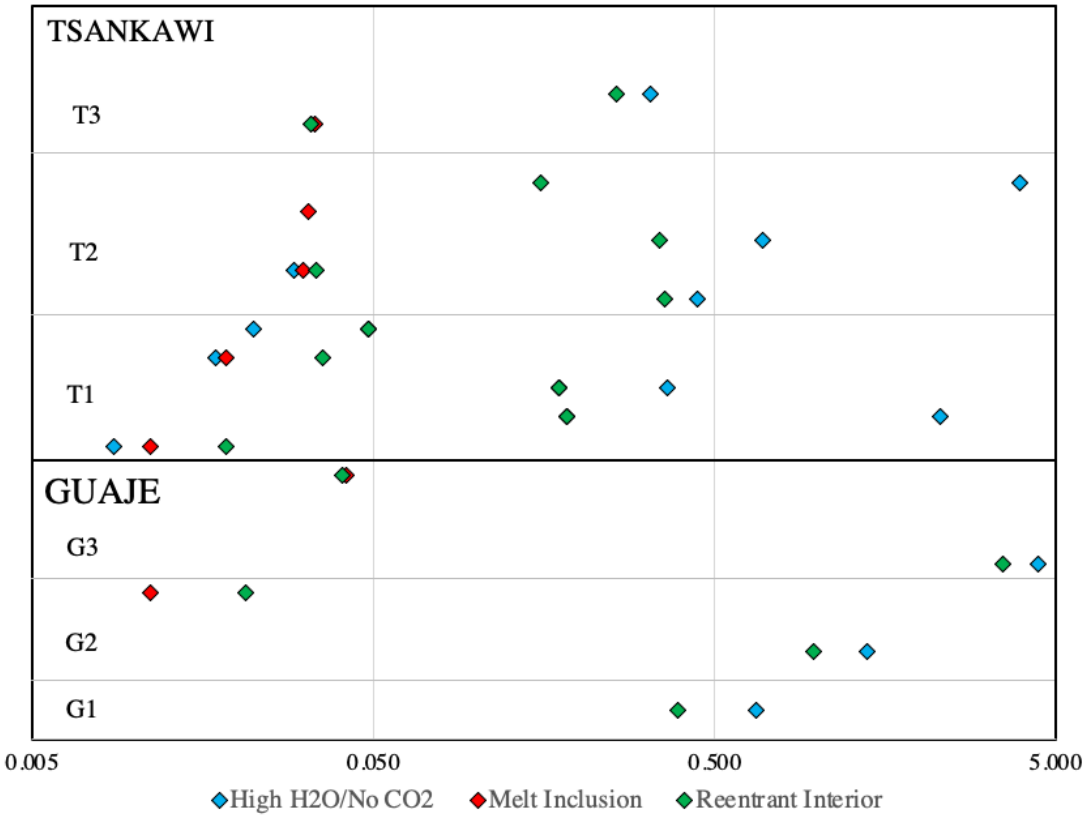

Stratigraphy vs. Misfit

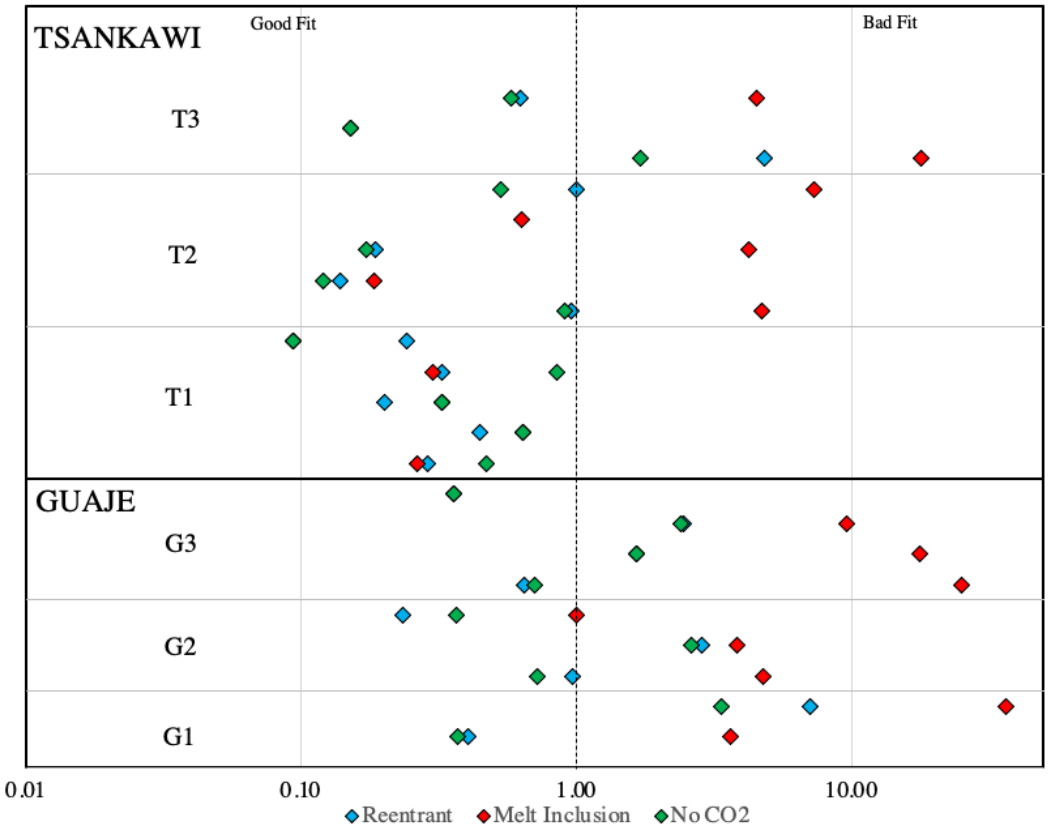

Supplementary Figure 2. (previous page) Comparison of stratigraphy vs. ascent rate (top) and stratigraphy vs. model misfit (bottom). Red = Melt Inclusion start, Blue = Reentrant Interior start, Green = High H_2O/No CO_2 start. Symbols falling to the right of the vertical dashed line indicate a "bad fit" (misfit > 1), symbols to the left of the dashed line indicate a "good fit" (misfit < 1). Note that the majority of samples in the Guaje fall into the "bad fit" while the majority of Tsankawi samples fall into the "good fit".

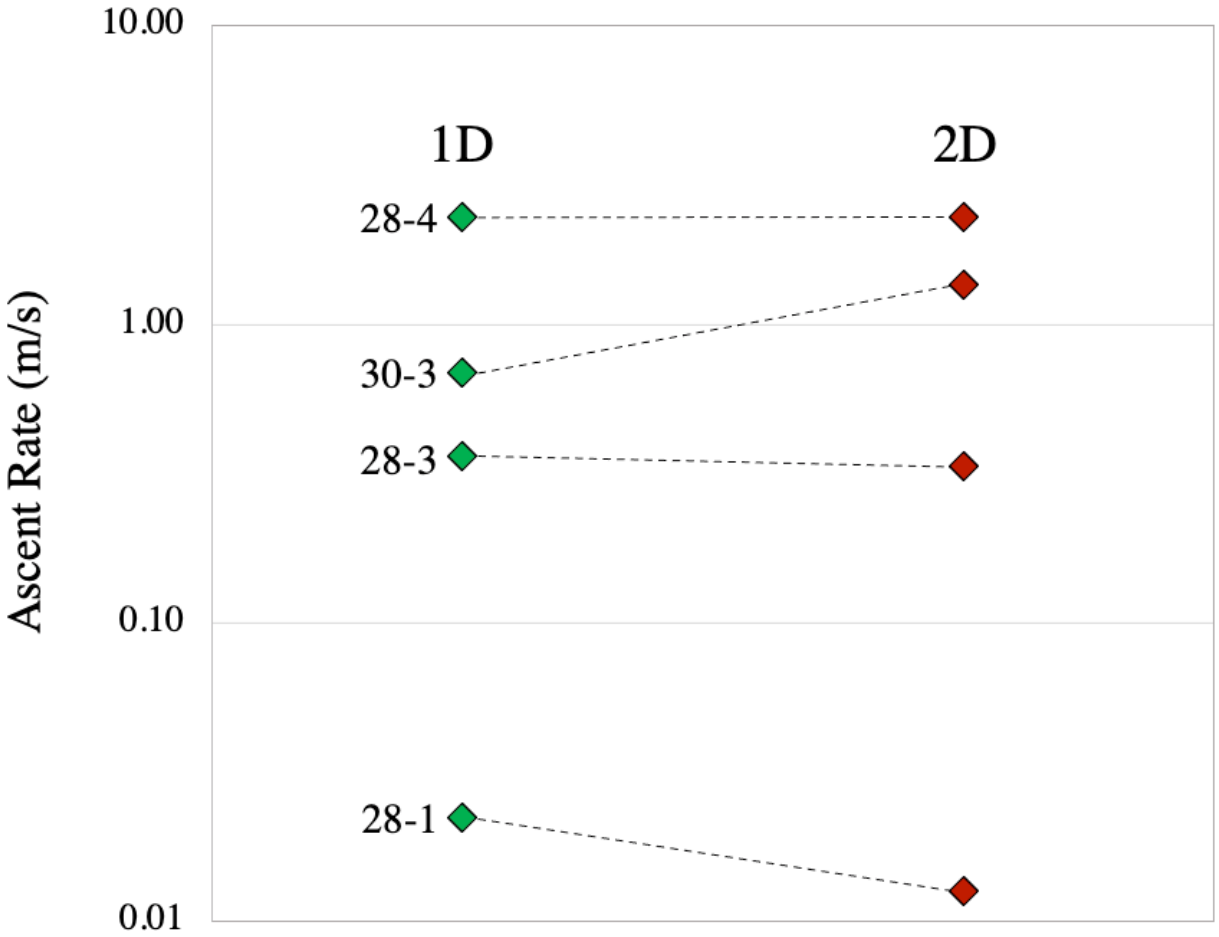

Supplementary Figure 3. Comparison of ascent rates between 1D and 2D diffusion modeling. Tie lines connect 1D and 2D results for each sample.

Tsankawi Embayment Water Profiles

28-1		
Distance from bubble	Water (wt.%)	Error ±
0	1.24	0.12
10	1.29	0.12
20	1.36	0.13
30	1.56	0.15
40	1.74	0.16
50	1.81	0.17
60	1.89	0.18
70	1.95	0.18
80	1.97	0.19
90	2.00	0.19
100	2.02	0.19
110	2.07	0.20

28-3		
Distance from bubble	Water (wt.%)	Error ±
0	1.19	0.10
10	1.84	0.15
20	2.07	0.17
30	2.15	0.18
40	2.18	0.18
50	2.28	0.19
60	2.28	0.19
70	2.42	0.20
80	2.42	0.20
90	2.46	0.20
100	2.52	0.21
110	2.58	0.21
120	2.60	0.22
130	2.51	0.21

28-2		
Distance from bubble	Water (wt.%)	Error ±
0	3.03	0.27
10	3.06	0.27
20	3.10	0.27
30	3.12	0.28
40	3.11	0.28
50	3.09	0.27
60	2.93	0.26
70	2.90	0.26
80	3.11	0.28
90	3.22	0.29
100	3.32	0.29
110	3.35	0.30
120	3.23	0.29
130	3.24	0.29
140	3.30	0.29
150	3.26	0.29
160	3.35	0.30
170	3.33	0.30
180	3.26	0.29
190	3.29	0.29
200	3.28	0.29
210	3.29	0.29
220	3.40	0.30
230	3.40	0.30
240	3.47	0.31
250	3.40	0.30
260	3.38	0.30
270	3.38	0.30
280	3.36	0.30
290	3.35	0.30
300	3.37	0.30
310	3.38	0.30
320	3.42	0.30

28-4		
Distance from bubble	Water (wt.%)	Error ±
0	1.67	0.13
10	1.95	0.16
20	2.42	0.20
30	2.49	0.20
40	2.70	0.22
50	2.68	0.22
60	2.74	0.22
70	2.83	0.23
80	2.65	0.22
90	2.88	0.23
100	2.80	0.23
110	2.76	0.22
120	2.84	0.23
130	2.83	0.23
140	2.59	0.21

33-1		
Distance from bubble	Water (wt.%)	Error ±
0	0.96	0.09
10	1.76	0.17
20	1.90	0.19
30	1.98	0.20
40	2.09	0.21
50	2.23	0.22
60	2.32	0.23
70	2.44	0.24
80	2.54	0.25
90	2.56	0.26
100	2.63	0.26
110	2.65	0.27
120	2.69	0.27
130	2.78	0.28
140	2.85	0.29
150	2.93	0.29
160	3.04	0.31
170	3.15	0.32
180	3.16	0.32
190	3.23	0.33
200	3.24	0.33
210	3.30	0.33

28-5		
Distance from bubble	Water (wt.%)	Error ±
0	1.74	0.19
10	1.78	0.20
20	1.85	0.20
30	1.88	0.21
40	1.93	0.21
50	2.13	0.23
60	2.07	0.23
70	2.10	0.23
80	2.08	0.23
90	2.09	0.23
100	1.77	0.19
110	1.83	0.20
120	1.92	0.21
130	2.00	0.22
140	2.06	0.23
150	2.12	0.23
160	2.13	0.23
170	2.02	0.22
180	2.10	0.23
190	2.14	0.23
200	2.11	0.23
210	2.18	0.24
220	2.15	0.24
230	2.22	0.24
240	2.22	0.24
250	2.22	0.24

33-2		
Distance from bubble	Water (wt.%)	Error ±
0	1.38	0.12
10	1.43	0.13
20	1.43	0.13
30	1.42	0.12
40	1.42	0.12
50	1.42	0.12
60	1.44	0.13
70	1.43	0.13
80	1.37	0.12

30-3		
Distance from bubble	Water (wt.%)	Error ±
0	2.56	0.20
10	2.64	0.21
20	3.16	0.25
30	3.31	0.26
40	3.41	0.27
50	3.54	0.28
60	3.52	0.28
70	3.65	0.29
80	3.67	0.29
90	3.78	0.30
100	3.79	0.30
110	3.93	0.31
120	4.04	0.32
130	4.12	0.33
140	4.06	0.32
150	4.03	0.32
160	4.31	0.34
170	4.16	0.33
180	4.13	0.33
190	4.24	0.34

30-2		
Distance from bubble	Water (wt.%)	Error ±
0	0.75	0.05
10	1.01	0.07
20	1.38	0.10
30	1.26	0.09
40	1.41	0.10
50	1.58	0.11
60	1.52	0.11
70	1.62	0.12
80	1.41	0.10
90	1.03	0.07

30-5		
Distance from bubble	Water (wt.%)	Error ±
0	2.46	0.22
10	2.64	0.23
20	2.80	0.25
30	2.95	0.26
40	3.01	0.27
50	3.13	0.28
60	3.23	0.29
70	3.37	0.30
80	3.39	0.30
90	3.38	0.30
100	3.43	0.31
110	3.30	0.29
120	3.41	0.30
130	3.55	0.32
140	3.64	0.33
150	3.92	0.35
160	4.07	0.37
170	4.02	0.36
180	4.25	0.38

33-3		
Distance from bubble	Water (wt.%)	Error ±
0	0.53	--
10	0.97	--
20	1.05	--
30	1.09	--
40	1.15	--
50	1.23	--
60	1.28	--
70	1.34	--
80	1.39	--
90	1.41	--

30-1		
Distance from bubble	Water (wt.%)	Error ±
0	2.98	0.28
10	3.14	0.30
20	3.16	0.30
30	3.29	0.31
40	3.49	0.33
50	3.45	0.33
60	3.57	0.34
70	3.48	0.33
80	3.61	0.35
90	3.51	0.34
100	3.63	0.35
110	3.57	0.34
120	3.67	0.35
130	3.64	0.35
140	3.65	0.35
150	3.55	0.34
160	3.67	0.35
170	3.76	0.36
180	3.66	0.35
190	3.23	0.31
200	3.72	0.36
210	3.74	0.36
220	3.67	0.35
230	3.56	0.34

30-4		
Distance from bubble	Water (wt.%)	Error ±
0	1.53	0.13
10	1.64	0.14
20	1.72	0.15
30	1.77	0.15
40	1.84	0.16
50	1.87	0.16
60	1.90	0.16
70	1.98	0.17
80	2.01	0.17
90	2.00	0.17
100	2.03	0.17
110	2.08	0.18
120	2.14	0.18
130	2.13	0.18
140	2.15	0.18
150	2.21	0.19
160	2.26	0.19
170	2.26	0.19
180	2.31	0.20
190	2.36	0.20
200	2.36	0.20
210	2.38	0.20
220	2.42	0.21
230	2.46	0.21
240	2.48	0.21
250	2.45	0.21

Guaje Embayment Water Transects

03A-3		
Distance from bubble	Water (wt.%)	Error ±
0	1.42	0.13
10	1.69	0.16
20	1.83	0.17
30	1.82	0.17
40	1.77	0.16
50	1.79	0.16
60	1.75	0.16
70	1.84	0.17
80	1.88	0.17
90	1.82	0.17
100	1.70	0.16
110	1.72	0.16
120	1.89	0.17
130	1.81	0.17
140	1.89	0.17
150	1.92	0.18
160	1.92	0.18
170	1.92	0.18
180	1.91	0.18
190	1.97	0.18
200	1.88	0.17
210	1.88	0.17
220	1.86	0.17
230	1.94	0.18
240	1.90	0.18

03B-4		
Distance from bubble	Water (wt.%)	Error ±
0	2.45	0.22
10	2.64	0.24
20	2.79	0.26
30	2.99	0.28
40	3.20	0.30
50	3.34	0.31
60	3.49	0.32
70	3.61	0.33
80	3.81	0.35
90	3.95	0.37
100	4.14	0.39
110	4.24	0.40
120	4.09	0.38

03A-4		
Distance from bubble	Water (wt.%)	Error ±
0	2.44	0.27
10	2.19	0.24
20	1.90	0.21
30	1.79	0.20
40	1.86	0.21
50	2.34	0.26
60	1.98	0.22
70	3.11	0.35
80	3.04	0.34
90	3.04	0.34
100	3.10	0.35
110	3.08	0.35
120	3.09	0.35
130	3.12	0.35
140	3.15	0.35
150	3.13	0.35
160	3.18	0.36
170	3.15	0.35
180	3.12	0.35
190	3.13	0.35
200	3.14	0.35
210	2.94	0.33

09-5		
Distance from bubble	Water (wt.%)	Error ±
0	2.20	0.22
10	2.44	0.24
20	2.63	0.26
30	2.86	0.29
40	3.06	0.31
50	3.18	0.32
60	3.31	0.33
70	3.43	0.35
80	3.51	0.35
90	3.60	0.36
100	3.68	0.37
110	3.75	0.38
120	3.82	0.39
130	3.90	0.39
140	3.94	0.40
150	3.97	0.40
160	4.03	0.41
170	4.07	0.41
180	4.11	0.42
190	3.50	0.35

04B-5		
Distance from bubble	Water (wt.%)	Error ±
0	2.90	0.36
10	3.05	0.35
20	3.17	0.34
30	3.28	0.32
40	3.42	0.31
50	3.58	0.29
60	3.73	0.28
70	3.86	0.27
80	4.02	0.26

04B-4		
Distance from bubble	Water (wt.%)	Error ±
0	2.40	0.20
10	2.63	0.22
20	2.72	0.23
30	2.97	0.25
40	3.20	0.28
50	3.17	0.27
60	3.44	0.30
70	3.61	0.31
80	3.62	0.31
90	3.73	0.32
100	3.97	0.34
110	3.77	0.33
120	4.17	0.36
130	4.06	0.35
140	4.32	0.38
150	4.65	0.41
160	4.99	0.44
170	4.95	0.44

04C-2		
Distance from bubble	Water (wt.%)	Error ±
0	2.63	0.22
10	2.99	0.25
20	3.24	0.27
30	3.46	0.29
40	3.68	0.31
50	3.85	0.32
60	4.00	0.34
70	4.12	0.35
80	4.19	0.35

09-2		
Distance from bubble	Water (wt.%)	Error ±
0	4.15	0.34
10	4.05	0.33
20	4.26	0.35
30	4.41	0.36
40	4.49	0.37
50	4.75	0.39
60	4.99	0.41
70	4.93	0.40
80	4.84	0.40
90	5.53	0.46
100	5.01	0.41
110	5.56	0.46
120	5.73	0.47
130	5.42	0.45
140	5.11	0.42
150	5.49	0.45
160	6.00	0.50
170	6.03	0.50
180	6.35	0.53
190	6.32	0.52
200	5.95	0.49
210	6.37	0.53
220	6.65	0.55
230	5.81	0.48

04B-3		
Distance from bubble	Water (wt.%)	Error ±
0	1.22	0.10
10	1.33	0.11
20	1.50	0.12
30	1.62	0.13
40	1.58	0.13
50	1.58	0.13
60	1.57	0.13
70	1.60	0.13
80	1.56	0.13
90	1.45	0.12
100	1.33	0.11

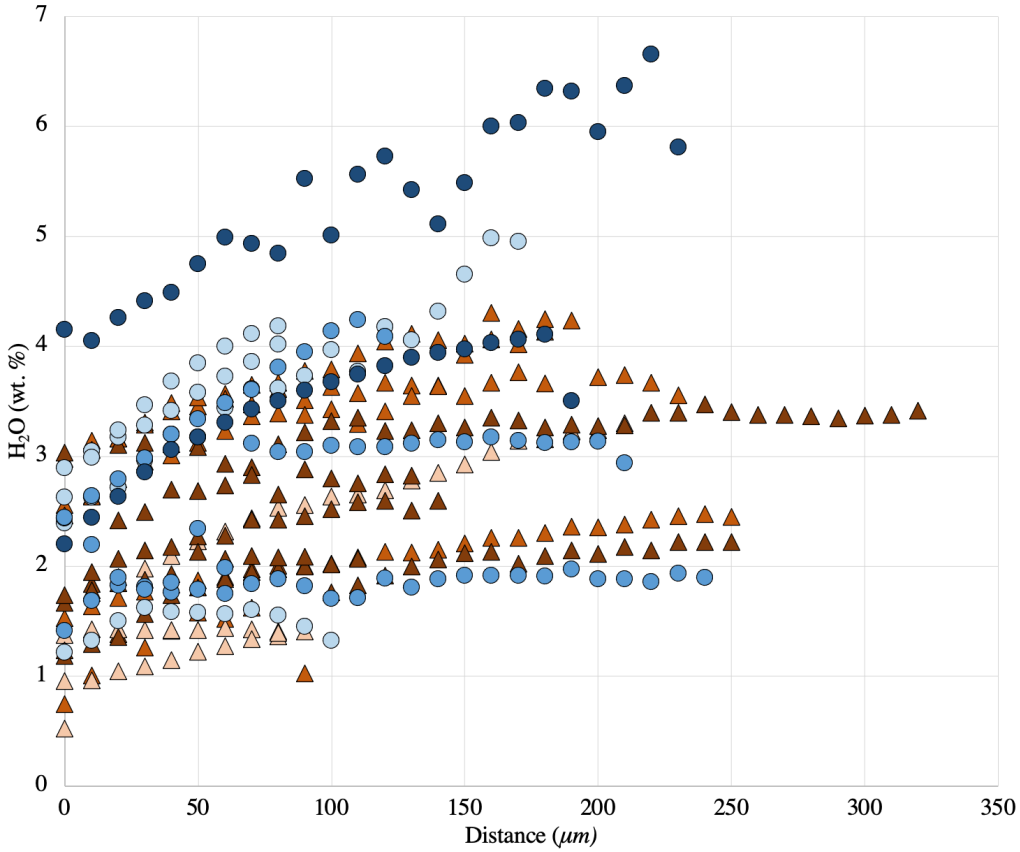

Supplementary Figure 4. Water transect date for all Tsankawi (orange triangles) and Guaje embayments (blue circles).

Supplementary Table 2. ICP-MS analyses and trace element concentrations

	Concentrations (ppm)																		
Sample	Li	Be	B	Na	Mg	Al	Si	P	K	Ca	Sc	**Ti**	V	Cr	Mn	Fe	Co	Ni	Cu	Zn
Interior	92.52		17.87	32911	546.36	117344	358384	95	27629	2750	0.85	**402**		4.56	770	11527		1.69	13.88	39.30
	95.73	36.00	16.34	35107	317.99	82245	358384	73	30826	4435		**396**		8.88	729	12504		1.69	3.99	166.59
	85.76	18.50	23.96	37515	319.48	82372	358384	51	33035	4047		**389**			698	12487	0.88			168.44
	81.14		18.10	37117	99.22	80229	358384	39	32896	3699		**380**			721	12312	1.02	0.07		148.34
	79.58		15.86	35829	94.68	79868	358384	74	33693	2968	3.62	**372**		14.07	695	12215		1.74		147.70
28-2	73.78	35.28	20.15	35322	78.96	78316	358384	49	34046	3248		**381**		49.78	723	12567		0.47		155.43
	75.93	25.08	19.06	36370	140.26	80394	358384	59	35046	2960		**430**		4.96	712	12844				144.58
	73.55		19.58	34005	233.36	80684	358384	49	33458	2076		**381**			711	12033		0.94		160.21
	74.54		20.85	32806		79824	358384	71	32999	4793		**374**			701	12135	0.18	1.54		150.54
	71.28	6.32	22.68	35242	166.29	80595	358384	59	34390	3611		**402**			704	12248		1.04		160.55
Rim	71.78		16.39	35866	103.23	79924	358384	82	32301	4074		**392**	0.13	20.76	705	11931			1.89	128.21
Interior	104.17		22.10	35062	178.76	79764	358384	26	35848	4208	3.98	**401**			717	12451		0.34	1.12	155.14
	102.78		23.82	32631	119.72	79049	358384	33	36681	3512	2.39	**400**			676	12137		0.09		126.95
	99.24		21.11	34692	0.61	84089	358384	46	39432	4112		**423**		10.41	722	12668	1.29			150.27
	93.57		22.61	33131		77135	358384	36	35271	2788		**389**		34.95	675	11618				132.07
	90.29	23.33	12.62	32873	214.29	81727	358384	36	36393	3728		**385**		1.44	703	12944				131.21
28-4	93.12		22.84	33562		77987	358384	63	37823	4356		**405**			694	12228		1.95		146.75
	88.46		23.61	32752		78968	358384	37	37571	3378		**399**			688	12393		0.07	1.25	139.03
	90.76		27.03	32558	206.99	78890	358384	49	38201	3691		**408**			686	12189	0.67	1.04		151.48
	90.76		20.98	35455		79983	358384	65	37593	5118		**390**			708	12575				141.56
	87.40		22.36	33251		75721	358384	59	38503	3429	5.50	**396**	0.96	36.26	690	11902	0.35	1.20		152.39
Rim	91.51		18.11	34207		79264	358384	52	38085	4937		**384**		5.10	707	12112		0.63	1.14	149.96
Interior	77.08	6.75	14.05	35398	239.05	81250	358384	23	35574	4793		**386**	0.60		709	12320	0.09	1.04		137.55
	72.06		24.82	34397		76173	358384	85	33292	4350		**381**	0.83	2.68	670	11910				146.01
	73.51		15.97	34467	134.57	77789	358384	76	34494	3878		**398**			701	12012				141.23
	73.84		17.21	35236		77786	358384	42	34256	2996		**384**			676	12202	0.07	0.31		135.95
28-3	68.10		23.55	34492	136.27	82062	358384	40	34265	4460		**408**	0.58		682	12698		0.65		125.94
	68.81		19.52	32336		71013	325799	56	32452	3655	2.40	**388**	0.20	12.06	652	11169	0.08			120.10
	65.29		16.75	31520	179.32	71805	325799	29	31233	3504		**341**			643	10932		0.06		134.26
	70.69	5.79	16.26	29562	121.05	74559	325799	52	31932	3217		**365**			641	11171		0.35		134.47
	65.67		19.15	30365	235.42	71278	325799	47	31256	2553	2.43	**362**		13.33	629	11531				140.57
Rim	69.84	6.26	22.62	34224	198.64	76600	358384	63	33190	4649	6.51	**359**	0.81		700	11921		0.60		133.35

Supplementary Table 2 (continued). ICP-MS analyses and trace element concentrations

	Concentrations (ppm)																		
Sample	Li	Be	B	Na	Mg	Al	Si	P	K	Ca	Sc	Ti	V	Cr	Mn	Fe	Co	Ni	Cu	Zn
Interior	116.05		17.69	36296		77657	358384	27	32651	3514		374			687	12023	0.58		0.52	159.91
	107.35		21.63	33712	52.78	77898	353377	58	33205	4127		377			686	12077		0.63		139.53
	104.97		19.50	34664	48.20	76661	353377	62	34208	3669	2.84	397			690	12239	0.14	2.10		149.47
	90.77		21.01	33592	17.52	75396	353377	53	33287	4182		381	0.19	18.75	666	11873		1.07		143.05
	98.30	15.90	21.16	33411	53.02	73666	353377	50	33682	3390		376	0.15		653	11644		0.65		121.79
	77.47	23.64	18.59	27861	72.96	64547	297753	40	29006	2360		316			571	9977		3.47		113.87
	77.81		16.78	27851	92.64	65010	297753	36	28909	3297		324		4.03	573	10138		0.98	0.89	107.66
28-5	73.03		18.35	28504		64328	297753	33	28888	3235		290			556	10100		1.45		109.78
	74.51		14.26	29559		65328	297753	30	29754	2992		323			601	10064				119.79
	58.54		17.55	23163	4.98	52138	244092	56	23285	2628	3.30	271			457	8295		0.93		90.51
	56.60		12.78	23130	194.44	54441	244092	19	24902	2678		269		1.08	472	8178	0.12			95.69
	58.23		12.00	22380	81.69	52539	244092	42	25082	2567		265		0.19	464	7753				94.47
	85.10		28.19	33892	55.46	79418	358384	50	37325	4039	2.13	372		29.14	704	12396			0.95	136.90
	63.23		11.47	25331	52.35	61356	273914	23	26318	3008		280	0.36		518	9020	0.60			96.27
Rim	62.47		18.96	26024	139.06	58351	273914	42	27723	3152		290	0.97	11.51	529	9242		0.11	0.20	102.23
Interior	100.88		26.05	35984		56354	358384	71	33640	3788		422		3.86	719	12703			2.23	163.25
	94.68		17.78	35832	8.33	55705	358384	86	38279	3304		400		3.37	648	11784		1.01		167.45
	95.85	13.25	21.34	33640	35.91	56130	358384	95	32849	3623		356			647	12062		1.72		145.05
	96.78		25.34	34797	116.63	53519	358384	76	35529	3318		348		6.88	643	11615		0.59		166.83
30-5	95.84		23.42	34306		56709	358384	72	36242	4021	0.24	357			653	12418	0.07			164.11
	94.67	26.61	30.44	35251		56381	358384	61	34472	3507		390			639	12075	0.16		2.07	170.53
	96.00		22.16	36610	208.07	58472	358384	102	37707	3999		385	0.95	7.66	652	12478		4.19		166.02
	92.98		17.82	37030	105.72	56967	358384	64	37664	3813		364		33.32	649	11592	1.27	2.79		143.36
	93.30		21.30	35589	155.71	59197	358384	97	38515	3115		400			625	12225	0.64	0.30		150.39
Rim	96.02		19.75	36740	40.43	55689	358384	71	35745	3922	3.17	370	0.53	14.92	656	12067			1.43	158.65
Interior	121.56		19.29	33845		63267	358384	49	35394	3941		384	0.87		682	12293			2.58	157.75
	114.80		27.87	35575	45.30	58517	358384	121	38107	3364		366		3.22	661	11863		4.00		167.35
	108.83	2.89	29.38	33447		62630	358384	69	40558	4023		377			675	11723		0.23		144.43
	109.03		29.40	36938	48.45	67939	358384	100	39762	4208	1.05	367			672	12706		1.15		156.77
	99.57		22.43	34689	145.93	61711	358384	55	36789	4150	3.84	391			651	11858		1.33		161.98
30-3	101.60		19.26	35301	81.99	58550	358384	89	41231	3391		405			669	11737	0.47	0.98		152.31
	96.30		31.91	34552	19.76	61942	358384	114	43997	3465	4.13	375		22.77	667	12529		1.45		146.21
	96.59		22.86	35736		64237	358384	111	41938	4346		376		22.21	676	12019				159.43
	96.25		28.92	33707		60463	358384	93	37659	4288		399			642	12065	0.33			173.27
	92.70		23.11	35523	69.43	56640	358384	84	40241	3415	3.63	377			666	11157		2.28		140.53
	94.88		26.37	34328	59.57	63615	358384	98	38040	4073	0.14	396	0.42		666	12101		1.54		149.05
Rim	97.09		25.21	37282	127.78	65313	358384	91	40439	4025	6.96	366			670	12395		0.30	0.64	146.50

Supplementary Table 2 (continued). ICP-MS analyses and trace element concentrations

	Concentrations (ppm)																			
Sample	Li	Be	B	Na	Mg	Al	Si	P	K	Ca	Sc	Ti	V	Cr	Mn	Fe	Co	Ni	Cu	Zn
Interior	115.29		24.98	34493	12.27	61986	358384	85	37456	3450		310			702	12004				142.64
	91.21		22.91	32273	78.79	52877	325799	70	34179	3717		284		16.66	609	10161		1.36		125.05
	85.02		21.44	30738		50206	325799	57	35263	2227		277			597	10383				114.15
	84.66		16.53	32722		53272	325799	82	37077	3193		302	0.23	14.94	632	10175		0.61		128.15
09-5	83.23		25.66	32427	24.60	54983	325799	64	35694	2414		324			644	11146		0.77		118.76
	80.00		19.56	33045		56928	358384	61	38812	4038	2.50	317			647	10969	1.05			140.02
	81.74	35.33	15.38	35011	17.59	56025	358384	67	37323	3467	0.66	331			678	11453				136.16
	79.62		16.32	35084		60049	358384	93	41601	3353		312			669	11568	0.08	1.14	0.14	127.20
	84.00	31.56	23.82	35304		60655	358384	96	43155	3529		315		6.99	708	12253		4.47		127.14
Rim	78.84		21.27	34775	158.28	54642	353377	79	39393	2183		333		13.54	661	11693				150.40
Interior	76.35	21.00	17.03	26182	121.94	45369	297753	60	35962	2687		284		20.81	589	9695	0.95	0.92		119.78
	59.08	5.51	13.38	21143	67.35	34472	244092	54	26970	2471		233			450	7725		0.39		88.03
	62.53		14.92	23427		38945	244092	67	29538	2739		227		0.78	431	7622		1.67		107.01
	66.65		16.08	27693	50.61	41994	273914	82	32566	2884		242		6.14	506	8847		1.30		92.82
03A-3	72.43		19.06	27856	58.18	44575	273914	61	31624	3105		267		0.33	536	8829		3.01		101.37
	93.75		23.82	36232	98.31	55789	358384	82	42452	3934	6.72	377			680	11634				150.16
	85.38		21.80	35129	54.68	60140	358384	87	42368	3737		325			686	11868	0.20			131.65
	92.12	44.89	22.75	33320		58475	358384	63	41010	3352		319			683	11598		1.01		147.43
	91.73		23.35	34019		59153	358384	92	38869	4122	3.10	371			702	12044				153.47
Rim	83.90		17.39	32708	57.12	59707	358384	71	40692	3621	0.52	315		30.46	684	11326				108.77
Interior	114.70		24.83	35150	57.84	60340	358384	63	36062	3358	5.78	333		11.37	812	12101		0.64		120.16
	99.77		20.70	39421		55897	358384	70	37030	3374	1.12	308			690	11645		0.19		136.54
03B-4	84.03		19.75	34338		58631	358384	82	35273	3873	1.52	312			653	10867	0.32	5.66		143.37
	69.39		21.50	37192	77.78	56832	358384	105	38644	3050		352			687	11964				147.39
Rim	58.23		15.68	38766	33.50	55198	358384	86	38008	3440		333		2.58	673	11624		1.65		120.30

Supplementary Table 2 (continued). ICP-MS analyses and trace element concentrations

	Concentrations (ppm)																		
Sample	Li	Be	B	Na	Mg	Al	Si	P	K	Ca	Sc	Ti	V	Cr	Mn	Fe	Co	Ni	Cu	Zn
Interior	74.68		10.06	30902	142.54	98339	358384	68	33926	4677		468	0.51		703	11799				40.63
	87.46		13.18	35763	36.89	62525	358384	72	37031	4129		401		2.36	598	11550		2.87		94.67
04C-2	83.46		8.72	35421	22.81	63328	358384	81	38306	3362		388			588	10404				127.54
	80.58		13.98	32185		64872	358384	44	43648	3147	13.58	372		9.39	587	11248				104.03
	77.30		14.77	32630		60971	358384	65	35795	3460		395		43.28	590	10782		1.19		108.19
Rim	70.06		14.35	32596	162.58	62188	358384	64	39476	3649	8.01	345		52.95	572	10471				113.10
Interior	107.40		18.83	34597	309.13	64996	358384	58	36824	4288		387	0.89	19.68	675	11425		3.15		123.14
	106.60		20.37	36130		64090	358384	77	40205	3215		370		4.21	647	11229		1.25		122.23
04B-3	103.45		14.11	31874		60246	358384	29	39306	2857	4.09	356			663	10848	0.36	0.86		124.86
	99.55		15.40	32595		65696	358384	46	40777	3492		369	0.47	17.76	631	11148		0.04		116.18
	94.55		20.75	31506		59795	358384	61	39027	3140	2.88	331		70.22	596	10747				123.76
Rim	88.68		22.03	33398		62680	358384	54	39913	3736		369		46.80	629	11217		2.91		124.34

Supplementary Table 2 (continued). ICP-MS analyses and trace element concentrations

	Concentrations (ppm)																			
Sample	Ga	Rb	Sr	Y	Zr	Nb	Cs	Ba	La	Ce	Pr	Nd	Sm	Eu	Gd	Tb	Dy	Ho	Er	Tm	Yb
Interior	24.61	286.86	8.29	283.94	764.60	228.28	10.36	22.92	77.77	102.36	15.67	68.07	20.93	0.10	26.75	5.60	37.89	8.32	28.14	4.23	26.09
	27.42	300.01	6.29	160.69	475.03	230.09	12.18	19.49	58.71	98.27	11.23	43.04	12.04	0.05	15.46	3.18	26.29	5.25	15.33	2.60	18.00
	26.96	326.68	6.30	160.47	470.63	237.72	11.40	17.86	60.13	103.91	12.41	47.35	11.71	0.05	15.26	3.05	25.20	5.51	15.63	2.50	16.22
	28.24	320.29	5.82	163.85	470.50	238.19	11.16	16.04	58.17	105.40	11.65	43.11	13.18	0.07	15.82	2.93	23.56	5.64	15.37	2.51	17.63
	25.71	313.45	6.30	168.79	467.72	227.16	11.85	19.44	59.55	104.58	10.92	44.72	13.70	0.02	15.98	3.05	23.70	5.07	17.60	2.46	16.12
28-2	26.04	325.29	6.55	164.66	456.27	222.89	12.07	18.39	54.10	98.08	11.58	40.20	11.51	0.01	15.06	2.88	24.83	5.28	16.57	2.66	17.41
	26.77	328.28	6.36	168.49	493.76	238.38	11.86	20.29	59.50	105.92	11.80	46.24	12.89	0.05	15.63	3.15	26.09	5.55	16.03	2.67	17.00
	26.49	319.93	6.39	166.81	479.53	230.91	11.12	20.10	56.22	104.81	12.37	46.25	13.18	0.01	15.16	3.14	24.40	5.23	16.10	2.97	14.80
	26.03	320.62	5.71	169.72	486.37	231.83	12.08	18.11	58.20	98.72	11.87	47.54	12.82	0.08	17.50	3.51	26.14	5.90	16.96	2.73	16.02
	25.27	326.04	6.48	168.05	479.19	232.53	11.99	15.91	57.98	103.37	11.60	45.99	12.94	0.03	15.86	3.19	23.64	5.09	16.52	2.76	16.68
Rim	25.72	314.79	5.95	166.94	487.37	224.49	11.82	16.37	55.60	101.67	11.78	44.01	12.78		17.99	3.34	23.32	5.14	16.92	2.64	15.87
Interior	26.09	299.68	7.65	170.09	464.59	235.57	11.52	21.08	55.11	108.54	11.83	46.77	12.29	0.03	15.56	3.05	24.49	4.87	14.34	2.57	16.80
	25.91	306.49	8.29	156.29	447.02	222.06	10.95	22.33	57.00	102.98	11.42	41.11	12.26	0.01	15.74	3.16	22.84	4.99	15.40	2.37	15.18
	27.62	330.06	6.94	172.44	486.61	238.00	12.46	19.54	61.87	111.66	12.63	44.16	13.92	0.04	17.60	3.49	23.91	5.63	15.49	2.22	14.96
	26.00	306.65	8.13	163.09	450.99	226.86	11.40	21.71	56.79	101.14	10.93	45.47	12.04	0.03	15.85	3.02	24.47	5.05	15.08	2.76	16.29
	25.73	313.33	7.35	160.41	455.12	229.07	11.35	23.01	56.53	108.75	11.70	41.06	11.27	0.03	14.72	3.31	24.87	5.20	16.30	2.26	16.03
28-4	27.46	332.75	7.76	167.83	485.50	245.19	11.89	22.53	58.84	109.68	11.89	45.06	12.60	0.01	16.09	3.38	25.31	5.28	16.42	2.25	15.92
	26.20	324.34	7.42	172.20	473.86	235.30	11.39	22.87	59.80	106.72	11.53	44.88	13.48	0.07	16.33	3.40	24.14	5.49	15.52	2.45	16.88
	27.52	327.49	7.22	162.36	482.93	233.36	11.65	21.49	59.37	109.74	11.90	44.85	14.52		14.20	3.34	22.62	5.53	15.68	2.76	16.49
	28.82	337.23	7.07	169.46	481.38	235.60	11.84	23.95	59.76	107.19	12.14	43.62	12.52	0.04	18.73	3.13	22.49	4.92	14.94	2.62	16.30
	26.82	332.31	6.74	160.39	467.73	232.69	11.18	19.95	58.39	106.65	11.90	42.47	14.51		15.73	3.16	25.12	5.26	15.43	2.38	14.84
Rim	26.47	337.82	7.91	161.98	479.49	239.05	12.38	24.92	60.40	109.51	12.22	41.83	12.77		17.47	3.54	24.26	5.13	15.80	2.60	15.47
Interior	27.79	329.48	5.82	174.52	509.54	244.43	11.56	19.52	61.13	113.24	12.35	47.39	15.29	0.03	16.05	3.60	27.18	5.71	17.44	2.58	17.46
	25.58	325.57	5.26	168.72	486.39	233.88	11.37	16.23	57.62	107.57	11.45	46.00	11.82	0.05	15.43	3.19	23.60	5.49	15.92	2.68	17.25
	26.92	321.67	6.00	172.92	493.74	236.82	11.63	22.32	60.97	108.32	11.90	43.11	13.83	0.04	17.87	3.57	25.58	5.54	16.67	2.57	17.22
	26.72	309.93	5.72	169.75	480.66	240.16	11.21	16.09	57.65	110.79	12.56	45.86	13.01		14.40	3.45	23.87	5.65	16.57	2.51	16.58
28-3	26.15	328.11	5.61	171.58	500.87	239.60	11.05	21.15	58.10	111.51	12.44	43.97	12.38		17.94	3.68	25.18	5.43	16.77	2.86	16.53
	25.66	303.38	5.84	163.57	456.94	224.05	10.36	16.27	56.68	100.55	11.37	41.15	12.15		15.50	3.09	23.89	5.23	16.49	2.57	15.43
	24.00	291.08	5.60	157.96	458.06	221.06	10.41	17.29	51.99	96.43	11.26	43.87	11.41		13.86	2.75	23.44	4.70	15.71	2.63	14.33
	23.30	288.65	5.46	156.14	456.34	213.11	10.60	16.58	57.04	99.70	11.65	41.12	11.57	0.00	15.77	3.32	22.37	5.12	15.47	2.60	14.70
	25.09	285.67	5.69	152.31	452.83	214.01	10.83	17.48	55.42	100.44	11.30	42.52	11.56	0.03	15.66	2.86	21.37	4.76	12.94	2.40	14.97
Rim	27.13	337.10	5.97	170.25	515.74	238.69	11.85	20.65	58.37	110.56	12.80	47.29	11.82		18.81	2.86	23.85	5.35	16.41	2.60	16.45

Supplementary Table 2 (continued). ICP-MS analyses and trace element concentrations

	Concentrations (ppm)																			
Sample	Ga	Rb	Sr	Y	Zr	Nb	Cs	Ba	La	Ce	Pr	Nd	Sm	Eu	Gd	Tb	Dy	Ho	Er	Tm	Yb
Interior	28.44	317.53	6.36	166.32	466.92	231.97	11.01	22.15	58.06	109.76	12.43	42.89	13.01		15.27	3.26	25.47	5.20	16.65	2.43	15.51
	28.27	307.15	6.64	159.56	467.08	235.97	11.58	21.56	59.29	107.79	11.51	45.83	13.06	0.00	14.82	2.85	23.99	4.87	16.07	2.40	15.50
	26.48	303.47	6.14	156.20	457.26	231.43	11.18	17.84	54.92	108.17	11.87	39.23	12.12		16.50	2.91	23.01	5.19	15.86	2.36	15.06
	26.08	309.37	6.49	158.44	459.76	223.38	11.66	17.84	54.64	111.20	12.23	43.67	11.37		14.97	3.08	20.75	4.96	15.21	2.34	16.20
	25.98	309.84	5.89	153.33	439.82	229.69	11.88	17.78	54.05	104.68	11.43	46.45	12.95		15.20	3.31	23.45	4.85	16.66	2.46	14.62
	23.35	262.17	5.90	135.27	385.36	193.52	10.01	17.26	48.60	91.69	10.18	38.14	8.87	0.02	12.36	2.70	21.16	3.98	12.12	2.25	14.05
	22.58	270.25	5.34	134.47	390.10	189.49	9.79	16.18	49.22	89.85	10.08	37.93	10.78	0.00	12.84	2.67	19.99	4.46	12.42	2.19	12.61
28-5	21.63	259.83	4.73	131.56	386.21	186.47	9.53	15.51	47.05	89.66	9.49	35.47	10.82		12.81	2.54	18.80	4.49	13.48	2.17	12.68
	22.76	285.35	5.60	141.51	409.60	202.01	10.35	18.68	50.09	95.08	10.36	39.65	10.42		13.13	2.57	19.82	5.00	12.46	2.10	13.69
	17.78	221.33	4.51	114.49	326.37	160.52	7.73	13.10	41.56	76.00	8.35	32.78	8.04		12.01	2.49	17.36	3.80	11.36	1.92	10.91
	18.46	227.82	5.02	119.03	347.90	164.83	7.79	13.57	42.06	75.91	8.45	31.57	9.38		10.24	2.26	16.71	3.53	11.09	2.06	11.75
	17.24	221.09	4.59	112.34	337.08	164.64	7.62	14.00	42.86	74.61	8.35	33.28	7.44	0.02	12.20	2.11	16.17	3.83	12.30	2.04	10.68
	27.64	334.20	6.93	173.87	505.60	236.01	11.83	20.34	60.04	116.35	12.36	45.91	11.26		15.22	3.43	27.93	5.28	17.41	2.48	17.57
	20.90	243.20	5.02	127.49	366.52	178.73	8.61	13.92	46.22	85.75	9.25	34.22	9.94	0.00	12.27	2.37	18.91	4.07	13.14	1.96	11.82
Rim	20.08	252.97	5.28	131.66	373.63	187.66	9.19	15.22	45.53	82.63	9.76	33.84	10.55	0.04	10.92	2.61	19.45	4.09	13.95	2.06	12.97
Interior	30.55	344.49	7.97	94.54	313.04	221.21	13.45	27.09	37.10	96.66	8.63	28.95	8.67		8.33	1.88	13.70	3.26	8.38	1.15	9.42
	29.97	363.67	7.74	91.32	293.96	216.57	12.76	24.21	38.13	96.75	8.78	25.91	8.00		7.89	2.17	13.53	2.47	10.18	1.28	8.70
	29.36	355.94	8.25	94.02	297.50	222.38	12.96	25.30	38.12	94.24	8.27	27.68	7.20	0.04	9.08	1.95	12.34	3.00	8.90	1.14	9.42
	31.10	337.15	8.20	92.38	288.21	210.96	12.73	24.73	37.38	92.42	8.11	26.50	7.63	0.01	8.85	1.91	12.95	3.05	8.68	1.44	9.31
30-5	30.38	362.83	8.62	99.64	308.92	218.80	12.97	25.76	40.39	96.85	8.14	28.00	9.36		8.50	1.75	13.31	3.29	9.59	1.38	9.49
	31.63	364.79	8.71	94.74	311.91	225.62	13.63	26.95	39.70	98.03	8.40	27.84	6.90	0.04	9.68	2.16	13.43	3.21	9.38	1.63	10.51
	32.31	363.75	6.91	95.28	318.42	223.33	12.39	26.49	37.21	98.62	8.25	30.88	7.69		7.37	1.52	14.73	3.13	9.31	1.40	9.33
	30.86	358.15	7.42	99.54	307.94	218.69	12.64	29.97	37.62	96.90	8.43	28.97	9.29		9.67	1.93	15.06	3.33	8.08	1.34	10.04
	30.74	360.40	8.01	93.68	311.71	219.25	12.54	23.76	36.40	97.12	7.99	25.73	8.16	0.02	8.04	2.15	15.25	2.55	8.98	1.27	9.30
Rim	30.66	364.69	8.31	93.46	298.75	216.35	13.49	25.30	39.25	99.62	8.41	28.11	7.74	0.02	9.08	2.05	15.11	3.07	8.47	1.42	9.97
Interior	29.06	342.81	9.47	105.76	344.22	226.11	12.08	23.84	44.59	105.68	9.79	33.81	8.86		11.15	1.91	14.85	3.22	10.45	2.00	11.14
	30.17	337.90	8.88	105.51	327.43	211.35	12.34	22.00	43.64	104.11	9.23	31.25	8.03		9.66	2.16	15.47	3.52	10.50	1.87	10.86
	29.71	333.02	8.63	103.27	325.88	231.85	12.88	31.96	44.10	103.68	9.89	33.72	8.54		10.55	2.13	16.45	3.53	10.20	1.70	10.22
	30.98	352.93	9.25	105.96	349.19	232.23	13.27	30.01	44.76	110.02	9.55	30.08	8.96		11.64	2.09	16.77	3.72	11.07	1.73	10.59
	26.35	347.81	8.66	105.57	332.41	220.61	12.87	24.12	45.46	104.49	9.54	32.50	10.93		9.87	1.68	14.73	3.35	10.97	1.62	9.86
30-3	29.66	363.36	8.60	104.00	338.72	227.02	13.03	29.68	43.41	101.44	9.27	32.60	7.55		10.77	2.07	16.39	3.74	10.32	1.50	11.38
	30.14	363.36	9.41	105.49	350.34	225.51	13.03	27.79	45.23	106.83	9.64	34.25	8.59	0.01	9.76	2.20	16.03	3.19	10.79	1.84	12.23
	30.30	361.18	8.97	106.50	339.40	221.52	12.30	30.87	43.22	101.07	9.84	34.76	9.09	0.02	10.58	2.18	14.68	3.17	12.26	1.54	10.27
	30.14	353.19	8.12	105.61	327.37	218.02	12.27	28.97	44.85	100.82	9.44	32.17	9.60		11.04	2.22	15.77	3.14	10.56	1.49	10.84
	29.52	349.99	9.49	109.97	331.82	217.98	12.68	29.67	42.55	101.69	8.81	32.02	7.33		10.26	2.17	14.87	3.38	9.68	2.04	10.54
	30.27	354.75	8.99	108.44	344.12	222.87	12.87	25.50	43.97	102.03	9.56	33.33	8.34		9.61	2.17	16.04	3.39	12.86	1.99	12.32
Rim	28.63	371.18	9.04	111.37	352.90	224.66	12.68	27.31	43.18	104.51	9.34	32.38	8.60		10.30	1.92	14.97	3.38	12.56	1.77	11.37

Supplementary Table 2 (continued). ICP-MS analyses and trace element concentrations

	Concentrations (ppm)																			
Sample	Ga	Rb	Sr	Y	Zr	Nb	Cs	Ba	La	Ce	Pr	Nd	Sm	Eu	Gd	Tb	Dy	Ho	Er	Tm	Yb
Interior	29.21	356.04	0.33	95.23	278.13	255.70	13.33		30.05	82.94	7.64	31.43	9.53		10.23	2.36	15.45	3.66	8.50	1.38	10.03
	25.01	317.67	0.26	80.76	250.57	231.37	11.96		25.32	73.45	7.50	27.20	9.54	0.00	8.95	1.66	13.43	2.83	8.00	1.06	7.85
	24.87	336.04	0.35	88.93	250.56	236.50	12.02		27.25	77.56	7.75	24.79	8.73		8.18	1.66	13.08	2.78	7.34	1.24	8.39
	27.45	350.54	0.30	88.62	255.14	233.46	12.64		27.25	78.33	7.19	27.60	7.07		8.92	1.76	11.95	3.16	8.22	1.52	8.24
09-5	26.78	373.56	0.18	88.29	265.00	245.02	12.18		28.12	80.02	7.48	27.42	9.18		10.60	1.86	14.17	3.15	8.97	1.09	8.28
	28.08	392.32	0.19	93.60	268.52	262.51	13.60		29.53	83.78	7.99	31.80	8.29		10.56	2.05	13.52	2.87	9.86	1.31	9.56
	31.16	400.76	0.18	97.60	275.58	267.42	13.23		30.79	82.77	8.30	33.41	8.20		9.53	1.98	14.09	2.79	8.07	1.62	9.49
	28.35	401.65	0.17	93.71	288.26	260.94	13.88		29.99	87.37	8.23	26.98	10.02		12.28	2.01	14.01	2.95	9.22	1.23	9.65
	29.33	411.58	0.31	95.71	276.80	285.02	13.84		31.54	88.78	8.86	30.67	8.83		10.99	1.99	16.00	2.87	9.33	1.46	8.45
Rim	29.76	418.48	0.40	92.66	268.84	261.50	12.07		29.33	84.08	8.54	29.61	7.11		10.27	1.87	13.44	3.03	9.41	1.54	9.26
Interior	23.76	319.93	0.29	85.83	228.76	216.12	11.03		27.06	78.17	7.52	31.67	8.98		9.78	1.68	14.01	2.47	8.74	1.26	7.35
	18.10	260.52	0.15	58.79	175.28	169.58	8.72		21.76	59.45	5.38	21.24	5.80		6.49	1.25	8.17	1.88	5.06	0.92	5.96
	19.59	274.81	0.12	62.09	173.47	170.17	9.05		22.37	60.43	5.43	21.08	6.51		7.53	1.40	10.04	2.07	5.59	0.94	6.36
	22.44	308.03	0.20	66.71	196.59	190.96	9.84		23.14	67.09	6.66	26.08	6.99		7.56	1.51	10.65	2.57	5.97	1.06	6.81
03A-3	24.01	321.04	0.15	76.32	221.62	199.03	9.93		26.19	73.94	7.23	26.46	7.02		8.64	1.59	10.85	2.53	7.72	1.30	7.83
	28.48	413.12	0.29	96.26	269.10	252.53	13.88		33.34	92.48	9.14	32.64	8.92		11.71	2.36	14.29	3.06	10.07	1.61	9.75
	29.66	407.06	0.43	91.26	249.19	254.25	12.60		30.52	88.76	8.97	34.29	9.08		10.81	2.01	14.46	2.83	8.71	1.56	9.22
	29.44	415.12	0.22	86.08	256.32	255.30	13.04		29.86	92.25	8.16	32.08	9.72		9.63	1.93	15.41	3.30	9.48	1.52	8.64
	29.84	442.40	0.54	95.80	261.81	268.90	13.75		33.37	92.08	9.31	32.19	7.90	0.00	9.61	2.18	17.41	3.21	9.30	1.46	9.89
Rim	28.45	405.69	0.22	89.36	257.22	253.93	11.86		31.60	87.70	8.78	34.30	10.16		10.25	1.96	15.22	3.21	9.21	1.46	8.88
Interior	29.79	360.48	0.38	96.97	253.82	251.43	13.56		29.31	82.57	8.00	30.46	7.68	0.03	8.84	2.08	13.67	3.06	9.12	1.20	10.29
	28.17	394.19	0.47	89.18	251.15	260.22	14.56		29.24	84.53	8.33	30.59	8.86		10.47	1.87	13.82	2.79	8.90	1.68	9.34
03B-4	28.90	415.98	0.32	86.33	251.28	256.35	13.89		30.46	87.95	7.98	33.11	9.10		10.26	1.91	13.89	2.58	8.61	1.42	8.59
	31.57	455.20	0.41	96.77	281.52	263.88	13.99		31.00	88.71	8.75	32.76	8.27		10.13	2.01	14.38	3.26	8.59	1.63	8.42
Rim	29.19	451.27	0.26	91.83	256.35	250.05	13.90		28.97	85.01	8.58	30.37	10.43		11.09	1.95	12.84	2.78	8.43	1.56	9.05

Supplementary Table 2 (continued). ICP-MS analyses and trace element concentrations

	Concentrations (ppm)																			
Analysis	Ga	Rb	Sr	Y	Zr	Nb	Cs	Ba	La	Ce	Pr	Nd	Sm	Eu	Gd	Tb	Dy	Ho	Er	Tm	Yb
Interior	21.69	237.66	0.51	173.72	477.82	195.38	7.88	1.11	62.24	105.20	14.97	60.94	18.05		19.11	4.80	29.12	5.54	15.86	2.74	16.43
	24.91	266.81	0.19	83.26	238.30	184.71	9.19		37.45	97.94	9.78	34.01	9.49		11.83	1.61	13.80	3.35	7.74	1.38	8.59
04C-2	25.29	283.98	0.36	83.32	228.84	186.47	9.21	0.69	37.30	95.58	9.14	35.89	11.71		10.04	2.02	13.13	3.21	6.71	1.33	8.70
	24.70	297.19	0.38	85.64	246.87	182.90	8.98		35.27	99.42	10.52	37.12	10.97		11.56	2.01	16.42	3.24	7.64	1.23	7.95
	25.14	304.43	0.21	81.23	247.34	187.42	8.62	0.34	38.66	98.77	8.78	38.46	9.55		11.16	2.03	14.20	3.00	8.14	1.26	8.22
Rim	24.28	311.92	0.50	83.12	241.65	183.76	8.43	1.10	36.05	94.08	9.69	37.20	7.72		10.24	1.72	13.30	2.61	8.19	1.05	6.97
Interior	27.00	330.27	0.17	103.91	280.83	224.87	10.45		38.26	94.92	10.55	39.33	10.56	0.00	14.28	2.34	17.65	3.71	9.44	1.48	10.01
	27.32	340.97	0.27	108.18	279.34	233.87	12.01		38.29	97.73	9.66	38.50	12.50		14.35	2.30	16.41	3.75	9.27	1.53	9.14
04B-3	27.57	343.89	0.36	106.13	272.99	220.47	11.18		36.12	93.65	9.58	40.01	13.01		13.18	2.46	18.88	3.54	10.49	1.31	9.82
	26.78	347.43	0.46	102.21	265.31	222.06	11.42	0.32	38.98	94.62	10.05	36.58	11.02		13.18	2.26	16.45	3.05	10.01	1.33	9.10
	23.71	342.35	0.34	96.10	263.67	211.20	10.37		36.07	92.30	9.71	39.17	10.11		11.96	2.17	17.07	3.15	10.93	1.42	9.25
Rim	26.42	365.31	0.26	107.47	275.41	229.89	10.38		37.71	94.40	9.77	39.05	10.97		13.73	2.19	16.58	3.52	10.96	1.68	9.75

Supplementary Table 2 (continued). ICP-MS analyses and trace element concentrations

							Isotope Ratios						
Sample	Lu	Hf	Ta	Pb	Th	U	208Pb 207Pb	% err (1s)	207Pb 206Pb	% err (1s)	208Pb 206Pb	% err (1s)	corr coeff
Interior	4.35	39.42	19.85	47.68	68.59	10.85	3.17	8.40	0.60	16.83	1.95	8.81	0.98
	2.44	25.37	16.77	56.69	46.84	12.47	2.66	7.32	0.73	11.34	2.13	5.79	0.83
	2.78	23.36	16.97	57.23	48.56	14.41	2.38	7.23	0.80	10.42	1.86	6.96	0.72
	2.31	24.33	15.80	55.52	45.91	13.49	3.18	10.12	0.61	14.51	2.11	5.60	0.86
	2.88	26.35	15.17	56.65	47.69	14.00	2.87	11.70	0.78	13.34	2.22	8.70	0.50
28-2	2.58	22.66	16.38	56.70	49.08	13.84	2.67	8.46	0.90	11.79	2.48	9.94	0.71
	2.77	24.53	17.05	57.92	49.93	15.04	2.79	7.34	0.73	11.39	2.13	7.09	0.78
	2.55	20.98	16.83	55.99	48.91	13.81	2.44	7.07	0.84	9.37	1.99	7.78	0.67
	2.77	22.16	17.04	57.02	49.51	14.58	2.73	10.42	0.88	17.40	2.51	8.48	0.90
	2.25	24.86	17.99	56.64	51.01	13.88	2.95	10.44	0.71	14.44	2.24	8.23	0.70
Rim	2.50	23.13	16.63	55.50	48.65	14.07	2.41	7.42	0.84	11.53	2.11	7.13	0.78
Interior	3.01	22.03	15.39	54.81	49.33	14.31	2.29	10.53	0.93	10.60	2.18	8.40	0.40
	2.57	20.54	14.53	52.77	45.36	13.50	3.00	10.55	0.80	15.19	2.28	9.12	0.73
	2.81	24.11	16.51	56.44	49.32	14.56	3.74	13.79	0.60	15.35	2.26	6.95	0.44
	2.64	22.78	14.69	52.58	46.12	13.40	4.11	16.59	0.62	18.51	2.22	9.32	0.45
	2.52	20.64	14.97	54.35	47.52	14.01	3.30	9.62	0.67	13.09	2.33	8.12	0.68
28-4	2.74	22.73	16.16	54.47	47.28	13.94	3.22	9.86	0.77	12.85	2.18	9.09	0.64
	2.82	20.40	15.45	55.71	47.21	13.72	2.73	7.91	0.71	9.18	1.82	6.13	0.53
	2.70	22.47	16.10	56.08	48.73	14.13	2.34	6.32	0.92	10.25	2.15	8.58	0.79
	2.51	20.96	15.37	57.30	46.47	13.98	2.81	9.89	0.83	10.40	2.18	6.57	0.39
	2.54	23.34	14.95	55.26	47.72	14.30	2.61	7.80	0.78	10.45	2.21	6.89	0.67
Rim	2.71	21.93	16.19	56.70	48.39	13.85	2.80	8.53	0.90	10.83	2.45	8.42	0.63
Interior	2.63	23.97	17.10	57.73	49.99	14.75	2.64	7.46	0.81	8.58	2.07	7.82	0.59
	2.73	22.24	16.87	54.81	52.27	14.03	3.47	9.71	0.55	16.14	2.11	10.34	0.82
	2.84	24.14	16.51	56.34	52.42	14.39	2.70	9.43	0.82	14.82	2.37	9.18	0.79
	2.61	23.84	17.11	57.52	49.50	14.70	2.94	7.14	0.73	10.24	2.19	8.45	0.72
28-3	2.92	24.51	17.41	58.40	49.52	14.28	3.57	8.87	0.81	10.99	2.20	9.65	0.64
	2.66	24.29	15.85	51.06	46.94	13.67	2.61	10.30	0.79	15.61	2.27	7.63	0.82
	2.28	22.84	15.45	50.20	47.63	13.15	2.87	12.24	0.57	16.44	1.87	7.73	0.71
	2.45	22.79	16.10	51.33	47.27	13.37	2.67	7.40	0.66	10.40	1.90	6.79	0.71
	2.55	21.82	15.08	52.14	46.10	13.28	2.86	9.25	0.86	11.16	2.26	7.63	0.57
Rim	2.68	26.39	17.56	55.04	51.64	15.33	2.98	10.35	0.79	13.82	2.29	8.61	0.66

Supplementary Table 2 (continued). ICP-MS analyses and trace element concentrations

							Isotope Ratios						
Sample	Lu	Hf	Ta	Pb	Th	U	208Pb 207Pb	% err (1s)	207Pb 206Pb	% err (1s)	208Pb 206Pb	% err (1s)	corr coeff
Interior	2.58	22.68	17.09	56.38	48.73	14.47	2.45	8.97	0.70	18.31	2.20	8.09	1.08
	2.32	22.73	15.92	58.92	49.16	15.03	3.20	9.16	0.56	12.20	1.97	8.61	0.66
	2.42	21.92	15.23	57.60	47.38	15.18	2.73	11.38	0.78	13.81	2.30	6.41	0.58
	2.49	21.80	16.24	55.75	49.13	14.75	3.25	8.81	0.50	14.16	2.01	8.31	0.82
	2.47	22.99	15.80	55.94	47.41	14.41	2.88	8.45	0.68	9.47	1.90	7.00	0.51
	2.16	20.11	13.51	47.91	40.61	12.70	2.71	8.44	0.79	9.74	2.00	4.78	0.50
	2.00	18.93	13.99	48.20	41.78	12.02	2.78	6.82	0.86	9.51	2.60	7.80	0.71
28-5	1.95	17.52	12.83	45.17	40.33	11.90	2.88	9.27	0.68	10.64	2.02	6.93	0.51
	2.39	20.58	13.77	46.89	41.95	13.20	2.83	8.96	0.66	12.45	1.84	6.93	0.71
	1.64	15.17	10.00	38.43	34.75	9.77	2.85	9.97	0.68	14.15	1.92	8.71	0.72
	1.77	17.05	11.52	38.90	35.69	10.27	3.29	8.10	0.63	12.18	2.12	7.85	0.76
	1.78	16.40	11.03	37.23	34.80	10.12	2.82	10.36	0.65	13.50	1.96	6.64	0.66
	2.62	24.72	17.62	57.00	49.81	14.48	2.63	10.14	0.84	12.90	2.24	9.24	0.62
	1.98	19.99	12.41	42.92	39.09	10.87	2.98	8.60	0.73	12.80	2.25	7.74	0.76
Rim	1.87	18.81	12.96	43.03	37.60	11.56	3.46	9.66	0.52	12.97	1.82	5.90	0.72
Interior	1.63	14.16	12.64	65.69	31.87	17.83	2.78	9.07	0.94	15.66	2.62	10.95	0.82
	1.45	13.39	12.30	63.41	31.42	16.19	2.81	8.20	0.74	9.59	2.11	6.28	0.53
	1.20	12.94	12.87	63.58	32.20	17.40	2.91	11.52	0.69	18.89	2.21	9.00	0.90
	1.39	14.68	13.47	61.54	32.67	16.41	2.72	10.59	0.95	15.52	2.31	10.96	0.73
30-5	1.57	12.77	12.53	62.92	31.08	17.23	2.73	10.63	0.68	14.15	1.97	7.68	0.67
	1.78	14.55	13.76	64.91	33.74	17.70	2.68	9.55	0.97	10.91	2.13	8.15	0.53
	1.56	12.32	13.15	63.57	31.41	17.15	2.64	9.85	0.82	14.44	2.09	8.44	0.75
	1.44	15.28	13.33	62.71	32.03	17.25	2.78	9.34	0.73	10.36	1.81	5.80	0.45
	1.40	15.52	12.91	62.82	32.61	16.71	2.24	7.27	0.81	14.24	1.90	9.84	0.88
Rim	1.51	12.43	13.47	65.32	32.23	16.86	3.50	10.71	0.49	15.54	1.86	7.91	0.77
Interior	1.66	15.69	14.25	66.73	36.55	17.34	2.61	7.38	0.73	11.01	1.83	7.89	0.74
	1.59	15.51	13.56	65.05	35.23	16.84	2.42	6.68	0.98	11.72	2.34	7.51	0.85
	1.56	14.47	13.44	66.15	33.86	16.66	2.70	11.03	0.98	12.90	2.34	7.20	0.52
	1.61	19.00	14.29	67.41	35.77	16.24	2.63	11.33	0.74	15.69	2.07	7.92	0.73
	1.67	14.96	14.13	63.71	36.45	15.87	2.89	9.52	0.72	11.51	2.08	8.05	0.58
30-3	1.45	15.58	13.88	63.11	34.58	16.32	2.89	10.90	0.69	14.74	2.17	6.18	0.75
	1.84	16.21	14.58	64.13	35.56	16.26	2.79	11.04	0.66	10.99	1.82	6.06	0.27
	1.62	16.99	15.26	63.25	35.92	16.42	2.78	8.10	0.98	8.85	2.66	8.05	0.54
	1.80	17.39	13.53	61.63	36.26	15.83	2.60	9.15	0.84	9.86	2.20	6.72	0.44
	1.85	13.78	14.00	63.62	35.72	16.67	2.74	12.32	0.76	15.91	2.39	10.15	0.63
	1.15	11.79	18.00	57.06	41.92	23.03	2.85	12.66	0.73	17.65	2.08	8.06	0.76
Rim	1.45	11.55	17.02	54.64	38.63	22.07	2.59	8.31	0.73	12.11	2.16	9.86	0.73

Supplementary Table 2 (continued). ICP-MS analyses and trace element concentrations

							Isotope Ratios						
Sample	Lu	Hf	Ta	Pb	Th	U	208Pb 207Pb	% err (1s)	207Pb 206Pb	% err (1s)	208Pb 206Pb	% err (1s)	corr coeff
Interior	1.81	12.47	17.44	53.44	40.48	23.05	2.80	10.11	0.64	14.75	1.77	9.81	0.73
	1.48	9.63	13.94	47.08	35.97	19.45	2.68	8.79	0.66	15.72	2.00	7.62	0.95
	1.25	12.09	14.80	49.89	36.16	19.75	3.55	14.79	0.46	20.55	1.94	8.61	0.78
	1.37	13.23	16.20	48.99	35.96	19.52	2.82	8.26	0.83	9.49	2.06	8.97	0.60
5-Sep	1.43	12.74	16.65	52.26	37.13	20.73	2.57	8.39	0.71	14.92	2.05	7.85	0.91
	1.49	9.96	17.38	53.17	38.23	21.72	2.14	8.85	0.90	13.54	2.08	10.96	0.76
	1.30	12.94	17.89	54.57	41.06	22.41	2.64	10.99	0.74	10.49	2.12	9.21	0.38
	1.27	13.67	17.12	52.86	38.47	21.27	2.80	8.28	0.63	13.11	2.03	9.70	0.78
Rim	1.42	13.21	18.11	55.86	38.58	22.16	3.89	14.37	0.53	14.51	1.99	9.39	0.34
Interior	1.25	9.63	15.26	43.98	33.66	18.49	3.30	13.84	0.54	16.50	1.74	10.40	0.55
	0.90	7.65	10.19	34.50	26.65	13.81	3.18	13.02	0.56	17.23	1.99	6.79	0.74
	0.95	8.61	11.38	37.06	27.47	14.96	4.49	12.48	0.56	16.06	2.28	11.35	0.63
	1.19	7.75	12.96	39.87	29.89	16.98	3.47	14.57	0.63	17.80	2.13	9.33	0.58
03A-3	1.18	10.28	14.33	41.12	32.25	18.06	2.56	14.46	0.86	18.61	2.15	10.19	0.64
	1.13	11.32	17.77	54.45	40.35	21.46	3.66	11.86	0.80	15.26	2.75	12.46	0.65
	1.33	13.24	17.89	51.28	39.77	22.01	3.63	17.60	0.57	20.82	2.20	8.36	0.56
	1.38	13.65	15.34	52.88	40.65	21.71	2.92	10.86	0.73	13.53	1.97	10.63	0.62
	1.65	11.55	17.42	54.55	41.69	23.00	2.98	12.10	0.66	17.85	2.24	10.99	0.75
Rim	1.51	14.05	18.45	50.40	38.95	21.43	2.57	9.43	0.86	14.26	2.14	10.94	0.75

Supplementary Table 2 (continued). ICP-MS analyses and trace element concentrations

							Isotope Ratios						
							208Pb	% err	207Pb	% err	208Pb	% err	corr
Sample	Lu	Hf	Ta	Pb	Th	U	207Pb	(1s)	206Pb	(1s)	206Pb	(1s)	coeff
Interior	1.32	10.74	16.81	50.45	38.76	20.84	3.51	14.83	0.60	16.80	2.36	8.64	0.47
	1.33	9.71	18.18	56.33	39.33	22.89	2.70	8.64	0.63	20.10	2.24	10.59	1.04
03B-4	1.56	12.43	17.48	53.46	36.86	22.74	2.39	10.08	0.83	20.38	2.27	13.29	0.91
	1.15	11.79	18.00	57.06	41.92	23.03	2.85	12.66	0.73	17.65	2.08	8.06	0.76
Rim	1.45	11.55	17.02	54.64	38.63	22.07	2.59	8.31	0.73	12.11	2.16	9.86	0.73
Interior	2.86	21.41	16.95	35.27	58.82	11.87	2.68	10.91	0.66	12.51	1.73	8.76	0.52
	1.18	10.78	12.17	40.11	33.71	14.80	3.88	9.54	0.49	14.97	1.94	10.04	0.78
04C-2	1.29	10.32	13.43	36.88	31.45	14.45	3.09	13.17	0.72	13.18	1.83	8.78	0.33
	1.15	12.49	12.98	40.53	34.93	15.14	1.91	7.33	1.29	14.69	2.37	10.29	0.89
	1.57	11.81	11.12	38.83	31.62	15.40	3.71	12.19	0.57	13.58	2.12	9.48	0.49
Rim	1.30	9.89	12.49	38.75	34.59	14.52	3.28	11.77	0.65	15.87	2.29	8.26	0.69
Interior	1.70	13.94	14.34	46.13	42.26	18.96	3.25	11.81	0.66	18.29	2.20	9.84	0.81
	1.86	14.37	15.91	47.11	40.57	18.42	2.78	9.53	0.82	17.51	2.24	8.96	0.94
04B-3	1.52	14.84	15.43	44.78	42.71	18.54	2.55	8.28	0.68	12.48	2.00	8.31	0.75
	1.72	13.55	15.84	44.27	40.54	17.47	3.02	15.24	0.58	14.91	1.81	6.19	0.15
	1.46	10.24	15.49	45.34	38.51	17.49	2.27	9.22	0.78	14.41	1.78	9.60	0.78
Rim	1.89	12.27	15.55	44.26	40.46	18.17	3.96	12.97	0.44	19.14	2.06	8.61	0.83

Microprobe Data

Sample	Na_2O	SiO_2	K_2O	Al_2O_3	FeO	MgO	CaO	Cl (ppm)	Ti	F (ppm)	Ti (ppm)
28-2	5.23	77.03	3.77	11.69	1.33	0.02	0.23	3787	501	2707	501
28-2	4.44	77.91	3.87	11.55	1.32	0.02	0.26	3345	503	2551	503
28-2	4.61	77.61	4.03	11.39	1.36	0.02	0.24	3319	515	3418	515
28-2	4.49	77.63	4.13	11.44	1.34	0.02	0.25	3346	539	3150	539
28-2	4.28	77.90	4.31	11.31	1.32	0.02	0.25	3289	473	2298	473
28-2	4.57	77.46	4.24	11.40	1.39	0.02	0.25	3281	483	3095	483
28-2	4.31	77.57	4.45	11.35	1.36	0.02	0.25	3334	520	3115	520
28-4	4.47	77.84	4.45	10.93	1.34	0.02	0.25	3438	498	3075	498
28-4	4.33	77.80	4.55	11.04	1.37	0.03	0.26	3322	540	2344	540
28-4	4.14	77.63	4.75	11.11	1.36	0.03	0.25	3337	519	3410	519
28-4	4.46	77.12	4.74	11.38	1.35	0.02	0.26	3381	542	2706	542
28-4	4.70	77.01	4.61	11.38	1.36	0.04	0.27	3298	558	2537	558
28-4	4.27	77.83	4.65	10.98	1.34	0.02	0.25	3238	568	2857	568
28-4	4.30	77.80	4.52	11.07	1.39	0.02	0.26	3280	527	2618	527
28-4	4.33	77.95	4.50	10.94	1.37	0.02	0.26	3181	478	2646	478
04C-2	4.55	76.51	4.58	11.97	1.26	0.01	0.22	7002	520	1423	520
04C-2	4.38	77.05	4.68	11.95	1.23	0.02	0.26	2026	486	1790	486
04C-2	4.26	77.15	4.82	11.83	1.24	0.02	0.26	1930	521	1638	521
04C-2	4.20	77.27	4.89	11.74	1.18	0.02	0.27	1993	560	1727	560
04C-2	4.08	77.57	4.77	11.61	1.22	0.02	0.27	1983	511	2065	511
04C-2	4.15	77.57	4.78	11.56	1.22	0.02	0.25	1957	526	1990	526
04B-4	3.97	77.77	5.00	11.18	1.32	0.01	0.25	2316	458	2153	458
04B-4	4.08	77.68	5.06	11.12	1.27	0.01	0.26	2282	499	2356	499
04B-4	4.10	77.58	4.98	11.30	1.29	0.01	0.26	2246	459	2126	459
04B-4	4.06	77.59	4.93	11.34	1.26	0.02	0.26	2224	527	2725	527
04B-4	4.18	77.73	4.85	11.27	1.22	0.02	0.26	2266	463	2091	463
04B-5	4.27	77.17	4.76	11.77	1.25	0.03	0.26	2300	508	2149	508
04B-5	4.38	77.13	4.77	11.66	1.23	0.02	0.26	2161	479	2846	479
04B-5	4.29	77.47	4.62	11.56	1.27	0.02	0.26	2167	468	2411	468
33-3	4.58	76.42	4.67	11.96	1.34	0.03	0.28	3328	551	3260	551
33-3	4.50	76.58	4.69	11.88	1.30	0.03	0.28	3262	534	3575	534
33-3	4.50	76.55	4.68	11.92	1.31	0.03	0.28	3282	591	3422	591
33-3	4.49	76.59	4.77	11.90	1.27	0.03	0.28	3275	572	2828	572
33-3	4.52	76.58	4.73	11.84	1.27	0.03	0.28	3179	569	3697	569

Microprobe Data

Sample	Na_2O	SiO_2	K_2O	Al_2O_3	FeO	MgO	CaO	Cl (ppm)	Ti	F (ppm)	Ti (ppm)
33-1	4.57	76.35	4.61	12.11	1.33	0.03	0.28	3274	598	3318	598
33-1	4.65	76.47	4.44	12.11	1.30	0.03	0.28	3226	611	3405	611
33-2	3.04	81.73	4.34	9.06	1.13	0.01	0.19	2579	425	1890	425
33-2	4.27	76.35	5.25	11.77	1.46	0.02	0.26	3326	478	2401	478
33-2	4.18	76.37	5.21	11.92	1.36	0.02	0.25	3378	524	3091	524
33-2	4.21	76.41	5.20	11.73	1.43	0.02	0.26	3380	526	3456	526
33-2	4.18	76.42	5.20	11.76	1.42	0.02	0.26	3328	459	3636	459
09-5	4.56	77.68	4.29	11.45	1.28	0.01	0.25	2574	459	1741	459
09-5	4.44	76.99	4.78	11.70	1.27	0.02	0.25	2583	482	2438	482
09-5	4.38	76.89	4.89	11.73	1.27	0.01	0.25	2562	440	2858	440
09-5	4.35	76.70	4.99	11.88	1.29	0.01	0.25	2591	485	2049	485
09-5	4.25	76.88	5.04	11.72	1.27	0.02	0.25	2593	495	2858	495
30-2	5.05	75.71	4.61	11.83	1.29	0.03	0.27	8146	558	3331	558
30-2	4.74	77.69	4.13	11.34	1.27	0.02	0.23	3016	447	2374	447
09-2	4.64	76.84	4.35	12.11	1.25	0.01	0.26	2777	468	2108	468
09-2	4.76	76.71	4.38	12.01	1.28	0.01	0.26	2725	508	2609	508
09-2	4.62	76.71	4.46	12.12	1.25	0.01	0.26	2675	442	2470	442
09-2	4.62	76.80	4.43	11.96	1.28	0.01	0.26	2648	418	3257	418
09-2	4.70	76.82	4.39	11.96	1.30	0.02	0.26	2540	464	2358	464
09-2	4.57	76.76	4.59	11.85	1.33	0.01	0.25	2682	456	3109	456
03A-3	4.31	77.01	5.07	11.50	1.25	0.02	0.25	2468	513	2924	513
03A-3	4.10	77.36	4.95	11.50	1.27	0.02	0.26	2446	486	2491	486
03A-3	4.19	77.26	5.05	11.42	1.26	0.02	0.26	2458	483	2573	483
03A-3	4.27	77.41	4.92	11.31	1.23	0.02	0.26	2488	438	2882	438
03A-3	4.19	77.39	4.99	11.29	1.31	0.01	0.26	2433	414	2821	414
03A-3	4.02	77.61	4.92	11.40	1.21	0.02	0.26	2456	489	2662	489
03A-3	4.18	77.31	5.07	11.33	1.31	0.01	0.26	2391	455	2456	455
03A-3	4.13	77.76	4.89	11.21	1.18	0.02	0.25	2344	445	2801	445
03A-3	4.05	78.01	4.93	11.01	1.22	0.02	0.25	2378	439	2346	439
03A-4	4.43	77.96	4.43	11.21	1.23	0.01	0.24	2685	483	1729	483
03A-4	4.50	77.56	4.46	11.53	1.21	0.01	0.25	2233	481	1990	481
03A-4	4.48	77.54	4.41	11.60	1.22	0.01	0.24	2127	440	2491	440
03A-4	4.47	77.56	4.46	11.58	1.21	0.01	0.24	2112	446	2148	446
03B-4	4.49	77.25	4.43	11.70	1.32	0.02	0.28	2913	419	1915	419
03B-4	4.49	77.19	4.51	11.75	1.26	0.02	0.25	2463	448	2510	448
03B-4	4.46	77.28	4.49	11.70	1.32	0.01	0.25	2386	531	2071	531
03B-4	4.38	77.54	4.54	11.52	1.25	0.01	0.25	2403	424	2294	424
03B-4	3.89	78.96	4.13	11.07	1.23	0.01	0.24	2346	418	1918	418
03B-4	4.14	76.95	5.15	11.52	1.32	0.02	0.27	3408	518	2435	518

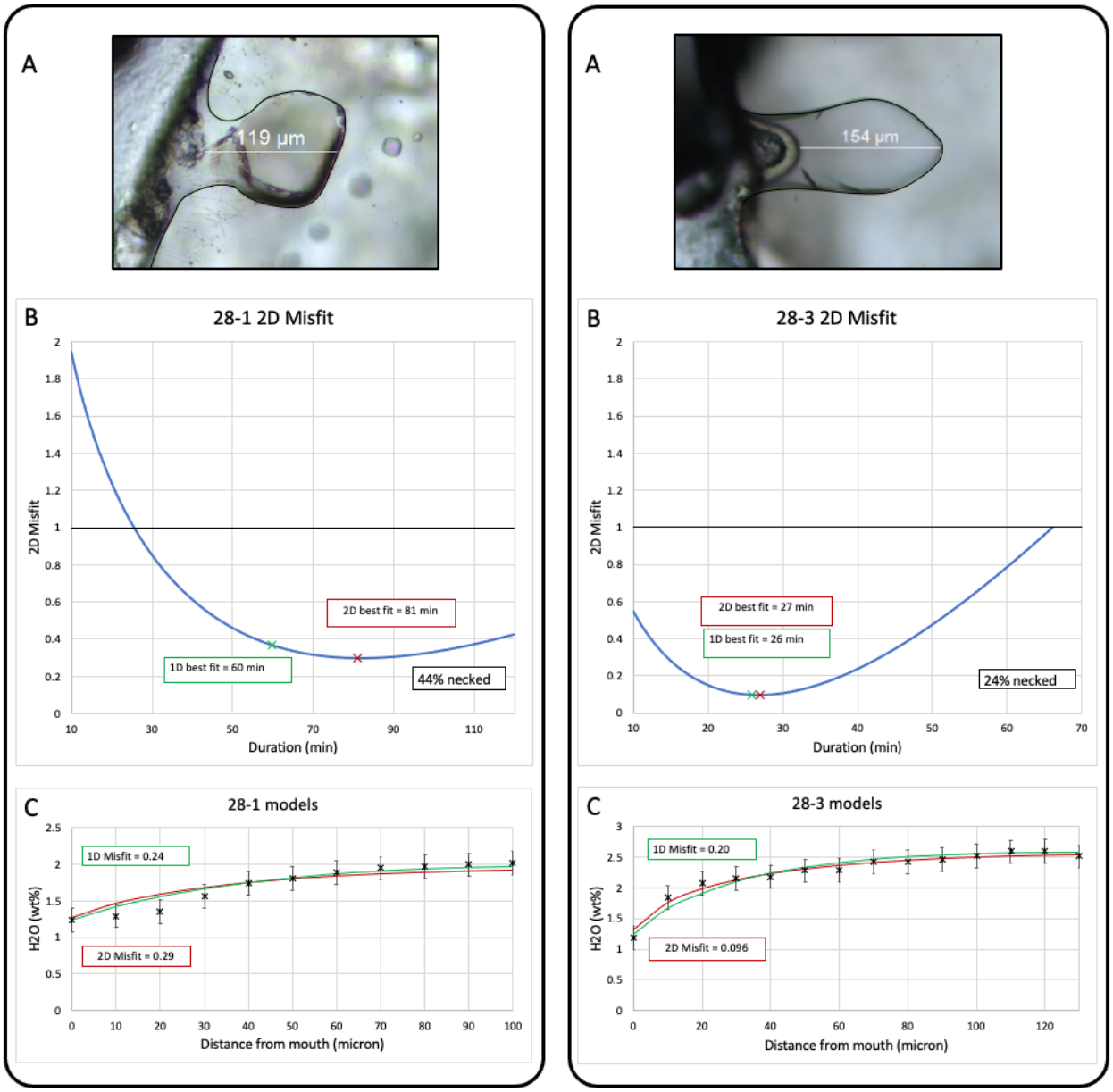

Supplemental Figure 5. A) Photomicrograph of reentrants B) Misfit of 2D model results. Misfit <1 (black horizontal line) is considered a good fit. Blue line represents model misfit in 2D, green X = 1D best fit Green circle in 30-3 represents the shortest duration that produces a misfit <1 in 1D. C) Embayment transect data from measured data, best-fit 2D model, and best-fit 1D model.

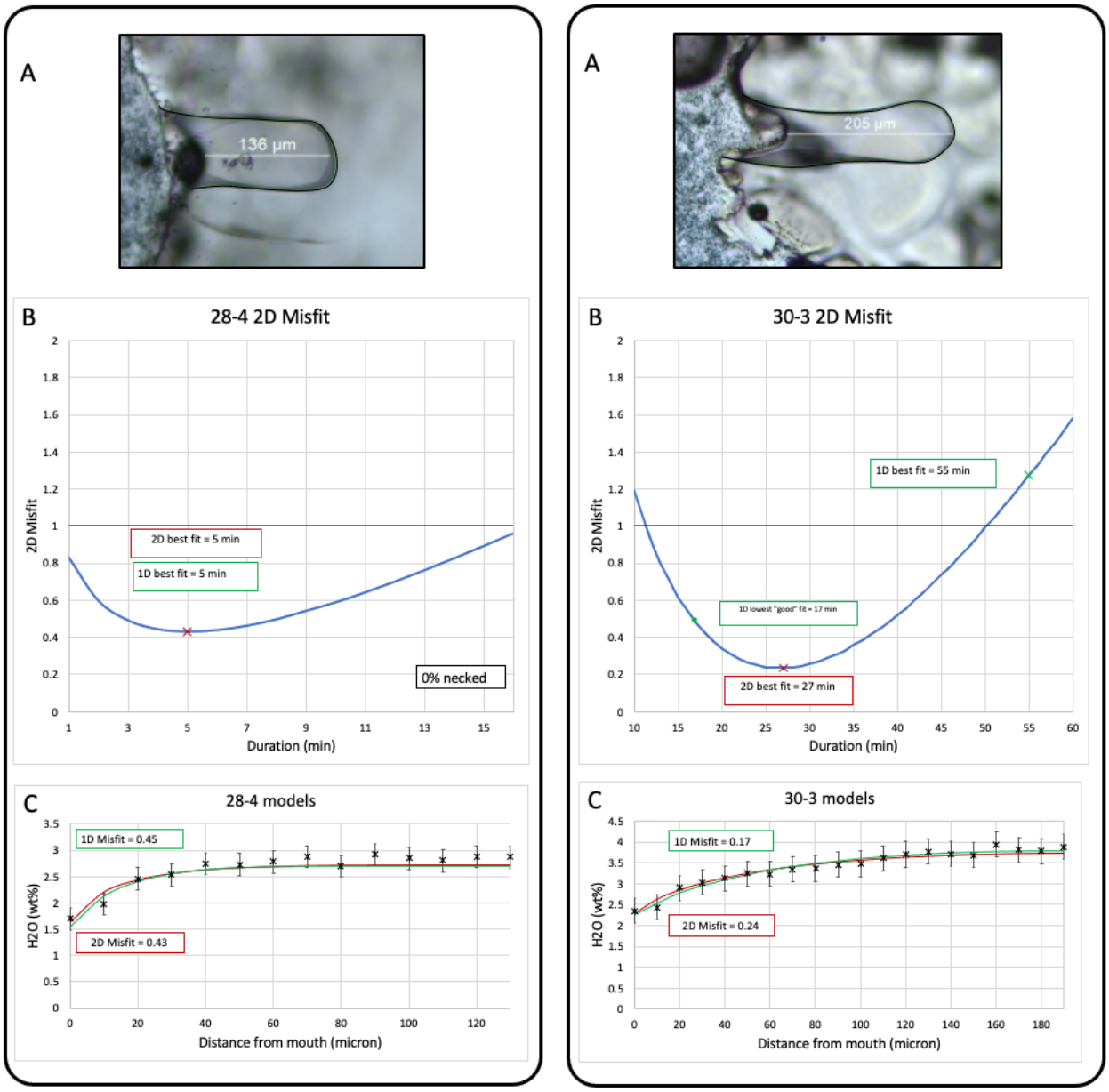

Supplemental Figure 5 (continued). A) Photomicrograph of reentrants B) Misfit of 2D model results. Misfit <1 (black horizontal line) is considered a good fit. Blue line represents model misfit in 2D, green X = 1D best fit Green circle in 30-3 represents the shortest duration that produces a misfit <1 in 1D. C) Embayment transect data from measured data, best-fit 2D model, and best-fit 1D model.

28-1

distance	2D	measured data	1D
0	1.2691	1.237	1.242
10	1.4682	1.293	1.4226
20	1.5948	1.356	1.5584
30	1.6874	1.565	1.6637
40	1.7569	1.742	1.7465
50	1.8092	1.81	1.8117
60	1.8486	1.886	1.8677
70	1.8784	1.947	1.9057
80	1.9008	1.973	1.9338
90	1.9172	1.996	1.953
100	1.9288	2.019	1.9641

28-3

distance	2D	measured data	1D
0	1.3156	1.187	1.2421
10	1.7595	1.843	1.6654
20	1.9844	2.067	1.9037
30	2.1293	2.146	2.0962
40	2.2324	2.175	2.2343
50	2.3095	2.275	2.3242
60	2.3689	2.281	2.4012
70	2.4152	2.424	2.4576
80	2.4515	2.424	2.4985
90	2.4801	2.459	2.5245
100	2.5023	2.52	2.5455
110	2.5194	2.582	2.5589
120	2.5323	2.596	2.5655
130	2.5416	2.507	2.5678

28-4

distance	2D	measured data	1D
0	1.6429	1.697	1.5421
10	2.2098	1.98	2.128
20	2.4355	2.459	2.4078
30	2.5549	2.535	2.5544
40	2.6238	2.741	2.6382
50	2.6643	2.726	2.6727
60	2.6879	2.784	2.6888
70	2.7013	2.879	2.6957
80	2.7087	2.697	2.6985
90	2.7126	2.928	2.6995
100	2.7145	2.846	2.6999
110	2.7154	2.803	2.7
120	2.7158	2.883	2.7
130	2.7159	2.874	2.7

30-3

distance	2D	measured data	1D
0	2.2884	2.353	2.2417
10	2.6356	2.43	2.5173
20	2.8575	2.904	2.773
30	3.0218	3.035	2.9432
40	3.1517	3.13	3.0846
50	3.2571	3.244	3.2034
60	3.3442	3.233	3.3222
70	3.4167	3.347	3.405
80	3.4779	3.363	3.4757
90	3.5297	3.462	3.536
100	3.5735	3.476	3.5967
110	3.6104	3.605	3.6388
120	3.6414	3.703	3.6742
130	3.667	3.771	3.7038
140	3.688	3.716	3.7322
150	3.705	3.689	3.7506
160	3.7184	3.943	3.7647
170	3.7287	3.809	3.7746
180	3.7362	3.784	3.7814
190	3.7412	3.88	3.7829

APPENDIX B

SUPPLEMENTARY TABLES FOR CHAPTER THREE

Table A1. Results of SNGPlag modeling. All models were run with 0% volume fraction antecrysts and nucleation and growth rates from Befus and Andrews (2018), at a temperature of 780°C, initial pressure of 220 MPa, and final pressure of 30 MPa.

Constant Rate Decompression

MPa/h	Crystal Fraction	EQB Crystals	Supersaturation	Nvd (mm^{-3})	Nvd 1-micron (mm^{-3})	Nvd 1-micron uncertainty	Characteristic microlite size (m), CSD50	Characteristic microlite size (m), S50	Characteristic microlite size (m), Sn	Surface Area (m^2)
0.1	0.23537	0.31387	0.07850	251564	240943	0.01584	1.58E-05	1.40E-05	9.51E-06	2.71E-06
1	0.20000	0.31387	0.11387	179605	172964	0.01874	1.58E-05	1.50E-05	9.98E-06	3.67E-06
2.5	0.17509	0.31387	0.13878	157949	152353	0.01999	1.58E-05	1.48E-05	9.88E-06	3.94E-06
5	0.14312	0.31387	0.17074	139511	134561	0.02127	1.58E-05	1.38E-05	9.49E-06	3.78E-06
10	0.09220	0.31387	0.22167	110494	105851	0.02681	1.26E-05	1.13E-05	8.45E-06	2.75E-06
15	0.06444	0.31387	0.24943	86656	82053	0.03397	1.00E-05	9.01E-06	7.61E-06	1.79E-06
20	0.05177	0.31387	0.26210	69590	64956	0.04253	7.94E-06	7.33E-06	7.13E-06	1.20E-06
30	0.04181	0.31387	0.27206	49028	44375	0.06379	5.01E-06	5.31E-06	6.74E-06	6.48E-07
40	0.03785	0.31387	0.27601	37614	32934	0.08172	3.98E-06	4.20E-06	6.63E-06	4.20E-07
50	0.03573	0.31387	0.27814	30423	25767	0.10195	3.16E-06	3.50E-06	6.62E-06	3.06E-07
60	0.03439	0.31387	0.27947	25502	20838	0.11136	3.16E-06	3.03E-06	6.66E-06	2.42E-07
70	0.03347	0.31387	0.28040	21942	17274	0.13470	2.51E-06	2.68E-06	6.71E-06	2.01E-07
80	0.03279	0.31387	0.28108	19226	14559	0.16146	2.00E-06	2.42E-06	6.78E-06	1.75E-07
90	0.03227	0.31387	0.28160	17094	12432	0.17123	2.00E-06	2.21E-06	6.87E-06	1.56E-07
100	0.03186	0.31387	0.28201	15388	10722	0.18047	2.00E-06	2.04E-06	6.96E-06	1.42E-07
120	0.03124	0.31387	0.28263	12790	8134	0.22210	1.58E-06	1.79E-06	7.17E-06	1.24E-07
150	0.03063	0.31387	0.28324	10177	5523	0.27938	1.26E-06	1.54E-06	7.56E-06	1.09E-07

6-hour stall at 70 MPa

MPa/h	Crystal Fraction	EQB Crystals	Supersaturation	Nvd (mm^{-3})	Nvd 1 micron (mm^{-3})	Nvd 1 micron uncertainty	Characteristic microlite size (m), CSD50	Characteristic microlite size (m), S50	Characteristic microlite size (m), Sn	Surface Area (m^2)
0.1	0.23538	0.31386	0.07848	251643	241013	0.01583	1.58E-05	1.40E-05	9.51E-06	2.70E-06
1	0.20085	0.31384	0.11299	180396	173678	0.01870	1.58E-05	1.50E-05	9.98E-06	3.58E-06
2.5	0.17913	0.31386	0.13474	160460	154723	0.01983	1.58E-05	1.48E-05	9.92E-06	3.74E-06
5	0.15663	0.31386	0.15723	146615	141439	0.02074	1.58E-05	1.42E-05	9.68E-06	3.59E-06
10	0.12887	0.31387	0.18500	132008	127201	0.02186	1.58E-05	1.32E-05	9.25E-06	3.11E-06
15	0.11243	0.31384	0.20140	122990	118287	0.02541	1.26E-05	1.24E-05	8.93E-06	2.70E-06
20	0.10201	0.31385	0.21184	116765	112110	0.02608	1.26E-05	1.19E-05	8.70E-06	2.39E-06
30	0.09000	0.31384	0.22384	108790	104154	0.02702	1.26E-05	1.11E-05	8.40E-06	1.99E-06
40	0.08347	0.31385	0.23038	103908	99314	0.02765	1.26E-05	1.07E-05	8.22E-06	1.75E-06
50	0.07940	0.31382	0.23442	100644	96043	0.03152	1.00E-05	1.03E-05	8.11E-06	1.59E-06

Table A1. (continued) Results of SNGPlag modeling. All models were run with 0% volume fraction antecrysts and nucleation and growth rates from Befus and Andrews (2018), at a temperature of 780°C, initial pressure of 220 MPa, and final pressure of 30 MPa.

Accelerating Decompression

	Crystal Fraction	EQB Crystals	Supersaturation	Nvd (mm^{-3})	Nvd 1 micron (mm^{-3})	Nvd 1 micron uncertainty	Characteristic microlite size (m), CSD50	Characteristic microlite size (m), S50	Characteristic microlite size (m), Sn	Surface Area (m^2)
0.1	0.22896			242009	232510	0.01615	1.58E-05	1.43E-05	9.52E-06	3.79E-06
1	0.18764			170243	164206	0.01925	1.58E-05	1.49E-05	9.90E-06	4.52E-06
2.5	0.15452			146658	141528	0.02074	1.58E-05	1.42E-05	9.63E-06	4.36E-06
5	0.10959			121778	117096	0.02554	1.26E-05	1.24E-05	8.86E-06	3.46E-06
10	0.06101			82802	78228	0.03475	1.00E-05	8.63E-06	7.48E-06	1.74E-06
15	0.04640			59816	55154	0.05147	6.31E-06	6.37E-06	6.90E-06	9.60E-07
20	0.04075			46332	41658	0.06562	5.01E-06	5.06E-06	6.70E-06	6.15E-07
30	0.03607			31693	27041	0.08903	3.98E-06	3.63E-06	6.61E-06	3.36E-07
40	0.03398			24015	19345	0.12875	2.51E-06	2.88E-06	6.67E-06	2.30E-07
50	0.03279			19272	14599	0.16126	2.00E-06	2.42E-06	6.78E-06	1.79E-07

Single-step Decompression

	Crystal Fraction	EQB Crystals	Supersaturation	Nvd (mm^{-3})	Nvd 1 micron (mm^{-3})	Nvd 1 micron uncertainty	Characteristic microlite size (m), CSD50	Characteristic microlite size (m), S50	Characteristic microlite size (m), Sn	Surface Area (m^2)
0.1	0.25882			204602	189518	0.01756	1.58E-05	1.54E-05	1.07E-05	1.82E-07
1	0.23499			181230	172013	0.01866	1.58E-05	1.60E-05	1.06E-05	2.96E-07
2.5	0.21980			172239	164676	0.01914	1.58E-05	1.59E-05	1.05E-05	4.55E-07
5	0.20368			164235	157741	0.01960	1.58E-05	1.56E-05	1.04E-05	6.75E-07
10	0.17980			153647	148060	0.02026	1.58E-05	1.51E-05	1.01E-05	1.00E-06
15	0.15933			144889	139748	0.02087	1.58E-05	1.44E-05	9.79E-06	1.21E-06
20	0.14038			136518	131638	0.02150	1.58E-05	1.38E-05	9.48E-06	1.32E-06
30	0.10737			119889	115233	0.02574	1.26E-05	1.22E-05	8.82E-06	1.29E-06
40	0.08322			104085	99476	0.02763	1.26E-05	1.07E-05	8.21E-06	1.11E-06
50	0.06763			90317	85705	0.03327	1.00E-05	9.32E-06	7.72E-06	9.06E-07
60	0.05793			78971	74349	0.03993	7.94E-06	8.20E-06	7.36E-06	7.35E-07
70	0.05175			69782	65143	0.04247	7.94E-06	7.30E-06	7.12E-06	6.04E-07
80	0.04761			62337	57685	0.05042	6.31E-06	6.57E-06	6.95E-06	5.06E-07
90	0.04471			56230	51581	0.05309	6.31E-06	5.97E-06	6.83E-06	4.32E-07
100	0.04257			51164	46507	0.05566	6.31E-06	5.48E-06	6.75E-06	3.75E-07

Table A2. Embayment modeling results. Samples in red indicate bad model fits.

Embayment Start Single Stage

Sample	Initial H_2O (wt.%)	Initial Pressure (MPa)	Frag pressure (MPa)	Best fit dP/dt (MPa/s)	error (-) (MPa/s)	error (+) (MPa/s)	Ascent rate (m/s)	Ascent time (min)	misfit
EW910612-1-1	2.83	54.2	30	0.3001	0.016	1	13.5515	1.344	0.56958
7-1-91-1A-1	2	30	15	0.0768	0.01	1	0.8109	3.2552	0.32249
7-1-91-1A-2	2.62	47.5	10	0.5	0.17	2.24	11.1212	1.25	0.60455
3292-2C-1	3.17	65.9	30	0.2538	0.07	1.3	10.9195	2.3575	0.68746
7-3-91-1A-1	2.56	45.6	20	0.0741	0.018	1.87	2.2019	5.758	0.35408
3292-2A-2	3.38	73.6	30	0.2322	0.089	0.779	9.8092	3.1295	0.81159
P22692-2E-4	3.12	64.1	30	0.1728	0.041	2	7.4748	3.289	0.3099
P22692-2E-5	1.82	25.6	10	0.1154	0.013	2	---	2.253	0.52177
910819-3-1	3.06	62	bad						
P22692-2E-3	4.32	112.8	bad						
7-1-91-1A-3	3.64	83.8	15	0.0367	---	---	1.1926	31.244	1.2471

Melt Inclusion Start Single Stage

Sample	Initial H_2O (wt.%)	Initial Pressure (MPa)	Frag pressure (MPa)	Best fit dP/dt (MPa/s)	error (-) (MPa/s)	error (+) (MPa/s)	Ascent rate (m/s)	Ascent time (min)	misfit
EW910612-1-1	6.35	220	5	0.072	NA	NA	2.5099	49.7685	34.3937
7-1-91-1A-1	6.35	220	15	0.033	0.011	0.066	1.2065	103.5354	0.016283
7-1-91-1A-2	6.35	220	5	0.083	0.074	0.0935	2.8933	43.1727	0.87232
3292-2C-1	6.35	220	30	0.0352	0.029	0.0417	1.3885	89.9621	0.84414
7-3-91-1A-1	6.35	220	25	0.015	0.005	0.025	0.5765	216.6667	0.084622
3292-2A-2	6.35	220	30	0.013	NA	NA	0.5128	243.5897	2.594
P22692-2E-4	6.35	220	30	0.0285	NA	NA	1.1242	111.1111	1.0637
P22692-2E-5	6.35	220	10	0.0167	0.0082	0.028	0.596	209.5808	0.37142
910819-3-1	6.35	220	5	0.005	NA	NA	0.1743	716.6667	10.9863
P22692-2E-3	6.35	220	30	0.094	NA	NA	3.7079	33.6879	18.3291
7-1-91-1A-3	6.35	220	15	0.0226	0.019	0.026	0.8262	151.1799	0.69878

Table A2. Embayment modeling results. Samples in red indicate bad model fits.

TWO STAGE											
Sample	Initial H_2O (wt.%)	Initial Pressure (MPa)	Frag Pressure (MPa)	first dP/dt (MPa/s)	second dP/dt (MPa/s)	Intermediate P (MPa)	Ascent time 1st (min)	Ascent time 2nd (min)	misfit	Total ascent time (min)	Total ascent time (hrs)
EW910612-1-1	6.35	220	30	0.0017	0.8	45	1715.6863	0.3125	0.26462	1715.9988	28.6000
7-1-91-1A-1	6.35	220	15	0.006	0.05	30	527.7778	5.0000	0.016378	532.7778	8.8796
7-1-91-1A-2	6.35	220	10	0.026	0.68	35	118.5897	0.6127	0.04877	119.2025	1.9867
3292-2C-1	6.35	220	30	0.0005	0.6	60	5333.3333	0.8333	0.44589	5334.1667	88.9028
7-3-91-1A-1	6.35	220	20	0.006	0.13	35	513.8889	1.9231	0.041169	515.8120	8.5969
3292-2A-2	6.35	220	30	0.004	0.44	60	666.6667	1.1364	0.092593	667.8030	11.1301
P22692-2E-4	6.35	220	30	0.0014	0.3	55	1964.2857	1.3889	0.79477	1965.6746	32.7612
P22692-2E-5	6.35	220	10	0.005	0.14	20	666.6667	1.1905	0.29683	667.8571	11.1310
910819-3-1	6.35	220	5	0.005	0.01	80	466.6667	125.000	16.1679	591.6667	9.8611
P22692-2E-3	6.35	220	30	0.02	1.5	100	100.0000	0.7800	6.1205	100.7778	1.6796
7-1-91-1A-3	6.35	220	15	0.024	0.014	20	138.8889	5.9524	0.97818	144.8413	2.4140

Table A3. EMPA transect results. Red values indicated totals outside the acceptable range.

		Matrix corrected Oxide (wt.%)												
Sample	Distance from rim (µm)	SiO_2	Al_2O_3	Na_2O	MgO	TiO_2	Cl	K_2O	CaO	FeO	MnO	SO_3	H_2O	Total
EW91061-1-1	0	71.97	12.04	3.67	0.18	0.12	0.12	2.91	1.01	0.65	0.02	0.02	2.86	95.55
EW91061-1-1	20	73.83	12.16	3.55	0.18	0.13	0.11	2.91	1.00	0.65	n.d.	0.01	2.86	97.37
EW91061-1-1	39	74.57	11.99	3.53	0.18	0.13	0.11	3.01	0.98	0.53	0.05	n.d.	2.86	97.94
EW91061-1-1	59	72.50	12.20	3.60	0.17	0.11	0.09	3.14	1.02	0.71	0.03	0.01	2.86	96.43
EW91061-1-1	79	73.16	12.10	3.65	0.18	0.13	0.11	3.00	0.91	0.71	0.01	0.01	2.86	96.83
EW91061-1-1	99	72.42	12.02	3.76	0.17	0.09	0.11	2.99	0.89	0.73	0.04	0.02	2.86	96.11
EW91061-1-1	118	72.58	11.99	3.76	0.18	0.11	0.15	3.05	0.92	0.68	n.d.	0.04	2.86	96.32
EW91061-1-1	138	72.28	11.99	3.51	0.19	0.13	0.11	3.12	0.97	0.69	0.03	0.00	2.86	95.87
EW91061-1-1	158	71.72	12.14	3.76	0.18	0.13	0.13	2.94	0.94	0.67	0.06	0.01	2.86	95.53
EW91061-1-1	178	72.91	12.04	3.69	0.20	0.11	0.11	3.01	0.99	0.77	n.d.	0.00	2.86	96.67
3292-2A-1	0	72.99	11.89	3.85	0.15	0.08	0.12	3.04	0.86	0.53	0.03	0.02	3.31	96.86
3292-2A-1	22	0.22	0.01	n.d.	n.d.	n.d.	1.03	0.00	n.d.	n.d.	n.d.	0.03	3.31	4.60
3292-2A-1	45	72.89	11.88	3.92	0.16	0.13	0.10	3.27	0.86	0.61	0.04	0.00	3.31	97.17
3292-2A-2	0	73.09	11.73	2.16	0.15	0.14	0.10	3.01	0.85	0.66	0.05	0.01	3.38	95.32
3292-2A-2	21	72.96	11.95	3.74	0.15	0.11	0.12	3.10	0.85	0.57	0.08	0.00	3.38	96.99
3292-2A-2	41	73.87	11.97	3.71	0.16	0.12	0.12	3.11	0.82	0.59	0.04	0.02	3.38	97.90
3292-2A-2	62	73.75	11.92	3.52	0.16	0.11	0.10	3.10	0.92	0.66	0.02	0.02	3.38	97.65
3292-2A-2	82	72.54	12.06	3.81	0.14	0.11	0.10	3.12	0.85	0.63	n.d.	0.01	3.38	96.75
3292-2A-2	103	71.72	11.79	3.91	0.15	0.09	0.11	3.07	0.79	0.62	0.09	0.02	3.38	95.74
3292-2A-2	124	73.02	12.13	3.74	0.15	0.09	0.12	3.33	0.84	0.68	0.01	0.01	3.38	97.50
3292-2A-2	144	71.46	12.00	3.87	0.15	0.10	0.11	3.25	0.90	0.69	0.05	0.02	3.38	95.98
3292-2A-2	165	72.04	12.17	3.74	0.15	0.10	0.10	3.02	0.82	0.64	n.d.	0.01	3.38	96.17
3292-2A-2	185	75.08	12.28	3.60	0.16	0.12	0.10	3.24	0.87	0.49	0.08	0.01	3.38	99.39

Table A3. (continued) EMPA transect results. Red values indicated totals outside the acceptable range.

		Matrix corrected						Oxide (wt.%)						
Sample	Distance from rim (µm)	SiO_2	Al_2O_3	Na_2O	MgO	TiO_2	Cl	K_2O	CaO	FeO	MnO	SO_3	H_2O	Total
3292-2C-1	0	75.25	12.16	3.78	0.19	0.14	0.11	2.98	0.98	0.71	0.03	0.02	3.17	99.53
3292-2C-1	19	75.65	12.01	3.72	0.19	0.15	0.12	3.01	1.04	0.67	0.03	0.02	3.17	99.75
3292-2C-1	39	75.62	12.10	3.66	0.19	0.14	0.11	2.80	1.01	0.74	0.05	n.d.	3.17	99.59
3292-2C-1	58	75.73	12.16	3.87	0.19	0.12	0.10	2.92	1.05	0.77	0.06	0.02	3.17	100.17
3292-2C-1	77	74.75	12.10	3.64	0.19	0.17	0.11	2.86	1.09	0.66	n.d.	0.01	3.17	98.74
3292-2C-1	96	76.57	12.41	3.85	0.19	0.16	0.11	2.82	1.07	0.76	0.03	0.00	3.17	101.14
3292-2C-1	116	75.04	12.24	3.60	0.17	0.17	0.12	3.07	1.16	0.78	0.04	0.02	3.17	99.59
P22692-2E-5	0	76.85	12.67	4.06	0.20	0.13	0.11	3.09	1.02	0.79	0.03	0.02	1.83	100.80
P22692-2E-5	24	76.35	12.58	4.06	0.19	0.13	0.12	2.81	1.01	0.65	0.07	n.d.	1.83	99.80
P22692-2E-5	47	77.35	12.60	4.08	0.19	0.13	0.10	3.13	1.00	0.68	0.05	0.00	1.83	101.15
P22692-2E-4	0	75.51	12.59	3.99	0.19	0.10	0.11	3.22	0.99	0.62	0.01	0.01	3.13	100.47
P22692-2E-4	20	74.55	12.45	4.05	0.17	0.13	0.13	2.93	0.94	0.67	0.07	0.01	3.13	99.21
P22692-2E-4	41	74.57	12.63	4.03	0.19	0.15	0.13	3.12	0.93	0.74	0.01	0.01	3.13	99.63
P22692-2E-4	61	76.62	12.62	4.00	0.17	0.11	0.11	3.04	0.95	0.67	n.d.	0.01	3.13	101.44
P22692-2E-4	81	76.34	12.55	4.08	0.19	0.12	0.11	3.05	0.99	0.70	0.01	0.00	3.13	101.27
P22692-2E-4	101	76.85	12.69	4.01	0.16	0.12	0.11	3.08	0.95	0.66	0.03	0.01	3.13	101.81
P22692-2E-3	0	74.98	12.19	3.56	0.17	0.15	0.10	3.36	0.98	0.61	0.05	0.02	4.33	100.48
P22692-2E-3	19	72.69	12.37	3.67	0.16	0.10	0.14	3.29	0.80	0.72	0.08	0.02	4.33	98.36
P22692-2E-3	37	73.62	12.28	3.74	0.17	0.12	0.12	3.40	0.89	0.60	0.05	0.01	4.33	99.33
P22692-2E-3	56	75.38	12.18	3.56	0.18	0.13	0.11	3.12	0.88	0.57	0.06	0.01	4.33	100.52
P22692-2E-3	75	73.75	12.15	3.80	0.16	0.11	0.11	3.31	0.92	0.69	0.08	0.01	4.33	99.41

Table A3. (continued) EMPA transect results. Red values indicated totals outside the acceptable range.

		Matrix corrected Oxide (wt.%)												
Sample	Distance from rim (µm)	SiO_2	Al_2O_3	Na_2O	MgO	TiO_2	Cl	K_2O	CaO	FeO	MnO	SO_3	H_2O	Total
P22692-2E-2	0	73.16	12.38	3.64	0.21	0.15	0.11	3.12	0.97	0.81	0.08	0.00	4.31	98.92
P22692-2E-2	23	73.96	12.21	3.92	0.20	0.12	0.10	3.07	0.96	0.67	0.03	0.01	4.31	99.54
P22692-2E-2	45	72.76	12.20	3.86	0.20	0.13	0.12	3.23	0.95	0.70	0.06	0.02	4.31	98.52
7-1-91-1A-1	0	76.26	12.55	4.09	0.18	0.11	0.10	2.93	0.96	0.64	n.d.	0.01	2.00	99.82
7-1-91-1A-1	11	76.02	12.86	3.94	0.18	0.12	0.12	3.03	0.98	0.66	0.02	0.02	2.00	99.96
7-1-91-1A-2	0	73.55	12.33	3.88	0.18	0.11	0.11	2.90	0.97	0.57	0.09	0.01	2.62	97.31
7-1-91-1A-2	20	72.54	12.32	4.06	0.18	0.12	0.10	2.81	0.98	0.74	0.01	n.d.	2.62	96.46
7-1-91-1A-2	39	73.84	12.04	3.93	0.19	0.14	0.13	2.86	0.94	0.67	0.01	0.01	2.62	97.37
7-1-91-1A-2	59	73.98	12.58	4.01	0.18	0.13	0.11	3.15	0.92	0.71	0.06	0.01	2.62	98.47
7-1-91-1A-4	0	75.15	12.32	3.83	0.17	0.11	0.11	3.02	0.99	0.59	n.d.	0.01	2.62	98.91
7-1-91-1A-4	26	74.52	12.20	3.84	0.16	0.12	0.13	2.94	1.00	0.78	0.03	0.01	2.62	98.35
910819-3-1	0	72.17	12.28	3.82	0.24	0.11	0.12	2.82	1.20	0.82	0.02	0.02	3.07	96.69
910819-3-1	24	74.72	12.45	3.74	0.21	0.12	0.11	2.57	1.22	0.75	0.02	0.01	3.07	98.98
910819-3-1	48	73.13	12.20	3.92	0.22	0.14	0.12	2.67	1.21	0.70	0.01	0.01	3.07	97.41

Table A3. (continued) EMPA transect results. Red values indicated totals outside the acceptable range.

		Matrix corrected Oxide (wt.%)												
Sample	Distance from rim (µm)	SiO_2	Al_2O_3	Na_2O	MgO	TiO_2	Cl	K_2O	CaO	FeO	MnO	SO_3	H_2O	Total
7-3-91-1A-1(1)	0	73.45	12.26	3.98	0.17	0.15	0.11	2.77	1.02	0.65	0.01	0.01	2.56	97.13
7-3-91-1A-1(1)	19	72.48	12.30	3.78	0.19	0.13	0.10	2.94	0.91	0.63	0.03	0.01	2.56	96.06
7-3-91-1A-1(1)	38	73.43	12.24	3.68	0.16	0.15	0.12	2.91	0.90	0.70	0.03	0.01	2.56	96.87
7-3-91-1A-1(1)	57	74.04	12.20	3.77	0.19	0.11	0.10	2.99	0.98	0.65	0.03	0.02	2.56	97.62
7-3-91-1A-1(1)	76	72.44	12.02	3.68	0.18	0.14	0.11	2.95	0.90	0.54	0.02	0.00	2.56	95.53
7-3-91-1A-1(1)	95	73.40	12.36	3.79	0.18	0.14	0.12	3.04	0.91	0.65	0.04	0.01	2.56	97.19
7-3-91-1A-1(1)	114	74.63	12.42	3.95	0.18	0.13	0.12	2.76	0.92	0.68	0.05	0.01	2.56	98.40
7-3-91-1A-1(1)	133	74.53	12.34	4.05	0.18	0.11	0.11	2.94	1.05	0.62	0.04	0.02	2.56	98.56
7-3-91-1A-1(1)	152	73.60	12.54	3.97	0.19	0.11	0.12	2.89	1.00	0.70	0.06	0.01	2.56	97.74
7-3-91-1A-1(1)	171	75.70	12.49	4.11	0.18	0.12	0.11	2.87	1.02	0.66	0.01	0.01	2.56	99.85
7-3-91-1A-1(2)	0	77.39	12.19	3.79	0.17	0.11	0.11	3.31	1.00	0.69	0.04	0.01	2.56	101.36
7-3-91-1A-1(2)	15	77.13	12.84	3.92	0.18	0.13	0.11	3.28	1.00	0.65	0.03	0.01	2.56	101.83
7-3-91-1A-1(2)	30	78.29	12.77	4.11	0.16	0.11	0.09	3.30	0.96	0.56	0.03	0.00	2.56	102.95

Table A3. (continued) EMPA transect results.

		Uncorrected Oxide (wt.%)											
Sample	Distance from rim (μm)	SiO_2	Al_2O_3	Na_2O	MgO	TiO_2	Cl	K_2O	CaO	FeO	MnO	SO_3	Total
EW91061-1-1	0	71.76	11.93	3.63	0.18	0.12	0.12	2.90	1.00	0.65	0.02	0.02	92.32
EW91061-1-1	20	73.62	12.06	3.51	0.18	0.13	0.10	2.89	0.99	0.65	-0.01	0.01	94.14
EW91061-1-1	39	74.36	11.89	3.49	0.17	0.13	0.11	2.99	0.97	0.53	0.05	-0.01	94.70
EW91061-1-1	59	72.30	12.10	3.56	0.17	0.11	0.09	3.12	1.01	0.71	0.03	0.01	93.19
EW91061-1-1	79	72.95	12.00	3.61	0.18	0.13	0.11	2.99	0.90	0.70	0.01	0.01	93.59
EW91061-1-1	99	72.22	11.92	3.71	0.17	0.09	0.11	2.98	0.89	0.72	0.04	0.02	92.87
EW91061-1-1	118	72.37	11.89	3.72	0.18	0.11	0.15	3.03	0.91	0.68	0.00	0.04	93.08
EW91061-1-1	138	72.07	11.88	3.47	0.18	0.12	0.11	3.10	0.97	0.69	0.03	0.00	92.63
EW91061-1-1	158	71.51	12.03	3.72	0.18	0.13	0.13	2.92	0.94	0.67	0.06	0.01	92.29
EW91061-1-1	178	72.70	11.93	3.65	0.20	0.11	0.11	3.00	0.98	0.77	-0.04	0.00	93.44
3292-2A-1	0	72.75	11.77	3.80	0.14	0.08	0.12	3.02	0.86	0.53	0.03	0.02	93.12
3292-2A-1	22		0.01	-0.01	0.00	-0.02	1.05	0.00	-0.02	-0.01	-0.03	0.03	1.27
3292-2A-1	45	72.64	11.76	3.87	0.16	0.13	0.10	3.26	0.85	0.61	0.04	0.00	93.42
3292-2A-2	0	72.84	11.60	2.13	0.14	0.14	0.10	2.99	0.85	0.65	0.05	0.01	91.50
3292-2A-2	21	72.71	11.83	3.69	0.15	0.11	0.11	3.08	0.85	0.56	0.08	0.00	93.16
3292-2A-2	41	73.62	11.85	3.67	0.16	0.12	0.12	3.10	0.81	0.58	0.04	0.02	94.08
3292-2A-2	62	73.50	11.80	3.47	0.16	0.11	0.10	3.08	0.92	0.65	0.02	0.02	93.83
3292-2A-2	82	72.30	11.94	3.76	0.14	0.11	0.10	3.10	0.84	0.63	-0.03	0.01	92.93
3292-2A-2	103	71.48	11.67	3.86	0.15	0.09	0.11	3.05	0.79	0.62	0.09	0.02	91.92
3292-2A-2	124	72.78	12.01	3.69	0.15	0.09	0.12	3.31	0.84	0.67	0.01	0.01	93.68
3292-2A-2	144	71.22	11.88	3.82	0.15	0.10	0.11	3.23	0.89	0.69	0.05	0.02	92.15
3292-2A-2	165	71.80	12.05	3.70	0.15	0.10	0.10	3.00	0.82	0.64	-0.02	0.01	92.35
3292-2A-2	185	74.82	12.15	3.56	0.16	0.12	0.10	3.22	0.86	0.49	0.08	0.01	95.56

Table A3. (continued) EMPA transect results.

		Uncorrected Oxide (wt.%)											
Sample	Distance from rim (μm)	SiO_2	Al_2O_3	Na_2O	MgO	TiO_2	Cl	K_2O	CaO	FeO	MnO	SO_3	Total
3292-2C-1	0	75.02	12.05	3.73	0.19	0.14	0.11	2.97	0.98	0.70	0.03	0.02	95.93
3292-2C-1	19	75.41	11.90	3.67	0.19	0.15	0.12	3.00	1.03	0.66	0.03	0.02	96.15
3292-2C-1	39	75.38	11.98	3.62	0.19	0.13	0.11	2.78	1.01	0.73	0.05	-0.01	95.99
3292-2C-1	58	75.49	12.04	3.83	0.18	0.12	0.10	2.91	1.04	0.77	0.06	0.02	96.57
3292-2C-1	77	74.51	11.99	3.59	0.18	0.16	0.11	2.84	1.09	0.66	-0.01	0.01	95.15
3292-2C-1	96	76.33	12.30	3.80	0.18	0.16	0.11	2.81	1.07	0.76	0.03	0.00	97.54
3292-2C-1	116	74.80	12.13	3.56	0.17	0.17	0.12	3.06	1.15	0.77	0.04	0.02	95.99
P22692-2E-5	0	76.71	12.61	4.03	0.19	0.13	0.11	3.08	1.02	0.79	0.03	0.02	98.71
P22692-2E-5	24	76.21	12.51	4.04	0.19	0.13	0.12	2.80	1.01	0.65	0.07	0.00	97.72
P22692-2E-5	47	77.21	12.54	4.05	0.19	0.13	0.10	3.12	1.00	0.68	0.05	0.00	99.07
P22692-2E-4	0	75.28	12.47	3.95	0.19	0.10	0.11	3.21	0.99	0.62	0.01	0.01	96.92
P22692-2E-4	20	74.32	12.34	4.00	0.17	0.12	0.13	2.91	0.93	0.66	0.07	0.01	95.67
P22692-2E-4	41	74.34	12.51	3.99	0.19	0.15	0.13	3.11	0.93	0.73	0.01	0.01	96.08
P22692-2E-4	61	76.39	12.51	3.95	0.17	0.11	0.11	3.02	0.95	0.67	0.00	0.01	97.89
P22692-2E-4	81	76.11	12.43	4.04	0.18	0.12	0.11	3.03	0.98	0.70	0.01	0.00	97.72
P22692-2E-4	101	76.62	12.57	3.96	0.16	0.12	0.11	3.06	0.95	0.66	0.03	0.01	98.26
P22692-2E-3	0	74.65	12.04	3.50	0.17	0.15	0.10	3.34	0.97	0.61	0.04	0.02	95.58
P22692-2E-3	19	72.37	12.22	3.61	0.15	0.10	0.14	3.27	0.79	0.72	0.08	0.02	93.46
P22692-2E-3	37	73.31	12.13	3.68	0.17	0.12	0.12	3.37	0.88	0.60	0.05	0.01	94.43
P22692-2E-3	56	75.06	12.03	3.50	0.18	0.13	0.11	3.10	0.87	0.57	0.06	0.01	95.61
P22692-2E-3	75	73.43	12.00	3.74	0.16	0.10	0.11	3.28	0.91	0.69	0.08	0.01	94.51

Table A3. (continued) EMPA transect results.

		Uncorrected Oxide (wt.%)											
Sample	Distance from rim (μm)	SiO_2	Al_2O_3	Na_2O	MgO	TiO_2	Cl	K_2O	CaO	FeO	MnO	SO_3	Total
P22692-2E-2	0	72.85	12.22	3.59	0.21	0.15	0.10	3.10	0.96	0.80	0.08	0.00	94.05
P22692-2E-2	23	73.65	12.05	3.86	0.19	0.12	0.10	3.05	0.95	0.66	0.03	0.01	94.66
P22692-2E-2	45	72.45	12.04	3.79	0.20	0.13	0.12	3.20	0.94	0.69	0.06	0.02	93.64
7-1-91-1A-1	0	76.11	12.47	4.06	0.18	0.11	0.10	2.92	0.96	0.63	0.00	0.01	97.55
7-1-91-1A-1	11	75.88	12.78	3.91	0.18	0.12	0.12	3.02	0.98	0.66	0.02	0.02	97.68
7-1-91-1A-2	0	73.36	12.23	3.84	0.18	0.11	0.11	2.88	0.97	0.57	0.09	0.01	94.34
7-1-91-1A-2	20	72.36	12.23	4.02	0.17	0.12	0.10	2.79	0.97	0.74	0.01	-0.01	93.50
7-1-91-1A-2	39	73.64	11.94	3.89	0.18	0.14	0.13	2.85	0.94	0.66	0.01	0.01	94.40
7-1-91-1A-2	59	73.79	12.49	3.97	0.18	0.13	0.11	3.14	0.92	0.70	0.06	0.01	95.50
7-1-91-1A-4	0	74.95	12.22	3.79	0.17	0.11	0.11	3.01	0.98	0.58	-0.01	0.01	95.94
7-1-91-1A-4	26	74.33	12.10	3.81	0.16	0.12	0.13	2.93	1.00	0.78	0.03	0.01	95.38
910819-3-1	0	71.95	12.17	3.78	0.23	0.11	0.12	2.80	1.19	0.82	0.02	0.02	93.22
910819-3-1	24	74.50	12.33	3.70	0.20	0.12	0.11	2.56	1.21	0.75	0.02	0.01	95.50
910819-3-1	48	72.91	12.09	3.88	0.22	0.14	0.12	2.66	1.20	0.70	0.01	0.01	93.94

Table A3. (continued) EMPA transect results.

		Uncorrected Oxide (wt.%)											
Sample	Distance from rim (μm)	SiO_2	Al_2O_3	Na_2O	MgO	TiO_2	Cl	K_2O	CaO	FeO	MnO	SO_3	Total
7-3-91-1A-1(1)	0	73.27	12.16	3.94	0.17	0.15	0.11	2.76	1.02	0.64	0.01	0.01	94.24
7-3-91-1A-1(1)	19	72.30	12.21	3.74	0.19	0.13	0.10	2.93	0.90	0.63	0.03	0.01	93.17
7-3-91-1A-1(1)	38	73.24	12.14	3.64	0.16	0.15	0.12	2.90	0.89	0.70	0.03	0.01	93.97
7-3-91-1A-1(1)	57	73.85	12.10	3.73	0.19	0.11	0.10	2.98	0.97	0.65	0.03	0.02	94.72
7-3-91-1A-1(1)	76	72.26	11.92	3.64	0.17	0.14	0.11	2.93	0.90	0.54	0.02	0.00	92.64
7-3-91-1A-1(1)	95	73.21	12.27	3.75	0.18	0.14	0.12	3.02	0.91	0.65	0.04	0.01	94.30
7-3-91-1A-1(1)	114	74.44	12.32	3.92	0.18	0.13	0.12	2.75	0.92	0.68	0.04	0.01	95.51
7-3-91-1A-1(1)	133	74.35	12.25	4.01	0.18	0.11	0.11	2.93	1.05	0.61	0.04	0.02	95.66
7-3-91-1A-1(1)	152	73.42	12.45	3.93	0.19	0.11	0.12	2.88	1.00	0.69	0.06	0.01	94.85
7-3-91-1A-1(1)	171	75.51	12.40	4.07	0.18	0.12	0.11	2.85	1.02	0.66	0.01	0.01	96.94
7-3-91-1A-1(2)	0	77.19	12.10	3.75	0.17	0.11	0.11	3.30	0.99	0.69	0.04	0.01	98.45
7-3-91-1A-1(2)	15	76.93	12.74	3.89	0.18	0.13	0.11	3.27	0.99	0.65	0.03	0.01	98.92
7-3-91-1A-1(2)	30	78.09	12.68	4.08	0.16	0.11	0.09	3.28	0.95	0.56	0.03	0.00	100.04

Table A4. Results of BND modeling.

Sample	N_{vcorr} (mm^3)	N_{vcorr} (m^3)	Toramaru (2006) dP/dt (0.025)	Toramaru (2006) dp/dt (0.06)	Hajimirza (2021) dP/dt (MPa/s) @780C	@850C	@950C	conduit radius (m) @780C
P22692-2C	1.17E+06	1.17E+15	10.5	60	0.297	0.425	0.769	17
	2.11E+06	2.11E+15	7.5	42	0.491	0.705	1.309	16
7-1-91-1A	3.48E+06	3.48E+15	15	90	0.752	1.09	2.045	14
	2.16E+06	2.16E+15	11	60	0.502	0.719	1.335	15
	2.38E+06	2.38E+15	11.5	70	0.545	0.784	1.453	15
3292-2A	9.78E+05	9.78E+14	6.5	37.5	0.256	0.365	0.653	17
	1.70E+06	1.70E+15	9.5	50	0.407	0.581	1.073	16
3292-2C	6.84E+05	6.84E+14	5	29	0.191	0.271	0.475	19
	2.32E+05	2.32E+14	2.5	14.5	0.085	0.126	0.205	23
	4.15E+06	4.15E+15	17	100	0.867	1.271	2.357	14
7-3-91-1A	7.39E+05	7.39E+14	5.5	31.5	0.204	0.291	0.511	19
	6.98E+05	6.98E+14	5	29	0.195	0.277	0.485	19
	1.23E+06	1.23E+15	7.5	42	0.311	0.441	0.802	17
P-6-21-91-1	1.78E+06	1.78E+15	9.5	50	0.425	0.608	1.125	16
	1.45E+06	1.45E+15	8.5	50	0.356	0.509	0.935	17
	2.80E+06	2.80E+15	12.5	70	0.625	0.901	1.679	15
P22692-2E	1.18E+06	1.18E+15	7	40	0.3	0.425	0.769	17
	8.18E+05	8.18E+14	5.5	31.5	0.221	0.315	0.551	18
	1.19E+06	1.19E+15	10	60	0.302	0.431	0.775	17

Toramaru Parameters:	
melt density	2350
C_{H2O} initial (%)	6.4
T(K)	1053
P_{SAT} (Pa)	220000000
D_{H2O} (m^2/s)	5.81E-11
V_M (m^3)	3.38E-29

Hajimirza Parameters:	
P_H2O	220
T	780
crys	0.38
theta	155
MDR	6.30E+06

Table A5. FTIR Water transect results. Struck out values indicate points with quartz interference which wer not included in modeling

3292-2C-1			
distance from bubble (μm)	absorbance (3570 cm^{-1})	H_2O (wt. %)	error (wt.%)
0	1.028	2.43	0.17
10	1.139	2.71	0.19
20	1.193	2.84	0.20
30	1.248	2.99	0.21
40	1.281	3.07	0.21
50	1.308	3.14	0.22
60	1.314	3.16	0.22
70	1.316	3.16	0.22
80	1.306	3.14	0.22
90	1.258	3.01	0.21
100	1.205	2.87	0.20
110	1.062	2.51	0.18

P22692-2E-5			
distance from bubble (μm)	absorbance (3570 cm^{-1})	H_2O (wt. %)	error (wt.%)
0	0.375	1.05	0.10
10	0.553	1.57	0.15
20	0.607	1.73	0.17
30	0.632	1.81	0.18
40	0.635	1.81	0.18
50	0.611	1.74	0.17
60	0.565	1.61	0.16
70	0.447	1.26	0.12

P22692-2E-4			
distance from bubble (μm)	absorbance (3570 cm^{-1})	H_2O (wt. %)	error (wt.%)
0	0.76	2.12	0.18
10	0.9	2.54	0.21
20	0.98	2.78	0.23
30	1.02	2.90	0.24
40	1.06	3.02	0.25
50	1.08	3.08	0.26
60	1.09	3.12	0.26
70	1.08	3.08	0.26
80	1.08	3.08	0.26
90	1.01	2.87	0.24
100	0.875	2.46	0.20

EW910612-1-1			
distance from bubble (μm)	absorbance (3570 cm^{-1})	H_2O (wt. %)	error (wt.%)
0	1.573	2.46	0.25
10	1.662	2.61	0.27
20	1.729	2.72	0.28
30	1.745	2.75	0.28
40	1.75	2.76	0.28
50	1.778	2.80	0.29
60	1.758	2.77	0.28
70	1.793	2.83	0.29
80	1.781	2.81	0.29
90	1.752	2.76	0.28
100	1.785	2.82	0.29
110	1.733	2.73	0.28
120	1.789	2.82	0.29
130	1.801	2.84	0.29
140	1.768	2.79	0.28
150	1.77	2.79	0.28
160	1.769	2.79	0.28
170	1.771	2.79	0.28
180	1.717	2.70	0.27

7-1-91-1A-1			
distance from bubble (μm)	absorbance (3570 cm^{-1})	H_2O (wt. %)	error (wt.%)
0	0.322	1.41	0.14
10	0.388	1.71	0.17
20	0.428	1.89	0.19
30	0.446	1.97	0.20
40	0.446	1.97	0.20
50	0.363	1.59	0.16

7-1-91-1A-2			
distance from bubble (μm)	absorbance (3570 cm^{-1})	H_2O (wt. %)	error (wt.%)
0	0	0.00	
10	0.634	1.17	0.11
20	1.119	2.11	0.20
30	1.295	2.46	0.23
40	1.367	2.61	0.24
50	1.34	2.56	0.24
~~60~~	~~1.221~~	~~2.32~~	~~0.22~~

Table A5. FTIR Water transect results. Struck out values indicate points with quartz interference which were not included in modeling

7-1-91-1A-3			
distance from bubble (μm)	absorbance (3570 cm^{-1})	H_2O (wt. %)	error (wt.%)
0	1.229	1.71	0.14
10	1.156	1.61	0.13
20	1.149	1.60	0.13
30	1.230	1.71	0.14
40	1.325	1.85	0.15
50	1.451	2.04	0.17
60	1.620	2.29	0.19
70	1.737	2.46	0.20
80	1.886	2.69	0.22
90	2.021	2.89	0.24
100	2.152	3.10	0.26
110	2.288	3.31	0.28
120	2.362	3.42	0.29
130	2.385	3.46	0.29
140	2.329	3.37	0.28
~~150~~	~~2.183~~	~~3.14~~	~~0.26~~
~~160~~	~~1.823~~	~~2.59~~	~~0.22~~
~~170~~	~~1.065~~	~~1.48~~	~~0.12~~

3292-2A-2			
distance from bubble (μm)	absorbance (3570 cm^{-1})	H_2O (wt. %)	error (wt.%)
0	0.757	2.18	0.15
10	0.922	2.69	0.19
20	1.006	2.95	0.21
30	1.055	3.11	0.22
40	1.1	3.25	0.23
50	1.12	3.31	0.24
60	1.133	3.35	0.24
70	1.138	3.37	0.24
80	1.135	3.36	0.24
90	1.128	3.34	0.24
100	1.119	3.31	0.24
110	1.111	3.28	0.23
~~120~~	~~1.093~~	~~3.23~~	~~0.23~~
~~130~~	~~1.076~~	~~3.17~~	~~0.23~~
~~140~~	~~1.056~~	~~3.11~~	~~0.22~~
~~150~~	~~1.027~~	~~3.02~~	~~0.21~~
~~160~~	~~0.999~~	~~2.93~~	~~0.21~~
~~170~~	~~0.955~~	~~2.79~~	~~0.20~~
~~180~~	~~0.892~~	~~2.59~~	~~0.18~~

910819-3-1			
distance from bubble (μm)	absorbance (3570 cm^{-1})	H_2O (wt. %)	error (wt.%)
0	0.032	0.10	0.01
10	0.039	0.13	0.01
20	0.075	0.24	0.02
30	0.163	0.53	0.05
40	0.309	1.01	0.09
50	0.502	1.67	0.15
60	0.689	2.33	0.21
70	0.832	2.84	0.26
80	0.891	3.06	0.28
90	0.847	2.90	0.26
~~100~~	~~0.66~~	~~2.22~~	~~0.20~~

7-3-91-1A-1			
distance from bubble (μm)	absorbance (3570 cm^{-1})	H_2O (wt. %)	error (wt.%)
0	1.139	1.72	0.22
10	1.36	2.07	0.27
20	1.443	2.20	0.29
30	1.519	2.33	0.30
40	1.564	2.40	0.31
50	1.624	2.50	0.33
60	1.656	2.55	0.33
70	1.657	2.55	0.33
80	1.659	2.55	0.33
90	1.605	2.47	0.32
100	1.502	2.30	0.30

P22692-2E-3			
distance from bubble (μm)	absorbance (3570 cm^{-1})	H_2O (wt. %)	error (wt.%)
0	1.118	3.30	0.33
10	1.241	3.69	0.37
20	1.376	4.14	0.42
30	1.371	4.12	0.42
40	1.429	4.32	0.44
50	1.423	4.30	0.44
60	1.337	4.01	0.41
~~70~~	~~1.232~~	~~3.67~~	~~0.37~~
~~80~~	~~0.979~~	~~2.86~~	~~0.29~~
~~90~~	~~0.623~~	~~1.77~~	~~0.18~~